Winter 2013

Visualizing and Understanding Tectonism and Volcanism on Earth and Other Terrestrial Bodies

Mladen M. Dordevic
Old Dominion University

VISUALIZING AND UNDERSTANDING TECTONISM AND VOLCANISM ON EARTH AND OTHER TERRESTRIAL BODIES

by

Mladen M. Dordevic
B.S. June 2008, University of Belgrade, Serbia
M.S. May 2010, Old Dominion University

A Dissertation Submitted to the Faculty of
Old Dominion University in Partial Fulfillment of the
Requirements for the Degree of

DOCTOR OF PHILOSOPHY

PHYSICS

OLD DOMINION UNIVERSITY
December 2013

Approved by:

Declan De Paor (Co-Director)

Jennifer Georgen (Co-Director)

Leposava Vušković (Member)

Alexander L. Godunov (Member)

Carol Simpson (Member)

ABSTRACT

VISUALIZING AND UNDERSTANDING TECTONISM AND VOLCANISM ON EARTH AND OTHER TERRESTRIAL BODIES

Mladen M. Dordevic
Old Dominion University, 2013
Co-Directors: Dr. Declan De Paor
Dr. Jennifer Georgen

This dissertation presents new methods of visualizing, teaching, assessing, modeling, and understanding tectonics on Earth and other celestial bodies. Tectonics is the study of planetary lithospheres and includes impact, plate, plume, cryo- and gravitational mechanisms. This dissertation is concerned with plate tectonics and plate/mantle plume interactions. Plate tectonics describes the mainly horizontal motion of lithospheric plates over the asthenosphere. Lithosphere is created at ridges and consumed at subduction zones. In addition to the plate tectonic system, mantle plumes also contribute to mass motions in the subsurface Earth. Both plate tectonics and plume upwelling processes help shape the present form of the planetary surface, including long volcanic island chains, deep ocean basins, and plate boundary triple junctions. Better understanding of these processes by visualization and numerical modeling is one of the primary goals of this study.

In the geospatial analysis lab at ODU, our research methodology starts with the creation of visualizations for teaching. These include Google Earth-based virtual field explorations enhanced with digitized specimens and emergent geological and geophysical cross sections. We test these in classes with IRB compliance and sometimes this leads to the discovery of tectonic research questions which we then explore. Settings studied in this investigation are Tonga Trench in the western Pacific Ocean, Artemis on Venus, the Hawaiian-Emperor seamount chain, and the Azores triple junction. Some of these cases pose specific geophysical problems that were selected for further study.

The Tonga Trench is a subduction zone that includes trench rollback and opening of a marginal basin–the Lau Basin. The rollback process is difficult to imagine, and therefore we created a set of instructional resources using COLLADA models and the Google Earth Application Programming Interface (API). Animated models for the

Tonga Trench and Lau Basin helped explained rollback as shown by our outcomes assessments tests and exploration of different initiations of the subduction process led to a new alternative hypothesis for rollback.

Virtual field explorations required the development of new interface features for the Google Earth API. All these instructional materials were combined into modular multi–user virtual field trip experiences and were subject to IRB-compliant evaluation of learning outcomes. Animated COLLADA models for the Hawaii Islands and Emperor Seamounts helped explain the origin and time progression of the island chain. From seismic data, a three-dimensional reconstruction of the Hawaiian mantle plume was created raising the question of the horizontal advection of the plume conduit in the mantle and its correlation with the change in trend of the islands. The Hawaiian–Emperor chain on Earth is spread out as the Pacific plate is moving over the Hawaiian mantle plume. On Venus, however, the Artemis structure was able to grow to super-plume size due to the absence of plate motion. For Venus, visualization was done on a much larger scale, including cross sections of the whole plate showing large plume structures, and Magellan SARS imagery of surface features.

In the Azores triple junction, dispersion of plume material is influenced by plate boundary geometry, creating anomalies in seafloor geophysical data for several hundred kilometers away from the plume center. To explore the interaction between a mantle plume and a plate boundary triple junction, a series of three-dimensional finite element numerical models was calculated. A parameter space investigation changed the location of the plume conduit and its volume flux, as well as the treatment of viscosity. Flow patterns, dynamical topography, relative crustal thickness variations and waist width scaling relationships resulting from these calculations give valuable insight into the importance of triple junction configuration in the dispersion of plume material.

ACKNOWLEDGMENTS

First, I would like to thank my dissertation advisor Dr. Declan De Paor without whom this research work would not be possible. I am vary grateful for all your patience, support, encouragement and understanding over these years. Also, I would like to thank my co-advisor Dr. Jennifer Georgen for her guidance and invaluable input about every problem I faced while working on this dissertation. Thank you for making your computational resources and software available for the numerical modeling work. I would like to express my sincere gratitude to my graduate committee for taking part in this work.

My special thanks goes to Dr. Leposava Vušković and Dr. Svetozar Popović for all their immense help and support in both professional and personal growth. The two of you, together with my flatmates: Ivan, Miloš, Milka, Ana, and Filip made my stay here filled with memories that I will cherish for ever. I consider all of you my second family.

To all my friends from Serbia, thank you guys for being there for me. Mom, dad, sis, thank you for all your unconditional love and support, I could not have made it without you. Finally to my little niece, I am excited to finally meet you. I dedicate this dissertation to you.

My research was supported in part by National Science Foundation (NSF) CCLI 0837040, NSF TUES 1022755, NSF GEO 1034643, and a Google Faculty Research Award. Any opinions, findings, and conclusions or commendations expressed in this thesis are those of the author and do not necessarily reflect the views of the National Science Foundation or Google Inc. I benefited from collaborations with Steven Whitmeyer, Vicki Hansen, John Bailey, and Richard Treves, and NSF independent assessor Janice Gobert.

TABLE OF CONTENTS

TABLE OF CONTENTS

LIST OF TABLES

LIST OF TABLES

LIST OF FIGURES

CHAPTER 1

INTRODUCTION

My study includes geophysical numerical modeling, computer visualization, and the development and testing of resources for geoscience education. The policy of the geospatial analysis group is to find research questions by developing cross–disciplinary (Physics and OEAS) educational resources. I created models to explain different types of tectonics and this lead to an interest in research problems related to plate tectonics versus plume volcanism.

Tectonics is concerned with the evolution of the rocky parts of planets and moons. There are four types of tectonics: Impact Tectonics, Plate Tectonics, Cryotectonics, and Gravitational Tectonics. This dissertation is concerned with past and/or present day plate tectonics and plume dynamics on Venus, Earth, Mars, and Io. Mercury and the Moon were omitted because their size precludes significant plate tectonics or plume convection and Io was included despite its small size because tidal stresses promote plume like upwelling there.

1.1 PLATE TECTONICS ON EARTH

Earth, along with other terrestrial planets, was created 4.568 b.y. ago from the inner portion of the proto planetary disk. The main composition of the proto planetary disk was chondritic and refractory as a result of elevated temperatures. The rate at which proto planetary bodies grew depended on their mass, so that larger ones ended up gravitationally pulling in smaller ones. This resulted in impacts that raised the mass and the internal temperature of proto-planetary bodies producing even faster growth. Between 30 and 100 m.y. after the start of accrtion, frequent [*Rudge et al.*, 2010] collisions with other smaller bodies and radioactive decay produced enough heat to melt the chondritic mixture of silicate, sulfide and iron that comprised the Earth. This melt and density difference in mixture led to core–mantle differentiation. Earth's initial komataiitic crust was a chilling of the magma ocean and was dominated by impact tectonics but none survives because of reworking by subsequent plate tectonics.

In subdivision by chemical properties, the two outermost layers of the Earth are the crust and mantle. The mantle contains the majority of the Earth's volume and mass, and it is mainly composed of Fe, Mg, Si, and O. The upper mantle has an average density of $3.3\,g/cm^3$. The overlying relatively thin crust consists of two types: oceanic and continental. Oceanic crust has an average thickness of $5-7\,km$. It is produced by mantle partial melting and is mainly composed of basaltic rock with an average density of $3.0\,g/cm^3$. Continental crust is produced at tectonic arcs and other locations and its thickness averages about $35\,km$. It is thin at passive margins and thick under mountains. Compared to oceanic crust, it has slightly lower density corresponding to granite rock, $2.65\,g/cm^3$.

In subdivision by mechanical and thermal properties, the two outermost layers of the Earth are the lithosphere and asthenosphere. The lithosphere is a rigid, brittle, and relatively cool layer that deforms by fracture except in narrow zones of ductile deformation. High viscosity in this layer make conduction the main mechanism for heat transfer. The lithosphere rests on the asthenosphere [*Foucher*, 1982; *Mutter et al.*, 1988]. The asthenospheric temperature is higher than the temperature in the lithosphere, resulting in lower viscosity and the ability to deforms plastically. Those properties enable it to flow over geological time resulting in mainly convective heat flow in a nearly adiabatic temperature environment. There is the possibility for partial melting over certain depth ranges in the asthenosphere [*Foucher*, 1982; *Mutter et al.*, 1988].

Having this categorization of Earth's layers in mind, the plate tectonics model describes the motion of the lithosphere over the asthenosphere. This lithospheric shell is broken into approximately twelve major and other minor plates that are in relative motion with respect to each other. There are three types of plate boundaries: divergent, conservative, and convergent.

Divergent plate boundaries are also known as spreading ridges. The thinnest and youngest lithosphere can be found along mid oceanic spreading ridges. Buoyant forces that are pushing lithosphere away from the spreading ridges, ridge push, are counted as one of the sources for plate motion. The second type of plate boundary, conservative, can be seen at transform faults and offsets where two plates are moving side by side. For the convergent plate boundary type, there are three distinct subtypes based upon the type of the crust participating: island arcs, continental arcs, and continent continent collision zones. In subduction zones, older and more dense

oceanic lithosphere returns to the asthenosphere pulling the trailing portion of the plate and therefore contributing to plate driving forces [*Forsyth and Uyeda*, 1975; *Chapple and Tullis*, 1977]. This force is known as slab pull [*Schellart*, 2004]. One method of continental growth is by arc accretion.

The regions along the plate boundaries in most cases are associated with volcanic chains and elevated seismicity. Large earthquake tend to occur in subduction zones, where strong stresses are present. Magma rises in island arcs (e.g. Tonga) or continental arcs (e.g. Andes). An excellent explanation for these patterns is provided by the plate tectonic model. Under ocean ridges the source of melt is upper mantle that is undergoing partial decompressional melting. Melt is allocated to crustal magma chambers, from which it erupts to the surface. On the cold subducting slab, the presence of volatiles and phase changes can trigger partial melting in the overlying mantle wedge [*Peacock*, 1990; *Kerrick and Connolly*, 2001].

A particularly interesting case of the complex tectonics ongoing in a subduction zone is the the Tonga Trench. The Tonga Trench is located in the vicinity of American Samoa Island Arc and is comprised of the Pacific plate subducting beneath the Australian plate [*Sykes*, 1966; *Frohlich*, 1989]. The trench terminates on its north end near the American Samoa transform. Above the point of the termination, the Pacific plate continues moving westward without subducting. Even though the Pacific plate is moving westward the immaterial line of the Tonga Trench is moving in the opposite direction, rolling back. This rollback is responsible for creating the marginal basin called the Lau Basin [*Uyeda and Kanamori*, 1979; *Moores and Twiss*, 1995; *Rosenbaum and Lister*, 2004]. This concept of trench rollback and marginal basins formation is hard to explain to students. We created animated Tonga models in Google Earth to help students visualize these processes. Creation of these teaching resources lead to research questions about new possible explanations for the Tonga rollback.

1.2 TECTONICS OF OTHER TERRESTRIAL BODIES

Despite surface differences, models for solar system evolution suggest that Venus and Earth share similar rocky mantle and metallic core compositions [*Wetherill*, 1990]. Geomorphic and geochemical arguments, along with limited data from the Soviet Venera and Vega landers, are consistent with a dry basaltic crust. Being dry, the crust is stronger than Earth's basaltic rocks despite temperatures that would

promote plastic deformation in wet rocks [*Mackwell et al.*, 1998]. Although Venus is ultra-dry today, water may have played a role in the past. Isotopic data are consistent with (but do not require) an extensive water reservoir $\sim$ 1 b.y. ago [*Donahue et al.*, 1997; *Donahue and Russell*, 1997; *Hunten*, 2002]. Conditions for retaining such reservoirs are not predicted by climate models [*Bullock and Grinspoon*, 2001; *Phillips et al.*, 2001; *Taylor and Grinspoon*, 2009].

Venus's surface features are similar to some on Earth, and yet also much larger. A wide variety of volcanic landforms, preserved at a range of scales, occur across the Venusian surface (see *Crumpler et al.* [1997]; *Lopez* [2011]). Volcanic shields, 1-20 km in diameter, occur in shield fields up to 300 km across and as "shield terrain" distributed across millions of square kilometers. Lava flows up to hundreds of kilometers long are commonly associated with volcanoes, coronae, and fractures. Volcanic forms are generally consistent with basaltic compositions [*Bridges*, 1995, 1997; *Stofan et al.*, 2000]. However, there are no arcuate volcanic arcs comparable to the products of subduction on Earth.

Earth like surface features such as river channels, sand dunes, etc., are completely absent from Venus. This presents a challenge both to the educator and the presenter of research results. Huge repositories of exciting data on Venus from NASA and ESA orbital missions but they are accessed mainly by dedicate researchers.

To help rectify this situation, we have created a Google Venus virtual globe built on a Google Earth foundation with extensive use of COLLADA models (http://collada.org). Our model includes atmospheric imagery, emergent blocks, and cross sections of the planet's crust and mantle that illustrate current interpretations of its internal structure. We present some of Venus's unique tectonic structures, the Ishtar region and the Artemis superplume structure. Google Venus effectively conveys the benefits of virtual globe style touring and zooming in helping geoscientists to truly understand planetary structures on a range of scales.

Similar instructional resources were produced for Mars and Io using Google Earth as the base. For Mars, an explanation of the size of Olympus Mons, the biggest volcano in the solar system was offered. A theoretical analogy was drawn to Earth's Pacific plate and the Hawaiian mantle plume, as if plate tectonics was not happening. By comparison of the area of Olympus Mons to the Earth's Kilauea volcano a sense of scale was obtained. On Io, on the other hand, using COLLADA models, the role of sulfur in volcanic eruption was developed. These learning resources were presented

at national conferences [*Dordevic et al.*, 2009, 2010] and offered for download on the DigitalPlanet.org and DigitalPlanets.org web sites. Due to the importance of Venus with its Artemis super plume structure, it was selected for more in depth development.

1.3 PLUME DYNAMICS ON EARTH

Plate tectonics fails to provide a reasonable explanation for the origin of islands and seamount chains like the Hawaiian Emperor chain far away from plate boundaries. It is believed that in such locations the source of ocean island basalts are deep mantle plumes [*Morgan*, 1972]. Chemical and thermal variations at the core mantle boundary, D", at approximately $2900\,km$ depth may become unstable due to heating from the core. These instabilities rise through cooler ambient mantle forming a long thin stem and a mushroom shaped head. Deep mantle plumes formed like this should meet the following criteria [*Courtillot et al.*, 2003; *Lvova*, 2010]: (1) an area of excess magmatism at the surface, (2) distinct geochemical differences relative to igneous rock produced by plate tectonics, (3) stationarity of the plumes with respect to the core and each other, and (4) correlation with geological structures. Studies have debated the number of deep mantle, or "primary," plumes. The remaining hotspots could either come from (1) plumes originating on the bottom of mantle transition zone ($\sim 420 - 670\,km$ below the surface) on the top of large transient domes corresponding to the superswells (e.g., *Courtillot et al.* [2003]) or (2) upper mantle features caused by tensional stresses in the lithosphere and decompressional melting (e.g., *Anderson* [1995]).

To help students visualize plume dynamics I designed an animated COLLADA model of the Hawaiian plume overridden by the Pacific plate. In this model students will be able to see important features as time progression, plume source, and plume stationarity. Alongside with a pictographic representation of the mantle plume, a three-dimensional model of the plume reconstructed from seismic data was done as well.

1.4 NUMERICAL MODELING AND SIMULATION

Beside plate-plume interaction far away from plate margins, a more common case is plume-ridge interactions at divergent plate boundaries. It is estimated the interaction of mantle plumes with nearby mid-ocean ridges results in physical and

chemical anomalies along $15 - 20\%$ of the total mid-ocean ridge system length [*Ito et al.*, 2003]. The length along the ridge axis with such anomalies is defined as the plume's waist width W. Based upon the spatial extent of bathymetric swells and magnetic isochron data, it can be determined that plume-ridge interactions may last tens of millions of years [*Ito and Lin*, 1995a; *Ito et al.*, 2003]. The interaction between a mid-ocean and a mantle plume, at different points in geologic time, is believed to have produced some of the largest volcanic features on Earth such as the Kerguelen Plateau and the Ontong Java Plateau [*Coffin and Eldholm*, 1993, 1994; *Coffin and Gahagan*, 1995; *Coffin et al.*, 2005, 2006].

This dissertation uses three-dimensional numerical modeling to address the geodynamical processes involved in the interaction between a ridge-ridge-ridge triple junction and a mantle plume. Earlier studies have examined the interaction of a plume with a single mid-ocean ridge [*Schilling*, 1991; *Feighner and Richards*, 1995; *Ito and Lin*, 1995a; *Ribe et al.*, 1995; *Ribe*, 1996; *Ito et al.*, 1997; *Albers and Christensen*, 2001] (see *Ito et al.* [2003] for a summary). Methods used in previous studies varied from experiments with corn syrup in a plexiglass tank [*Feighner and Richards*, 1995], to use of the lubrication theory [*Ribe et al.*, 1995] and thin layer [*Ribe*, 1996] models, to finite element modeling of Rayleigh-Benard convection with the Boussinesq approximation [*Ito et al.*, 1997; *Albers and Christensen*, 2001; *Hall and Kincaid*, 2003]. These studies yielded various scaling relationships for correlating observable waist width to plume and ridge characteristics.

The influence of triple junction plate boundary configuration on mantle dynamics has been studied by *Georgen and Lin* [2002], *Georgen* [2008], and *Georgen and Sankar* [2010]. Plume-triple junction interaction was first numerically modeled by *Georgen* [2011]. The primary differences between this investigation and earlier studies are that it performs a systematic investigation of the parameter space of several variables that are important in plume-triple junction interaction, it derives a scaling law for plume waist width in a triple junction setting, and it incorporates dehydration of the mantle into the calculation of viscosity. In the numerical modeling, the mantle is treated as an incompressible viscous fluid with zero Reynolds number and infinite Prandtl number. The fully-coupled nondimensional equations for energy, mass and momentum conservation are solved to steady state using the finite element analysis software COMSOL Multiphysics (version 3.5.). Model results are applied to the Azores plume-triple junction system. Scaling relationships for plume-triple junction

interactions are compared to earlier studies that used a single ridge to establish the importance of the triple junction configuration on the waist width.

This dissertation follows the style of *American Geophysical Union* publications

CHAPTER 2

EMERGENT AND ANIMATED COLLADA MODELS OF THE TONGA TRENCH AND SAMOA ARCHIPELAGO: IMPLICATIONS FOR GEOSCIENCE MODELING, EDUCATION, AND RESEARCH

The focus of this chapter is the introduction of COLLaborative Design Activity (COLLADA) models as a visualization and research tool. By exploring numerous possibilities for Tonga Trench formation a new hypothesis arose. My contribution involves development and creation of the Tonga slab COLLADA model using the hypocenter data from GeoMapApp (http://www.geomapapp.org). I integrated models in to Google Earth stand alone application with semi interactive micro plates as well as coded their animation in KML. I also addressed the problems related to the anti meridian and caching. The work reported in this chapter has been published in the peer-review journal Geosphere (see *De Paor et al.* [2012a]).

2.1 ABSTRACT

We report on a project aimed at developing emergent animated COLLADA models of the Tonga-Samoa region of the western Pacific for teaching and outreach use with Google Earth. This is an area of historical importance to the development of plate tectonic theory and is important today owing to neotectonic activity including a 29 September, 2009 tsunamigenic earthquake. We created three types of models: an emergent digital elevation model of the Tonga Slab with associated magmatic arc and back-arc basin based on GeoMapApp data-mining (http://www.geomapapp.org); animated models of alternative plate tectonic scenarios; and a large scale model that permits users to view the subsurface down to lower mantle levels. Our models have been deployed in non-science-major laboratory classes and positive learning outcomes have been documented in an independent study by *Gobert et al.* [2012]. The models have also been made available to colleagues and the public

via ODU's Pretlow Planetarium and via an outreach and dissemination web site, http://www.digitalplanet.org. In the process of constructing a complete set of tectonic models for the area of interest, we added cases which have not been described in the research literature. Thus this study spans the three functions of modern academia - research, teaching, and outreach - and the multifaceted aspects of creating, using, testing, and disseminating electronic geospatial learning resources.

2.2 INTRODUCTION

On 29 September, 2009, a deadly tsunamigenic earthquake occurred south of the Pacific islands of Western Samoa and American Samoa, drawing the attention of the world to a region of complex oceanic plate tectonics [*Okal et al.*, 2009; *Lay et al.*, 2010]. The magnitude 8.1 earthquake [*USGS*, 2009] occurred near the point where the Pacific plate's active western margin turns sharply from a northerly-trending convergent boundary to a westerly-trending transverse boundary (Figure 1).

Historically, tsunamis in this region are associated only with convergent tectonics. The extensional event [*USGS*, 2009] on 29 September was in a part of the plate subject to significant lithospheric flexure and tangential longitudinal strain, close to but not on the active plate boundary.

Because of the nature of the tectonic setting we created a set of emergent and animated COLLADA models [*Arnaud and Barnes*, 2006; *De Paor*, 2007a,b, 2008a; *De Paor et al.*, 2009, 2010] in Google Earth that would clearly illustrate the three-dimensional structure and its temporal evolution. Our purpose was principally instruction and outreach, since visualizations have been demonstrated (e.g. *Gobert* [2000, 2005]) to play a key role in many novices' conceptualization of tectonic movements. In the process of designing instructional visualizations, however, we found that attempting to cover all multiple working hypotheses lead us to additional models not previously described in the tectonic literature of the region. Our target audience was three-fold: (i) the large number of non-major students who study courses involving plate tectonics as part of their general education requirements in the US undergraduate education system; (ii) visitors to the Pretlow Planetarium who can view our models beside models of lunar and planetary structures in a museum-style informal education setting; and (iii) visitors to our web site http://www.digitalplanet.org which is sponsored by the NSF for the purpose of disseminating results of our funded

Figure 1. A view of the Tonga-Samoa region from our data-mining source, GeoMapApp (see text) (http://www.geomapapp.org). Red star marks the epicenter of the Sept. 29, 2009 tsunamigenic earthquake south of Samoa. Yellow line marks the Tonga trench. Red line is center of Lau marginal basin. Blue line is Vitiaz Lineament. Principle emergent island names are in green.

research. Learning outcomes were tested with the first category only and are reported by an independent study (*Gobert et al.* [2012]; see summary below). Given the positive learning gains they recorded, the visualizations could well prove beneficial to other groups, including geoscience majors taking courses in structural geology and tectonics, geophysics, or geodynamics, and also to citizens ranging from first responders in earthquake- and tsunami-prone regions to casual museum visitors.

We chose to create COLLADA models because they can be viewed with the highly popular Google Earth virtual globe [*De Paor*, 2007a], the basic version of which is free (the commercial Google Earth Pro can be used to view our models but it is not required). Google Earth is both a desktop application and a web browser plug-in that contains many built-in geoscience data sets in its primary database, including surface imagery, water bodies, volcanoes, and earthquakes, all of which can be used to study subduction zones and marginal basins. In general, Google Earth is most

suited for studying processes at or above the surface (e.g. *De Paor et al.* [2007]; *Mc Donald and De Paor* [2008]), however we have developed several techniques for visualizing the sub-surface as outlined in detail below (see *De Paor and Pinan-Llamas* [2006]; *De Paor and Williams* [2006]; *Whitmeyer and De Paor* [2008]; *De Paor and Whitmeyer* [2010]).

This paper is aimed towards readers with an interest in the tectonics of the region, as well as those who would wish to use the models we have created in their classrooms or informal education settings, and also towards those who wish to discover how to create their own 3D COLLADA models of global scale processes elsewhere for viewing on Google Earth. In the past, modeling was done mainly by computer programmers. However just as non-technical people are increasingly contributing to Web content (especially via social media such as Facebook that facilitate easy uploading of custom content), so also the old distinctions between teacher, researcher, and programmer are breaking down as increasing numbers of academics create, test, and disseminate their own computer-base learning, research, and outreach resources.

2.3 GEOLOGICAL BACKGROUND

The Pacific plate (Figure 2) is formed by the tectonic processes of mantle upwelling, partial melting, crustal magmatism, and seafloor spreading on a network of current (East Pacific Rise) and past spreading ridges. Unlike the Mid-Atlantic Ridge which is symmetrically positioned roughly equidistant from the Atlantic Ocean Basin's eastern and western passive margins, the East Pacific Rise is located much closer to (in places actually on) the Pacific's eastern active margin along the Americas. The Pacific plate thus extends westward across thousands of kilometers of Earth's surface before encountering the various plates and micro-plates that mark the western active margin of the Pacific Ocean Basin. As it moves away from the spreading ridge, the plate becomes older, colder, thicker, and denser [*Parker and Oldenburg*, 1973; *Yoshii*, 1975] and eventually is subducted along the western part of the so-called "Pacific Ring of Fire". Owing to variations in strike of the western active margin, tectonism varies in style from convergent to transverse, and associated marginal basins commonly undergo minor divergent tectonism.

In this paper, we focus on a study area (Figure 3) covered by longitudes from W170° to the Anti-meridian 180°, and by latitudes from S13° to the Tropic of Capricorn (S23.5°). The overall structure of the region consists of:

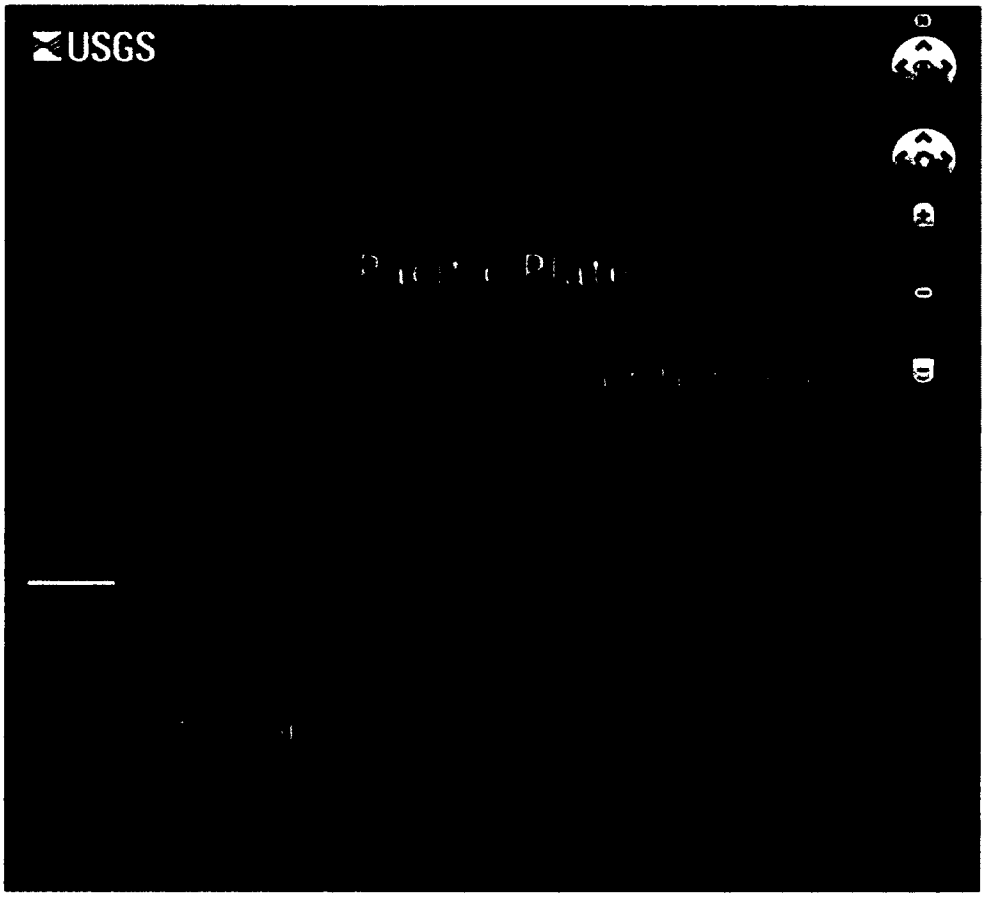

Figure 2. Google Earth representation of tectonics of Pacific Ocean Basin. Red lines mark East Pacific Rise. Northern Tonga trench is shown in yellow and the Samoan transform boundary in cyan. Island of Tonga is indicated in green. Modified from KML file downloaded from USGS website.

- The westward spreading Pacific plate,
- The older extension of that plate north of American Samoa,
- The Tonga-Kermadec trench,
- The Tonga volcanic arc,
- The Lau Back-arc Basin,
- The Lau remnant arc, and

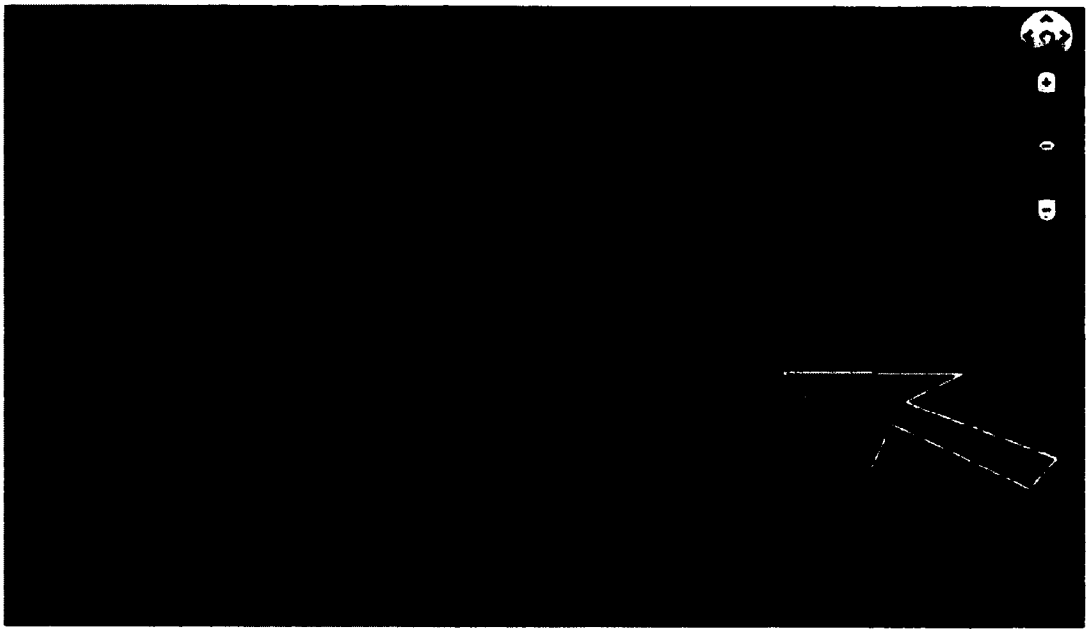

Figure 3. Current study area outlined in green. Pacific plate motion direction in white. Yellow line marks Tonga trench. Cyan line is Vitiaz Lineament. Red line represents a complex region of back-arc spreading.

- The South Fiji Basin.

A complication occurs south of this study region where a line of seamounts are currently subducting near Monowai, resulting in the differentiation of the northern Tonga and southern Kermadec trenches. To avoid this complexity, our study is confined to the region north of Monowai. To the west, the Lau Back-arc Basin meets the South Fiji Basin which is influenced by subduction of opposite polarity coming from the New Hebrides convergent zone further west. Our study area is thus strategically chosen to avoid unnecessary complications.

In all but the northernmost part of our study area, the ~100 million year old Cretaceous crust of the Pacific plate meets the recently formed edge of the Indo-Australian Plate along a 6-10 *km* bathymetric depression called the Tonga trench [*Muller et al.*, 2008]. A 100 *km* thick descending lithospheric slab dips westwards under the Lau Basin to form the Tonga Subduction Zone. Slab morphology has been determined to various mantle depths by *Gudmundsson and Sambridge* [1998] and *Syracuse and Abers* [2006] and data are readily available in the GeoMapApp on-line

database [*Ryan et al.*, 2009; *GeoMapApp*, 2012] (http://www.geomapapp.org).

The chosen study area is of interest for several reasons. It is important for the scientific history of the theory of plate tectonics because seismic studies in this region were the basis for the original identification of subduction by *Isacks et al.* [1968]. The relationships illustrated within the dotted parallelogram of Figure 4 (modified slightly from that paper's famous figure) were inspired by the Tonga - Samoa region. Furthermore, the Lau Basin is a classic teaching example of back-arc spreading due to trench rollback and trench suction [*Uyeda and Kanamori*, 1979; *Moores and Twiss*, 1995; *Rosenbaum and Lister*, 2004]. In the rollback process, the immaterial line of maximum lithospheric flexure entering the trench migrates horizontally eastward as material in the plate continues to travel westward and turn downwards. This creates a so-called trench suction force that extends the overlying arc and causes divergence in the back-arc basin (Figure 5). Roll-back is a spatio-temporal concept involving different directions and rates of movement of material versus immaterial geometries and is thus potentially difficult to visualize, even by experts.

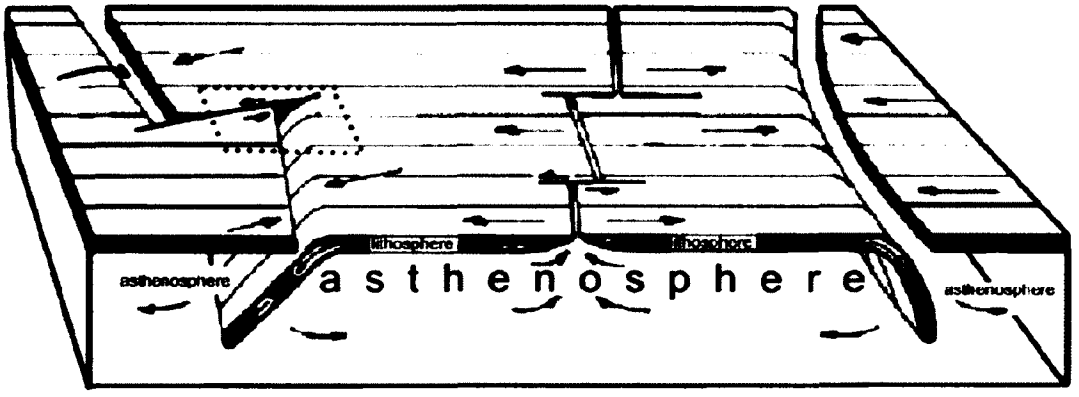

Figure 4. Plate tectonics explained in famous illustration (slightly modified) from *Isacks et al.* [1968] (their Figure 1). Width of Pacific plate not to scale. Asymmetric position of East Pacific Rise not shown. Dotted parallelogram marks present study area.

Towards the north, the Tonga trench ends abruptly along the Vitiaz Lineament just south of the approximately east-west trending Samoan Archipelago of islands and seamounts (Figures 1, 3). Here, the strike of the convergent plate boundary

Figure 5. COLLADA models raised above Google Earth surface showing structure of study region. Arc, basin, and slab can be selectively shown or hidden.

turns sharply from north to west, to become parallel to the plate movement vector, and the boundary therefore transitions into a transform boundary. North of this latitude and continuing beyond the study area, the Pacific plate forms the ocean floor for thousands of kilometers westward, progressively aging from Cretaceous to Jurassic before subducting at locations such as the Mariana trench, whereas to the south of the Vitiaz Lineament, a six million-year-old Cenozoic marginal basin called the Lau Basin overlies the subducting Tonga Slab [*Lupton et al.*, 2003; *German et al.*, 2006], dividing the active Tonga volcanic arc to its east from the extinct Lau remnant arc to its west.

The change from convergent to transform plate margin correlates with geophysical evidence from *Smith et al.* [2001] that the lithosphere is in the process of tearing just southwest of American Samoa (Figure 6). An instructional analogy can be created easily, either by cutting partially through a sheet of paper or wood panel, or by holding ones fingers as shown in Figure 6 (inset). However, the transition is complicated and obscured because the Vitiaz Lineament has been alternately interpreted as a dormant compressional structure dating from times when plate movement vectors were different [*Pelletier and Auzende*, 1996] or a product of rapid eastward tearing of the lithosphere [*Hart et al.*, 2004].

At the northern end of the Tonga trench, rates of subduction exceeding 20 centimeters per year are amongst the highest documented anywhere on Earth [*Muller et al.*, 2008; *Bonnardota et al.*, 2009]. *Holt* [1995] notes a south-to-north increase in down-dip velocities of the slab and the widening of the Lau Back-arc Basin is consistent with a northward increase in the rate of rollback, reaching as high as 10 centimeters per year. The trench continues along strike to the south beyond the study area, where it is known as the Kermadec trench. However, the character of the downgoing slab varies along strike as revealed by seismic tomography (Figure 7). Tomography shows a lithospheric slab dipping steeply all the way down to mid-mantle levels (1,600 *km* out of the mantle total of 2,981 *km*) south of Tonga, whereas in the current study area a shallow segment is imaged in the 410-660 *km* transition zone [*Van der Hilst*, 1995; *Mussett and Khan*, 2008]. These depths correspond to the olivine-spinel and spinel-perovskite phase transitions which are thought to affect slab density and kinematics. *Bonnardota et al.* [2009] present evidence of slab detachment at intermediate depths.

The Samoan Archipelago of islands and seamounts that forms the northernmost

Figure 6. Hiding Tonga Arc and Lau Basin reveals how southern (nearer) portion of Pacific plate subducts along Tonga trench whilst northern part continues westward on Earth's surface. Inset: hand analogy helps some students visualize situation.

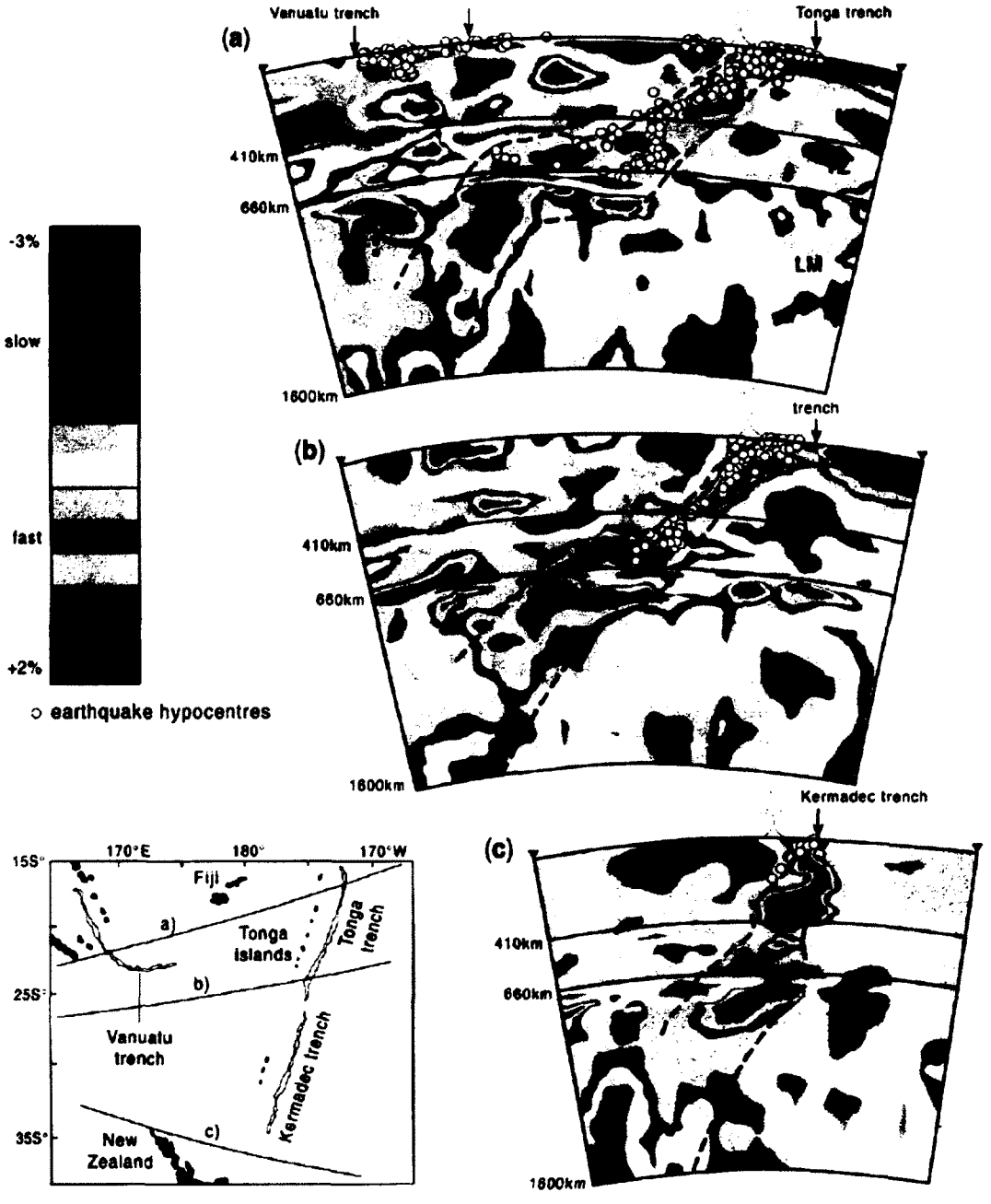

Figure 7. Seismic tomography of Tonga-Kermadec slab from *Mussett and Khan* [2008]. Note mid-mantle flat-slab developed in north but not in south.

strip of the study area has been interpreted alternatively as attributable to drift of the Pacific plate over a deep-seated Samoan hotspot analogous to the Hawaiian hotspot [*McDougall*, 2010] or as a result of warping and stretching along an east-west-trending lithospheric monocline in the proximity of the transform boundary and tear point [*Hart et al.*, 2004]. In either case, the volcanic lineament adds complexity and intrigue to the story of this region.

2.4 COLLADA MODELS IN THE GOOGLE EARTH DESKTOP APP

To aid with visualization of complex tectonics, we constructed interactive emergent and animated COLLADA models of the Tonga - Samoa region. We include a description of the model coding process here both for those readers who are interested in how COLLADA works and for those those who might wish to create similar models elsewhere. The authors' recent experiences in co-presenting several over-subscribed Geological Society of America short courses and workshops on the topic of Google Earth modeling with COLLADA point to growing interest in this approach amongst geoscience researchers and educators. The following account should be accessible to readers without experience in programming languages such as FORTRAN or C. If readers can format a Web page with HTML, they can modify the types of scripts discussed below to work in their own area of interest (for more details of scripting for Google Earth, see *Wernicke* [2009]; *De Paor et al.* [2010]).

One of the more powerful features of Google Earth is the ability it offers users to display their own content [*Goodchild*, 2008]. Custom content can be added using Google Earth's menus or by creating a file written in the Keyhole Markup Language (KML), a dialect of XML designed specifically for virtual globes. The basic structure of a KML file is shown in Figure 8. This script places a default yellow map pin in the center of North America. The custom content we are most interested in here consists of 3D COLLADA models. Like KML, COLLADA is another dialect of XML and is used mainly to add 3D buildings to Google Earth, for example using the SketchUp modeling program. Fortunately, the dimensions of COLLADA models can be set to regional or global in magnitude so that a program intended for modeling buildings can be used to create crustal blocks on the scale of mountains [*De Paor*, 2008b,c] or even continents [*Dordevic et al.*, 2009, 2011; *De Paor and Whitmeyer*, 2011]. COLLADA models saved in Digital Asset Exchange (DAE) files are recognized and imported by Google Earth. The example in Figure 9 adds a model of the Tonga slab as seen in

Figure 6.

```
<?xml version="1.0"?>
<kml>
    <Document>
        <Placemark>
            <Point>
                <coordinates>-95.45, 37.68, 0</coordinates>
            </Point>
        </Placemark>
    </Document>
</kml>
```

Figure 8. An example of code for creating a Placemark in KML.

To create Figure 6, we digitally mined data from *Syracuse and Abers* [2006] which is openly available on GeoMapApp [*GeoMapApp*, 2012] (http://www.geomapapp.org). GeoMapApp is a free desktop application that gives the user a Google Maps-style interface with a wide-range of geological data (Figure 1 is a screen shot). Among the global data sets made accessible in GeoMapApp are earthquake hypocenters (http://www.geomapapp.org). The first step to creating our models was to select a rectangular region in GeoMapApp, export the hypocenter points, and load them into an Excel file. This file was used to create points with correct depth tags for compatibility with KML. Once the points were in the KML file, a snapshot of the region of interest was taken in Google Earth. This picture was saved as a PNG image file which was then edited with photographic editing software. We used the free open-source application called GIMP [*GIMP*, 2011], however owners of a commercial application such as Adobe Photoshop could use it equally well. In SketchUp, a rectangle was created with the same dimensions as the area from which the Google Earth terrain image was taken. The edited PNG file was then used as a so-called texture pasted on the rectangle (that is, an image covering a model surface like wallpaper). In the case of the GeoMapApp data, to aid computer memory management, several small sections were exported onto six different rectangles. Next, points were dropped to the correct depth beneath the surface. If several data were clustered together the deepest one was selected (usually the depths were within five kilometers of one another). After all the points were correctly located in the z-dimension, the regions were stitched together using geological markers and longitude/latitude lines. The

```
<?xml version="1.0"?>
<kml>
	<Placemark>
		<Model>
			<altitudeMode>relativeToSeaFloor</altitudeMode>
			<Location>
				<longitude>85.935848221848</longitude>
				<latitude>-18.36255792927627</latitude>
				<altitude>200000</altitude>
			</Location>
			<Orientation>
				<heading>21.732</heading>
				<tilt>0</tilt>
				<roll>0</roll>
			</Orientation>
			<Scale>
				<x>0.816</x>
				<y>0.776</y>
				<z>0.796</z>
			</Scale>
			<Link>
				<href>files/TongaSlab.dae</href>
			</Link>
		</Model>
	</Placemark>
</kml>
```

Figure 9. An example of code for a COLLADA model in KML.

data points were then connected into depth profile lines. An outline of the surface slab was copied and offset 5 *km* to simulate ocean crustal thickness and a second copy of the slab was offset 100 *km* to create a bounding surface at the bottom of the lithosphere. These slab surfaces were intersected by vertical planes on the sides using a SketchUp 'intersect' command to complete a solid model. The geo-referenced slab was saved in a DAE file which was imported into Google Earth.

A similar process was used to create 3D models of the arcs and back-arc basin, except that these were constrained by the subducting slab geometry, not by seismic data. Finally, a KML Placemark containing the model (Figure 9) was replicated and a KML TimeSpan element was added to each replica Placemark (Figure 10). The begin and end time tags of the Timespan and the model's altitude tag were incremented in unison (in KML, the altitude is in meters so "200000" represents an altitude of 200 *km*.) As the Google Earth slider is moved and a slider value is reached, the code responds by changing the elevation of the COLLADA model. All tectonic domains were elevated in unison but different domains were placed in separate KML Folders so that they could be selectively shown or hidden.

Two difficulties were encountered in the above process. First, the study area bordered the Earth's Anti-meridian and Google Earth was found to behave erratically in this region. We overcame this by draping the famous NASA Blue Marble image of the Earth [*NASA*, 2005] over the Google Earth surface imagery and moving the origin of longitude so that the models were safely away from the Anti-meridian (a second ground overlay snapped from the Google Earth terrain was superimposed in the Tonga region in order to provide local detail) (Figure 11). A side effect of this solution is that the lat/lon grid must be left turned off. The second difficulty was that the time slider technique gave the viewer only one slider control whereas we wanted to be able to both elevate and animate the block. Initially, we animated blocks that were already elevated to a fixed altitude (see *De Paor et al.* [2012b] - Movie1) but later we switched to the Google Earth API (see next section).

Animating models in Google Earth (Figure 12) was similar to elevating emergent models (Figure 10). Instead of incrementing the altitude of a single model, we created a sequence of gradually differing models at a constant altitude (a marker was used to ensure that models were all exported from the same spot to prevent unwanted jittering or wobble) and we changed the name of the linked model file in the KML Placemark sequence. This introduced an unanticipated problem. Although the

```
<?xml version="1.0"?>
<kml>
        <Placemark>
                <TimeSpan>
                        <begin>-100</begin>
                        <end>-200</end>
                </TimeSpan>
                <Model>
                        ...
                        <Location>
                                <longitude>...</longitude>
                                <latitude>...</latitude>
                                <altitude>200000</altitude>
                                ...
                                ...
                                ...
        </Placemark>
        <Placemark>
                <TimeSpan>
                        <begin>-200</begin>
                        <end>-300</end>
                </TimeSpan>
                <Model>
                        ...
                        <Location>
                                <longitude>...</longitude>
                                <latitude>...</latitude>
                                <altitude>300000</altitude>
                                ...
                                ...
                                ...
```

Figure 10. Sample code for emergent COLLADA model in KML.

Figure 11. Seafloor detail for Tonga region snapped from Google Earth and draped over NASA Blue Marble image of Earth. Both were moved through longitude to get away from the Anti-meridian, a region where Google Earth has difficulty handling models (see text).

images used as textures were relatively small (under 100 Kb), the long sequence of models used in this animation proved to be hesitant to load even on a fast computer. Google Earth displayed the blank, white-sided model frame first and applied texture images after a brief interval. Even though this was less than a second in most cases, white flashes interrupted the immersive effect of the animation. Our solution was to wait for all frames to load before playing the animation, however this approach is tedious. Hopefully, future versions of Google Earth will cache textures before displaying models or build visualizations in an off-screen bitmap and only move them on-screen with completely loaded; this is standard practice in other applications.

```
<?xml version="1.0"?>
<kml>
    <Placemark>
        <TimeSpan>
            <begin>-100</begin>
            <end>-200</end>
        </TimeSpan>
        <Model>
            ...
            ...
            ...
            <Link>
                <href>files/200.dae</href>
                ...
                ...
                ...
    </Placemark>
    <Placemark>
        <TimeSpan>
            <begin>-200</begin>
            <end>-300</end>
        </TimeSpan>
        <Model>
            ...
            ...
            ...
            <Link>
                <href>files/300.dae</href>
                ...
                ...
                ...
```

Figure 12. Animated COLLADA model in KML.

2.5 THE GOOGLE EARTH API AND JAVASCRIPT CONTROLS

In addition to the well known stand-alone desktop application, Google Earth is available as a web browser plug-in that allows one or more instances of the virtual globe to be embedded in a Web page and controlled with client-side JavaScript (an example of script is shown in Figure 13) or by means of server-side scripts written with a scripting language such as PHP, Python, or Ruby. All features do not transfer over from the Google Earth desktop application to the Google Earth API - for example, there is no sidebar with Places and Layers. However individual features such as tools in the application toolbar may be coded in JavaScript. Content control using JavaScript is an advantage to the API. Maps, cross-sections, COLLADA models, etc. can be independently controlled and modified. Ease of viewing content is a big plus to the Google Earth API. A person wishing to display content no longer has to download and launch a file, but can view Google Earth directly in their web browser. The Google Earth API is controlled by standard controls found in HTML forms (buttons, sliders, menus, text boxes, etc.). This style of control enables the creation of more robust user interaction with the content. Thus, in the Google Earth API a new control may be added for every user interaction needed. The main controls used in our time-evolved models are the elevation control with a slider and visibility and time/motion controls with buttons. The slider works by allowing the user to vary any KML element over a range of values. It would not be difficult for readers to add their own spot quizzes or text areas for gathering student responses, for example.

For our elevation slider we used an inexpensive commercial product called TigraSlider Control [*SoftComplex*, 2010]. A free version is offered but does not have necessary functionality. Were we starting afresh we would use the free native slider input built into HTML5 and supported by all new browsers. Such a slider can be added to a web page with the single line:
<input name="slider" type="range " min= "0" max="10" value="5"> and its value can be read with the JavaScript function document.getElementById('slider').value. The visibility controls are standard HTML form buttons which enable model components to be shown or hidden, thus revealing or obscuring sections of the model behind them. A quick method used to accomplish this task was to change the HTML href hyperlink to the .dae file. If a model component needed to be invisible, the href link was pointed to a non-existent .dae file, thus nothing was loaded.

2.6 IMPLEMENTATION

Since 2008 we and our colleagues [*Whitmeyer et al.*, 2011] have been distributing geological COLLADA models to a cohort of educators in a variety of universities and colleges and we have made them freely available for download both from our academic web sites and from www.digitalplanet.org. The animated emergent models described here, along with similar models in a variety of tectonic settings, have been used by us in several undergraduate courses at four east coast universities and are available to visitors to the ODU Pretlow Planetarium in an informal education setting. During leave-of-absence by De Paor in 2010, co-author Wild developed a set of Google Earth API-based laboratory activities including animations using the above technique (see Figures 14, 15, 16, [*Wild et al.*, 2011], and movies 1, 2, 3 [*De Paor et al.*, 2012b,c,d]). These were combined in a single laboratory class along with similar activities addressing the Iceland spreading ridge and hot spot, and presented as a test with IRB compliance to 127 non-science-majors as part of a broad survey of the solar system. Pre- and post-tests were administered by Wild and analyzed by NSF-sponsored independent assessor Gobert, and results are reported by *Gobert et al.* [2012]. Quoting their abstract, these authors "found: 1) overall learning gains; 2) no differences in learning gains when comparing those with prior coursework in Geology or geography to students without this prior coursework; and 3) no differences in learning gains when comparing males and females." They report a gender difference favoring males in terms of items completed during the class period and a correlation between students' pre-test and embedded laboratory scores.

Testing in the informal education setting of a planetarium has not yet been attempted. Here, models can be displayed on a portion of the dome using a peripheral LCD projector during planetarium shows and on peripheral computer screens that visitors can casual browse. Future plans include eye-tracking studies of such browsing as we have recently acquired the necessary equipment.

```
<!DOCTYPE html ...>
<htmL>
        <head>
                <script language="JavaScript" type="text/javascript" src=
"http://www.lions.odu.edu/org/planetarium/steve/Tonga_API/tonga_roll_js/openfile.js">
                </script>

        </head>
        <body>
                <form>
                        <input type="button" value="Load Case 1" onclick="openfile(1)">

                </form>
        </body>
</html>
```

Figure 13. API JavaScript interface.

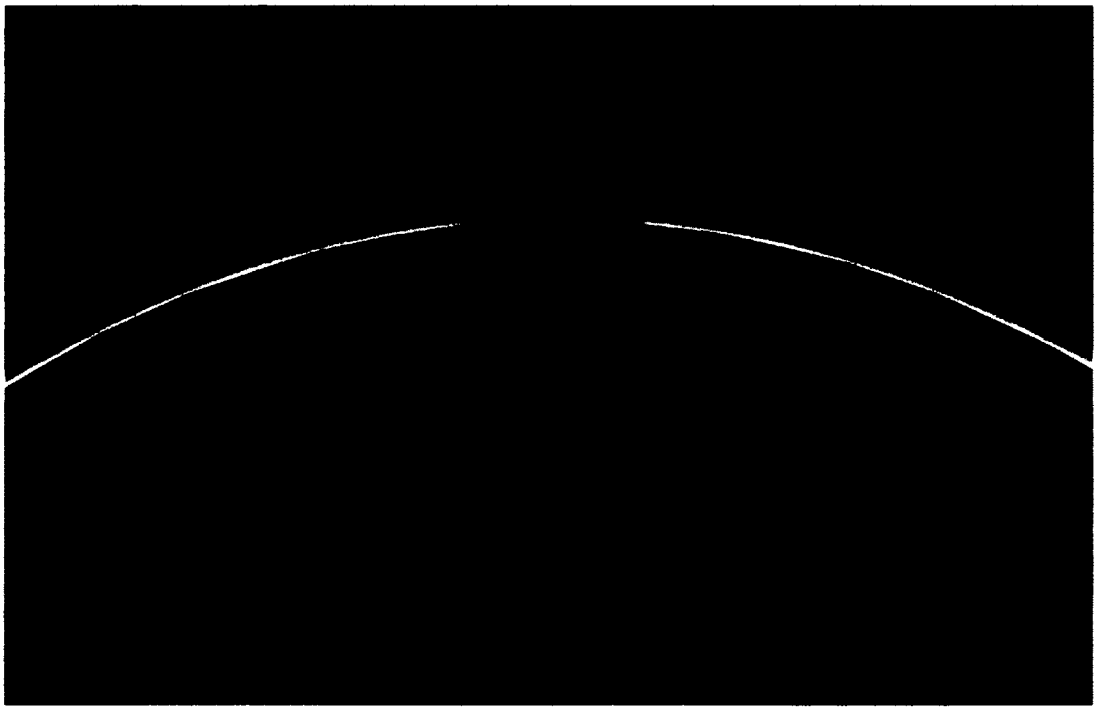

Figure 14. Google Earth API, COLLADA models manipulated in Google Earth instance embedded in web page.

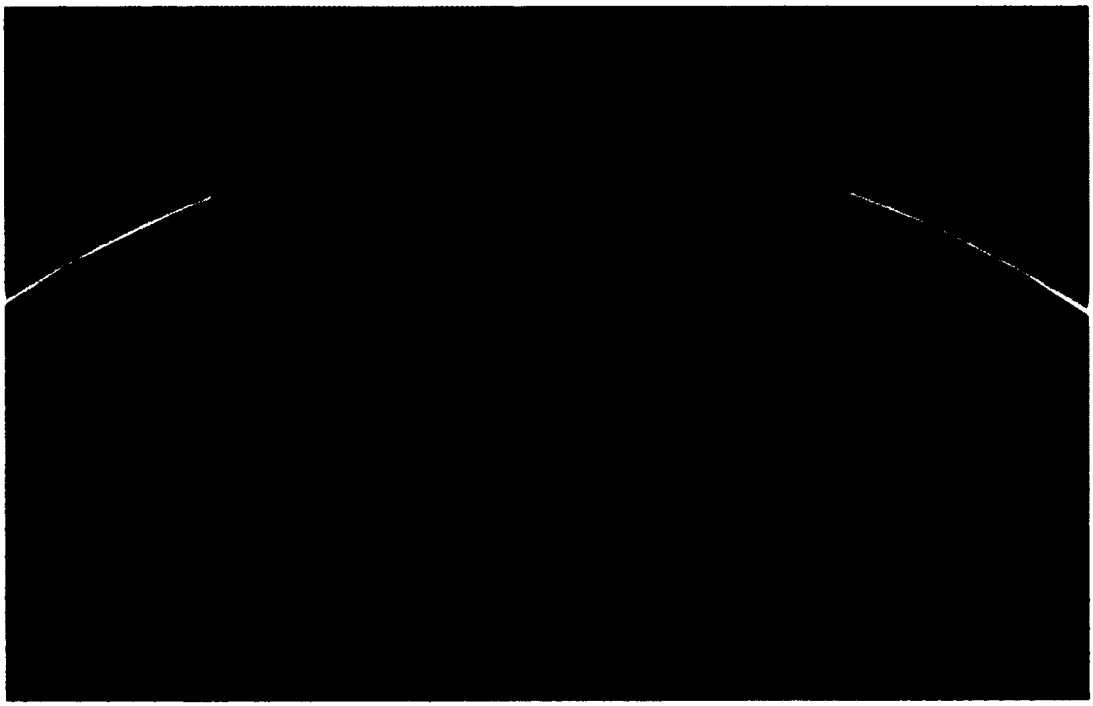

Figure 15. Alternative models of trench rollback and slab kinematics. See text.

2.7 ENHANCED VISUALIZATION USING GOOGLE MARS

In addition to the emergent COLLADA models described above, we developed methods of viewing sub-surface tectonic structures in situ. The radius of Earth's outer core (3,500 *km*) is within 3% of the mean radius of Mars. Consequently we can use the Google Mars virtual globe to represent Earth's core-mantle boundary. The Martian 3D terrain is turned off and a plain image overlay is used to cover all of the built-in Martian surface imagery. At the Earth's core-mantle boundary depth of 2,900 *km*, the peak black-body radiation is white-hot, however white is not a suitable color for modeling, therefore we use red or gray overlay images (Figure 17) to convey temperature or metallicity respectively (an informal poll taken by *De Paor and Whitmeyer* [2011] revealed that ten of the fourteen voters favored the red core whereas three favored gray and one white). A spherical COLLADA model representing Earth's surface to scale is draped with a semi-transparent PNG image of the NASA Blue Marble. Figure 18 shows the core with three slices of the mantle under Tonga. The upper part of each slice is textured with seismic tomography from

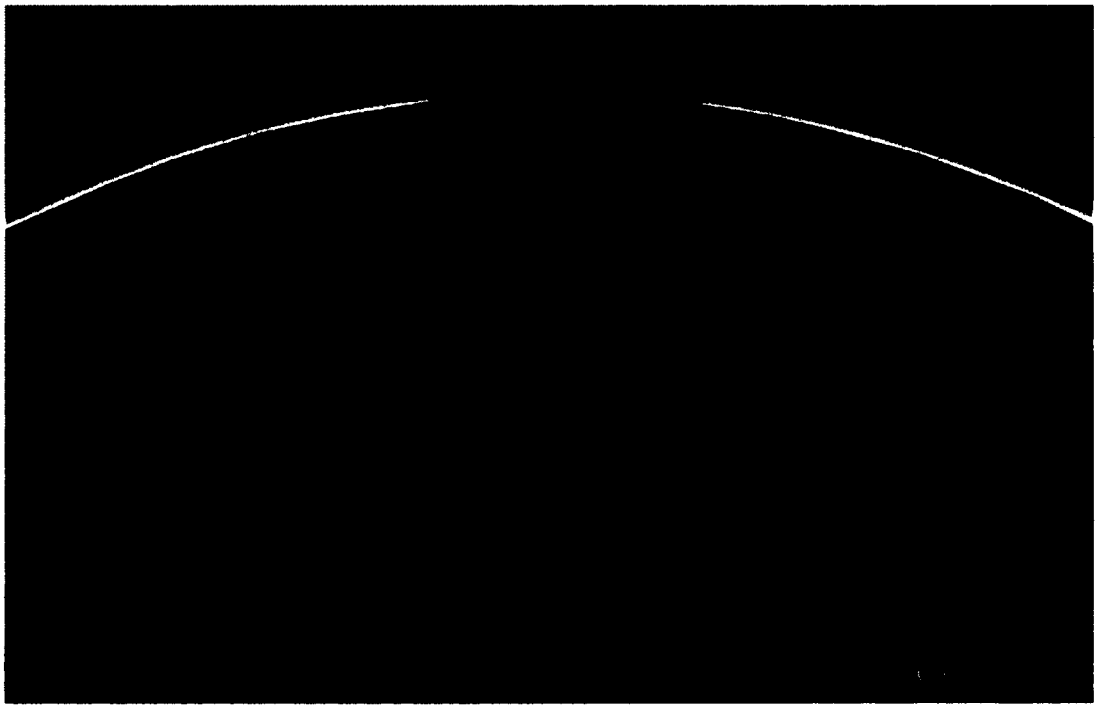

Figure 16. Block model that can be raised and reorientated while animation is running using multiple JavaScript controls.

Mussett and Khan [2008]. The lower part is colored purple to emphasize the relative proportion of the mantle not reached by the tomographic data. Elements of Figures 17 and 18 are combined in Figure 19, with a circular cut-out revealing the interior. All three models can be downloaded from our Web site [*Digital-Planet*, 2011].

Figure 17. Visualizing subsurface using Google Mars with plain red image overlay and Blue Marble COLLADA model of Earth's surface.

Specific to this study area, inclusion of deep mantle tomography lead us to consider tectonic models of the Tonga subduction system extending beyond the depth of the *Syracuse and Abers* [2006] data. The feature of particular interest in the tomographic section is the region of shallow or 'flat' slab dip between 430 *km* and 670 *km* as discussed below.

Figure 18. Slices of crust and mantle shown with seismic tomography from *Mussett and Khan* [2008]. Note flat subduction at mid-mantle levels. Purple represents lowermost mantle below limit of tomographic data. Red sphere representing Earth's core.

Figure 19. Visualization with circular cut-out revealing underlying mantle. Yellow, red, and blue lines mark surface tectonic lineaments. Note that Arctic, North America, and Russia are seen inverted on inner surface of sphere behind core.

2.8 TECTONIC MODELS OF THE TONGA REGION

Creating learning and outreach resources for the Tonga-Samoa region required the assembly of six alternate plate tectonic models including mostly well-established but also some novel ideas. To a casual observer, this might seem excessive. Geologists are so used to viewing two-dimensional cross sections of subduction zones that they may not ponder how such zones must change in four dimensions of space and time. On a finite spherical Earth, a subduction zone cannot continue along strike forever and neither Andean-style magmatic arcs nor Lau-style back arc basins can be understood in terms of a steady-state subduction system akin to a descending escalator. Yet plate tectonics texts tend to skimp on discussion of complications such as lateral terminations or rollback and static illustrations strongly suggest a steady-state process of subduction at a fixed trench location. By presenting over-simplified models of subduction to students and the public we make it impossible for them to truly understand the genesis of arcs.

The rigid Pacific plate is contiguous east of the study area, and its absolute Euler pole of rotation lies far away (Figure 20), so the velocity of the seafloor approaching the Tonga trench must be approximately the same as its velocity along the Samoan Archipelago north of the subduction zone (web reference [*GSI*, 2004]). Consequently the variables of interest are the absolute and relative velocities of the tear point. Absolute velocities may be stated relative to the global hotspot reference frame whereas relative velocities are stated with reference to an arbitrary material point in the lithospheric plate.

2.8.1 MODEL 1: NO TEARING OR SLOW TEARING.

In this end-member case (Figure 21), the tear point southwest of American Samoa is not currently active but rides along passively with the plate, a scenario that results in horizontal absolute velocity vectors for all points both on the surface and on the slab. This end-member case cannot be the whole story because it does not allow subduction to get started in the first place, however, it is a temporary condition which is possible at some later time. In order for the slab to move horizontally westward, the arc material in front of it must either 1) move west at an equal or greater pace, or else 2) deform to form a contractional forearc accretionary wedge or a foreland thrust belt, or both (Figure 21). If the tear point propagates eastward

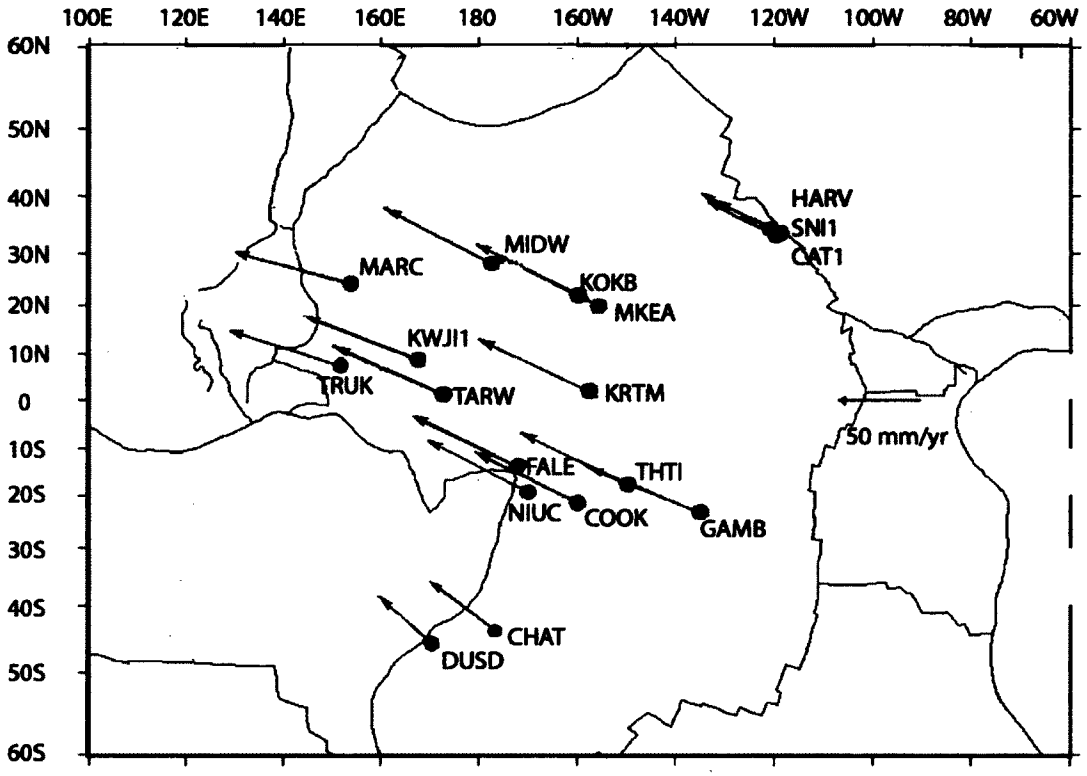

Figure 20. Velocity vectors for the Pacific plate from GPS measurements. Web reference [*GSI*, 2004].

more slowly than the plate moves westward then the movement vectors for material in the slab will dip westward more shallowly than the dip of the slab itself and the scenario will also correspond to Model 1 (Figure 22).

Figure 21. Structure of Andean Arc oriented to correspond to polarity of Tonga Subduction Zone, view to the north. Green denotes forearc and foreland sedimentary basins. Black lines are thrust faults near surface and shear zones at depth. Red denotes magmatism.

The structure of the lithosphere above the Tonga Subduction zone in Model 1 depends on the absolute velocity of the Australian plate west of the study area. Back-arc spreading west of Tonga could be compatible with Model 1 if the Australian plate drifted west faster than the Pacific plate or if rollback of the opposite-polarity

Figure 22. Tear point migrating slowly eastward (white arrow) resulting in dipping absolute movement vectors (black).

New Hebrides Subduction Zone west of Fiji created the necessary extension. As it happens, the direction of absolute plate motion of the Australian Plate is northward, approximately perpendicular to the Pacific plate [*Kreemer*, 2009; *Stadler et al.*, 2010], therefore it does not have a significant orthogonal component of movement relative to the trench and is equivalent to a stationary block for the purposes of this model. Furthermore, the New Hebrides structure cannot be responsible for all back-arc spreading because its influence does not extend beyond the northern end of the Lau Basin. Thus, if Model 1 were valid, there ought to be a mountainous magmatic arc bordered by forearc and foreland thrust belts, which are shown in Figure 22 but not seen in ground truth. If there were ever a period during which the tear point drifted passively with the plate or ripped slowly, it could not have lasted long, else a large compressional arc would have grown and endured.

Despite the obvious unlikeliness of Model 1 to an expert (professor), we included it amongst our alternatives in order to challenge novices (students) to think of reasons to reject it, or equivalently, to envisage the type of data that would support it but are not seen.

2.8.2 MODEL 2: BAND SAW TEARING.

Our second model requires an immaterial tear point fixed in an external reference frame (Figure 23). The western drift of the Pacific plate can then be compared to pushing a sheet of plywood westward through a band saw and holding the north side level (Figure 23 inset) whilst letting the south side sag (to include the Samoan Archipelago in the analogy, one would add a candle in a fixed location under the north side of the sheet close to the band saw).

The absolute velocity vector of any material point in the slab in this case would be directed down-dip, i.e., parallel to the top and bottom of the slab, consequently the arc forming above the slab would be under no lateral stress, neither forming an Andean-style compressional structure such as a thrust belt nor an extensional structure such as a back-arc spreading ridge. Nevertheless, the the model would lead to a prediction of gradual magmatic arc build up to significant size.

It is not intuitively obvious that there are two independent questions to be addressed in this scenario. First, is the Samoan Archipelago a hotspot trail caused by the Pacific plate drifting slowly westward over a fixed hotspot? And second, has the tear point always been located close to the hotspot? If the latter were true, the tear

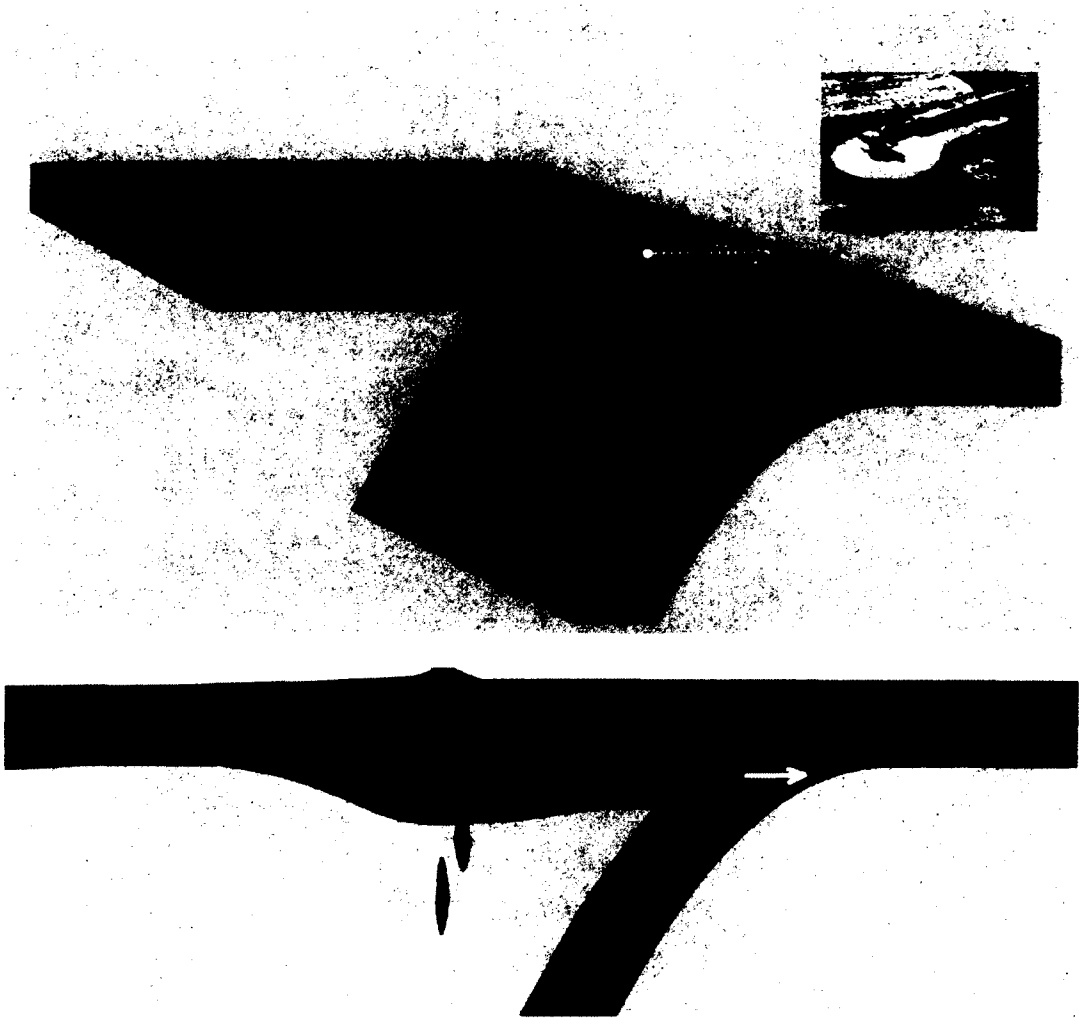

Figure 23. Model 2: Tear point fixed in external reference frame. Velocity (white arrow) equal and opposite to plate velocity. Velocities in slab parallel to dip (black arrows).

point southwest of the youngest island - American Samoa - today would have been southwest of the older Western Samoa in the recent past and southwest of the oldest Wallis and Futuna Islands before that, with each of these islands presumed to have formed over the stationary deep mantle hotspot before the younger ones existed. Thus a test of the hotspot trail model would be a progression of island ages and thermally induced decreasing altitudes or bathymetries, comparable to the Hawaiian chain. The hotspot answer was in doubt because of the occurrence of recent vulcanism at both the west and east end of the Samoan volcanic lineament. However, studies by *Mahoney and Spencer* [1991], *Koppers et al.* [2003], and *Hart et al.* [2004] have shown plume hot spot activity similar to Hawaii. Recent volcanism along the Samoan lineament is seen by them as a separate phenomenon superposed on the hotspot progression and therefore requiring a separate explanation.

2.8.3 MODEL 3: RAPID ROLLBACK.

Our third model involves the eastward relative migration of the tear point at a faster rate than the westward absolute movement of the Pacific plate over the hotspot, resulting in eastward absolute movement of the tear point and absolute velocity vectors for material in the slab that are steeper than the slab dip (Figure 24). An analogy would be the act of cutting cloth by moving a scissor forward whilst pulling the cloth backwards towards oneself (students have also suggested a comparison with the Michael Jackson moon-walk). In this case, the original tear point would have been at the western end of the Samoan Volcanic Lineament, well west of the fixed mantle hotspot and would have migrated rapidly east so that it happens to be close to Vailulu'u today. Rapid migration of the tear point could account for the superposition of recent vulcanism on the age progression of the Samoan Archipelago as discussed above by flexure of the lithosphere close to the line of tearing. If we could see into the future, the tear point might continue to migrate east of the current hotspot. On the other hand, its current proximity to the hotspot might trap the tear in a steady-state phase in the future as represented by Model 2.

Since relative motion of the tear point is key, Model 3 can also result from modest tear velocities in combination with slow plate velocities. In the end-member case there is no horizontal component of plate motion and the slab vectors are vertical (Figure 25). Clearly the Pacific plate does have a significant horizontal velocity, so the end-member case is not practical.

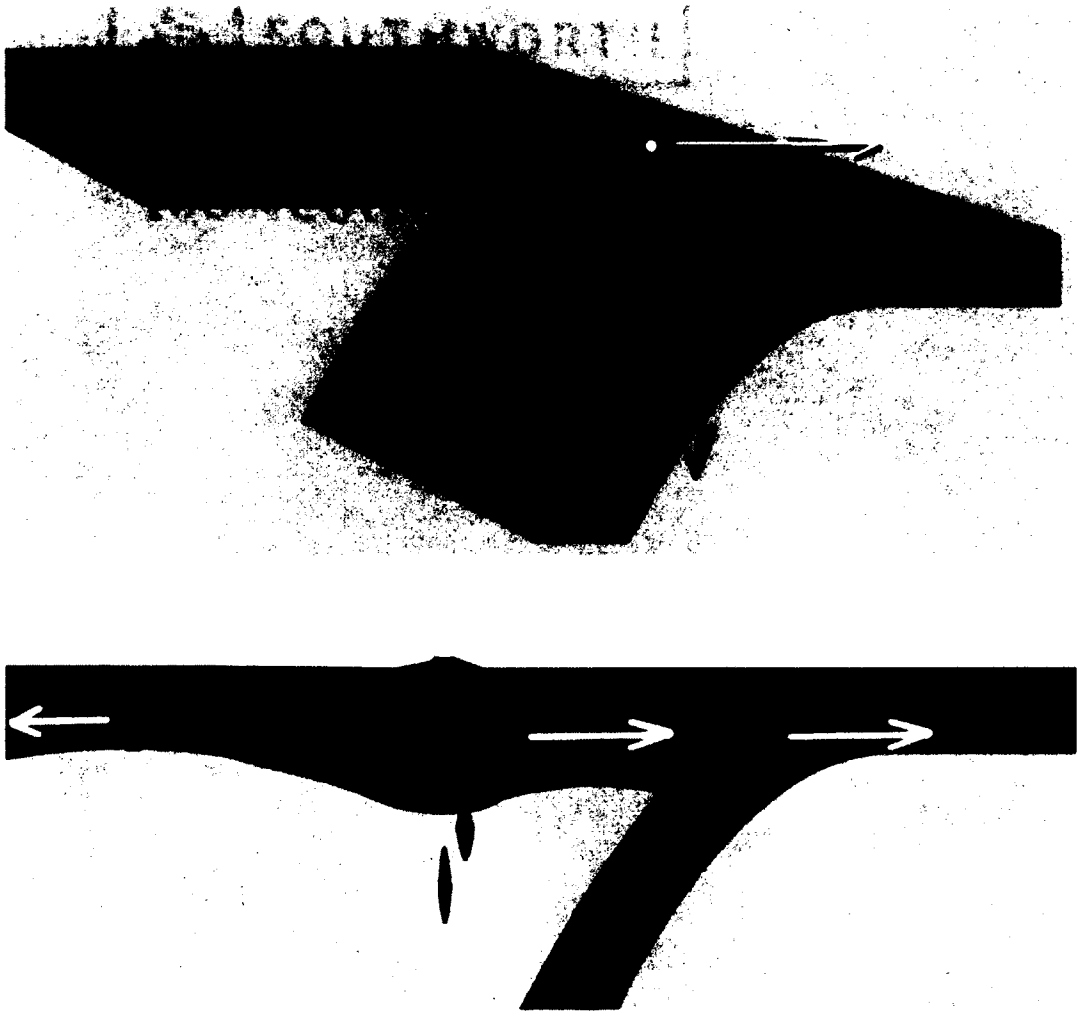

Figure 24. Model 3: Rapid eastward migration of tear point (white arrow). Absolute slab velocity vectors steeper than slab dip. Stress in arc causes extension and dike intrusions, opening Lau Basin.

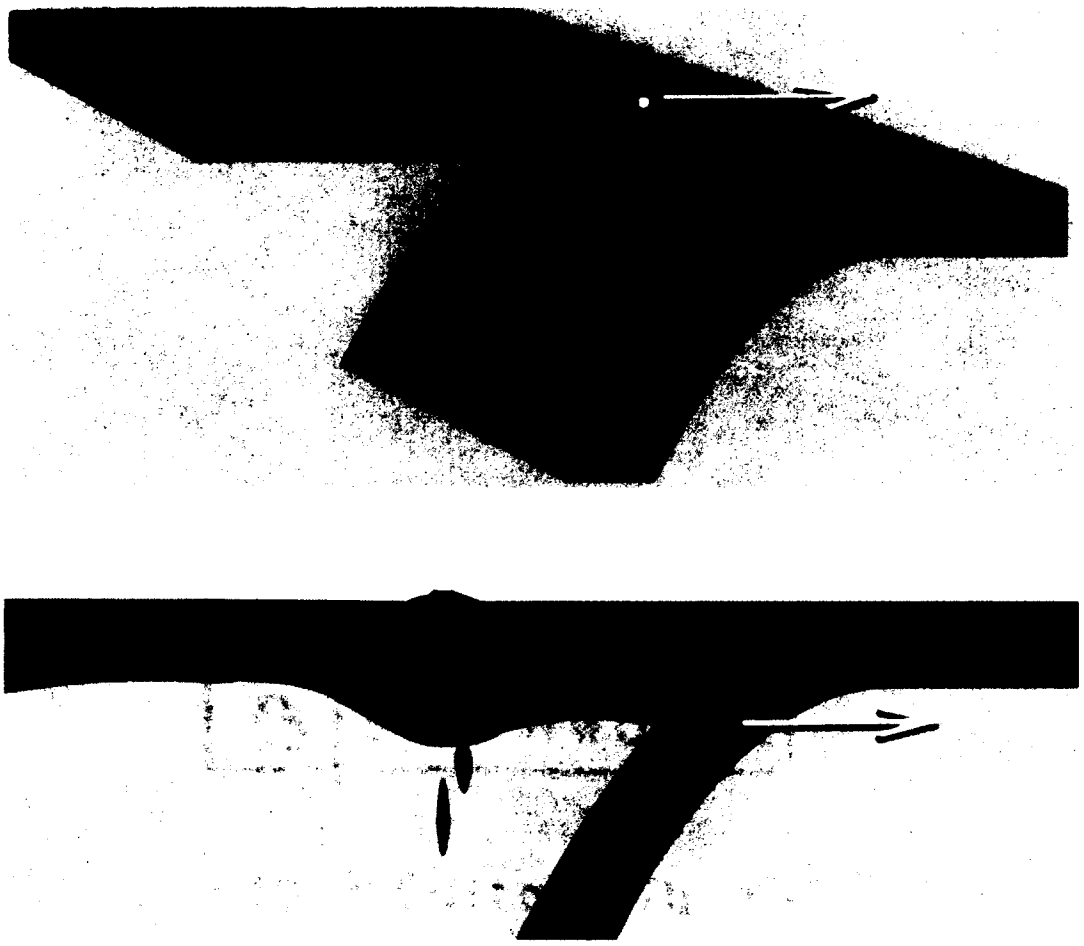

Figure 25. Model 3 (contd.): Dominance of rollback over horizontal plate motion. Steep to vertical absolute velocities in slab (black arrows). Stress in back arc region is tensional.

2.8.4 MODEL 4: DEEP MANTLE ROLLBACK.

Model 3 can account for the development of a subduction zone and extensional back-arc basin, but we also need to account for the flattening of the slab dip approximately between 400 and 600 *km* depth. *Kincaid and Olson* [1987] suggested that the subduction system may have initially followed Model 2 (no rollback) and that rollback and back-arc spreading may have ensued when the slab hit the 430-670 *km* mantle discontinuity after about 10 million years at 7 centimeters per year. In this scenario, the slab encounters resistance to subduction due to mid-mantle phase and viscosity changes (430 *km* is marked by the olivine-spinel transition whereas the spinel-perovskite transition occurs at 670 *km*) and it develops a bend that itself rolls back (lower white arrows in Figure 26).

2.8.5 MODEL 5: FOUNDERING FLAT-SLAB.

As far as we can ascertain, this fifth model (Figure 27) is not previously described in the tectonic literature. In this scenario, the western Pacific plate first cracked along the Tonga trench and tore at a point to the west of the Samoan Archipelago causing the southern portion to subduct. A magmatic arc built but there was no significant back-arc spreading. The seamounts and islands of the Samoan Archipelago pierced the plate progressively along a line to the east of the tear point. Islands and seamounts aged and subsided as they drifted westward. At about 6 million years, the tear point ripped rapidly eastward as in Model 3, superimposing recent volcanism of the Vitiaz Lineament and ending in proximity with the hotspot. This rapid rollback resulted in a shallow-dipping slab segment at shallow depth with steep-dipping absolute movement vectors. The flat slab then continued to founder to its present mid-mantle level. In the third dimension, the structure involves a near-pole rotation (cf. *De Paor et al.* [1989]) resulting in the narrowing of Lau Basin towards the south and widening to the north. At about 2 million years ago, trench rollback started a near-pole rotation process about an Euler pole located around S 24. The rotation occurred at a rate of 7° per million years.

2.8.6 MODEL 6: SUBDUCTION STEP-BACK.

Our final model is one in which subduction initiates in the west under the Lau Arc and then instantaneously steps back to the longitude of the Tonga Arc (Figure

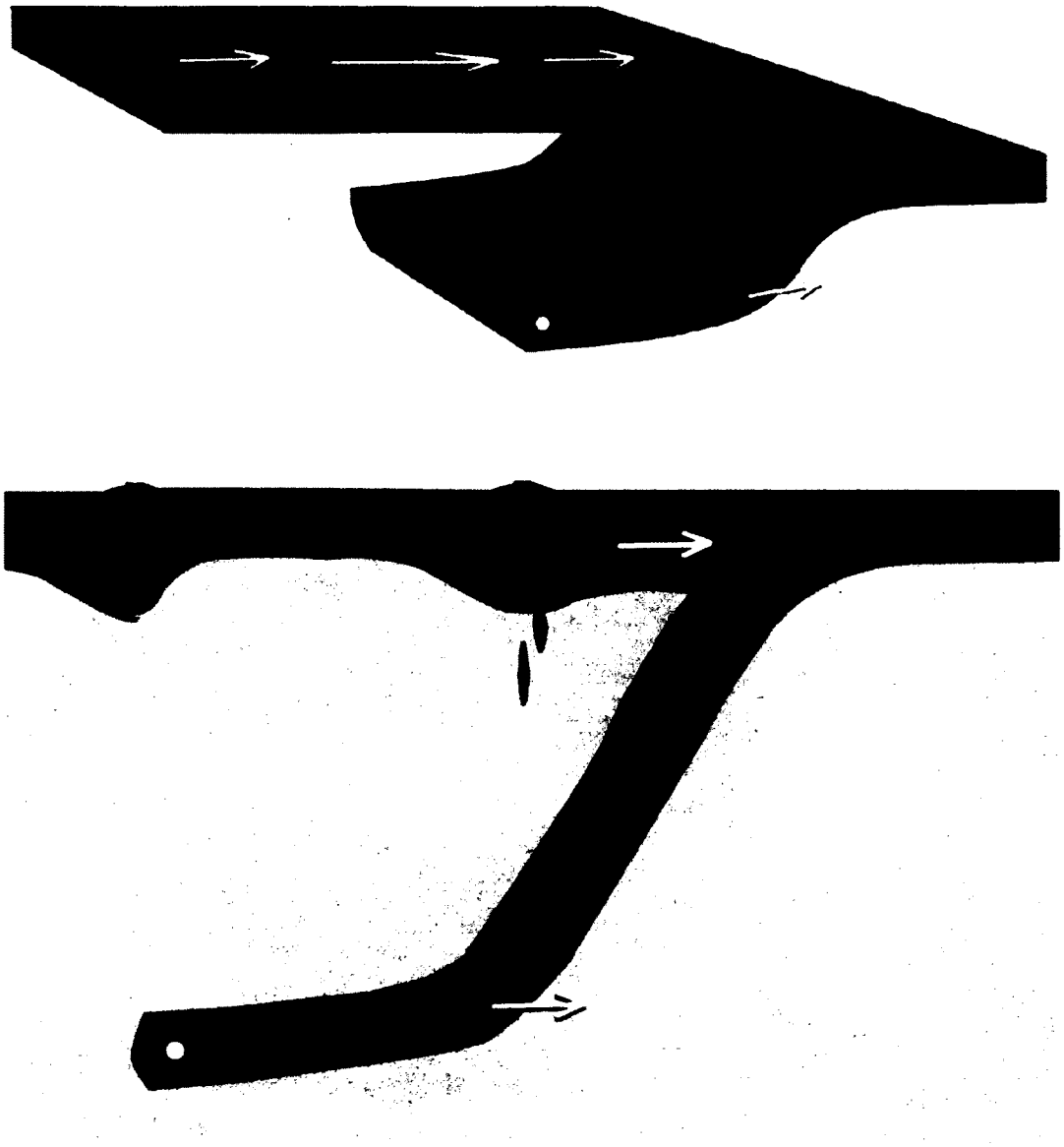

Figure 26. Deep Mantle Rollback (lower white arrow) may have created flat slab segment at about 600 *km* and also drive surface rollback (upper white arrow). White spot marks point where slab started to go flat due to mid-mantle resistance.

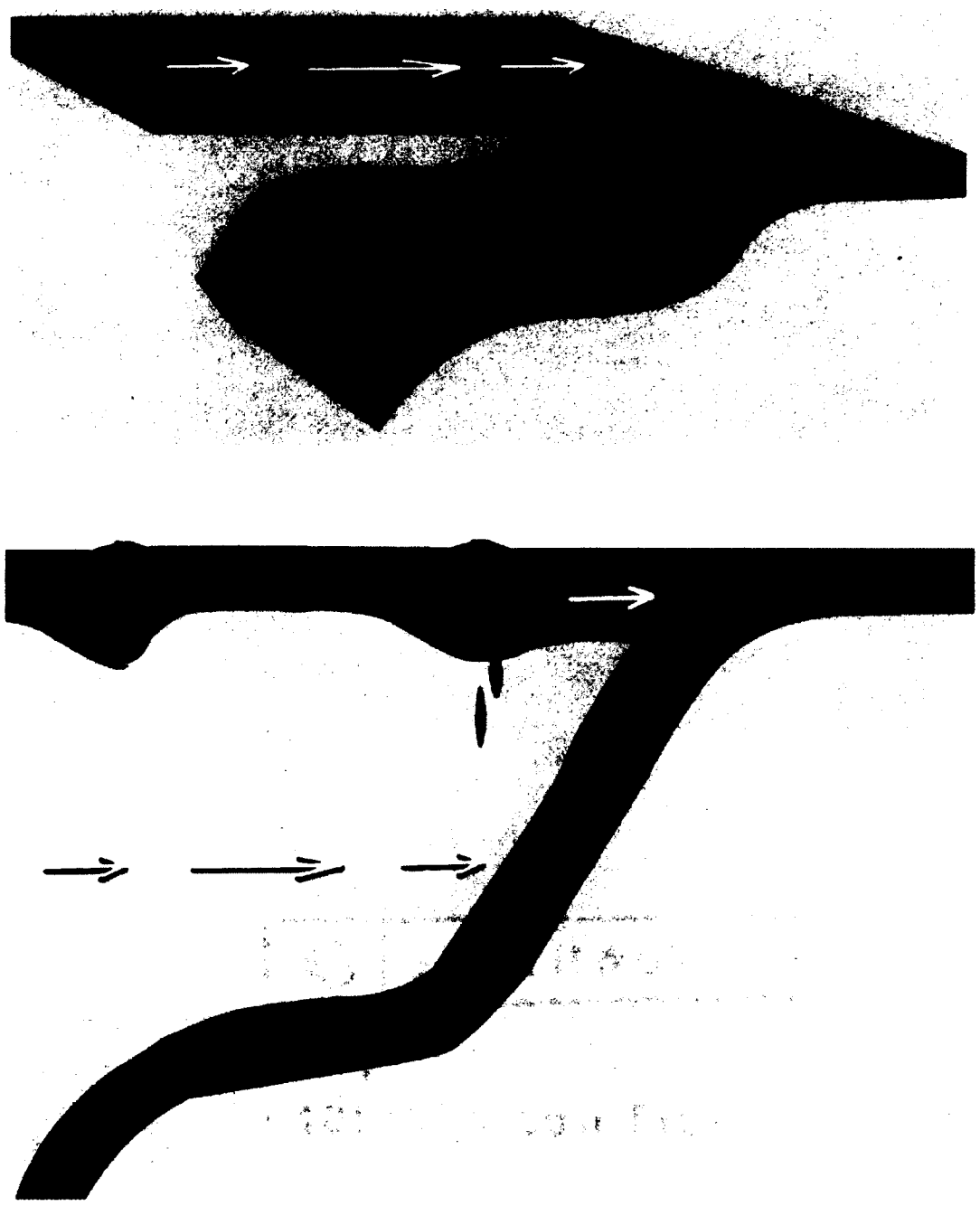

Figure 27. Model 5. Foundered flat slab. See text for discussion.

28). There is no back-arc spreading, rather the marginal basin is floored by a broken off and abandoned segment of the Pacific plate. This model is established elsewhere: it has been proposed to explain part of the evolution of the Mariana system, among others. However, diffuse magnetic patterns in the Lau Basin imply [*Lawver and Hawkins*, 1978] that it formed by distributed back-arc spreading driven by trench rollback [*Uyeda and Kanamori*, 1979] and trench suction [*Chase*, 1978] rather than by entrapment of normal oceanic lithosphere behind a newly formed Tonga Arc to its east (these different models of marginal basin formation are discussed by *Karig* [1974]).

Figure 28. Model 6. Subduction step-back. Subduction initiates in west, then steps instantaneously to east (oceanward). See text for discussion.

We leave the task of debating the fine details of alternate models to regional tectonic experts. As usual, there are end-member cases that can be rejected but no

single hypothesis that trumps all others. Under-constrained alternatives help guide tectonic experts towards the types of data that need to be collected in the future. For instructional purposes, it is useful to present these multiple working hypotheses as an example of the oft-misunderstood process of science (e.g. *Brickhouse* [1990]; *Handelsman et al.* [2004]).

2.9 DISCUSSION AND CONCLUSIONS

Ever since its inception, Google Earth has been adopted with great enthusiasm by geoscientists (e.g. *Butler* [2006]) and it has been widely used in geographical and geological education (e.g. *Stahley* [2006]; *Patterson* [2007]; *Rakshit and Ogneva-Himmelberger* [2008, 2009]). *Cruz and Zellers* [2006] have established its efficacy for the study of landforms. COLLADA models have been used in conjunction with Google Earth by *De Paor and Whitmeyer* [2008]; *De Paor et al.* [2009]; *Selkin et al.* [2009]; *Brooks and De Paor* [2009]; *Pence et al.* [2010]; *Whitmeyer et al.* [2011]; *Gobert et al.* [2012]. Anecdotally, students in several of our classes have reacted positively to the tactile nature of the process of lifting blocks out of the subsurface. They seem to "get it." However, in order to spur further evaluation studies, there needs to be a greater cohort of academics who create and distribute learning resources for Google Earth using COLLADA and KML.

Previous studies have documented the benefits of learning with visualizations in general [*Kali et al.*, 1997; *Orion et al.*, 1997; *Reynolds et al.*, 2005] and specifically with Geographic Information Systems by *Hall-Wallace and McAuliffe* [2002]. There are also many studies of the positive role of student research projects in undergraduate education by *Libarkin* [2001]; *Jenkins et al.* [2007]. In some cases, instructors already know the right answers and by mentoring student inquiry rather than just lecturing, they help students to discover those answers. In other cases, questions are more open-ended and students discover new findings thereby acting as genuine researchers as well as learners. This paper presents a case where construction of engaging instructional resources blurred the boundary between academic education and research at the instructor level. It is commonly stated that one does not truly understand any topic until one is asked to teach it. Clearly, the process of preparing course materials is an important aspect of research and with modern methods of data mining and data visualization, teachers who are not topic experts have the opportunity to help promote not only their own comprehension but the research community's

understanding also.

We are keenly aware of: 1) the potential of complex 3D visualizations such as Google Earth to cause visual overload and loss of attention [*Rensink et al.*, 1997; *Parkhurst et al.*, 2002; *Martin and Treves*, 2008]; and 2) the ease with which students can wander off task given simple mouse controls and a whole earth to explore. Adding emergent blocks to Google Earth helps solve the first problem by creating salience and a focal point for student attention. In separate lab exercises, we use the KML NetworkLink and FlyToView elements as a means of geo-fencing (e.g. *Rashid et al.* [2006]); when a student wanders away from the region the KML script automatically resets the view angle. Serendipitously, our solution to the Anti-meridian rendering problem in Google Earth (above) reduces visual overload by replacing the complexly overprinted surface imagery and 3D DEM with the simple NASA Blue Marble image of the Earth. *Simpson et al.* [2012] have taken the concept further by draping a plain beige image over all of the Google Earth surface except for the Archean Kaapvaal Craton which is their area of interest.

Given our recent courses, our classroom use of COLLADA models and Google Earth have been mainly with non-science majors, *Goodchild* [2006] has promoted the notion that general education requires geospatial reasoning as a "fourth R" in addition to reading, writing and arithmetic. Furthermore, there is no reason to believe that students majoring in geosciences and other geospatial disciplines would not benefit also. In a previous small (eight student) class of geoscience majors studying structural geology, a student questioned two weeks after the laboratory activity was able to correctly estimate crustal thickness as a proportion of the width of a block. This student might also have been able to give a numerical answer but evidently had developed a useful visually-based mental concept of scale.

We hope that the electronic media linked this paper will lead to widespread dissemination, implementation, and testing of our models in many settings and to the development of new COLLADA models in Google Earth by our colleagues in many second and third level educational institutions. Since Google Inc. handed control of KML to the open-source community, its free availability is ensured for the foreseeable future and it has the potential to be truly transformative in the field of geoscience modeling, education, and outreach [*De Paor*, 2011a,b; *De Paor and Whitmeyer*, 2011].

Having created and developed these visualization tools for exploring tectonic processes the next step is to develop and implement tests to study the validity of using Google Earth as an educational tool. Only by testing to measure learning outcomes can one determine if the visualizations have merit.

CHAPTER 3

GOOGLE VENUS

This chapter takes production of instructional resources even further. We are moving away from the Earth and exploring the terrestrial planet, Venus. Comprehensive visualization of the surface of Venus as well as its interior are done with emphases on tectonic features resulting from a super-plume. My contribution to this paper was creation of the COLLADA visualization models for the Venus cross section and image pyramids for the surface imagery with implementation in KML. The work reported in this chapter has been published in the peer review journal Geological Society of America Special Papers (see *De Paor et al.* [2012e]).

3.1 ABSTRACT

Google Earth includes digital elevation models and surface imagery for the Earth, Moon, and Mars, but not for Venus. To help geoscientists visualize Venusian geology, geophysics, and geodynamics, we have built a "Google Venus" virtual globe on a Google Earth foundation. We present here details of how this was done and offer regional samples to show the power of the virtual globe, NASA and ESA imagery, and COLLADA models in displaying surface data and global, crust-to-core cross sections. We show how web data sources can be linked to Venusian locations in an engaging, interactive format. Our approach could be adapted to other planets and moons of the Solar System and to models of exoplanets.

3.2 INTRODUCTION

Anecdotal evidence from conversations with students and colleagues suggests that, of Earth's two planetary neighbors, Venus is the less well known and understood by geoscientists. This may reflect Venus's shroud of cloud, the relative paucity of space missions (especially landings), a smaller cohort of researchers, and a lack of earthly analogues for many of Venus's surficial and tectonic structures. Despite the fact that Venus is almost as large as the Earth whereas Mars is closer to the size of Earth's core, nevertheless earth like surface features such as river channels, sand dunes, etc.,

are ubiquitous on Mars but completely absent from Venus. This presents a challenge both to the educator and the presenter of research results. In fact, there is a huge repository of exciting data on Venus from NASA and ESA orbital missions but it is accessed mainly by dedicate researchers.

To help rectify this situation, we have created a Google Venus virtual globe built on a Google Earth foundation with extensive use of COLLADA models (http:// collada.org). Our model includes atmospheric imagery, emergent blocks, and cross sections of the planet's crust and mantle that illustrate current interpretations of its internal structure. We showcase some of Venus's unique tectonic structures, notably the Ishtar region and the Artemis super–plume structure. Google Venus effectively conveys the benefits of virtual globe style touring and zooming in helping geoscientists to truly understand planetary structures on a range of scales.

3.3 PLANET VENUS

Orbiting at 0.72 *AU* (astronomical units) from the Sun, Venus is 95% the diameter and 81.5% the mass of the Earth. Its slow retrograde rotation makes the Venusian day longer than its year (243 vs 225 Earth days). There are no seasons on Venus. Its rotation axis is less than 3° off vertical and its orbit is even less eccentric than Earth's, consequently, solar insolation is everywhere virtually constant year round.

Venus differs from Earth in that it lacks a magnetic field, and its upper atmosphere super rotates at an estimated 300 km/h. Atmospheric composition (96% CO2), surface pressure (about 95 bars), and surface temperature (up to 475 $°C$) vary radically from equivalent values on Earth. The thick insulating atmosphere results in negligible diurnal temperature variations and an enhanced global greenhouse effect, making terrestrial–style surface processes impossible. Venus thus lacks the weathering, erosion, and transportation that lead to sedimentary deposits on Earth [*Phillips et al.*, 2001].

Venus also lacks any evidence of plate tectonics or of regions analogous to Earth's continents [*Solomon et al.*, 1991; *Phillips and Hansen*, 1994]. Clearly the planet's interior cools through mechanisms other than mantle convection. Geomorphological and geochemical arguments, along with data from Soviet landers, are consistent with dry basaltic crust [*Grimm and Hess*, 1997]. The crust is stronger than Earth's basaltic rocks despite temperatures that would promote plastic deformation in wet

conditions [*Mackwell et al.*, 1998]. A wide variety of volcanic landforms occur [*Crumpler et al.*, 1997; *Lopez*, 2011] but there are no arcuate volcanic arcs comparable to the products of plate tectonics on Earth. Long, low viscosity, basaltic lava flows are common [*Bridges*, 1995, 1997; *Stofan et al.*, 2000]. Volcanic shields, 1 20 *km* in diameter, occur in shield fields and as shield terrains distributed across millions of square kilometers.

Although Venus is ultra dry today, water may have played a role in the past. Isotopic data are consistent with extensive water reservoirs more than 1 b.y. ago that has since been lost to space [*Donahue et al.*, 1997; *Donahue and Russell*, 1997; *Hunten*, 2002].

Venus and Earth are described as sister planets because they share planetary scale attributes such as size and composition despite very different surface processes. In the absence of weathering, surface features record past processes on Venus that hold clues to its evolution, and might also provide clues to early Earth history. Clearly this planet merits study with all the visualization tools available today, including virtual globes.

3.4 GOOGLE VENUS

The current version of Google Earth (v. 6.2) includes three virtual globes with digital elevation models (DEMs) and surface imagery (also known as primary databases) for the Earth, Mars, and Moon. In the desktop application, alternate globes (as well as the Google Sky option) are accessed via the "View explore..." menu item or the "Switch between Earth, Sky, and other planets" tool on the toolbar. When an instance of Google Earth is embedded in a web page using the Google Earth plugin and its Javascript Application Program Interface (API), the planet selection is made by the person designing the web page by specifying the primary database in the Javascript initialization function and it cannot be changed thereafter (Figure 29).

In personal communications, Google engineers contrast Venus with the Moon and Mars in terms of missions and especially landings, with their human interest stories and toy like, youth attracting rovers, and they convey little likelihood of a Google Venus option being built into future versions of Google Earth, therefore if we are to explore Venus as a virtual globe we must use Google Earth with the atmosphere and 3D terrain switched off, hide the primary database, and superimpose images and models to represent features of the Venusian atmosphere, surface, and interior

(Figure 30).

3.5 THE VENUSIAN ATMOSPHERE

Viewed through an earthbound telescope, or even from an orbiting spacecraft, Venus is permanently shrouded in cloud. Its dense atmosphere is opaque to visible light between 30 and 60 *km* altitude. Sulfuric acid droplets produced in the cloud tops reflect 70% of incoming visible light, making Venus the third brightest object in the sky after the Sun and Moon. Curved beige cloud bands, accentuated in ultraviolet photography, are the only discernible features outside of the polar regions.

3.5.1 ATMOSPHERIC SUPER–ROTATION

We present the atmosphere using a ground overlay image elevated 45 *km* and covering 90° to -90° latitude and 180° to -180° longitude (Figure 31). To hide the underlying Earth terrain, we cover the ground with a black image. In this image the effect of atmospheric super rotation [*Durand-Manterola*, 2010] is seen in the curvature of cloud bands indicating differential rotation at the equator (a day on Venus is 243 Earth days long but the atmosphere rotates in only four Earth days). The Keyhole Markup Language (KML) file linking to the atmospheric image (venus_atmos.kml) is available in the GSA Data Repository[1].

3.5.2 ATMOSPHERIC POLAR VORTICES

NASA and ESA orbital missions have provided many images of atmospheric vortices at Venus's poles (e.g., http://www.windows2universe.org/venus/venus_polar_atmosphere.html). However, it is not possible to drape these images as ground overlays because ground overlays cannot enclose the poles. This problem could be solved in future were Google earth programmers to adopt the Universal Transverse Mercator (UTM) projection system which switches to stereographic projection in the polar regions. Meanwhile, we must use COLLADA models (Figure 33,32) to display polar vortex images as illustrated in Figure 34. Double vortices are discussed in *Lebonnois et al.* [2006] and can be explored in the KML file "venus_voritces.kml" in the GSA Data Repository[1].

[1] GSA Data Repository item 2012305, KML files, is available at http://www.geosociety.org/pubs/ft2012.html, or on request from editing@geosociety.org

```
1 google.earth.createInstance('map3d', initCB, failureCB, {
2 database: 'http://khmdb.google.com/?db=earth' });
3
4 google.earth.createInstance('map3d', initCB, failureCB, {
5 database: 'http://khmdb.google.com/?db=mars' });
6
7 google.earth.createInstance('map3d', initCB, failureCB, {
8 database: 'http://khmdb.google.com/?db=moon' });
```

Figure 29. Javascript code options for selecting among planetary databases in the API. One of these options is added to the Javascript initialization function.

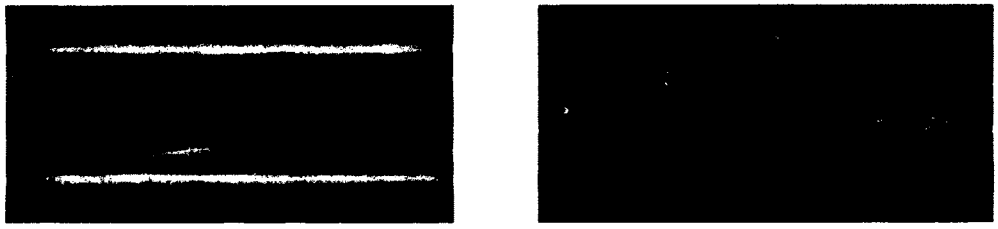

(a) (b)

Figure 30. Google Venus created by draping visible light cloud tops and Magellan radar altimetry over the Google Earth surface imagery. Mercator, Miller, or Plate Carrée (Simple Cylindrical) projections work best.

```
1  <GroundOverlay>
2    <name>atmosphere</name>
3    <Icon>
4      <href>images/venus_atmos.jpg</href>
5    </Icon>
6    <altitude>25000</altitude>
7    <altitudeMode>absolute</altitudeMode>
8    <LatLonBox>
9      <north>90</north>
10     <south>-90</south>
11     <east>180</east>
12     <west>-180</west>
13   </LatLonBox>
14 </GroundOverlay>
15 <GroundOverlay>
16   <Icon>
17     <href>images/black.tiff</href>
18   </Icon>
19   <altitude>0</altitude>
20   <altitudeMode>clampedToGround</altitudeMode>
21   <LatLonBox>
22     <north>90</north>
23     <south>-90</south>
24     <east>180</east>
25     <west>-180</west>
26   </LatLonBox>
27 </GroundOverlay>
```

Figure 31. Code snippet from http://www.digitalplanet.org/gv/venus_atmos.kml. The black ground overlay conceals Earth's surface imagery. The image file "venus_atmos.jpg" is wrapped around the entire planet at an elevation of 25 *km* (25,000 meters).

```
<Placemark>
  <name>Double vortex at North Pole</name>
  <visibility>1</visibility>
  <description><![CDATA[
  More...
  <br> <br>
  http://www.youtube.com/watch?v=WtxqkmIvikU
  ]]></description>
  <Model>
    <altitudeMode>absolute</altitudeMode>
    <Location>
      <longitude>0</longitude>
      <latitude>90</latitude>
      <altitude>-230000</altitude>
    </Location>
    <Scale>
      <x>0.5</x>
      <y>0.5</y>
      <z>0.15</z>
    </Scale>
    <Link>
      <href>models/nPole.dae</href>
    </Link>
  </Model>
</Placemark>
```

Figure 32. South polar vortices are displayed using the sPole.dae COLLADA model.

```
1  <Placemark>
2    <name>Double vortex at South Pole</name>
3    <visibility>1</visibility>
4    <description><![CDATA[
5    More...
6    <br> <br>
7    http://www.esa.int/esaMI/Venus_Express/
8    SEMYGQEFWOE_0.html
9    <br><br>
10   http://www.atm.ox.ac.uk/main/Science/
11   posters2006/2006cw2.pdf
12   ]]></description>
13   <Model>
14     <altitudeMode>absolute</altitudeMode>
15     <Location>
16       <longitude>-90</longitude>
17       <latitude>-90</latitude>
18       <altitude>-1600000</altitude>
19     </Location>
20     <Link>
21       <href>models/sPole.dae</href>
22     </Link>
23   </Model>
24 </Placemark>
```

Figure 33. North polar vortices are displayed using the nPole.dae COLLADA model. The scale element was adjusted iteratively to fit the image used.

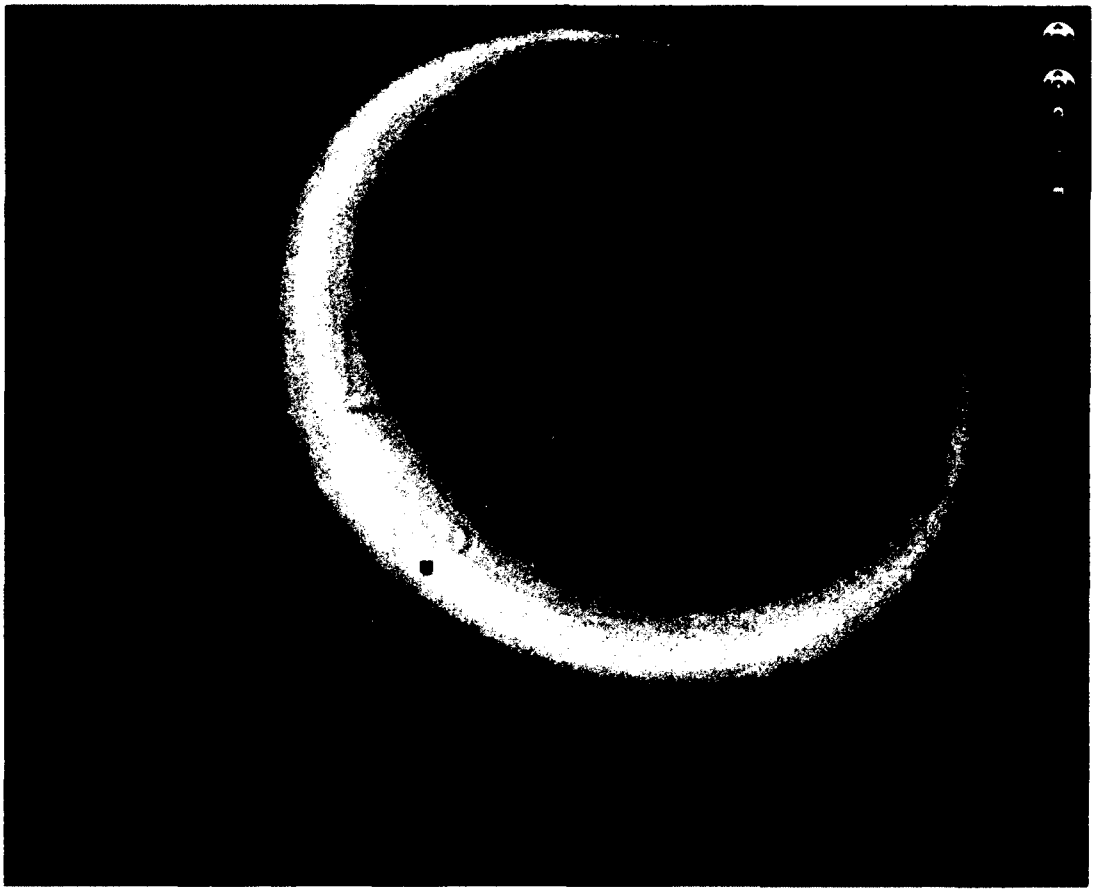

Figure 34. The dipole vortex at Venus's north pole is added as a COLLADA model because ground overlays cannot be draped across the poles. Despite the option of displaying UTM coordinates (white), Google Earth does not project surface imagery using UTM.

```
1  <Document>
2    <name>venus_hfa</name>
3    <LookAt>...</LookAt>
4    <description>...</description>
5    <visibility>1</visibility>
6    <Placemark>
7      <name>Hot Flow Anomaly</name>
8      <Model>
9        <altitudeMode>absolute</altitudeMode>
10       <Location>
11         <latitude>90</latitude>
12         <longitude>0</longitude>
13         <altitude>0</altitude>
14       </Location>
15       <Link>
16         <href>models/hfa.dae</href>
17       </Link>
18     </Model>
19   </Placemark>
20 </Document>
```

Figure 35. A COLLADA model extending twice the diameter of the planet is used to display hot flow anomalies caused by solar wind.

3.5.3 SOLAR WEATHER

Venus does not have a magnetic field to protect its atmosphere from the solar wind, consequently solar weather has an impact close to the ground. Recently, hot flow anomalies have been detected on Venus (http://www.nasa.gov/mission_pages/sunearth/news/venus-explosions.html). We display these using a COLLADA model that extends to twice the diameter of the planet (Figure 36 and Figure 35):

http://www.digitalplanet.org/gv/venus_hfa.kml

This is just one example of a wide range of atmospheric data that can be displayed on Google Venus with COLLADA and KML.

3.6 SURFACE IMAGERY

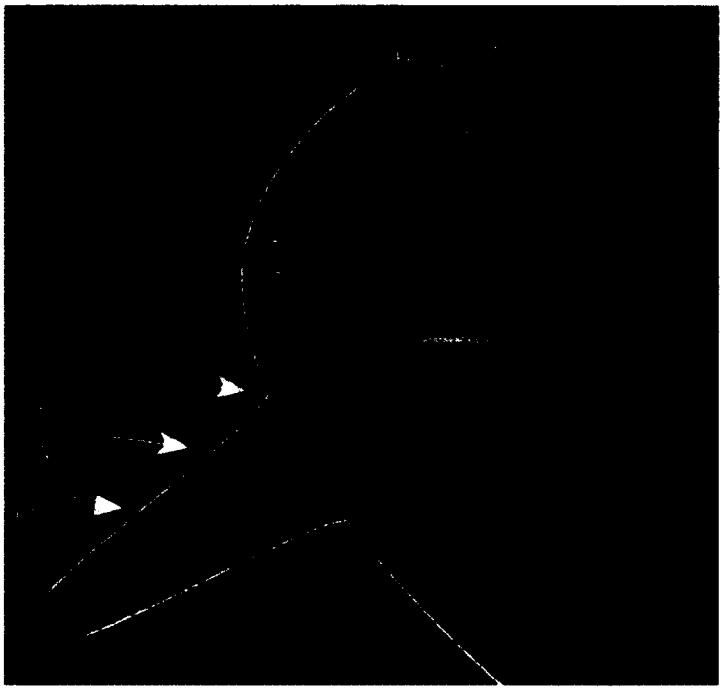

Figure 36. Solar weather on Venus is intense at low atmospheric altitudes owing to the lack of magnetic field protection. Recently discovered hot flow anomalies (HFAs) are illustrated using a COLLADA model that extends twice the diameter of the planet. Source: http://www.nasa.gov/mission_pages/sunearth/news/venus-explosions.html. The colored image at the South Pole is a COLLADA model of the southern dipolar vortex.

3.6.1 MAGELLAN ALTIMETRY AS PRIMARY DATABASE

To serve as a primary database we used a global altimetry image from NASA's Magellan mission (Figure 37) which is available in simple cylindrical (Plate Carrée) projection, the appropriate projection for Google Earth. Because it covers the entire globe, we call this the tablecloth (file "tablecloth.kml" in the GSA Data Repository[1]).

Note that, owing to file size, we did not simply drape an image as a ground overlay as in the case of the atmosphere. Instead, we linked to the root of an image pyramid which sharpens the focus of the surface as the viewer zooms in, by loading progressively more detailed image tiles, as explained in the next section.

3.6.2 SURFACE IMAGERY MANAGEMENT

A fundamental feature of Google Earth is the efficient management of surface imagery across a range of scales. When the user zooms in from the elevation of the Space Shuttle to that of a helicopter, progressively higher resolution images are automatically draped on the surface DEM. If the most detailed ground imagery were loaded regardless of viewer elevation, there would be terabytes of data to cache and the application would grind to a halt even on a supercomputer. When creating Google Venus, we had to emulate Google Earth's surface image management system. We did so by downloading the highest resolution surface images available from NASA and making image tiles (also known as image pyramids or super overlays) using a freely available application called MapTiler (http://www.maptiler.com). For example, the source of the Magellan tablecloth covering the Earth surface imagery is a 5 MB file. MapTiler converted this into a pyramid of tiles each of which is less than 256 KB. Successive levers in the pyramid structure cover different surface areas of the virtual globe. At level zero, a single 256 KB tile covers 90° to -90° latitude and all 360 degrees of longitude, which is displayed only when the view is zoomed all the way out.

The file and folder structure for an image pyramid is shown in Figure 39(a) and sample code is listed in Figure 38. Each KML document in the pyramid contains an image tile and links to four nested documents. The Region element checks the level of detail (Lod) to ascertain whether the current tile occupies a minimum of 128 pixels of the main viewer window space and if it does that tile is loaded. Setting maxLodPixels to "-1" denotes no cut–off level–of–detail, so the image remains visible

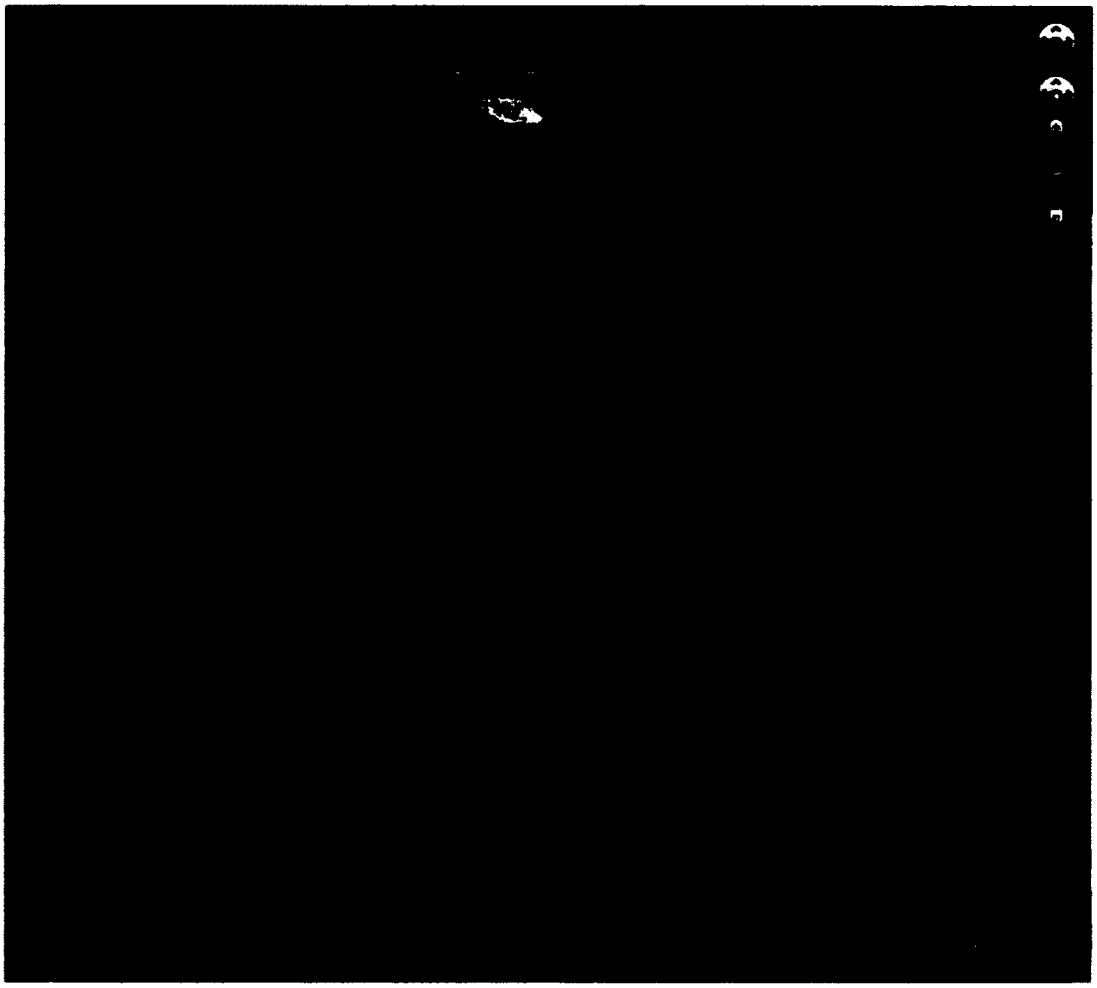

Figure 37. Google Venus's primary database was created by draping Magellan altimetry over the Google Earth surface imagery. White graticule shows longitude convention for Venus (see text). Latitude is measured identically on both planets. Venus has an equator and prime meridian but no tropics or arctic/antarctic circles.

```
<NetworkLink>
  <name>1/0/0.png</name>
  <Region>
    <Lod>
      <minLodPixels>128</minLodPixels>
      <maxLodPixels>-1</maxLodPixels>
    </Lod>
    <LatLonAltBox>
      <north>0</north>
      <south>-90</south>
      <east>-90</east>
      <west>-180</west>
    </LatLonAltBox>
  </Region>
  <Link>
    <href>../../1/0/0.kml</href>
    <viewRefreshMode>onRegion</viewRefreshMode>
  </Link>
</NetworkLink>
```

Figure 38. Sample network link from an image pyramid. The Region element determines whether the current image (1/0/0.png) will be displayed based in the level of detail (Lod). If this image occupies more than 128 pixels, a more detailed image links to ../../1/0/0.kml is tested recursively.

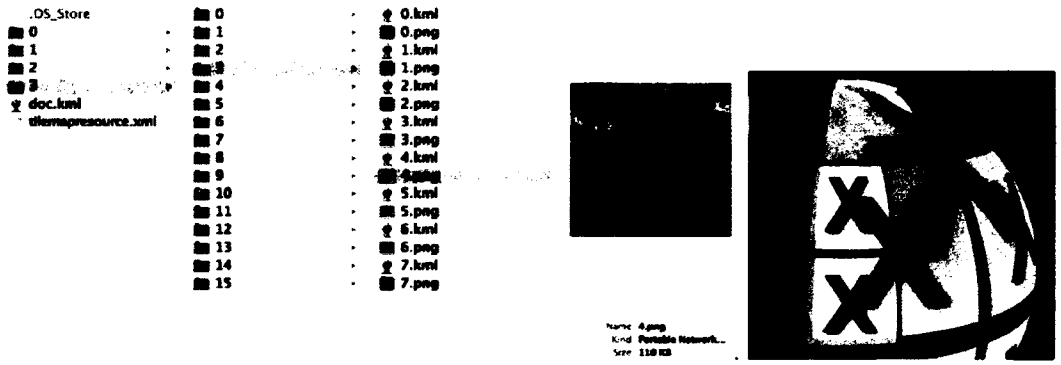

Figure 39. a) Image tiles or pyramids are essential for file size management. This figure shows the nested folder and file system created by MapTiler for the Magellan Tablecloth image pyramid. b) The structure of an image pyramid revealed by red X symbols replacing missing image files.

as one zooms in to ground level. Consequently, in an inclined view, the tiles near the viewer will be relatively high resolution draped over the larger, lower resolution tiles visible in the distance. The code snippet in Figure 38 tiles one eighth of the globe's surface in the southeast. Figure 39(b) illustrates the structure of a 4 level image pyramid. Here, image tile files were purposely removed, causing Google Earth to substitute a red X for each missing image.

3.6.3 VENUSIAN LAT–LON GRID

Planets have a natural origin of latitude - their equator - but not of longitude. Earth's prime meridian, passing through Greenwich England, was selected arbitrarily. On Venus, longitude is measured from 0° to 359° , increasing eastward from the prime meridian, which is arbitrarily set to pass through the peak of Ariadne Crater. Because Venus's axial tilt is less than three degrees off vertical, there are no useful Venusian analogs of the Tropics of Cancer and Capricorn nor of the Arctic and Antarctic Circles, which reflect Earth's 23.5° tilt. (Strictly speaking, Venusian tropics border the equator at 2.7° north and south, and the circles encircle the poles at the same angle. However, there are no seasonal climatic implications analogous to Earth.) To avoid the confusion that might result from using the "Grid" feature built into Google Earth, we created a graticule appropriate to Venus ("venus_latlon.kml", see footnote 1; it is turned on in Figure 37).

Note that Google Earth's W180° to E180° longitude convention must be used when creating content in KML code. Correct longitude conversion can be checked by turning on and comparing the custom Venus grid and the built-in Google Earth grid.

3.6.4 EARTH'S CONTINENTAL OUTLINES AS GEOGRAPHIC REFERENCE

Because viewers unfamiliar with Venus's surface may find it difficult to orient themselves in a global context, we created a layer that projects the outlines of Earth's continents onto the Google Venus surface ("venus_conts.kml", see footnote 1; Figure 40). This method was previously shown to help students with spatial awareness [*Brooks et al.*, 2010] - their verbal reports suggest that the outlines helped develop their sense of place and scale.

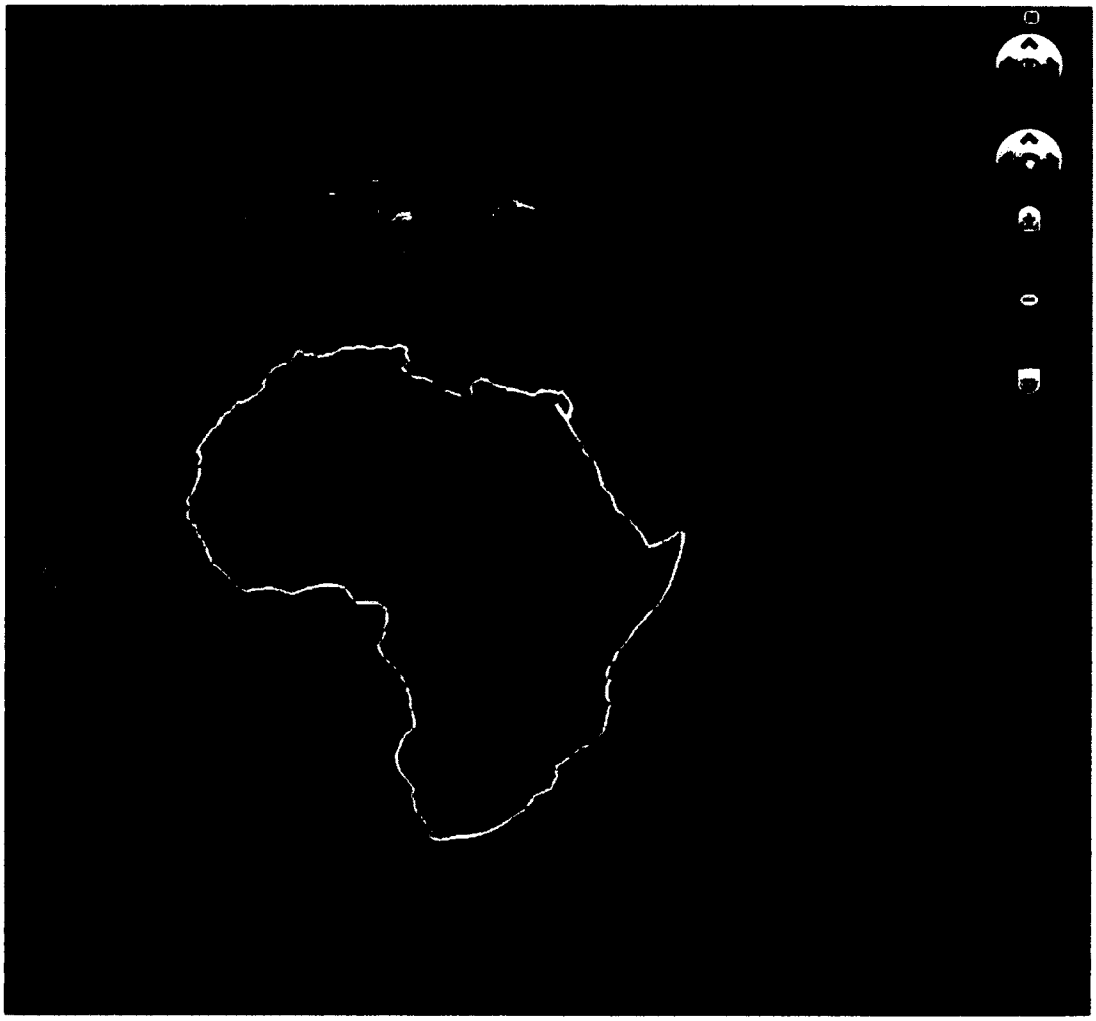

Figure 40. Outlines of Earth's continents (white) help students locate features on Venus.

```
<Placemark>
  <name>Any Placemark</name>
  <Style>
    <BalloonStyle>
      <text>
      [Balloon text here]
      [No driving instructions!]
      </text>
    </BalloonStyle>
  </Style>
  <Point>
    <coordinates>0,0,0</coordinates>
  </Point>
</Placemark>
```

Figure 41. Creating a custom balloon style suppresses default driving instructions.

3.6.5 GOOGLE EARTH TOOLS AND LAYERS

The built-in Google Earth ruler tool can be used for measurements on Google Venus bearing in mind that the ruler overestimates surface distances and areas because Venus is slightly smaller than Earth. The mean radius of Venus is 6,052 *km* compared to Earth's 6,378 *km*, therefore great circle distances between equivalent points on Venus are approximately 95% the lengths of those arcs on Earth and surface areas are about 90%. The Search Box and Layers in the sidebar of the Google Earth desktop application are of no use on Venus and should be kept collapsed, leaving only the Places sidebar panel expanded. Also, driving instructions in placemark balloons should be suppressed by creating custom balloon styles (Figure 41).

3.7 MISSIONS TO VENUS

It may come as a surprise that since the 1960s, more than twenty successful missions to Venus have been launched by the former Soviet Union (USSR), the United States (NASA), and the European space agency (ESA). For details, see http://planetary.org/explore/topics/venus/missions.html. A Japanese space agency (JAXA) mission is currently en route to the planet (http://www.jaxa.jp/projects/sat/planet_c/index_e.html). Of these, only the Soviet Venera and Vega missions placed landing craft on the surface.

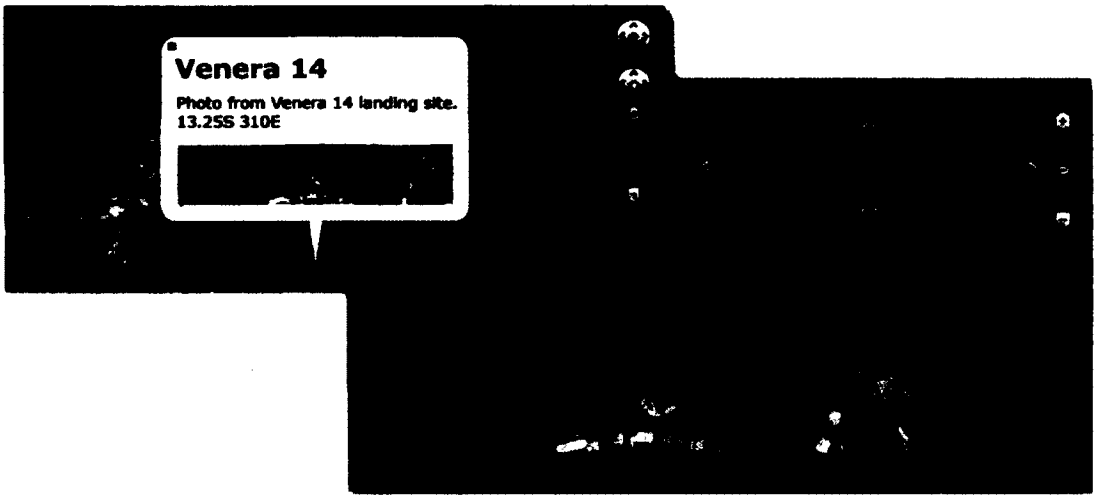

Figure 42. Surface image of Venus from the Soviet Venera mission shows a dry, fine-grained, probably basaltic crust with no sign of the varied granitic rock types that characterize Earth's continents. This placemark is at the Venera 14 landing site. Source: http://solarsystem.nasa.gov/multimedia/gallery/venera141TOP.jpg

3.7.1 VENERA LANDING SITES

We have included four Venera landing sites in Google Venus, each with a photo overlay taken from the surface (Figure 42). They are grouped in a radio button-style folder and can be visited as a miniature virtual field trip ("venera_landing.kml", see footnote 1).

Sample code for the Venera 9 photo overlay is shown in Figure 43. Fortunately, the camera angle and view parameters do not require coding by hand - they can be generated automatically by adding a photo in the desktop application and adjusting the settings in the New Photo Overlay box. When a photo overlay is saved to MyPlaces or Temporary Places, the automatically generated code can be accessed by selecting the photo overlay in the places sidebar; right-clicking and copying; switching to a text editor or code editor; and pasting into a KML document.

```
<PhotoOverlay>
  <name>Venera 9</name>
  <description><![CDATA[
  Photo from Venera 9 landing site, 31.01N, 291.64E.
  <br/>
  <img src='images/venera_9.jpg' width='400'>
  ]]></description>
  <Camera>
    <longitude>-68.36000000099992</longitude>
    <latitude>30.99999999999999</latitude>
    <altitude>194.8600000003038</altitude>
    <heading>2.099355619496519e-05</heading>
    <tilt>87.7595142797512</tilt>
    <roll>-8.844200208292416e-10</roll>
  </Camera>
  <Style>...</Style>
  <Icon>
    <href>images/venera_9.jpg</href>
  </Icon>
  <ViewVolume>
    <leftFov>-45.615</leftFov>
    <rightFov>45.615</rightFov>
    <bottomFov>-12.615</bottomFov>
    <topFov>12.615</topFov>
    <near>68.201</near>
  </ViewVolume>
  <Point>
    <coordinates>-68.36,31,194.86</coordinates>
  </Point>
</PhotoOverlay>
```

Figure 43. Code snippet for the photo overlay at the Venera 9 landing site.

3.7.2 FLY-BYS, PROBES, AND ORBITAL MISSIONS

Since the 1960s, there have been several fly-by missions to Venus, some of which dropped probes into the atmosphere (http://nssdc.gsfc.nasa.gov/planetary/chronology_venus.html). These collected useful information on extreme atmospheric temperatures, crushing pressures, and the lack of a magnetic field. However, the most important missions were those that placed spacecraft in orbit and mapped the surface remotely - most notably the 1989 Magellan mission [*Ford et al.*, 1993].

Although opaque to visible light, the Venusian atmosphere is transparent in microwave or radio frequencies. Synthetic aperture radar (SAR) imagery collected as part of the Magellan mission provides spectacular views of the surface, covering 98% of the planet with resolutions up to 100 m/pixel. SAR data taken together with Magellan altimetry reveal basic surface features stereoscopically. Magellan altimetry represents the major global data set that we use as a "base map" for Google Venus, with SAR images projected onto the surface in specific areas. The altimetry data have low-resolution SAR data imbedded within the color-coded output. These data allow recognition of highland and lowland regions, and global-scale zones of localized tectonism and volcanism.

3.7.3 SAR IMAGE PYRAMIDS

Because of the very large file sizes involved, SAR images must be tiled before being draped over the surface in order to avoid slowing the performance of Google Venus. For example, a 60 MB image of Bonnevie crater was tiled to 7 levels of detail to create a deeply zoomable viewing experience (Figure 44(a)). The image pyramid may be loaded using the root file "bonnevie.kml" (see footnote 1).

Care must be taken, however, when more than one image pyramid is viewed as tiles may interfere. In Figure 44(b), for example, the foreground tiles are from the gray SAR pyramid but the background tiles are from the colored Magellan tablecloth pyramid. As one flies over this region, tiles may compete for prominence, as illustrated by the zig-zag boundary and the isolated gray tile in the top right corner. The solution would be to carefully control the KML <drawOrder> used in different image pyramids. However, this process is not automated and would be tedious to implement by hand given dozens of nested KML documents. A simpler solution is to turn off all but one image pyramid at a time. We have created the following

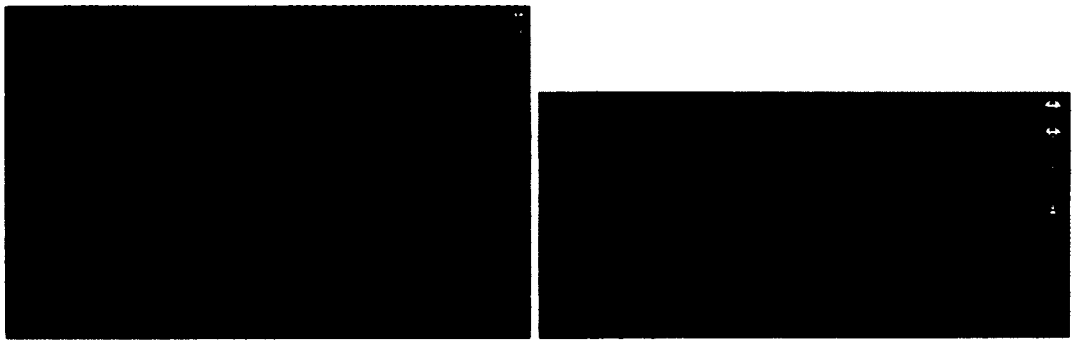

(a) (b)

Figure 44. a) A 60 MB PNG file of Venus's Bonnevie Crater was tiled to 7 levels to create a surface image that is zoomable. b) Superposition of tiled images sometimes causes competition for drawOrder. See text for discussion.

image pyramids from SARs files (posted to the GSA Data Repository; see footnote 1). The first three are named for use in student exercises, while the remainder are named for their SARs database references. It is important to load these sequentially, not simultaneously, otherwise, Google Venus responsiveness will grind to a halt. If performance deteriorates gradually, it may help to clear the caches.

3.8 EXPLORING THE SURFACE

Global topography, defining the shape of the surface, provides fantastic clues to how a planet evolved, and to dynamic interior processes. Topography on Venus is keyed to mean planetary radius, or MPR (6051.9 *km*) since sea-level is meaningless on a dry planet. The range of topography is similar to Earth, with the highest point (Maxwell Montes) about 11 *km* above MPR and the lowest (Diana-Dali Chasma) approximtely 7 *km* below MPR. However the distribution of Venus's topography is quite different from Earth's. Venus has a unimodal distribution of topography with most of the planet close to MPR, unlike Earth's bimodal topographic division into low oceans and high continents.

Magellan altimetry and SAR data reveal basic surface features and permit the definition of three types of terrain based on altitude - Highlands, Mesolands, and Lowlands - as well as distinctive features such as craters and uniquely Venusian structures discussed below.

3.8.1 LOWLANDS

Just as most of the Earth's surface (72%) is oceanic, most of Venus's surface (80%) comprises lowlands which include relatively smooth plains called planitiae, deformation belts that can extend hundreds of kilometers, and narrow channels or "canali" ranging from tens or hundreds of kilometers long (up to 6,900 *km* long in the case of Baltis according to *Banerdt et al.* [1997]). Lowland regions also host thousands of inliers of ribbon tessera terrain (see below).

Lowland surfaces are deformed by so called wrinkle ridges and linear fractures. Long sinuous ridges mark the crest of wrinkles, or folds. Linear fractures are the surface expression of dikes at depth where magma traveled possibly thousands of kilometers [*McKenzie et al.*, 1992]. Wrinkle ridges and fractures define patterns traceable across tens of millions of square kilometers, and mapping out these patterns can provide critical clues to Venus's volcanic and tectonic processes. Coronae (see next section) occur rarely as isolated features in the lowlands.

3.8.2 MESOLANDS

The mesolands together with the highlands account for the remaining 20% of the surface. These middle altitudes host most of the planet's approximately 500 coronae - quasi-circular features generally ranging from 60-800 *km* in diameter and typically forming chains spatially associated with troughs called chasmata [*Stofan et al.*, 1997]. Although coronae are widely accepted as representative of diapirism, formation by impact has also been proposed (e.g., *Vita-Finzi et al.* [2005]).

3.8.3 HIGHLANDS

Highland features include volcanic rises and crustal plateaus. Volcanic rises are large domed regions of radial volcanic flows ranging from 1,500-2,500 *km* in diameter and 1-3 *km* in elevation. They are thought to be thermally supported expressions of deep mantle plumes under the thick lithosphere (e.g., *Phillips and Hansen* [1994]; *Smrekar et al.* [1997]; *Nimmo and McKenzie* [1998]. Coronae form clusters associated with some volcanic rises (e.g., Themis Regio, Bell Regio, and Eastern, Western, and Central Eistla Regio). The KML file "venus_rises.kml" (see footnote 1) features numerous volcanic rises.

Crustal plateaus, similar in planform to rises, are steep-sided, rising 0.5-4 *km*

above their surroundings. Widely accepted as relatively old features, they are likely isostatically supported by thick crust, or low-density mantle residuum (e.g., *Phillips and Hansen* [1994]; *Simons et al.* [1997]; *Hansen* [2006]). They are marked by ribbon-tessera terrains consisting of short folds with long orthogonal 'ribbon' structures and graben that imply layer extension perpendicular to fold crests. Lava flooding structural lows indicate accompanying volcanic activity [*Phillips and Hansen*, 1994; *Ivanov and Head*, 1996; *Hansen and López*, 2010]. Ribbon tessera terrain can be viewed at two Google Venus locations: Ovda Region Tessera Terrain, and in the Bell Regio Area. Several plaeteaus are described in the "venus_plateus.kml" file (see footnote 1).

3.8.4 IMPACT CRATERS

Venus has some 1,000 craters randomly distributed in Lowlands, Mesolands, and Highlands. Craters range in diameter from 1-270 *km* [*Schaber et al.*, 1992; *Phillips et al.*, 1992; *Herrick et al.*, 1997] and show evidence of progressive degradation [*Izenberg et al.*, 1994; *Basilevsky and Head*, 2002] which allows for delineation of relative age relations [*Phillips and Izenberg*, 1995; *Hansen et al.*, 1997]. Venus lacks small craters due to screening by its thick atmosphere which unfortunately hampers crater density dating. Low crater density implies a mean model surface age of 0.5 1.0 b.y. [*McKinnon et al.*, 1997].

The early interpretation that most of Venus's craters were pristine not faulted or volcanically embayed lead to the widely accepted idea that Venus was catastrophically resurfaced at about 500 Ma [*Schaber et al.*, 1992; *Bullock et al.*, 1993; *Strom et al.*, 1994]. Catastrophic resurfacing was defined as a near-global event that flooded at least 80% of the planet with lava to a depth of 1 *km* or more within a 10-100 million year period, wiping out essentially all of Venus's early history. This resurfacing event was assigned a major role in Venus's climate evolution (e.g., *Bullock and Grinspoon* [2001]; *Taylor and Grinspoon* [2009]). However, a growing body of data is difficult to reconcile with catastrophic resurfacing hypotheses, and it is likely that Venus's surface preserves a rich record of past geological processes (see: *Guest and Stofan* [1999]; *Hansen and Young* [2007]; *Hansen and Olive* [2010]; *Bjonnes et al.* [2012].

3.8.5 UNIQUE FEATURES - ISTHAR AND ARTEMIS

Structures such as impact craters, volcanic cones, and wrinkle ridges are common

on planets and moons of the Solar System. However, Venus has features unlike anything seen elsewhere. Prominent among these are the mutually antipodal Isthar Terra and Artemis structures.

3.8.5.1 ISHTAR

Ishtar Terra forms a huge continent-like region represented by the 4 *km* high plateau of Lakshmi Planum, surrounded by expanses of tessera terrain and mountain belts (or "montes"), including Venus's highest point, Maxwell Montes. The region has been proposed to form above a huge downwelling mantle convection cell which resulted in low-density mantle melt residuum uplifting the thickened crust like an iceberg [*Hansen and Phillips*, 1995].

3.8.5.2 ARTEMIS

Artemis, as historically defined, includes an interior topographic high surrounded by Artemis Chasma, a large narrow circular trough, and an outer rise that transitions to the surrounding lowland (Figure 45). However, recent geologic mapping indicates that these are only the center of a more expansive feature, including a 5,000-*km*-diameter topographic trough and suites of radial dikes and concentric wrinkle ridges that extend for 14,000km [*Hansen and Olive*, 2010]. Artemis's global footprint thus affects more than one fourth of the planet's surface-perhaps the largest tectonic feature in the Solar System.

Hypotheses for the formation of Artemis Chasma and surrounding regions have included subduction, bolide impact, and a mantle plume (e.g., *Griffiths and Campbell* [1991]; *McKenzie et al.* [1992]; *Brown and Grimm* [1995, 1996]; *Hamilton* [2005]; *Schubert and Sandwell* [1995]; *Smrekar et al.* [1997]; *Hansen* [2002]). Detailed geologic mapping of Artemis Chasma favor a plume hypothesis [*Bannister et al.*, 2010], however, the recognition of the Artemis super-structure suggests an additional super-plume component [*Courtillot et al.*, 2003; *Hansen and Olive*, 2010] affecting ~25% of the surface of Venus with radial dikes and/or concentric wrinkle ridges. The incredible size and radial nature of the dike swarm and the concentric nature of the wrinkle ridge pattern provide evidence of a huge axisymmetric global stress field. One way to consider the size of the Artemis super-plume signature is by way of comparison. When scaled to the host planet's size, the Artemis radial fracture suite is proportionally similar to the Tharsis radial dike system on Mars which includes the

Figure 45. The Artemis Structure and Artemis Chasma. Outline of Australia conveys the scale. Source: http://solarsystem.nasa.gov//multimedia/display.cfm?IM_ID=9603

famous Olympus Mons volcano- familiar to many as the largest volcano in our solar system [*Wilson and Head III*, 2002]. This comparison might provide clues to possible global-scale mantle flow patterns in terrestrial planets lacking plate tectonics.

The incredible areal extent of radial dikes and wrinkle ridges record the effect of the Artemis super-plume across the surface, however, it is also likely that the super-plume affected flow patterns within the mantle. Global-scale upwelling associate with the super-plume would flow outward in a radial pattern from Artemis Chasma, with flow along the base of the lithosphere. Ultimately, return flow might converge in a global-scale downwelling. Just as the upwelling would be centered on Artemis, one might expect a global downwelling to be antipodal. Ishtar Terra is located in an antipodal position to Artemis, and could represent a surface expression of a global-scale downwelling. These processes can perhaps be best viewed in global scale COLLADA models, which allow one to view both surface and interior features simultaneously.

3.9 VENUS'S INTERIOR

Despite surficial differences, models for Solar System evolution suggest that Venus and Earth share similar rocky mantles and metallic cores [*Wetherill*, 1990]. Although we can make seemingly sensible arguments for Venus's deep structure, these arguments are almost all based on analogy with Earth, given that we lack critical data, particularly seismologic data. This lack of data affects our understanding of the internal structure and rheological layering, which has implications for thermal evolution. Mechanisms of heat transfer, conduction, convection, and advection, depend, at least in part on rheology. On a basic level, terrestrial planets have a stiff lithosphere that conducts heat, and a deeper mantle that convects heat. Venus, unlike Earth, exhibits strongly correlated long-wavelength gravity and topography fields [*Phillips and Lambeck*, 1980]. For example, long-wavelength geoid highs correlate with high topography of volcanic rises, crustal plateaus, and Ishtar Terra, whereas long-wavelength geoid lows correlate with lowlands such as Niobe and Rusalka Planitiae. This correlation is variably interpreted as evidence for either a thick ($\sim$300 km) strong thermal lithosphere or mantle convection beneath $\sim$150 km thick lithosphere. To the first order, lithosphere thickness is inversely proportional to heat flow, thus this debate is relevant to discussions of present-day heat loss-which remains unknown.

A reasonable working hypothesis assumes Venusian effective mantle viscosity is similar to Earth, with a strong temperature-dependent viscosity profile. Large viscosity contrasts are likely across thermal boundary layers: notably across the lithosphere and core-mantle boundaries. In contrast to Earth however, Magellan gravity and topography data do not require a low viscosity asthenosphere (e.g., *Simons et al.* [1997]) likely contributing to a lack of plate tectonics on Venus. Another potentially important, but currently unconstrained difference between Earth and Venus mantle viscosities may result from differing volatile contents. A lack (presence) of volatiles will increase (decrease) strength and increase (decrease) the solidus of mantle materials.

3.10 VISUALIZING THE INTERIOR

Concepts that many Venus scientists accept are illustrated in speculative crust-to-core cross-sections (e.g., [*Schubert et al.*, 1997; *Smrekar and Stofan*, 1997]) as COLLADA models in the Google Venus environment, as discussed below. Lowlands lie above mantle downwellings; volcanic rises are thermally supported and underlain by deep-mantle plumes; crustal plateaus garner isostatic support due to either thick crust or low-density mantle melt residuum. Chasmata chains (e.g., Diana-Dali, Parga, and Hecate Chasmata) represent large cylindrical mantle upwellings; coronae can be spawned within the shallow part of this upwelling environment, or within some plume heads (e.g., Bell or Themis Regiones). COLLADA models allow us to view the mantle, gaining a global 3D understanding of the planet (Figure 46(a)).

Schematic cross-sections were created in a drawing program and saved as portable network graphics (PNG) image files. These were imported into Google SketchUp (http://sketchup.google.com) and used as surface textures on spherical-slice models. The models were then exported as Digital Asset Exchange (.dae) files. For the desktop application version, the models may be loaded from the "venus_mantle.kml" file (see footnote 1).

Loading this file prompts the viewer to switch from Google Earth to Google Mars. The radius of Mars is thought to be a good approximation to Venus's core, therefore we draped the Google Mars surface imagery with an orange PNG file and superimposed the COLLADA models of Google Venus's mantle and crust.

The three cross-sections allow one to view and postulate possible spatial - and by extension, temporal - relations between surface geology and mantle. Two longitudinal

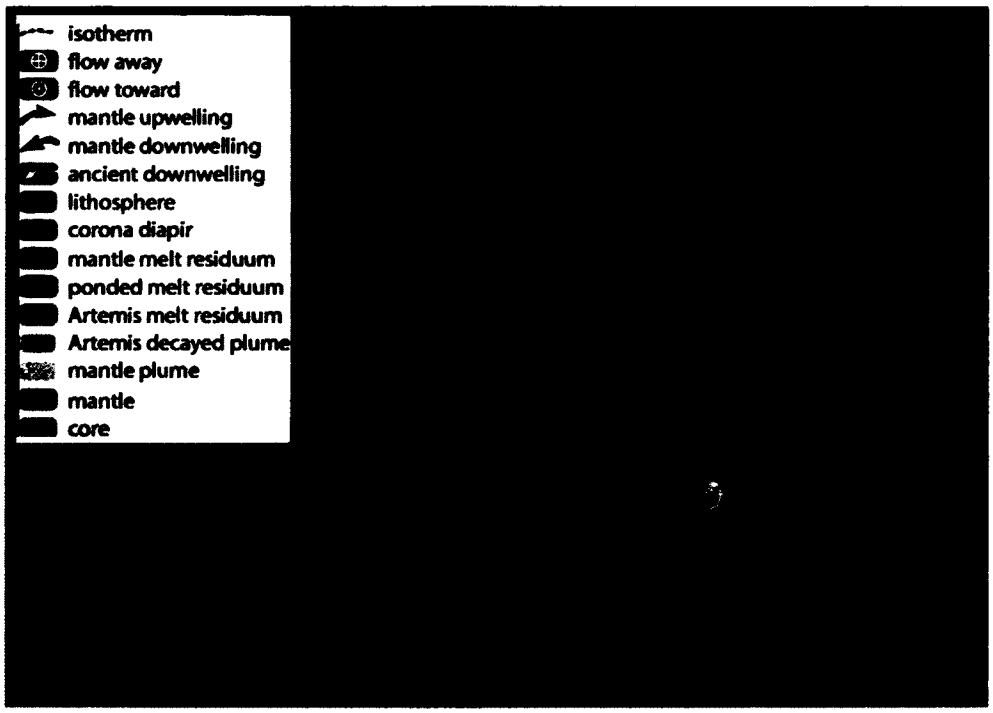

(a)

(b)

Figure 46. a) COLLADA models of the interior of Google Venus. b) Turning on the Venusian lat–lon grid on the core identifies the mantle cross sections in the COLLADA models of the interior of Google Venus.

sections cut from the north to south pole: the 135E longitude section cuts through Artemis, and the 45E longitude section cuts the western edge of the surface expression of the Artemis super-plume, as marked by the concentric wrinkle ridge suite. The third section parallels the equator, slicing the planet between the two longitudinal sections. Sections are easily identified when the lat-lon grid is turned on (it appears on the surface of the core, Figure 46(b)).

3.10.1 135E LONGITUDE SECTION

This sections cuts from the surface to the core slicing through the Artemis plume, represented by the faded pink thermal plume. The Diana-Dali Chasma upwelling affects this region just north of Artemis. Thetis Regio with thickened crust or low-density upper mantle occurs within this cross-section. North of Thetis and south of Artemis mantle downwellings draw the surface downward forming the lowland regions of Niobe Planitia and Zhibek Planitia. South of Artemis, Zhibek and Imapinua Planitiae are separated by a small corona-chasmata chain that might signal a local mantle upwelling as shown on the cross-section.

3.10.2 45E LONGITUDE SECTION

Just north of the center of this section a mantle plume that supports Eastern Eistla Regio rises from the core. A similar plume supporting corona dominated volcanic rise Bell Regio also appears in the section to the north. Bell Regio is centered slightly east of Eastern Eistla, and therefore, depending on thickness of a plume root (unknown), a root for Bell might not lie within the plane of the section. South of Eastern Eistla return flow of the mantle results in the formation of a broad lowland extending southward to and including Fauna Planitia.

3.10.3 EQUATORIAL SECTION

The equatorial section from 45E to 135E cuts through much of Aphrodite Terra, the largest highland region on Venus. Near 45E, remnants of thickened crust and/or mantle melt residuum associated with the formation of ancient ribbon tessera terrain are likely. Further east such a unit is clearly present, providing isostatic support for the huge mass of Ovda Regio (90E), Venus's largest crustal plateau. Within this section the strongest flow is likely outward to the north and south from the generally

WNW-trending Diana-Dali Chasma region.

3.11 CONCLUSIONS

Google Venus provides a new and exciting means to explore Earth's sister planet, with lessons for both Venus and Earth. Virtual exploration allows students and researchers to appreciate a wide range of spatial relationships, on the surface, and in three-dimensions at a truly global scale and in a way not previously possible. We hope that Google Venus will continue to grow and evolve as a community resource. Venus's surface, long veiled by thick, heretofore impenetrable clouds, can now be viewed by anyone with an Internet connection by loading the "venus.kml" file (see footnote 1).

As space missions deliver more detailed surface images of the planets and moons of the Solar System, there will be new opportunities to create virtual globes for numerous bodies. Following the methods described here, readers could create their own Google Europa, Google Titan, etc.

3.11.1 ACKNOWLEDGMENTS

Hansen acknowledges support from the McKnight Foundation and NASA grants NNX06AB90G and NNX11AQ86G. De Paor and Dordevic were supported by NSF TUES 1022755, NSF GEO 1034643, and a Google Faculty Research Award. Any opinions, findings, conclusions or recommendations expressed in this paper are those of the authors and do not necessarily reflect the views of NASA, National Science Foundation, the McKnight Foundation, or Google Inc. Comments of reviewers Eric Pyle and Jen Piatek greatly improved the manuscript.

CHAPTER 4

EARTH: THE HAWAIIAN PLUME

This chapter introduces an instructional model for plume dynamics far away from plate boundaries. Material in this chapter was presented previously in several conferences [*Dordevic et al.*, 2010].

4.1 ABSTRACT

Using geospatial visualizations tools such as Google Earth for teaching, research and dissemination proved to be a very effective method to help people visualize complex tectonic processes and also helped me to discover geophysical research questions addressed later in this dissertation. In this chapter I present methods for data visualization in Google Earth. In particular I introduce an emergent cross section of Hawaii, using Google Earth API and JavaScript, with pictographic representation of the Hawaiian mantle plume. Using seismic tomography data of Hawaiian thermal anomaly I made 3D reconstruction of the plume using SketchUp (sketchup.com) and used it for comparison of the learning outcome of real data versus pictographic text book representation for mantle plumes. In order to illustrate the interaction of the Hawaiian mantle plume with the moving overlying lithosphere I recreated the evolution of the Hawaiian Emperor (HE) volcanic chains. A set of still pictographic representations of the plume-plate interactions through time coupled with the corresponding motion of the Pacific plate created an animated model.

4.2 INTRODUCTION

The presence of a plate boundary on the surface can be manifested by volcanic chains as well as seismic activities. The plate tectonic model provides an excellent explanation for these. At the contact point of two plates, melt is generated by decompression melting due to upwelling. Melt propagates upward through cracks and dikes to form magma chambers resulting in creation of volcanic edifices. The cracks are being formed at the places that are under highest shear and can propagate laterally for several hundred kilometers. Under ocean ridges the source of melt is the

upper mantle that is undergoing decompressional melting [*Whitehead et al.*, 1984]. This melt is pooled to the crustal magma chambers and from there it is erupted to the surface [*Niu*, 1997; *Asimow et al.*, 2001]. On the cold subduction slab, presence of water, methane and carbon dioxide can trigger partial melting in overlying mantle by changing its bulk composition [*Peacock*, 1990; *Kerrick and Connolly*, 2001].

What plate tectonics fails to explain is the origin of volcanic islands and seamount chain like Hawaiian Emperor away from plate boundaries. Early development of deep mantle plume theory [*Morgan*, 1971] is inspired by this chain. According to *Morgan* [1971] Hawaiian hotspot is fueled by the plume originating in the deep mantle and there are about twenty others whose positions are fixed relative to one another. Time progressive volcanic track and high volcanic rates were key components of hotspots caused by deep mantle plumes.

The Hawaiian–Emperor chain is located in the Pacific Ocean and it stretches for 5800 km from the Big Island of Hawaii to Alaska's Aleutian Trench. At the southeastern end of the chain, the Big Island of Hawaii is host to one of the most active volcanoes, Kilauea, with Mauna Kea and Loihi volcanoes nearby. This chain is divided into parts. The first part is known as the Hawaiian Ridge and it is comprised of the main Hawaiian and Northwestern Hawaiian Islands extending some 3000 km northwest across the Pacific. At this point, the chain turns sharply toward the north and makes the Emperor Seamounts extending until the Aleutian Trench at the Kamchatka Peninsula in Siberia. An unknown number of seamounts have already been subducted at the northern end of the chain.

This sharp turn in the chain is associated with the rapid change in the direction of the Pacific plate's motion over the fixed hotspot about 47 million years ago. Some theories [*Norton*, 1995] imply that this abrupt change in the direction of the Pacific plate is caused by the collision of India with Asia or by a change in circum-Pacific geometry [*Gordon et al.*, 1978]. The collision of India and Asia initiated subduction along western Pacific plate transform boundary. This subduction was followed by the strong westward slab pull leading to the change in the direction of the Pacific plate motion [*Patriat and Achache*, 1984]. On the other hand, *Tarduno* [2007] claims that based on paleomagnetic data there is a southward motion of the Hawaiian mantle plume from 81 to 47 Ma significantly contributing to the morphology of Hawaiian–Emperor chain. It is our goal to help teach the above mentioned concepts to students and assess their understanding using Google Earth based visualization methods.

4.3 MODELING THE HAWAIIAN MANTLE PLUME WITH SKETCHUP

For modeling the Hawaiian mantle plume I used the freeware version of the Sketchup. SketchUp is a lightweight 3D modeling tool that allows me to geotag and directly export created objects to the Google Earth supported format COLLADA. The first step here is to determine what is the most common method used so far to visualize mantle plumes. According to the literature, teaching materials and in on line lectures, the most common method for visualizing a mantle plume is using a pictographic representation with an elongated thin stem and mushroom shaped head. Representing a plume alone not be as helpful to the students but instead, I

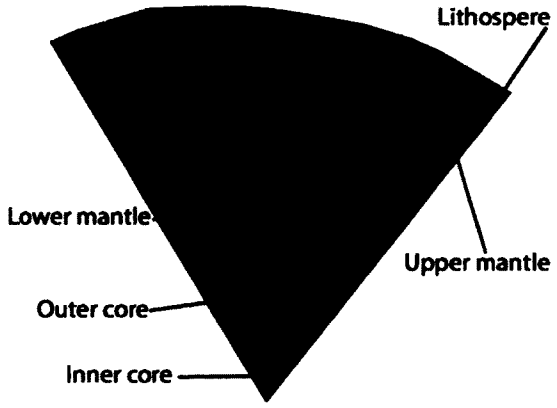

Figure 47. Earth's cross section with color coded layers representing inner core, outer core, lower mantle, upper mantle and asthenosphere going from bottom to top. All the layers have appropriate thickness [*Turcotte and Schubert*, 2002].

seated the plume in its surrounding. The surroundings are represented as a slice of the Earth's surface following the line of the Hawaiian Emperor seamount chain on one side and an arbitrary border at the other side. From the top surface the model is converging to the center of the Earth forming an irregular shaped cone. The sides of the cone are color coded representing different layers of the Earth's interior (Figure 47).

Using the data from the mantle S-wave velocity model of *Wolfe et al.* [2009] I

made 3D reconstructions of the deep Hawaiian mantle plume from the S-wave velocity anomalies data that were stratified at 100, 300, 400, 600, 900 and 1200 km. In the image editor GIMP [*GIMP*, 2011] by using the color selection tool I extracted surfaces that were outlined by the contours representing S-wave velocity anomaly of -0.7% from each depth. Those boundaries define an isosurface that likely enclose hotter deep mantle plume material (greater negative values of S-wave velocity anomaly). Such prepared surfaces are imported into SketchUp and applied as texture mapping to the planes that have vertical and horizontal positions as in the original *Wolfe et al.* [2009] data. By manually tracing out the -0.7% anomaly contour on each plane and cutting off unnecessary parts (larger than -0.7%)I converted data from image to the COLLADA format. Exploiting the SketchUp Sandbox tool that converts contour data into terrain I recreated the shape of the deep mantle plume (Figure 48). From

Figure 48. Mantle plume shape determined from observational data.

Figure 48, when compared to textbook example of the deep mantle plume, the first thing that can be noted is the lack of the plume's head. Oceanic plateaus and flood basalt represent the initial stages of plume volcanism [*Campbell and Griffiths*, 1990], so if the Hawaiian Emperor chain began like this, the plateau produced is not present at the Pacific plate. Since oceanic plateaus are not thought to be subductable, one of the possible explanations could be that the plume head was scraped off and accreted

to Aleutian arc, but no evidence for this so-called "off-scraping" has been documented.

The particular shape of the plume tail extending to 1200 km is of interest too. Text books commonly explain plume tails to be elongated quasi cylindrical [*Turcotte and Schubert*, 2002] shaped upwellings of hotter material, while here, we have an irregular shape (Figure 48). The question that arises from this 3D visualization is whether the plume tail, in its vertical shape, preserved the record of the mantle shear flow beneath the Pacific plate and in particular the change in direction of the Pacific plate 47 millions years ago.

According to *Steinberger and O'Connell* [1998] analytical model, where one-dimensional mantle flow was discussed, deflection of the plume conduit of about 150 km is expected in the uppermost 300 km of the Hawaiian chain. The total deflection because of the bend in Hawaiian–Emperor chain is no more that 200 km [*Griffiths and Richards*, 1989] in uppermost layer and about 750 km in the region from 300 to 900 km depth. Similar results were obtained in the laboratory experiment by *Richards and Griffiths* [1988] using plexiglass tanks filled with glycerol and mixture of glycerol and water for the plume material that was feed to the bottom of the tank. Those number are in general agreement with the measurements taken from my visualized model of the Hawaiian deep mantle plume. Thus this serves as a good example of our efforts to have reserach questions emerge from the process of creating learning objects.

4.4 ANIMATING THE EVOLUTION OF THE HAWAIIAN CHAIN

Using the 3D models created above (Earth's cone cross section, pictographic representation of deep mantle plume and real data plume), I created a web application for displaying them all together. For this I used the Google Earth web based plug in that enables the user to view the Google Earth content on a web page. To control the elements of the web page (Listing B.2) and link them to the elements of the Google Earth API instance, within this page, I used the JavaScript scripting language (Listing B.1). The user interface as seen in Figure 49(d) gives the possibility of controlling what aspect of the model will be shown. User can independently show and hide the Earth cross section and mantle plume cross section as well as apply the time evolution of the Pacific plate over the mantle plume. In order to make this I created a series of the Earth cross section with different Euler angles as Euler poles and rotation angles are used to describe plate motion. Next, appropriate textures

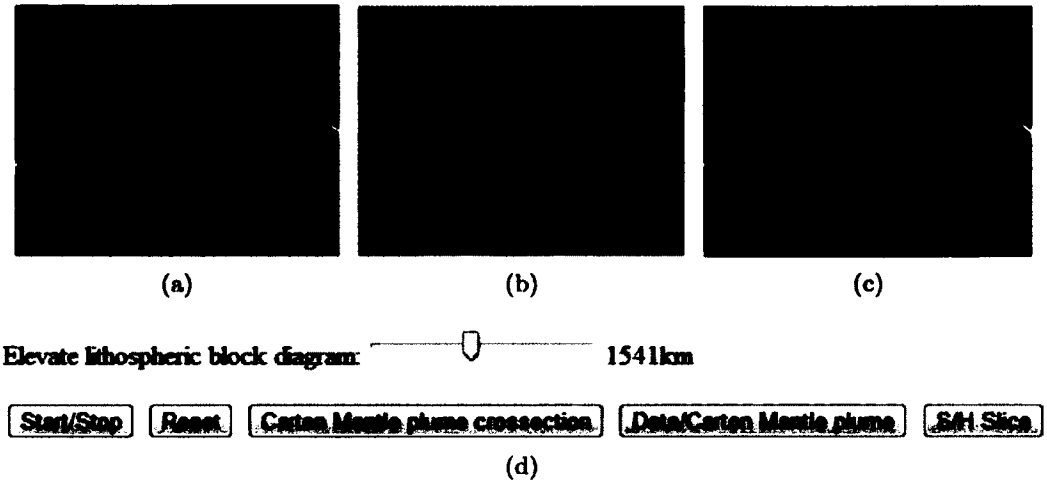

Figure 49. Web page with the user interface for the Hawaii deep mantle plume. a) Mantle plume from real data [*Wolfe et al.*, 2009], b) Lithosphere sitting on top of the mantle plume with melting migrating vertical (white color) and signs of the remnant volcanology left from it, c) Pictographic representation of the deep mantle plume cross section originating from the core mantle boundary, d) Interface where a user can adjust the elevation of the whole system (plume, cross section) in *km*, start or stop the animation of the Pacific plate moving over the deep mantle plume, turn on or off the cross section of the pictographic mantle plume, choose between the way mantle plume is represented (real data or pictographic representation) and show or hide Earth's cross section

for the top of the model were made by the image manipulation to the present day appearance of the Hawaiian Emperor chain. Major volcanic events in the history of the Hawaiian Emperor chain [*Raymond et al.*, 2000] are represented and corresponding time jumps are made. With all these elements incorporated the user can watch the animated sequence of the evolution of the Hawaiian Emperor chain, and can pause, restart and change the position of the camera as he or she pleases in order to maximize efficiency of learning. Following the motion of the whole cross section over the mantle plume according to the real data it can easily be noted that the plume conduit is being deflected by the mantle flow and that it preserves the history of the Pacific plate motion.

4.5 CONCLUSION

Google Earth can effectively be used [*Gobert et al.*, 2012] as a visualization tool for geophysical processes. Visualizing S-wave velocity data using SketchUp in a 3D visualization reopened revealed the interesting question about a possible correlation between the shape of the plume conduit and the motion of the overlying lithospheric plate. Comparison of literature calculations and our model found good agreement for the amount of deflection in the plume. From this it is concluded that the plume conduit is preserving the record of the lithospheric plate motion.

Composing this 3D model with pictographic representation of the plume and then embedding it into the web page proves to be convenient and effective teaching material. Richness of the web interface proved to be more user friendly compared to presentation of the material in Google Earth stand alone application.

CHAPTER 5

AVATARS AND MULTI-STUDENT INTERACTIONS IN GOOGLE EARTH - BASED VIRTUAL FIELD EXPERIENCES

All instructional material covered so far was meant for a single-user experience. Here design and coding of basic framework for multi user interaction in virtual Google Earth environment will be presented. The intent is that all the visualization and instructional material produced so far be modularly implemented in this framework enabling massive multi–user experience thus simulating real field trips. The work reported in this chapter has been published in a GSA Special Paper on Google Earth and Virtual Visualizations (see *Dordevic and Wild* [2012]).

5.1 ABSTRACT

We have developed object-oriented programming methods to enable avatar movement across the Google Earth surface in response to student actions, either on their own, or in groups attached to a field vehicle avatar (a Jeep). Students can communicate using text messages sent from their web page text field to balloons that pop up from the avatars' placemarks in Google Earth. Students can be located locally in a lab class or at great distances from one another, as in a distance education course.

Our programming methods help to create a more engaging virtual field trip in which the students take the lead and decide where to go rather than simply reading text and viewing graphics in a tour designed by their instructor. The user interactivity with avatar in web page embedded Google Earth is controlled by JavaScript and PHP. Since the position of each avatar is known it is possible to track their movements and offer text-message advice when they stray off-task or wander about aimlessly. Our methods will be included in new virtual field trips being developed for Iceland, Hawaii, and other locations.

5.2 INTRODUCTION

Google Earth [*Google*, a] comes in three forms: (i) a stand-alone application available for Windows, Macintosh, and Linux platforms, (ii) a mobile device app available for iOS and Android operating systems, and (iii) a web browser plug-in compatible with a variety of JavaScript-enabled web browsers including Chrome, Firefox, and Safari [*Google*, b]. The plug-in permits the programmer to incorporate one or more instance of Google Earth in a web page and to control each with familiar Hypertext Markup Language (HTML) interface elements such as buttons, text fields, and sliders. This paper focuses on the web browser plug-in form of Google Earth because of its extensive JavaScript Application Programming Interface (API) and the possibility for client-server-client communication.

The majority of work done in the area of Google Earth-based virtual field trips involves a single person using a computer to view images, read text, etc. see *Simpson and De Paor* [2010]. Interaction includes following pre-recorded tours or clicking on placemarks and reading associated HTML content. Few tools are available for users (students, teachers, administrators, etc.) to actually interact with the virtual surroundings other than panning and zooming the camera view. What we have done is to simultaneously bring multiple users together and allow them to interact and explore on the same virtual globe, thereby simulating a real field experience where each user would be able to communicate with colleagues and collaborate on collective tasks. Interaction in a virtual environment or Google Earth is not new [*Roush*, 2007]. However, the hybridization of Google Earth API for a virtual-interactive geological environment is.

To achieve the above goals, designing the client-side application is not sufficient. Being able to synchronize multiple client instances of Google Earth over the Internet requires server side programming as well. The server has to log and process incoming traffic from clients. For this purpose, the PHP scripting language was chosen for its flexibility. First, it has the ability to generate HTML pages. PHP scripts can also be embedded into HTML pages. Finally, PHP scripts can manipulate MySQL- type databases. We might equally have chosen Python or Ruby-on-Rails for this task instead of PHP.

The purpose of this paper is to demonstrate how to implement the programming tasks necessary to support user interaction on Google Earth. To this end, we will

present the client-server-client communication code with a web-chat example. Passing of other data, for example avatar location, will be discussed along with server polling. Data logging is an extra benefit gained whose usefulness for educators and programmers will be explored. The combination of these parts makes creating virtual field trips possible.

5.3 WEB-CHAT EXAMPLE USING AJAX AND PHP

The backbone of the interactive Google Earth programming is the client-server-client communication. Once communication is established data such as chat messages, latitudes, longitudes, etc., may be exchanged among users. Communication between client and server is done via Ajax [*Garrett*, 2011]. Ajax enables web pages to communicate with a server, send and receive data asynchronously without refreshing the page, and therefore avoid reloading Google Earth plug-in at every update. The code snippets that handle the Ajax interface (courtesy of http://icodesnip.com/search/ajax/1) are in the form of a function,

function Ajax_Send(GP,URL,PARAMETERS,RESPONSEFUNCTION)

The function's parameters are as follows:

- **GP** represents the type of request (POST or GET);
- **URL** is the address of the PHP script that will be executed;
- **PARAMETERS** is the string that contains variables and values stored in it (var1=value1&var2=value2&var3=value3);
- **RESPONSEFUNCTION** is the function that will be evaluated upon server response with XMLHttpRequest.responseText as its argument.

To help the reader understand this AJAX-based communication, we will first explain the data structure and data handling on the server. In the entry string, the tag <!@!> separated row variables, and '/n' denoted a new row. PHP retrieved variables values from a file containing this entry string with the explode() method (e.g. the example in Figure 50).

In our case, the single data packet from the client contains variables that tell the server the following:

- what action is required;

```
1  //Example of data entry on the server in the data.txt file:
       1299265835.4478<!@!>mike<+@+>Hi<+@+>24.999<+@+>-39.999<+@
       +>25494105.783<+@+>0<+@+>0.0000018 /n
2
3  //PHP script that checks if your chat box is up to date. Takes the
       time (in UNIX format) from client when he did his last update and
        assigns it to $lastreceived
4  $lastreceived = $_POST['lastreceived'];
5
6  //Finds the physical location of the file with the conversation from
        the server and assigns it to a array variable $data where every
       new line is listed as the nest element of array
7  $data = file("data.txt",FILE_IGNORE_NEW_LINES);
8
9  //Checks the number of lines in $data, if 0, there is no need to
       continue execution
10 if(count($data) == 0){
11   exit();
12 }
13
14 /*Start a loop over the $data line by line */
15 for($line = 0; $line < count($data); $line ++){
16
17   //Separates the current line ( $data[$line]) into array elements
         at '<!@!>'.
18   $messageArr = explode("<!@!>",$data[$line]);
19
20   //If there is new entry in data.txt, send it to the client
21   if($messageArr[0] > $lastreceived) echo $messageArr[1]."<+newline
         +>";
22 }
23
24 //else, only send the time of the last entry from the 'data.txt'.
25 echo "<SRVTM>".$messageArr[0];
```

Figure 50. Code snippet for data entry on server.

- the integer value of the last received row from the table that contains chat messages and locations of the other avatars;
- the user name of the client making a chat request;
- the user's group. Upon arrival of the data packet from the client, the server first decides what action to perform.

For example, if user1 (refer to here as the sender) starts a web-chat by sending a new message to user2 (the receiver), the data sent from the sender are:

- user name of the message receiver (can be a single other user or a whole group);
- content of the message;
- the name of the sender.

The code on the client side is a function defined as in Figure 51:

```
1 function sendMessage(){
2
3   //Define the string that is being sent to the server
4   data = "action=send&to_who=milisav&content=" + document.
        getElementById('message').value +
5   "&sender=" + Avatar.userName;
6
7   //Function invoking XMLHttpRequest
8   Ajax_Send("POST", "stuIndex_ch.php", data, sentOk);
9 }
```

Figure 51. Code for client side sender function.

The sender makes a connection with the server using the standard XMLHttpRequest protocol [*van Kesteren*, 2012]. The server then:

- picks up the string with the variables mentioned above using the $_POST['variable name'] (in this case the string is called data) ;
- cleans it (a standard procedure of filtering clients input so that corrupted, incorrectly formatted, or harmful data are not stored in the database); and

- stores the string into the database.

The next step is to ensure that the receiver is notified of the new message. All clients periodically query the server for updates by sending their user name, group, and a number that tells what database row they last read (lastReceived). The frequency of queries is set by the native JavaScript function: setInterval(). The time interval between successive queries needs to be experimentally determined and fine-tuned. In our case, the function called updateInfo() queries every 800ms (Figure 52.):

```
1 function updateInfo(){
2
3   //Define the string that is being sent to the server
4   var data = "action=updateStat&lastReceived=" + lastReceived + "&
        iam="+Avatar.userName +
5   "&myGroup=milisav";
6
7   //Function invoking XMLHttpRequest
8   Ajax_Send("POST", "stuIndex_ch.php", data,sentOk);
9 }
```

Figure 52. Code snippet that checks for updates.

When the server receives an update request from a client, it passes the query to the database with values from the user making the update request:

- the number (lastReceived) must be smaller than the current queue number in the database table;
- the receiver name must match the client user name making a request for an update;
- the entry must have been posted with a maximum time interval (currently 50 minutes).

Entries matching the query are sent to the client who made the request in JSON format [*json*, 1999] by the procedure called echo(). The snippet of PHP code that the server uses to do this is shown in Figure 53:

Two functions are involved in processing the received data on a receiver's side. The first function is sentOk(), which is the fourth argument (RESPONSEFUNCTION) of the Ajax_Send() operation in updateInfo(). See Figure 54:

```
1  case "updateStat":
2
3    //Checking to see if all variables in received string are defined.
         true: proceed, false: send error and exit
4    if(isset($_POST['lastReceived'],$_POST['iam'],$_POST['myGroup'])){
5
6      //Assign received values to local variables after cleaning them
         to prevent corrupt data from being passed
7      $lastReceived=clean($_POST['lastReceived']);
8      $iam=clean($_POST['iam']);
9      $myGroup=clean($_POST['myGroup']);
10
11     //Making the mySQL query
12     $res=mysql_query("SELECT * FROM chat WHERE $lastReceived<
           id_chat AND ('$myGroup'=to_who OR '$iam'=to_who) AND (5000>(
          NOW()+0. -time_of_send+0.))");
13
14     //List results of the query
15     while($row = mysql_fetch_array($res)) {
16
17       //Fill the mesageStr array with listed results
18       $mesageStr[]= $row['sender'].":  ".$row['content'];
19       $lastReceivedNew=$row['id_chat'];
20     }
21     $res=mysql_query("SELECT username FROM user INNER JOIN online ON
           online.id_user=user.id");
22     while($row = mysql_fetch_array($res)) {
23       $online[]= $row['username'];  }
24
25       //If database query returned any result for new chat, echo it
           with the online user list
26       if(isset($mesageStr)){
27         $json=array('mesage'=>$mesageStr,'lastReceived'=>
             $lastReceivedNew,'online'=>$online);
28         echo json_encode($json);
29       }
30
31       //Echo online user list
32       else{
33         $json=array('online'=>$online);
34         echo json_encode($json);
35       }
36       exit();
37   }
38   echo "Error: variables in updateStat not defined";
39   exit();
```

Figure 53. Code snippet of switch statement.

```
1  function sentOk(res){
2
3    //Ensure the received data from server is in JSON format
4    if(res.isJSON()){
5
6      //Convert received JSON string to the Object p
7      var p=res.evalJSON([sanitize = true]);
8
9      //Check that fields are defined in Object p
10     if(typeof p.lastReceived != 'undefined' && typeof p.mesage != '
           undefined'){
11
12       //Updates the last received row from the chat table
13       lastReceived = p.lastReceived;
14
15       //Run the function that dynamically populates the chat box
             with newly arrived messages
16       populatingTables(p.mesage,'chatBox');
17     }
18 //... (more function)
19 }
```

Figure 54. SentOk code snippet.

This function looks for the part of the sent data that contains the message (p.message) and passes it to a function called populatingTables() (see Figure 55).

Figure 57 shows two students chatting about differences in rocks in the Andes near S33°, which is the result of the completion of the above function that arrived from the server (Figure 56).

5.4 PASSING OTHER DATA: AVATAR MOVEMENT

Web chat information is not the only type of data that can be sent using the above approach. Avatar location and movement are other examples. There are two aspects of avatar movement. The first is controlling the movement of one's personal avatar using an approach adapted from the Google Earth API sample code called 'Monster Milk Truck' [*Wikipedia*, 2011]. Keyboard input controls the local avatar movement and a function responsible for sending of the user's avatar position even while the user is stationary is nested in setInterval().

The second part of the avatar movement is updating positions of non-local avatar's or everybody but the local avatar. This is accomplished with the same approach for

```
1  //arguments: 'cont', array that contains messages to be applied to
       the chat box 'User : message', and 'who', string id of the field
       where the message is applied
2
3  function populatingTables(cont, who){
4
5  //Lists all elements of the 'cont' and passes them to the anonymous
       function as argument 'n'
6    cont.filter(
7      function(n){
8
9        //Creates the div element
10       var el = document.createElement("div");
11
12       //Assign text 'n' to 'el' div
13       el.innerHTML = n;
14
15       //Finds 'who' and appends the div, 'el' element to it
16       var a = document.getElementById(who);
17       a.appendChild(el);
18       a.scrollTop = a.scrollHeight;
19     }
20   )
21 }
```

Figure 55. PopulatingTables code snippet.

data handling used in the web-chat mentioned above. The same timing function that updates the avatar position is used to poll the server for updates to the non-local avatars' positions (latitude and longitude). The server responds with the changes and the data are parsed and all non-local avatar positions are updated on the Google Earth terrain accordingly. Figure 58 contains an initial screen shot of two avatars and the field vehicle exploring in the Andes. An advantage of the virtual environment is that vehicles can travel anywhere - alternatively, a set of horse icons could be substituted for the Jeep in this setting! Figure 59 shows an updated position of the "steva" avatar. This is the result of the "steva" user:

- moving locally;
- sending position update to the server;
- server processing update;
- second user "mladen" getting update from server;

```
1  //Google Earth update with the new message that pops above the
       sending avatar's hed
2  function ballonMessage(mesage, user){
3
4    //Try to remove any existing balloons first
5    try{
6      ge.setBalloon(null)
7    }catch(err){};
8
9    //Create balloon and set it's content
10   var balloon = ge.createHtmlStringBalloon('');
11
12   //Select the avatar of the associated balloon
13   var placemark = Avatar.holder[Avatar.names.indexOf(user)].
         placemark;
14   balloon.setFeature(placemark);
15   balloon.setMaxWidth(300);
16   balloon.setContentString(mesage);
17   ge.setBalloon(balloon);
18
19   //Remove the balloon after 2 second
20   setTimeout( function(try{ge.setBalloon(null)} catch(err){}},2000)
21 }
```

Figure 56. Code snippet for chat-message balloon.

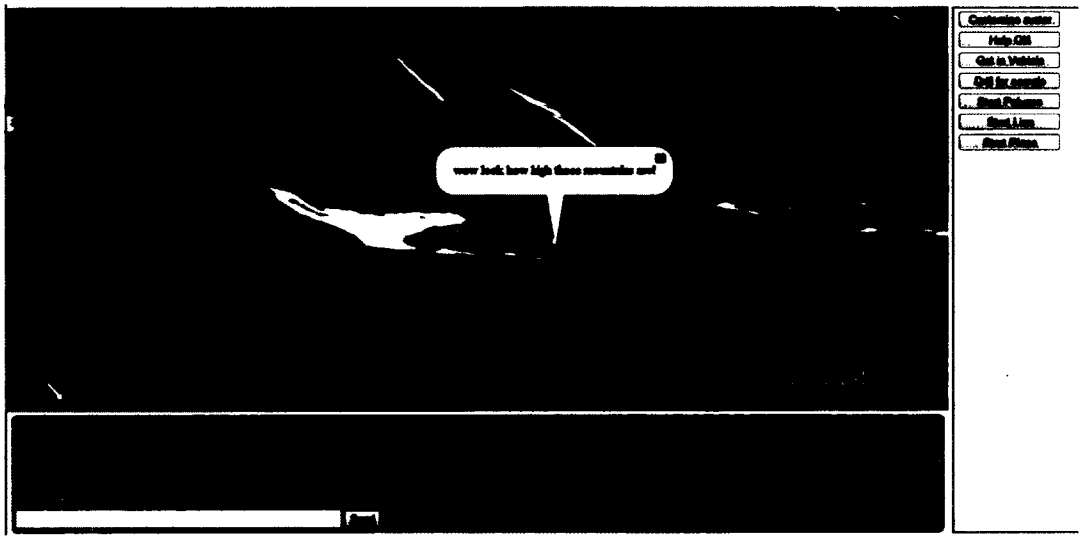

Figure 57. Two students discussing rocks in the Andes. Screenshot of "text balloon" after message is sent from one user to the server and then to the other user.

- "mladen" locally parsing data and updates avatars.

The current iteration uses a MySQL database type instead of XML which was used in the web-chat example.

Figure 58. Screen shot of two students and the field vehicle. This is a reference shot taken on "mladen's" screen to see the "steva" avatar move in Figure 59. The region is in the Andes near S33°, as is the region for Figure 59.

5.5 DATA TRAFFIC

One challenge in client-server-client communications is polling, which relates to the timing of client-server or server-client communication. When the server receives more requests than in can fill, it stacks them and responds in order. During the response it hands out the most recent data set available. The issue that can arise at this moment is the update of the position. A local-user may miss an update of a non-local by being ahead in the queue or miss a non-local position update because a non-local user had his position updated twice before the local user received the update. The first problem is not so large while highly accurate positions of non-local avatars in some small time window are not vital to the virtual geology experience. The server is providing updates every 800 milliseconds. The second problem is handled

Figure 59. Second screen shot of user "mladen's" screen. This shot is taken after user "steva" has moved locally on his Google Earth. His movement is sent to the server and the server then sends the data to user "mladen" . The data are parsed locally and the "steva" avatar is moved. The "steva" avatar has moved many times to have noticeably changed.

by linear interpolation to move the avatars from update to update. The interpolation helps minimize skipping a missed point by moving them on a linear path from update to update.

In future iterations we will try to implement new technologies for communication that have become available with the draft release of HTML 5 Web socket [*Hickson*, 2012]. While currently in the testing phase, AJAX does not create any problems in terms of polling, but for scalability it may require migration to more efficient solutions that would cut back unnecessary traffic and server load.

5.6 DATA-LOGGING

One benefit gained in creating client-server-client communication is data-logging. The logging process occurs when users push their data to the server. The data recorded are latitude, longitude, and heading of every client (student in this case) with a time stamp and a log of their chat conversations with other students. Recording the users' actions has the potential to be useful to both code developers and educators.

Helping developers debug and optimize the code and therefore enhance to the virtual field trip experience is another potential use of logging. Developers can also

post-track users. Post-tracking is just reviewing the user activity on a map either sequentially or as a scatter plot. When developing it becomes important to know where and how much time the user spends on tasks. If a developed task is analyzed to not be useful in the given context it could be removed or adapted to better suit the user.

Data logging is potentially valuable for teachers as well. The available feedback could enable teachers to scaffold their student learning activities, assess learning outcomes, and evaluate students for credit if desired [*Buckley et al.*, 2010; *Horwitz et al.*, 2010; *Sao Pedro et al.*, 2010; *Jacobson and Reimann*, 2010]. Here again, post-tracking of users could be useful to help educators understand the ways in which students learn. In future iterations of the application, we will be recording students' submitted work such as locations of the sites they chose for data collection and their mapping efforts (identification of virtual specimens, drawing of contacts etc.). Also, as new tool sets become available for the client on different field trips, we will record their interactions within Google Earth.

5.7 CONCLUSIONS

Client-server-client communication enables virtual field trip developers to produce more interactive, efficient, and engaging learning experiences. Processes of communication were explored with example code for a web-chat. The first process involved a client sending information to the server, the server processing the information, and the server returning a result. The second process involved sending a request for information update to the server, the server processing the request, and the server returning the information requested. Our program has been demonstrated at national meetings by *Dordevic et al.* [2011] and beta testing with structural geology students at ODU took place during the Spring Semester 2012. From early user reactions, we are confident that it will be a useful addition to the tools available to instructors in the geosciences. We anticipate that in future years, instructors will move away from virtual field trips in which the students are passive observers of content created by the instructor, towards interactive alternatives that constitute active virtual field work [*Ross et al.*, 2008].

CHAPTER 6

DESIGNING INTERACTIVE SCREEN OVERLAYS TO ENHANCE EFFECTIVENESS OF GOOGLE EARTH GEOSCIENCE RESOURCES

This chapter addresses the importance of the user interface and its limitations in the Google Earth stand alone application. Therefore, migration and development of the new user interfaces for web based Google Earth are needed to enhance effectiveness for geoscience resources. Here interactive screen overlays will be presented with their possible implementation. The work reported in this chapter has been published in a GSA Special Paper on Google Earth and Virtual Visualizations. (see *Dordevic* [2012]).

6.1 ABSTRACT

The effectiveness of a computer application depends, among other things, on an efficient user interface. In order to visualize subsurface geologic phenomena using the Google Earth application, we initially employed the built-in Google Earth time slider. Dragging the slider's right thumb elevated a COLLADA model that initially loads at a sub-surface altitude. However, the double-thumb feature of the time slide caused users some difficulties. It is not possible to turn off this feature when not required so it can be misleading to users. Because of this and because of the need for more control, we transitioned from the stand-alone Google Earth application to the web based Google Earth plug-in. To overcome some of the limitation for the existing user interface, such as the inability to make controls appear semi- transparent, we designed and implemented a screen overlay using the plug-in's Application Program Interface. This approach opened new possibilities to build more customizable user interfaces. A demonstration of the approach and sample usage of JavaScript to create buttons, draggable images, "powerpoints" , and slider controls is presented.

(a) (b)

Figure 60. Google Earth Time Slider with advanced functions. In the blue slider background, two gray thumbs can be dragged. Thumbs can be separated to select a time span. On left image only a single value selected 8/20/8 and on right image, time span from 2/27/9 to 12/29/11 is selected. It is not possible to show custom units, instead dates always appear.

6.2 INTRODUCTION

One of the great challenges of using Google Earth for the geosciences is visualization of the sub-surface. One technique employs 3-D COLLADA models of the subsurface and exploits the build-in Google Earth time slider control for elevating models into view [*De Paor and Williams*, 2006; *De Paor et al.*, 2008a]. The KML TimeSpan tag has the capability to store information about the position, and appearance of models in specified time intervals. Selection of a particular time interval is achieved by dragging the time slider thumb (Figure 60). By defining different altitudes for the model in every time step using the "begin" and "end" tags, it is possible to elevate lithospheric blocks above the ground level and visualize them in cross section. Problems were encountered using this approach during the user testing of the lab modules [*Gobert et al.*, 2012]. The inability to turn off advanced features of the Google Earth time slider created many opportunities for error in their usage. One of these features makes it possible to select a single time or a time interval by moving the right or left piece (thumb) of the slider (Figure 60). This created confusion with users as a result of unintentionally selecting time intervals. By doing so, models at different altitudes were seen to overlap. Furthermore, the display of appropriate units and values for elevation was not possible the time slider might read "14 Jan 2001 " when the desired output would be, say, 350 meters elevation.

A solution for this problem was found by migrating from the Google Earth standalone application to the web based Goole Earth plug-in [*Google*, a]. This transition offered more control over the models by using customizable interface elements on the web page containing the plug-in [*Stenback et al.*, -].Before the release of the working

draft of HTML 5 [*Hickson*, 2012], a user interface element slider was usually available as a paid third party add-on. Now, with the release of HTML5, the slider feature is natively supported in modern web browsers [*Sights*, -]. Instead of having hundreds lines of code to create a slider, it is possible to do it with the single line:

```
<input type="range" min="0" max="50" value="10" />
```

This code creates a slider on a web page with the range 0 to 50 and with a current value of 10. It could possibly control the altitude of an elevating cross section or other COLLADA model. A problem could arise if the application that one builds has a lot of interface elements and the user is running it on a small laptop screen. There is a trade-off between the available space for a Google Earth container [*Google*, -a] and space for other interface elements. Four cases will be discussed with various portions of the screen used for each component.

1. Make the size of the Google Earth container big enough to fit the internet browser window and get the maximal screen usage. Sliders could be located on the web page beside the Google Earth container so they would exceed the physical size of the browser window resulting in the appearance of a scroll bar. When an action is to be performed, the user scrolls the screen possibly losing partial visibility of the Google Earth window and therefore losing sight of the action performed by the slider (Figure 61(a)).

2. Shorten the length or width of the Google Earth container relative to the size of the browser and position the sliders on the freed-up window space (Figure 61(b)). This removes the need to scroll and the action of the slider can be seen as it is performed. The downside is that the Google Earth container is smaller, which might not be wise in order to perform an action that only might be required only once.

3. Make the size of the Google Earth container big enough to fit the internet browser window as in case one with the sliders located on a hiding menu bar (Microsoft n.d.). The hiding menu bar appears on demand, automatically resizing the Google Earth container. Under this action, the Google Earth container changes its size to a predefined one and the end result is as in case two (Figure 61(c)).

4. The same setup as in case three, with the difference being the hiding menu extends over half of the Google Earth container [*Williams*, -] and produces a similar result to case one (Figure 61(d)).

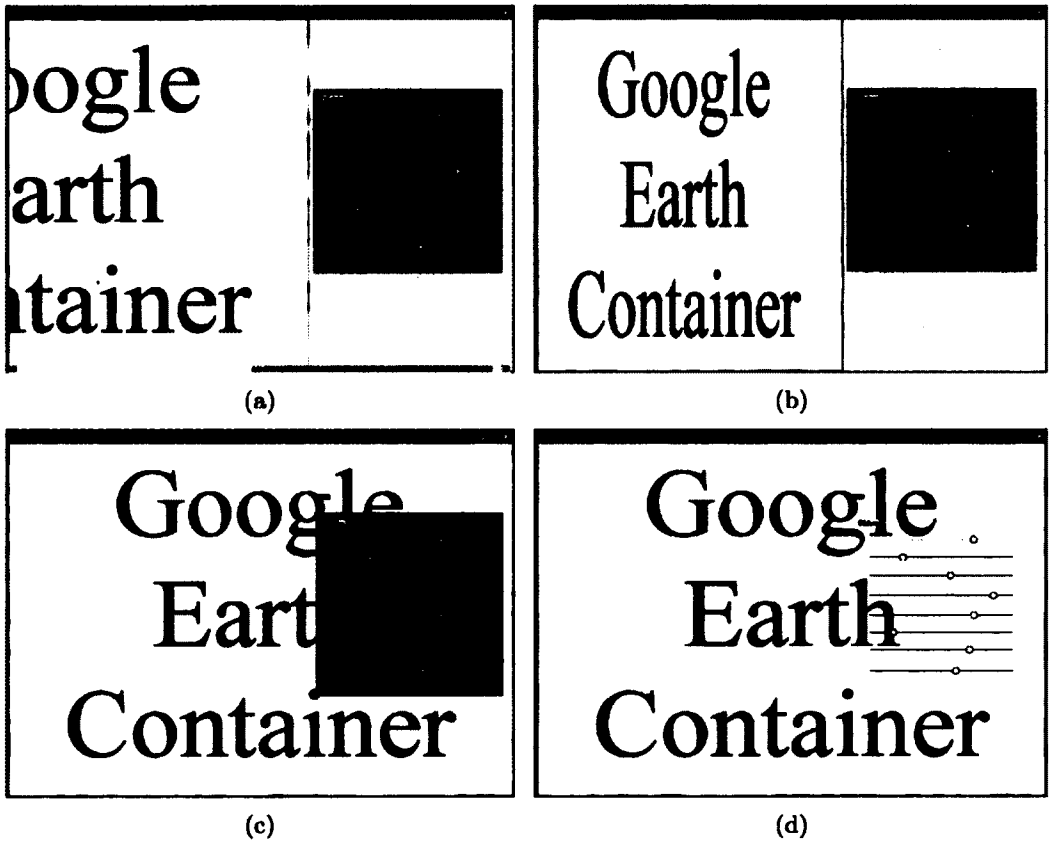

Figure 61. Possible arrangement of Google Earth container and sliders on smaller screen. a) size of Google Earth container fits browser window; sliders located on side and exceed physical size of browser window resulting in appearance of scroll bar, b) Google Earth container and slider fitted to share browser window. c) Slider on top of Google Earth container on hiding menu, d) Slider on top of Google Earth container on semi-transparent hiding menu.

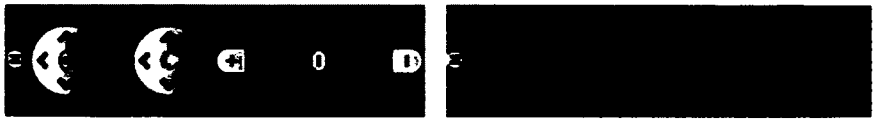

(a) (b)

Figure 62. Native Google Earth navigation interface, a) active and b) hidden.

A good ratio of the Google Earth container to the slider area visibility would be that described in case four, with the possible addition of semi-transparency to the hiding menu. This way, only parts of the Google Earth container that are directly under the sliders controls would be invisible and therefore minimizes the obstruction similar to native Google Earth navigation controls (Figure 62).

The current technique for making hiding menus is using IFRAME shims [*King*, -] but with limited-to -no capability of making them semi-transparent [*Google*, -a]. An advantage of this technique is that all the interface elements on the hiding menu are HTML-native, which is easy for implementation. A different technique is suggested here to build semi-transparent hiding menus. Using Google Earth screen overlays, it is possible to build some of the web page's main interface elements (such as a slider, button or check box) and assign them a corresponding functionality.

The idea behind using screen overlays as part of the interface is to achieve customizable look, size, and position. They could be used to embed a PowerPoint-style presentation in a Google Earth Tour, as geological map keys, or as buttons, sliders, or check boxes controlling the viewing experience. In this paper the application and integration of such an interface is explained with a few examples.

6.3 CREATING LOW-LEVEL FUNCTIONALITY

In order to overcome the lack of functionality built into Google Earth's screen overlays (for example, the inability to add event listeners as is possible with Placemarks, [*Google*, -b]), we designed virtual buttons. A virtual button is a predefined area of the Google Earth container (preferably square for simplicity) that is checked after every mouse-down event to determine if the mouse pointer is inside the area. If inside, a predefined action for that area is executed; if not, monitoring continues until the next mouse-down event is detected.

```
1 Number.prototype.toFractionX = function(){
2   return this / $('map3d').offsetWidth
3 }
4 Number.prototype.toFractionY = function(){
5   return this / $('map3d').offsetHeight
6 }
```

Figure 63. Number prototype for conversion between pixels and fraction.

To make virtual button areas of the Google Earth container visible and recognizable by a user, a Google Earth screen overlay is used with a corresponding size and position. Consequently, the user is aware that clicking on the Google Earth screen overlay may result in some sort of action, pictographically or textually, represented by the image. It is also possible to simulate the pressed state of a button by changing the overlay image on receiving the mouse-down event and returning it to the original state on mouse-up. The two examples that will be given are for a button and a slider. We start with the more basic example, the button.

6.3.1 BUTTON

It is useful to add two methods (in the object-oriented programming sense of the word) to the window "Number" object. These methods are called toFractionX and toFractionY (Figure 63) and they serve to convert from pixel to a fraction size based on the Google Earth container's width or height. They are written under the assumption that the instance of Google Earth is stored in a HTML DIV element with id = "map3d" and that a prototype framework is used [*Prototype*, -]. Now we can add the screen overlay to Google Earth and set up its parameters as describe in the Google Code Playground [*Google*, -c] (Figure 64).

To achieve the effect of semi-transparency, we use an image format such as PNG with a predefine level of transparency, or alpha layer. By adding an event listener that will monitor for a mouse-down event, this button will become interactive or clickable. An event listener is added using the Google Earth default function that accepts three arguments:

google.earth.addEventListener(object on which to add listener, type of event, action upon event)

```
1  %Create the ScreenOverlay
2  var button = ge.createScreenOverlay('');
3
4  %We chose an image and set it to the top left corner of the Google
       Earth container, and we set its size to 60x60 %pixels.
5  var buttonX = 0.1;
6  var buttonY = 0.1;
7  var buttonSizeX = 60;
8  var buttonSizeY = 60;
9
10 % Specify a path to the image and set as the icon
11 var icon = ge.createIcon('');
12 icon.setHref('http://www.google.com/intl/en_ALL/images/logo.gif');
13 screenOverlay.setIcon(icon);
14
15 % Set the ScreenOverlay's position in the window
16 button.getOverlayXY().setXUnits(ge.UNITS_FRACTION);
17 button.getOverlayXY().setYUnits(ge.UNITS_FRACTION);
18 button.getOverlayXY().setX(buttonX );
19 button.getOverlayXY().setY(buttonY );
20
21 % Set the overlay's size in pixels
22 button.getSize().setXUnits(ge.UNITS_PIXELS);
23 button.getSize().setYUnits(ge.UNITS_PIXELS);
24 button.getSize().setX(buttonSizeX );
25 button.getSize().setY(buttonSizeY );
26
27 % Add the ScreenOverlay to Earth
28 ge.getFeatures().appendChild(button);
```

Figure 64. Create screen overlay.

```
1  function inTheBox(event){
2    %Check that mouse pointer X coordinate is to the right of the left
         edge of the button
3    if((buttonX  + buttonSizeX.toFractionX() / 2 ) > event.getClientX
       ().toFractionX()
4
5    %and that mouse pointer X coordinate is to the left of the right
       edge of the button
6    && (buttonX - buttonSizeX.toFractionX() / 2 ) < event.getClientX()
       .toFractionX()
7    %and that mouse pointer Y coordinate is to the above of the bottom
         edge of the button
8    && (buttonY + buttonSizeY.toFractionY() / 2) > 1 - event.
       getClientY().toFractionY()
9    %and that mouse pointer Y coordinate is to the below of the top
       edge of the button
10   && (buttonY - buttonSizeY.toFractionY() / 2) < 1 - event.
       getClientY().toFractionY()){
11         % if all conditions satisfied, mouse is inside of the area
               define by the button
12         %perform action on button click
13   }
14 }
15 %add vent listener to Google Earth window that monitors for mouse
     button down and triggers the function inTheBox defined above
16 google.earth.addEventListener(ge.getWindow(), 'mousedown', inTheBox)
```

Figure 65. Detecting the mouse position relative to the area of the button.

where the first argument identifies the Google Earth window, the second is "mousedown" in this case, and the third argument will be executed upon the event. The triggered function needs to check whether the mouse pointer at the moment of an event is in the area defined by the button. This is done by checking four conditions, two for each x and y mouse coordinates (Figure 65). Since the position of the button in the Google Earth container is given in fractions and the mouse pointer is in pixels, it is necessary to convert them to the same units using the functions described above (Figure 63).

If all conditions in the above "inTheBox" function return as true, we proceed with the execution of the code for the button action.

6.3.2 SLIDERS

Every slider consists of two elements, the draggable piece ("thumb") and the track along which the thumb can travel ("background") (Figure 60). Once those two elements are set and appended to the Google Earth window using the approach described above, listening for three consecutive events starts.

1. Event: on mouse-down - Response: the code checks the current mouse position. The function "inTheBox" could be reused here: is the mouse pointer in the box that is defined by the thumb? If so, we set a Boolean "drag" flag to indicate that the current slider is being dragged and return to listening for the next event.

2. Event: on mouse-move - Response: if the "drag" flag is true, we monitor the position of the mouse and, upon every horizontal change in position for the horizontal slider or vertical change for the vertical slider, we reposition the thumb and recalculate the thumb value of the slider based upon the new thumb versus background positions. JavaScript publishes this value change so that custom functions can respond to it. In this example, the response is to change the altitude attribute of the model representing the emergent cross section.

3. Event: on mouse-up - Response: The "drag" flag is set to false and the function waits for the next mouse-down event. It is also important to be aware of page resizing issues. If the size of Google Earth container is set in percentages and a user re-sizes the page, the background is going to be shorter or longer so rescaling of the slider is also in order. To fix this, we listen for the HTML window.onresize event and restart sliders by removing them and adding them again. To conserve CPU usage on resize events, we put the action on re-size in the function called setTimeout(function(),100). In that way it is triggered at a slower rate.

6.4 INTERACTIVE SCREEN OVERLAYS

The first example is shown in Figure 66. It is possible to input the URL of any image from the web and click the "Post" button. This image immediately appears as a screen overlay in the Google Earth container. The screen overlay can be dragged and resized as shown in Figure 66.

It is not necessary for a input URL to be located on the same page as the Google Earth container. For example, a teacher could decide what image to shows as the screen overlay and ask students to respond to a corresponding question by searching

(a) (b)

Figure 66. Draggable and resizable screen overlay in Google Earth with capability for user to enter image URL and see changes on-the-fly.

the globe. Alternatively, several small screen overlays could be floated over the Google Earth container and students could be instructed to click the correct one for a given geoscience lab exercise.

6.5 SCREEN OVERLAYS AS INTERACTIVE MAP KEYS

Previous authors have used both opaque and semi-transparent screen overlays as map keys. Figure 67 shows an example from *Whitmayer* [-]. In Figure 67, the map key has been made interactive. Note how the Pennsylvanian formations have been unchecked in the key; consequently they disappear from the map. Showing and hiding individual formations can be done in the Google Earth desktop application in the Places sidebar, but the interactive map key opens up many possibilities that are not possible with built-in Google Earth functionality - for example, choice of colors or symbols.

6.6 SCREEN OVERLAYS AS POWERPOINT PRESENTATIONS

Google Earth cannot be embedded in Microsoft PowerPoint, Apple Keynote, or Google Doc presentations, and so presenters must either interrupt their slide show in order to give a live demonstration or pre-save screen grabs and movies. An interactive screen overlay could have forward and reverse buttons for navigating through a set of slides, thus embedding a PowerPoint-style presentation in Google Earth.

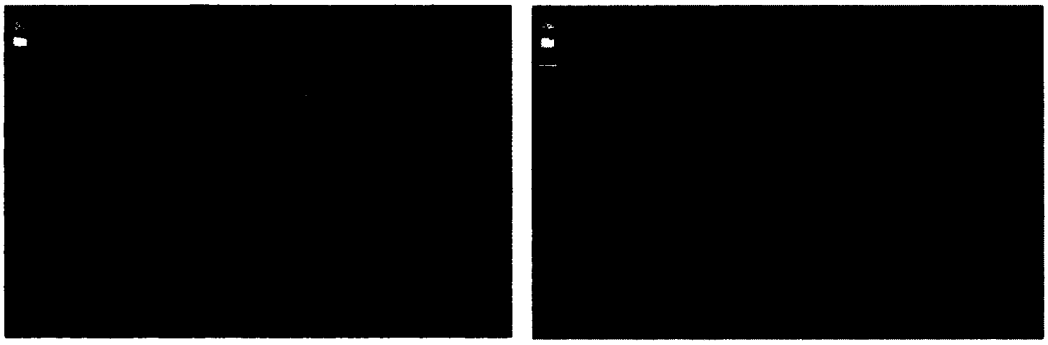

(a) (b)

Figure 67. Screen overlay used as button. Legend fully interactive; it is possible to turn on and off map sections. On the image a) Tertiary and Proterozoic Piedmont formations have been unchecked in key legend.

6.6.1 SCREEN OVERLAYS AS SLIDER CONTROLS

Previous authors have also used Google Earth's built-in time slider [*De Paor et al.*, 2008a] and tour slider to control features such as emergent cross sections. The time slider's two thumbs, as described, are difficult to move together and when they separate they create an overprinting of models. Figure 68 shows a pair of custom sliders that control emergent cross sections of the subsurface (see *De Paor et al.* [2008b]). Each slider consists of two screen overlays, a stationary bar (light blue) and a draggable thumb (dark blue). The orientations of these sliders are horizontal and vertical but other angles are also possible.

6.7 CONCLUSION

In conclusion, as the usage of the Google Earth web plug-in becomes more diverse every day, the need of specialized user interface elements grows. We have described how one can use a screen overlay to make such interface elements. Basic examples of implementation have been given for button and slider controls. Among the geoscience applications that immediately come to mind are; (i) interactive maps keys (screen overlays) linked to maps (ground overlays), (ii) more control over the style of the map key, symbol color and shape is also convenient, (iii) PowerPoint-style presentations embedded in the Google Earth container, controlled by forward and

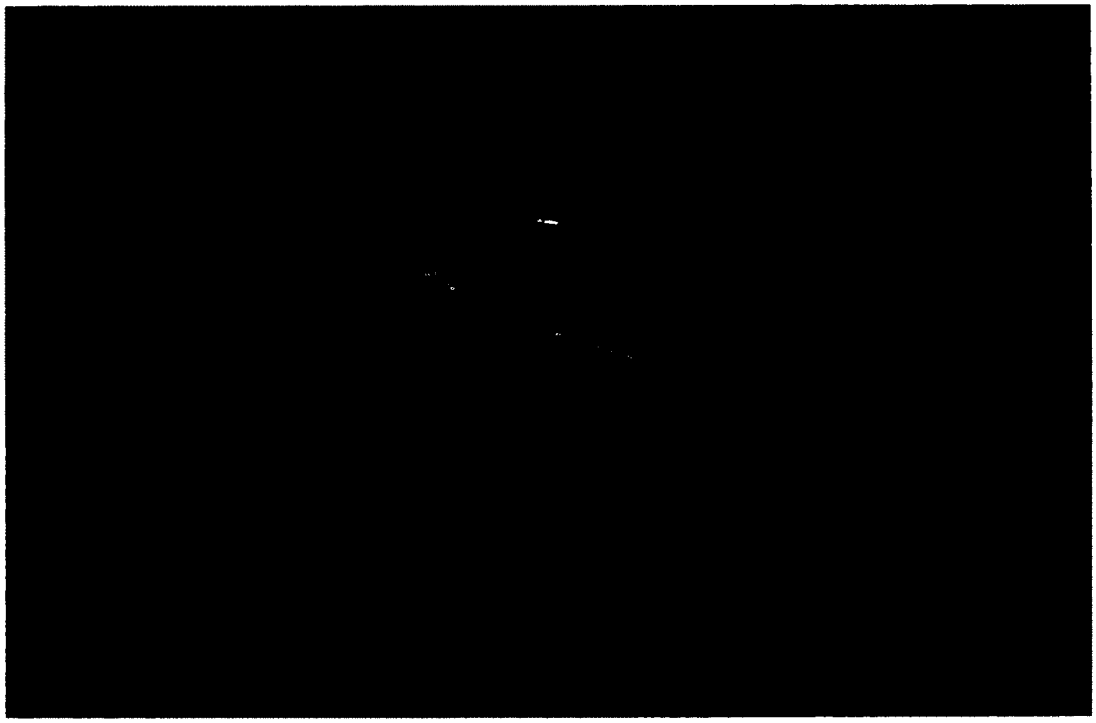

Figure 68. Screen overlay used as slider in Google Earth. Two fully functional sliders used to control emergent cross sections.

reverse buttons; and (iv) remote control of the screen overlay content by an educator, enabling different tasks to be assigned to students both locally and in a distance education setting. We strongly believe that, until other advanced features are developed for Google Earth, interactive screen overlays will give one more useful tool in applications writing and we hope these examples motivate and inspire readers to implement this interface in their own creations.

CHAPTER 7

DYNAMICS OF PLUME-TRIPLE JUNCTION INTERACTION: RESULTS FROM THREE-DIMENSIONAL NUMERICAL MODELS

7.1 ABSTRACT

Evidence that near-ridge plumes interact with divergent plate boundaries can be found in the geochemical composition of oceanic island basalt along ridges, elevated bathymetry, and gravity anomalies. This study uses finite element modeling to investigate the interaction of a mantle plume and a ridge- ridge-ridge triple junction. The purpose of this study is to determine the spatial distribution of plume material dispersion along the ridges as well as the scaling laws controlling plume-triple junction interactions.

The size of the numerical domain used in this study is 1000x1000x225 km. The top domain boundary is composed of three diverging plates with prescribed half spreading rates corresponding to the Azores triple junction. The bottom boundary is kept at the constant temperature of 1350 $°C$ except in the area of an imposed Gaussian-shaped thermal anomaly with excess temperature of 180 $°C$ and variable diameter that was used to control plume volume flux. The mantle is simulated as an incompressible fluid with pressure and temperature dependent viscosity, with some model runs incorporating the effects of melting-related dehydration. Maximum ($10^{21}\ Pa\,s$) and minimum ($5 \times 10^{18}\ Pa\,s$, $1.5 \times 10^{19}\ Pa\,s$) cutoff viscosity limits are established, high enough for formation of the lithospheric layer and low to represent hot plume material. A series of models explore plume-triple junction parameter space by varying plume diameter, the location of the plume with respect to the triple junction, and the viscosity contrast between the plume and the ambient mantle, yielding scaling relationships that provide insight into the overall behavioir of the geodynamical system.

7.2 INTRODUCTION

7.2.1 BACKGROUND: PLUME–RIDGE INTERACTIONS

Hot spots and mid ocean ridges are the surface expressions of subsurface mantle upwelling and magma generation processes. At mid ocean ridges, lithospheric plates diverge and the mantle upwells, creating the oceanic crust through decompressional melting. Hot spots are typically associated with elevated topography or shallow bathymetry, and often also with linear volcanic chains with systematic age progression of the eruptive products. Age progression has been used to infer that there is a fixed position in mantle relative to the overlaying moving plate [*Morgan*, 1972] that could be responsible for the hot spot. It is widely believed that many hotspots are associated with mantle plumes [*Morgan*, 1971; *Morgan and Rodriguez*, 1978; *Morgan*, 1981; *Ito et al.*, 2003]. A mantle plume is often deïñÆne as a region of the mantle that is hotter compared to surrounding material, originating from convective thermal boundary instabilities [*Olson*, 1990]. It is estimated the interaction of mantle plumes with nearby mid ocean ridges results in physical and chemical anomalies along $15 - 20\%$ of total mid ocean ridge system length [*Ito et al.*, 2003] (Figure 69). Based upon the spatial extent of the bathymetric swells and magnetic isochron data, it can be determined that plume ridge interactions may last tens of millions of years [*Ito et al.*, 2003]. The interaction between a mid ocean and a mantle plume, at different points in geologic time, is believed to have generated some of the largest volcanic features on Earth such as Kerguelen Plateau and Ontong Java Plateau [*Coffin and Eldholm*, 1993, 1994; *Coffin and Gahagan*, 1995; *Coffin et al.*, 2005, 2006].

One example of plume ridge interaction occurs at the Galapagos spreading center in the eastern Pacific Ocean, where the Cocos–Nazca ridge with a half–spreading rate of $2.1\,cm/y$ is located near the Galapagos plume [*DeMets et al.*, 1990]. Between $97\,°W$ and $91.42\,°W$, the oceanic crust thickens by about $2.3\,km$ [*Canales et al.*, 2000; *Detrick et al.*, 2002] due to excess magmatic production from the plume. Estimated temperature anomalies in the subaxial mantle due to the proximity of the plume have decreased from $86\,°C$ to $50\,°C$, as the ridge has migrated away from the plume conduit [*Ito and Lin*, 1995b].

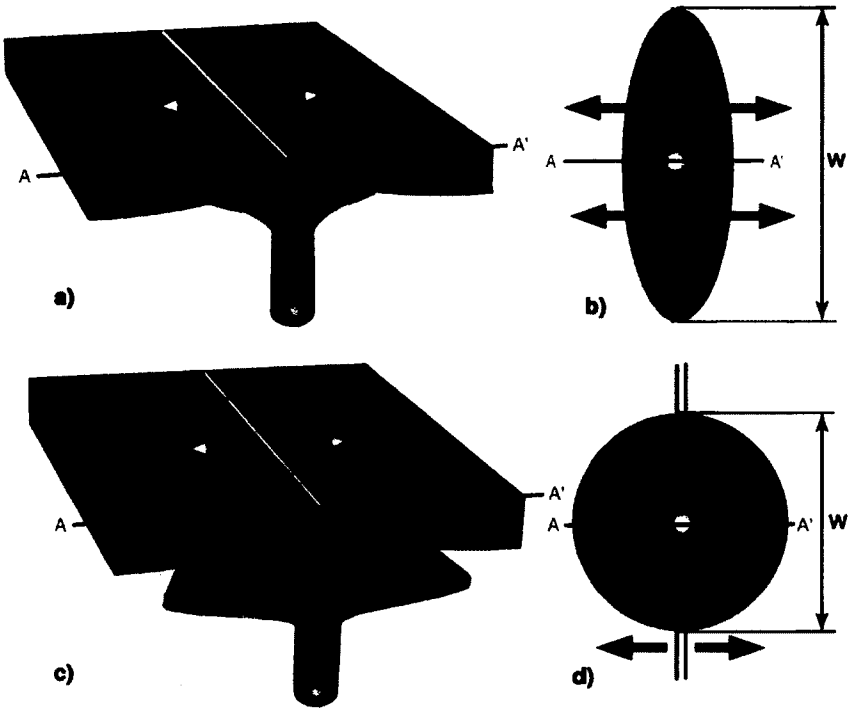

Figure 69. Schematic cartoons of the dispersal of ridge centered plume, following [*Schilling*, 1991], contrasting shallow, along axis dispersion of plume material with deep, radial dispersion. a) A schematic plume (red and orange colors) upwells to the base of the lithosphere, and disperses in a channelized fashion along the ridge axis. The along axis dispersion of the plume material is guided by the lithosphere asthenosphere boundary, which deepens as a function of seafloor age. b) Plan view of plume material dispersal for the geometry in (a). Black dot with "bull's eye" shading in the center of the panel represents the plume conduit. Heavy black arrows indicate plate divergence, thin black arrows show the pattern of plume dispersal, and light gray shading depicts plume material dispersion. Waist width (W) is the length of ridge axis that has plume related anomalies in data such as bathymetry, gravity, and basalt geochemistry. c) Cartoon depicting plume upwelling to the depth of the dry solidus, and then radially dispersing in a broad fashion at depth. This dispersion geometry is based upon the models of [*Ito et al.*, 1999] which incorporate mantle dehydration during melting. d) Same as for (b), but for the radial dispersion model.

Another example of plume ridge interaction involves Iceland and the Mid Atlantic Ridge [*Ribe et al.*, 1995; *Ito et al.*, 1999, 2003], which has a half spreading rate of $0.9\,cm/yr$ [*Schilling*, 1991]. Along the Mid Atlantic Ridge, anomalies in bathymetry, gravity, and basalt geochemistry occur over an along axis distance ("waist width;" see Figure 69) of $\sim 1600\,km$ [*Klein and Langmuir*, 1987; *Ribe et al.*, 1995; *Shen and Forsyth*, 1995; *White et al.*, 1995; *Wolfe et al.*, 1997; *Ito et al.*, 1999]. In some locations, crustal thickness exceeds $30\,km$ [*McKenzie and Bickle*, 1988; *Ito et al.*, 1999], compared to average oceanic crustal thickness of $5-7\,km$ [*White et al.*, 1992; *Bown and White*, 1994]. From numerical modeling constraints, *Ribe et al.* [1995], found that crustal thickness is about $70\,km$ using plume with an excess temperature of $263\,^{\circ}C$ [*Schilling*, 1991] and radius of $62\,km$. Using a different treatment of the plume, *Ito et al.* [1999] suggested that the Iceland plume has an excess temperature of approximately $150\,^{\circ}C$, a radius less than $200\,km$, and volume flux $Q = 202m^3/s$. Overall, plume ridge interaction is an important process helping shape the surface of our planet at present as well as in the past.

Previous authors have established scaling laws for plume ridge dynamical interaction and tested them against experimental data obtained either in the lab using corn syrup tanks (e.g. [*Feighner and Richards*, 1995]), or using solutions from numerical models [*Ito et al.*, 1996, 1997; *Ribe et al.*, 1995; *Ribe*, 1996; *Albers and Christensen*, 2001]. In the case of a ridge migrating away from or towards a plume source, *Schilling* [1991] inferred dispersal of the plume material using isotope and trace elements ratio anomalies coupled with topographic variations. *Schilling* [1991] also estimates the volumetric flux of several plumes and their excess temperatures. *Schilling* [1991] develops two methods for estimating plume discharge rate into a migrating ridge. The first method relies on the waist width of geochemical anomalies along migrating ridge axes, assuming steady state interaction between a plume source and a ridge sink. Volumetric plume flux Q is given as

$$Q = 2k_1 \int_0^{W/2} H(y)S(y)P(y)dy = k_1 \frac{HSW}{2}$$

where y is the direction of along-axis distance, $S(y)$ is full spreading rate, and $H(y)$ is thickness of fully developed lithosphere. In the first approximation both $S(y)$ and $H(y)$ are assumed to be independent of y. $P(-W/2 \leq y \leq W/2) = 1 - |2(y/W)|$ describes the plume contribution to the lithosphere accretion. Parameter k_1 takes into

account that not all the material reaching the ridge axis participates in lithosphere accretion. The second method uses excess elevation ΔE and buoyancy flux of the plume:

$$B = 2k_2(\rho_m - \rho_w) \int_0^{W/2} \Delta E(y) S(y) dy = k_2 \Delta E(0) SW(\rho_m - \rho_w)/2$$

where $\Delta E(y) = \Delta E(0) P(y)$, ρ_m and ρ_w are the densities of mantle and water, and k_2 corrects for the contribution of the thicker crust to the ridge elevation anomaly. Buoyancy of the plume is assumed to be purely thermal in origin, so plume flux can be expressed as

$$Q = \frac{B}{\rho_m \alpha \Delta T}$$

where ΔT is plume excess temperature and α is the coefficient of thermal expansion. The volume fluxes and excess temperatures calculated for 13 plumes using the above two methods were good agreement with observations made by *Sleep* [1990] for plume flux based on bathymetric observations and simplified fluid dynamical considerations.

Feighner and Richards [1995] explored plume dynamics using plexiglass tanks filled with corn syrup to mimic the mantle and mixture of water and corn syrup to simulate a chemically buoyant plume. Plume fluid was continuously introduced into tank with known volume flux and the system evolution was monitored. Using this experimental setup *Feighner and Richards* [1995] were able to investigate two cases of plume spreading, first beneath a fixed plate and second beneath two diverging plates simulating mid ocean ridge. It was observed that plume material will rise through a narrow conduit and spread near the top plate, similar to a pancake. In the case of the fixed top plate, spreading of the plume head is controlled by two opposing forces, the horizontal gravity force acting over the vertical cross section of the plume

$$F_b \sim \Delta\rho g h^2 D^2$$

and viscous drag

$$F_d \sim \eta_0 U_n D$$

Here $\Delta\rho$ represents density difference between the background material and the plume fluid, h is the average thickness of the plume head, D is the lateral extent

of the plume material, η_0 is background viscosity, and U_n is radial speed of the plume head's front. By balancing forces and adding the conservation of mass equation

$$D^2 h \sim Qt$$

where Q is the plume volume flux and t is time, *Feighner and Richards* [1995] obtained plume's lateral spreading rate to be

$$\frac{\partial D}{\partial t} \sim \frac{\Delta \rho g Q^2 t^2}{\eta_0 D^4}$$

Integrated over time, this expression gives a prediction for the spreading of the plume

$$D \approx k \left(\frac{\Delta \rho g}{\eta_0} Q^2 t^3 \right)^{1/5}$$

where k is the parameter that was experimentally determined. In the first approximation, spreading of the plume head is limited by the background viscosity, since the viscosity of the plume material is irrelevant.

The second case with diverging plates presented a bigger change. Following dimensional analysis done by *Bridgman* [1931] and the Buckingham Π theorem *Feighner and Richards* [1995] suggested

$$W = Lf(B_n, I)$$

showing how the diameter of plume head along the diverging plates (W) changes with the "primitive" length scale

$$L = \sqrt{\frac{Q}{U}}$$

U being velocity of the diverging plate, buoyancy number

$$B_n = \frac{\Delta \rho g Q}{\eta_0 U^2} \tag{1}$$

and intrusion number

$$I = \frac{\Delta \rho g Q}{\eta_p U^2}$$

η_p being viscosity of the plume. In essence by fitting experimental data *Feighner and Richards* [1995] found that plume waist width scales as

$$W = 2.10\sqrt{\frac{Q\eta_r}{U}}$$

with η_r being the ration of intrusion and buoyancy number I/B_n.

On the other hand, *Ito and Lin* [1995a] analyzed gravity and bathymetry data along the paleoaxes of oceanic ridges (i.e., magnetic isochrons) in the vicinity of the hotspots such as Azores, Galapagos, Tristan and Iceland. They assumed that the volume flux of plume material carried away by the thickening lithosphere is proportional to

$$Q = \int_{-W/2}^{W/2} P(y)Udy = \frac{hUW}{2}$$

where $P(y)$ is the portion of accreted lithosphere made from plume material with $P(0) = 1$ decreasing linearly to $P(\pm W/2) = 0$, and h is the thickness of the fully developed lithosphere. The ridge is supplied by the plume volume flux equal to

$$Q = w_1 w_2 \left(V - \frac{U}{4}\right)$$

with w_1 and w_2 being the width and the height of the channel connecting the plume and the ridge axes and V being the average velocity of the plume material. Combining the two above equations yields waist width as

$$W = \frac{2w_1 w_2}{hU}\left(V - \frac{U}{4}\right)$$

If this equation is compared to the results of *Feighner and Richards* [1995] it can be noted that the dependence of the waist width on plate velocity and plume volume flux is linear, as opposed to a power dependence. The explanation for this is the consideration of an end-member case scenario that presumes that horizontal spreading of the plume material is only ridge-parallel. An interesting point is that *Ito and Lin* [1995b] used the volume flux of the plume material that reaches the ridge, not the whole volume flux, which allows for extrapolation to plumes that are not ridge-centered.

A solution for the horizontal spreading of plume material can be obtained using lubrication theory in order to solve the governing equations for isoviscous flow. Similar solutions using this method were produced by *Ribe et al.* [1995] and *Ribe* [1996]. By doing triple integration over the plume head thickness S

$$\frac{\partial^2 \vec{u}}{\partial dz^2} = \frac{g\Delta\rho}{\eta}\nabla_{x,y}S$$

where $\vec{u}$ is the horizontal component of the plume material velocity and $\nabla_{x,y}$ is the horizontal Laplacian, horizontal plume flux can be written as

$$Q_H = \int_0^S \vec{u}dz - \frac{g\Delta\rho}{48\eta}\nabla_{x,y}S^4$$

The continuity equation for the plume in stationary state can be written as

$$\nabla_{x,y} \cdot Q_H = Q\delta(x,y)$$

where the plume source is introduced to the system as a delta function with volume flux Q. Combining the two above expressions yields an equation describing the steady state thickness of the plume head $S(x,y)$

$$\nabla_{x,y} \cdot \int_0^S \vec{u_p}dz = \frac{g\Delta\rho}{48\eta}\nabla^2_{x,y}S^4 + Q\delta(x,y)$$

The integral on the left can be expressed using a stream function for two-dimensional corner flow (e.g. *Reid and Jackson* [1981]) that satisfies the boundary condition $\Psi_z(x, z=0) = U$

$$\Psi(x,S) = \frac{2}{\pi}US\arctan\left(\frac{x}{S}\right)$$

The final equation is

$$\nabla_{x,y} \cdot \frac{2}{\pi}US\arctan\left(\frac{x}{S}\right) = \sigma\nabla^2_{x,y}S^4 + Q\delta(x,y)$$

where $\sigma = g\Delta\rho/48\eta$ is often referred to as plume "spreadability" . The first term on the left involve the stream function for corner flow describing advection of the material, the first term on the right is buoyancy-driven self-spreading and the second term on the right is a source term. From this equation, by balancing the source term and the self spreading term, length scale for the plume thickness can be obtained

$$S \sim \left(\frac{Q}{\sigma}\right)^{1/4} \equiv S_0$$

and by balancing the advection and source terms, a length scale for the width perpendicular to the spreading direction can be derived

$$L(x >> 0) \sim \left(\frac{Q^3\sigma}{U^4}\right)^{1/4} \equiv L_0$$

At the ridge, $L(0)$. The advection term scales as U and when balanced with the source term the waist width length scale becomes

$$W \sim \sqrt{\frac{Q}{U}} \equiv L_s$$

From dimensional analysis it can be determined that W/L_s depends only on the ratio of L_0 and S_0, and that that quantity squared gives buoyancy number[*Feighner and Richards*, 1995]

$$B_n = \frac{Q\sigma}{U^2} \equiv \left(\frac{L_0}{S_0}\right)^2 \tag{2}$$

where the numerical coefficients and the functional dependence needs to be experimentally determined

$$W = c_1 L_s f_1(B_n)$$

This expression can be modified to allow for the situation where the plume and background material have different viscosity

$$W = c_1 L_s f_1(B_n) f_2(\gamma)$$

where $\gamma = \eta_0/\eta_p$

Continuing upon his previous work *Ribe* [1996] also developed scaling laws for plume ridge interaction with off ridge plumes using thin layer theory. The equation describing stationary state of plume head thickness is given as

$$\nabla_{x,y}\Psi(x, S+b) - \sigma\nabla_{x,y}S^4 - 4\sigma\frac{\partial}{\partial x}\left(S^3\frac{\partial b}{\partial x}\right) = Q\delta(x_p, y)$$

where b is the thickness of the lithosphere and x_p is the ridge perpendicular distance to the plume source. The first term on the left-hand side is stream function describing corner flow modified by the presence of the lithosphere, the second is buoyant self–spreading, and the third is upslope flow. The expression on the right hand side is the source term. Keeping the same length scales from previous work *Ribe* [1996] defined the form of the scaling law as

$$W = W_0 f(x_p/W_0, P_b, P_u)$$

where P_u is upslope number, defined as the ratio of lithosphere thickness to plume thickness

$$P_u = \left(\frac{Q\sigma^3\kappa^4}{U^8}\right)^{\frac{1}{8}}$$

7.2.2 BACKGROUND: TRIPLE JUNCTIONS

A triple junctions is defined as the point where three plate boundaries meet [*Mckenzie and Morgan*, 1969]. Triple junctions represent important geological settings along the global mid–oceanic ridge system, where mantle dynamics are influenced by the motions of three plates. Each branch of the triple junction can be a ridge, trench, or transform fault, resulting in sixteen basic possible configurations, of which only some are stable [*Mckenzie and Morgan*, 1969]. From the velocity vector method it can be shown that ridge ridge ridge (RRR) triple junctions are stable for all possible spreading rates and ridge orientations. Several previous studies [*Mitchell and Parson*, 1993; *Searle*, 1980; *Searle and Francheteau*, 1986; *Sclater et al.*, 1976] have investigated plate kinematics and the geological characteristics of the seafloor near RRR triple junctions. One example of an RRR triple junction currently existing along the global plate boundary system is the Azores triple junction (Figure 70).

Previous authors (e.g., *Georgen and Lin* [2002]; *Georgen* [2008]; *Georgen and Sankar* [2010]; *Georgen* [2011]) have used numerical modeling to explore generalized properties of mantle flow and thermal patterns in the vicinity of RRR triple junctions. *Georgen and Lin* [2002] investigated the case of a slower spreading ridge quasi orthogonally intersecting two nearly collinear faster spreading ridges. The mantle was assumed to be an incompressible, isoviscous fluid driven by diverging surface plates. Heat was exchanged via advection and diffusion, and no source of buoyancy was included. Plates' divergence rates were changed by a fixed scaling factor to simulate the half spreading rates of three physical triple junctions (Azores, Rodrigues, and Galapagos, in the northern Atlantic, Indian, and eastern Pacific oceans, respectively). The study found that the flow patterns of the collinear ridges were not significantly influenced by the presence of the triple junction. On the other hand, upwelling velocities along the axis of the slowest ridge were greatly enhanced,

as much as threefold, toward the triple junction. Strong flow along the axis of the slowest spreading ridge, away from the triple junction, was also predicted. With linear multiplicative increases of the spreading rates, the presence of the triple junction had less influence on the flow patterns of slowest ridge.

Continuing upon previous work, *Georgen* [2008] investigated a plate boundary configuration similar to the Rodriguez triple junction. This work focused mainly on the mantle dynamics of slowest spreading ridge, and incorporated pressure and temperature dependent mantle viscosity. Results were significantly quantitatively different from the isoviscous case [*Georgen and Lin*, 2002], with estimated increase in upwelling velocity and along axis flow up to $100\,km$ away from the triple junction. Similarly, within a few hundred kilometers of the triple junction, temperatures at a depth within the partial melting zone increased by $40\,°C$ and the crust thickened about $1\,km$.

The Azores triple junction is formed from two nearly collinear branches of the Mid Atlantic Ridge with half spreading rates of $\sim 1.1\,cm/yr$ and $\sim 1.2\,cm/yr$ (Figure 70). The third branch, the Terceira Rift, intersects the Mid Atlantic Ridge quasi orthogonally. *Luis and Miranda* [2008] suggested that the Terceira Rift has had a component of divergence for the past 25 million years.

Georgen and Sankar [2010] focused on the Azores Plateau and Azores triple junction, and specifically on geodynamical processes along the Terceira Rift, the slowest spreading of the three ridge branches. By incorporating a discontinuity bounding the axis that simulated the Gloria Fracture Zone, diffuse deformation near the three ridges' intersection, and time dependent spreading history, *Georgen and Sankar* [2010] explored additional factors that could affect crustal accretion around the Azores triple junction.

Evidences for the existence of a mantle plume at the Azores triple junction can be found in geophysical data. For example, crustal thickness determined from seismic or gravity data is in the range of $\sim 8 - 12\,km$, higher than average oceanic crustal thickness [*Searle*, 1976; *Detrick et al.*, 1995; *Luis et al.*, 1998; *Gente et al.*, 2003; *Georgen and Sankar*, 2010]. Pulsating sources of the magmatism can be inferred from shaped V-ridges in seafloor topography extending south of the Azores plateau [*Cannat*, 1999; *Escartin*, 2001]. Seismic tomography measurements [*Montelli et al.*, 2006; *Silveira et al.*, 2006] indicate low velocity regions in the upper mantle.

The interaction of a plume with a triple junction was studied in a numerical model

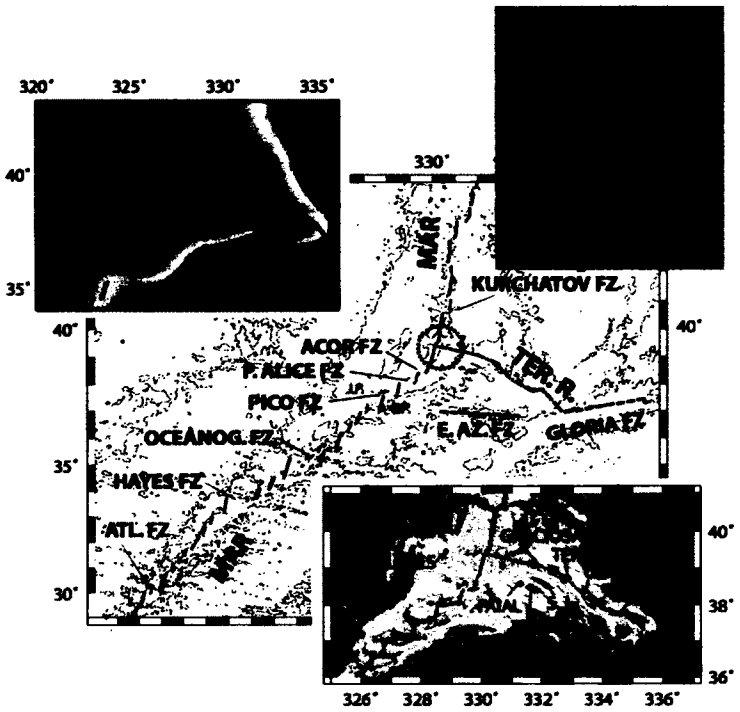

Figure 70. Figure modified form *Georgen* [2011]. Geological setting of the Azores. (Central panel) Dashed circle marks the position of the Azores triple junction. Abbreviations: MAR, TER. R., E. Az. FZ, and J.P. are Mid-Atlantic Ridge, Terceira Rift, East Azores Fracture Zone, and Jussieu Plateau respectively. (Left inset) Filtered bathymetry of the Azores plateau. A low pass filter with a cutoff wavelength of 300 km applied to the bathymetry data of Smith and Sandwell [1997]. Contour lines mark 1.9, 2.7, and 3.5 km depth. (Bottom right inset) Locations of islands in the Azores Archipelago. Abbreviations: S. J., S. Mig., C. B., and Hr. B. are Sao Jorge Island, Sao Miguel Island, Castro Bank, and Hirondelle Basin, respectively. (Top right inset) Simplified schematic representation of the Azores triple junction. Simplifications include disregarding the existence of the transform offsets, microplates and disconnection of ridges with triple junction point. Black arrows indicate direction of plate motions relative to the triple junction. The location of the plume conduit at the time of excessive volcanism was in the vicinity of the today's Faial and Pico islands [*Cannat*, 1999; *Escartin*, 2001].

by *Georgen* [2011]. Model predicted seafloor depth variations were compared with a bathymetry profile from observational data and found to be in good agreement. Specifically, preferential flow along the Terciera Rift and the portion of the Mid–Atlantic Ridge to the south of the triple junction was in general qualitative agreement with observations of asymmetric plume dispersion along the ridge system [*Dosso et al.*, 1993; *Detrick et al.*, 1995; *Thibaud et al.*, 1998; *Goslin*, 1999; *Vogt and Jung*, 2004; *Maia et al.*, 2007; *Shorttle et al.*, 2010].

7.2.3 STUDY OBJECTIVES: PLUME–TRIPLE JUNCTION INTERACTIONS

The primary objective of this dissertation chapter is to improve understanding of the dynamics of plume triple junction interactions as well as to assess the role of the topography of the lithosphere asthenosphere boundary in governing the dispersion of plume material in the upper mantle. Results from these numerical models can provide insight into the generation of large igneous provinces and submarine plateaus. A related goal is to perform a parameter space investigation of several parameters that are important in plume ridge interaction, to gain insight into the overall system behavior.

Parameters varied include the location of the plume with respect to the triple junction, plume flux, and mantle viscosity structure. Using this suite of model runs, scaling laws relating factors such as waist width and plume flux were calculated, allowing waist width to be estimated for any geometrically similar plume triple junction system from plume parameters (and vice versa).

Future studies may include time dependence, ridge migration and ridge segmentation. Time dependent versus stationary solutions of numerical models would permit simulation of a pulsating plume (i.e., time dependent volumetric plume flux), a mechanism that has been invoked to explain the V-shaped topographic ridges along the Mid Atlantic Ridge south of the Azores [*Cannat*, 1999; *Escartin*, 2001]. Incorporation of ridge segmentation patterns would move modeling from generic cases of triple junction geometry to more specific geological settings. Finally, as lithospheric plates are in constant motion with respect to underlying mantle plumes, the addition of ridge migration would produce a more realistic dynamical model.

Overall, this study, like that of *Albers and Christensen* [2001], is focused on quantifying the broad geodynamical framework of the interaction between plumes and

divergent plate boundaries. The emphasis is on fluid dynamics. Subsequent studies can combine geodynamical calculations with petrological melting models. Melting can be incorporated with the conservation equations, and the buoyancy force can include contributions from melt retention and melt depletion.

7.3 NUMERICAL METHODS AND MODEL DESCRIPTION

7.3.1 GENERAL OVERVIEW OF MODEL DOMAIN

The physical system is described by an incompressible fluid layer that is confined in between two parallel, horizontal surfaces (Figure 71). The top surface is divided into three diverging plates to simulate spreading ridges with prescribed opening rates. The temperature of the top plate is held constant at T_c and the temperature of the bottom plate is T_h, $(T_h > T_c)$, on top of which is added a Gaussian shaped thermal anomaly ΔT at a specified location to simulate the plume source. The bottom heated fluid rises buoyantly, transferring heat toward the top plate. Small changes of the density across the fluid relative to the ambient density are ignored except in the buoyancy force term in the momentum equation, where they are directly proportional to temperature. This approximation is known as the Boussinesq approximation of Rayleigh Benard convection.

7.3.2 GOVERNING EQUATIONS AND NONDIMENZIONALIZATION

The numerical models solves the heat advection–diffusion equation with the incompressible Navier Stokes equations:

$$\vec{u} \cdot \nabla T = \kappa \nabla^2 T \tag{3}$$

$$g\rho = \nabla p + \rho(\vec{u} \cdot \nabla)\vec{u} - \nabla \cdot (\eta(p,T)\nabla \vec{u}) \tag{4}$$

$$\nabla \cdot \vec{u} = 0 \tag{5}$$

In these equations, $\vec{u}$ is velocity vector, T is the temperature, g is gravitational acceleration, κ is the coefficient of thermal expansion, p is pressure and $\eta(p,T)$ is temperature and pressure dependent viscosity (Table 1).

For numerical simplicity, standard normalized and nondimensional forms of the above equations are solved [*Wang*, 2004]. The nondimensionalized equations are formed by introducing h to represent a typical length scale, thermal diffusion time

Table 1. Model parameters.

Variable	Meaning	Value	Units
E	Activation energy	2.5×10^5	J/mol
V	Activation volume	4×10^{-6}	m^3/mol
η_0	Minimum ambient viscosity	10^{19}	$Pa\,s$
ρ_0	Reference mantle density	3300	kg/m^3
g	Gravitational acceleration	9.81	m/s^2
R	Universal gas constant	8.314	$J/mol\,K$
α	Coefficient of thermal expansion	3×10^{-5}	K^{-1}
κ	Thermal diffusivity	1	mm^2/s
$\vec{u}$	Velocity vector		cm/yr
T	Temperature		$°C$
T_h	Temperature at bottom boundary without thermal anomaly	1350	$°C$
T_c	Temperature at top boundary	0	$°C$
p	Pressure		Pa
x	Distance in direction parallel to slowest spreading ridge axis		km
y	Distance in direction perpendicular to slowest spreading ridge axis		km
z	Depth below surface		km
A	Dehydration parameter	1, [1, 50]	$Pa\,s$
η_{max}	Maximal cutoff viscosity	10^{21}	$Pa\,s$
η_{min}	Minimal cutoff viscosity	5×10^{18}	$Pa\,s$
F	Body forces		N
ΔT	Mantle plume excess temperature	180	$°C$
d	Plume diameter	125, 165	km
θ	Azimuth of the plume relative to R_1		o
r	Radial distance of the plume from the triple junction	50, 75, 100	km
ρ_w	Reference water density	1030	kg/m^3
ρ_c	Reference crustal density	2700	kg/m^3
u, v, w	x, y, z components of $\vec{u}$		cm/yr

h^2/κ as a typical time, typical velocity as a ratio between typical length over typical time κ/h, typical viscosity as η/η_0, and a temperature scale where top plate is $T_c = 0$ and $T_h = 1$.

Substituting these dimensionless parameters into equations 3, 4, 5 yields the nondimensional forms of the corresponding expressions:

$$\vec{u} \cdot \nabla T = \nabla^2 T \tag{6}$$

$$RaT = \nabla p + \frac{(\vec{u} \cdot \nabla)\vec{u}}{Pr} - \nabla \cdot (\eta(p,T)\nabla \vec{u}) \tag{7}$$

$$\nabla \cdot \vec{u} = 0 \tag{8}$$

The properties of the system are now integrated into the geometry of domain and two dimensionless numbers. One dimensionless number is the Rayleigh number, that describes the tendency of a fluid to convect:

$$Ra = \frac{g\alpha(T_h - T_c)h^3}{\kappa\nu} \tag{9}$$

where ν represents dynamic viscosity. The second dimensionless number is the Prandtl number, which describe the ratio of momentum diffusivity to thermal diffusivity:

$$Pr = \frac{\nu}{\kappa} \tag{10}$$

7.3.3 NUMERICAL DOMAIN AND BOUNDARY CONDITIONS

This system of equations is solved using the finite element numerical approach within a Cartesian box of dimensions 1000x1000x225 km (Figure 71). Guided by earlier studies [*Georgen and Sankar*, 2010; *Georgen*, 2011] the horizontal $(x - y)$ extent of the domain was chosen to capture distribution of the plume material along 500 km for each ridge. Previous authors [*Ito et al.*, 1999; *Hall and Kincaid*, 2003] investigating plume ridge interactions used maximum domain depths corresponding with the upper mantle transition zone. They found that the majority of the plume lithosphere interaction occurred in the upper 200 km of the domain. Therefore, this study uses a maximum depth of 225 km to save computational time. The domain was discretized with a variable octagonal mesh of 40x40x11 elements (P2, P1 and quadratic shape functions for $\vec{u}, p$ and T), yielding resolution spanning from 35 km far away from the ridge to 12.5 km at the ridge axes in both the horizontal and vertical planes.

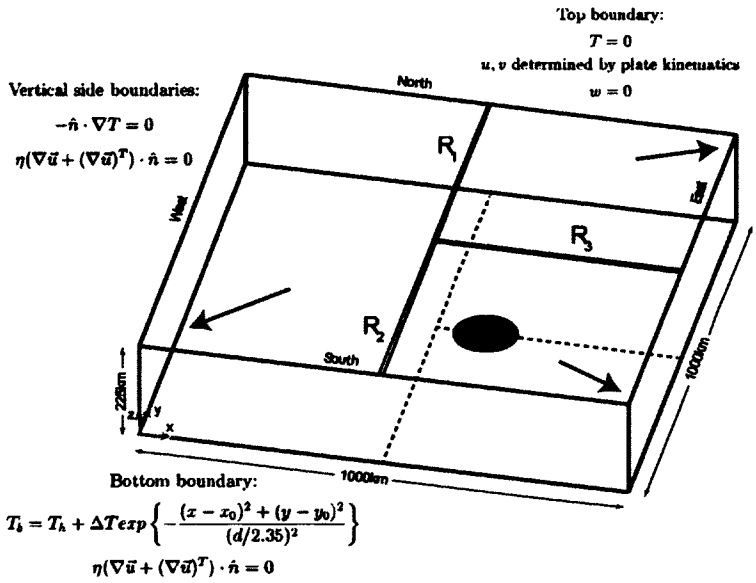

Figure 71. Computational domain representation. Three plates diverge from the triple junction located at ($x = 500\,km$, $y = 500\,km$). (Plate velocities can be found in Figure 72). R_1 and R_2 represent branches of the Mid Atlantic Ridge and R_3 represents the Terceira Rift. On the bottom boundary, the red circle marks the plume conduit location from Model 1 (Table 2). Dashed lines are projections of the top plate boundaries onto the bottom of the model domain, for reference.

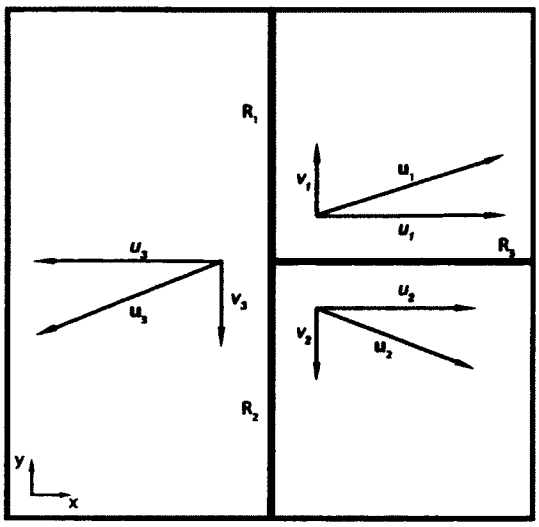

Component	Value $[cm/yr]$
$\lvert\vec{u_1}\rvert$	1.265
u_1	1.205
v_1	0.400
$\lvert\vec{u_2}\rvert$	1.078
u_2	1.000
v_2	-0.400
$\lvert\vec{u_3}\rvert$	1.307
u_3	-1.205
v_3	-0.501

Figure 72. Top plate velocities relative to triple junction.

On the top surface the position of the ridges and triple junction were fixed (Figure 72). Ultraslow spreading ridge R_3 analagous to the Terceira Rift, intersects two faster spreading ridges (R_1 and R_2, analagous to the Mid Atlantic Ridge) at a right angle, similar to the Azores triple junction (Figure 70). Assuming a fixed triple junction, plate divergence vectors were determined from *Luis et al.* [1994] and *Luis and Miranda* [2008]. The x and y components of each plate divergence vector yield half spreading rates similar to the Azores triple junction rates (Figure 72).

The vertical sides of the model domain are set to be insulated walls with no shear stress (Figure 71):

$$-\hat{n} \cdot \nabla T = 0 \tag{11}$$

$$\eta(\nabla\vec{u} + (\nabla\vec{u})^T) \cdot \hat{n} = 0 \tag{12}$$

The bottom boundary is set as open boundary with normal stress being zero:

$$[-p\vec{I} + \eta(\nabla\vec{u} + (\nabla\vec{u})^T)] \cdot \hat{n} = 0 \tag{13}$$

The bottom boundary is kept at a constant temperature T_h except in the area assigned a superimposed Gaussian shaped temperature anomaly that represents mantle plume:

$$T_b = T_h + \Delta T exp\left\{-\frac{(x-x_0)^2 + (y-y_0)^2}{(d/2.35)^2}\right\} \tag{14}$$

where T_b the temperature distribution at the bottom boundary, x and y are model Cartesian coordinates, x_0 and y_0 are the coordinates of the thermal anomaly, d is the diameter of the anomaly and ΔT is thermal anomaly excess temperature relative to the ambient temperature T_h. The position and size of the mantle plume are changed as parameters in the suite of models. Following *Albers and Christensen* [2001] the plume diameter is defined to be the full width at the quarter maximum of the Gaussian shaped thermal anomaly, and the limits of the plume material are delineated by an isosurface with temperature $\Delta T/4+T_h$. The numerical parameter 2.35 in Equation 14 is the relationship between the standard deviation and the diameter of the plume at the quarter maximum $d = 2\sigma\sqrt{ln4}$. An excess plume temperature of $180\,°C$ was chosen because the buoyancy flux of the Azores hot spot, when interpreted as resulting from a thermal anomaly, suggests an excess temperature in the range from 100 to $200\,°C$ [*Schilling*, 1991; *Escartin*, 2001]. Uncertainty exists in the size of the plume conduit, so similar to work done by [*Georgen*, 2011], the plume diameter is assigned to be either $125\,km$ or $165\,km$. These chosen values for plume diameter and excess temperature yield plume volume fluxes ranging from 5.2 to 28 m^3/s depending upon the specific model case.

Similarly to studies such as *Ito et al.* [1997, 1999] and *Albers and Christensen* [2001], viscosity was calculated according to the Arrhenius formula, with an exponential dependence on temperature and pressure:

$$\eta = A\eta_0 exp\left\{\frac{E+\rho_0 g(h-z)V}{RT} - \frac{E+\rho_0 ghV/2}{RT_h}\right\} \tag{15}$$

where E is activation energy, V activation volume, R is the ideal gas constant η_0 is minimal ambient mantle viscosity determined at the half depth of the fluid layer thickness, and A is dehydration parameter. For the purposes of numerical stability, maximal and minimal cutoff viscosities are established. The maximum cutoff value is sufficiently high for the formation of a rigid lithosphere layer at the top of the model box. This study uses two values for minimum cutoff viscosity, 1.5×10^{19} and $5 \times 10^{18}\,Pa\,s$ (Figure 73). The higher value for minimum cutoff viscosity (Figure 73 bottom panel) was used as the base case because it eliminates active flow of the plume material due to viscosity contrast and leaves only the thermal buoyancy contribution. The lower value of minimum viscosity cutoff (Figure 73 top panel) allows for plume material viscosity to be lower than that of the ambient mantle η_0. Also, the viscosity limits used in this study are set due to size of the numerical domain, which is in turn

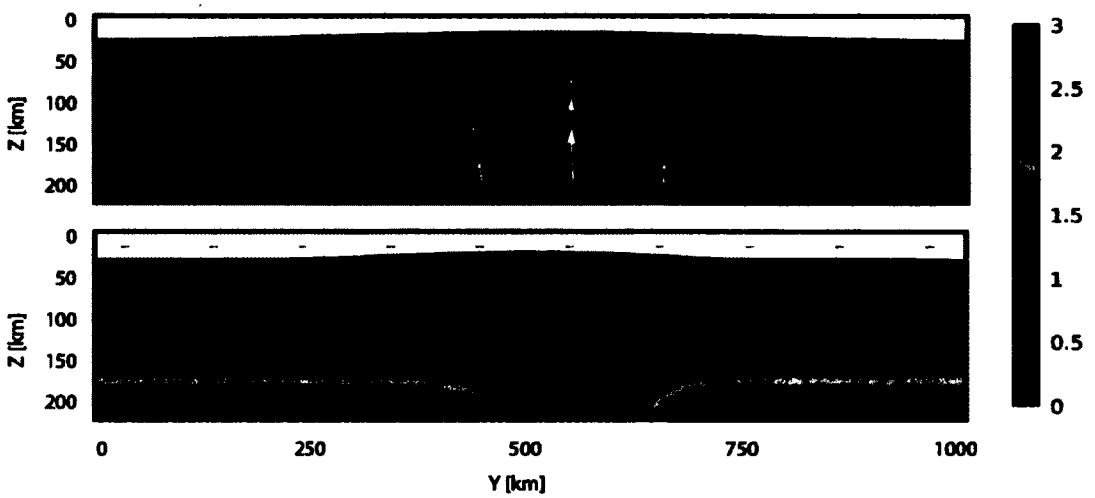

Figure 73. Calculated viscosity and velocity solutions extracted along a vertical plane at X = 400 *km* for models 24 (bottom panel) and 96 (top panel). Color bar represents viscosity in nondimensional units and white color shows nondimensionalized viscosity larger than 3. Red contour shows 1395 °*C* isotherm.

dependent on the amount of RAM available. Bigger viscosity contrasts between the plume and the ambient mantle could produce larger waist widths that would exceed the size of domain and therefore could not be able accurately modeled.

The pre–exponential parameter A is introduced to simulate the effect of dehydration during mantle melting. As the mantle rises and crosses the dry solidus, it may experience an increase in viscosity by a factor of approximately 10-100 due to dehydration during melting [*Hirth and Kohlstedt*, 1995; *Braun et al.*, 2000]. Accordingly, in this study, A is set to be 1 when temperature of the mantle is beneath the dry solidus and 50 when it is above. To avoid infinite gradients in viscosity, the dehydration parameter is a step function with adjustable smoothing length. Here, the transition length for dehydration is set to 5 °*C* , defining the abruptness of the transition.

Ito et al. [1999] showed that by incorporating dehydration in the mantle rheology, upwelling rates in the melting zone can decrease by an order of magnitude, compared to the case without dehydration. This decrease in upwelling results in lower melting rates in the upper mantle, thinner crust, and more pronounced lateral spreading of the plume material beneath the dry solidus (Figure 69). In a study exploring the dynamics of an off–ridge mantle plume, *Hall and Kincaid* [2003] used

a similar treatment of dehydration. They concluded that because of the "viscous plug" at depths less than approximately $100\,km$, a significant portion of the plume material travels towards the ridge axis at sub solidus depths, rather than closer to the lithosphere asthenosphere boundary. Also, they noted that in order to achieve interaction between an off–axis plume and a ridge, greater plume volume flux is required for the case with dehydration.

A series of models was run according to the parameters specified in Table 2, with the purposes of determining the spatial distribution of the plume material and establishing scaling laws. Materials properties and parameters that were held constant through all model runs are listed in Table 1

7.3.4 NUMERICAL SOLVER DIAGNOSTIC AND CONVERGENCE

In order to achieve convergence, the model calculations were approached using a series of steps of increasing computational difficulty, starting with the loosely coupled system of equations on a low resolution octagonal mesh of 15x15x11 elements. Each consecutive step used the previous solution as the initial condition for the next iteration run, proceeding until the desired parameter values and mesh resolution were achieved. In normalized, nondimensional units, the steps taken were:

1. $T_b = 1$, $Ra = 0$, $\eta_{max} = \eta_{min} = \eta_0$
2. $T_b = 1$, $Ra = 100$, $\eta_{max} > \eta_0 > \eta_{min}$
3. $T_b = 1$, $Ra = 10^5$, $\eta_{max} > \eta_0 > \eta_{min}$
4. $T_b = T_h + \Delta T exp\left\{-\frac{(x-x_0)^2+(y-y_0)^2}{(d/2.35)^2}\right\}$, $Ra = 10^5$, $\eta_{max} > \eta_0 > \eta_{min}$
5. Setting the full mesh resolution for domain 40x40x11.

Since the system of governing equation is fully coupled, the computations used the stationary parametric MUltifrontal Massively Parallel sparse direct Solver (MUMPS) to solve for the dependent variables p, T, $\vec{u}$. MUMPS is an algorithm that solves sparse systems of linear equations of the form $Ax = b$ in three stages: (1) an analysis stage where the matrix is preprocessed to improve structural properties, (2) matrix factorization as $A = LU$ or $A = LDL^T$, and (3) solution for x using forward and backward substitution. The flow portion of the problem uses streamline and crosswind diffusion for stabilization and domain decomposition is done using P2+P1

elements. The thermal portion used quadratic decomposition with streamline diffusion for stabilization.

To ensure that size of the numerical domain was sufficient to avoid edge effects the results of a series of models with different domain sizes were compared. Each domain had the triple junction located on the top of the domain ($x = 2, y = 2, z = 0.9$). Five domain dimensions were used (2.6x2.6, 2.8x2.8, 3.0x3.0, 3.2x3.2, 3.4x3.4 and 4x4), all with the same depth of 0.9. Due to computational constraints, 4x4x0.9 was the biggest possible domain to run without compromising mesh resolution. Models 1 to 12 inclusive (Table 2) were run on all domain sizes, and solutions for velocity were compared on concentric subdomains, meaning that location of the triple junctions were consistently maintained in the center of the model for different sized domains, (Figure 74).

A Matlab script (Listing A.5) extracts velocity components $u(x, y, z, i, \theta, d)$ (parallel to x axes), and $v(x, y, z, i, \theta, d)$ (orthogonal to u in xy plane) along the walls of each subdomain, where i, θ, d denote the size of the domain, the azimuth of the plume origin relative to the R_1 axis, and the diameter of the plume, respectively. The largest subdomain was defined to be the reference case, to which the other smaller subdomains were compared.

$$max(|v(x_{ref}, y_{ref}, z, ref, \theta, d) - v(x_i, y_i, z, i, \theta, d)|) \tag{16}$$

For simplicity in presenting the results, the sides of the subdomains were labeled North (N), East (E), South (S), and West (W) (Figure 71). On the x-axis of Figure 75, values indicate what sizes of the box were compared. For example, the set of points located at $x = 3.4$ on N side indicates comparison of $|u_{4.0} - u_{3.4}|$, with the y-axis recording the corresponding extreme values in cm/yr.

The relative differences in velocities converge towards the 4x4x0.9 sized box (Figure 75). The maximal differences, especially along N and S sides (Figure 75(a) and 75(d)), are strongly dependent on the plume azimuth. For example, following the velocity differences along S side, it is apparent that the influence of the edge effect increases the closer the plume is to the S boundary, and it peaks for the azimuth of 180° when the plume is closest to the S wall. Performing the calculations on the largest model domain minimizes edge effect errors.

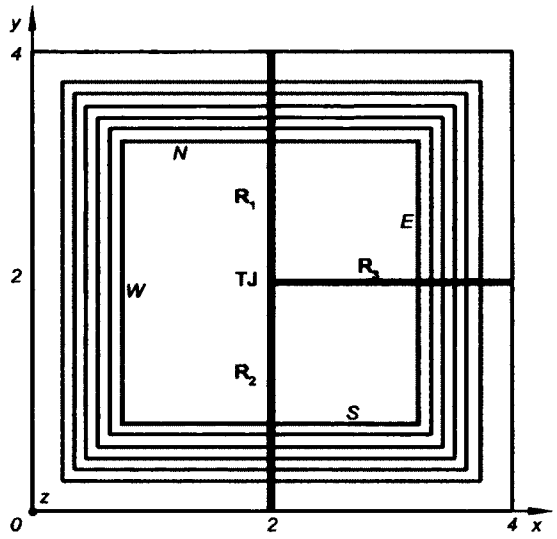

Figure 74. Top down view of setup for investigating the influence of domain size on the calculated velocity. Velocity comparisons are performed along the red square (the sides of the smallest domain, with dimension 2.4x2.4x0.9) for domains of increasing size (black squares). Red letters mark the sides of the subdomain walls, with N = North, E= East, S = South, and W = West. Ridges R_1, R_2 and R_3, indicated with double black lines, form the triple junction (TJ).

Table 2. Model parameter details.

Model	d $[km]$	η_{min} $[Pa\,s]$	θ [°]	r $[km]$	A
1	125	1.5×10^{19}	90	50	1
2	165	1.5×10^{19}	90	50	1
3	125	1.5×10^{19}	135	50	1
4	165	1.5×10^{19}	135	50	1
5	125	1.5×10^{19}	180	50	1
6	165	1.5×10^{19}	180	50	1
7	125	1.5×10^{19}	225	50	1
8	165	1.5×10^{19}	225	50	1
9	125	1.5×10^{19}	270	50	1
10	165	1.5×10^{19}	270	50	1
11	125	1.5×10^{19}	315	50	1

Continued on next page

Table 2 – continued from previous page

Model	d [km]	η_{min} [$Pa\,s$]	θ [°]	r [km]	A
12	165	1.5×10^{19}	315	50	1
13	125	1.5×10^{19}	90	75	1
14	165	1.5×10^{19}	90	75	1
15	125	1.5×10^{19}	135	75	1
16	165	1.5×10^{19}	135	75	1
17	125	1.5×10^{19}	180	75	1
18	165	1.5×10^{19}	180	75	1
19	125	1.5×10^{19}	225	75	1
20	165	1.5×10^{19}	225	75	1
21	125	1.5×10^{19}	270	75	1
22	165	1.5×10^{19}	270	75	1
23	125	1.5×10^{19}	315	75	1
24	165	1.5×10^{19}	315	75	1
25	125	1.5×10^{19}	90	100	1
26	165	1.5×10^{19}	90	100	1
27	125	1.5×10^{19}	135	100	1
28	165	1.5×10^{19}	135	100	1
29	125	1.5×10^{19}	180	100	1
30	165	1.5×10^{19}	180	100	1
31	125	1.5×10^{19}	225	100	1
32	165	1.5×10^{19}	225	100	1
33	125	1.5×10^{19}	270	100	1
34	165	1.5×10^{19}	270	100	1
35	125	1.5×10^{19}	315	100	1
36	165	1.5×10^{19}	315	100	1
37	125	1.5×10^{19}	90	50	[1,50]
38	165	1.5×10^{19}	90	50	[1,50]
39	125	1.5×10^{19}	135	50	[1,50]
40	165	1.5×10^{19}	135	50	[1,50]
41	125	1.5×10^{19}	180	50	[1,50]

Continued on next page

Table 2 – continued from previous page

Model	d [km]	η_{min} [$Pa\,s$]	θ [°]	r [km]	A
42	165	1.5×10^{19}	180	50	[1,50]
43	125	1.5×10^{19}	225	50	[1,50]
44	165	1.5×10^{19}	225	50	[1,50]
45	125	1.5×10^{19}	270	50	[1,50]
46	165	1.5×10^{19}	270	50	[1,50]
47	125	1.5×10^{19}	315	50	[1,50]
48	165	1.5×10^{19}	315	50	[1,50]
49	125	1.5×10^{19}	90	75	[1,50]
50	165	1.5×10^{19}	90	75	[1,50]
51	125	1.5×10^{19}	135	75	[1,50]
52	165	1.5×10^{19}	135	75	[1,50]
53	125	1.5×10^{19}	180	75	[1,50]
54	165	1.5×10^{19}	180	75	[1,50]
55	125	1.5×10^{19}	225	75	[1,50]
56	165	1.5×10^{19}	225	75	[1,50]
57	125	1.5×10^{19}	270	75	[1,50]
58	165	1.5×10^{19}	270	75	[1,50]
59	125	1.5×10^{19}	315	75	[1,50]
60	165	1.5×10^{19}	315	75	[1,50]
61	125	1.5×10^{19}	90	100	[1,50]
62	165	1.5×10^{19}	90	100	[1,50]
63	125	1.5×10^{19}	135	100	[1,50]
64	165	1.5×10^{19}	135	100	[1,50]
65	125	1.5×10^{19}	180	100	[1,50]
66	165	1.5×10^{19}	180	100	[1,50]
67	125	1.5×10^{19}	225	100	[1,50]
68	165	1.5×10^{19}	225	100	[1,50]
69	125	1.5×10^{19}	270	100	[1,50]
70	165	1.5×10^{19}	270	100	[1,50]
71	125	1.5×10^{19}	315	100	[1,50]

Continued on next page

Table 2 – continued from previous page

Model	d [km]	η_{min} [$Pa\,s$]	θ [°]	r [km]	A
72	165	1.5×10^{19}	315	100	[1,50]
73	125	5×10^{18}	90	50	1
74	165	5×10^{18}	90	50	1
75	125	5×10^{18}	135	50	1
76	165	5×10^{18}	135	50	1
77	125	5×10^{18}	180	50	1
78	165	5×10^{18}	180	50	1
79	125	5×10^{18}	225	50	1
80	165	5×10^{18}	225	50	1
81	125	5×10^{18}	270	50	1
82	165	5×10^{18}	270	50	1
83	125	5×10^{18}	315	50	1
84	165	5×10^{18}	315	50	1
85	125	5×10^{18}	90	75	1
86	165	5×10^{18}	90	75	1
87	125	5×10^{18}	135	75	1
88	165	5×10^{18}	135	75	1
89	125	5×10^{18}	180	75	1
90	165	5×10^{18}	180	75	1
91	125	5×10^{18}	225	75	1
92	165	5×10^{18}	225	75	1
93	125	5×10^{18}	270	75	1
94	165	5×10^{18}	270	75	1
95	125	5×10^{18}	315	75	1
96	165	5×10^{18}	315	75	1
97	125	5×10^{18}	90	100	1
98	165	5×10^{18}	90	100	1
99	125	5×10^{18}	135	100	1
100	165	5×10^{18}	135	100	1
101	125	5×10^{18}	180	100	1

Continued on next page

Table 2 – continued from previous page

Model	d [km]	η_{min} [$Pa\,s$]	θ [°]	r [km]	A
102	165	5×10^{18}	180	100	1
103	125	5×10^{18}	225	100	1
104	165	5×10^{18}	225	100	1
105	125	5×10^{18}	270	100	1
106	165	5×10^{18}	270	100	1
107	125	5×10^{18}	315	100	1
108	165	5×10^{18}	315	100	1
109	125	5×10^{18}	90	50	[1,50]
110	165	5×10^{18}	90	50	[1,50]
111	125	5×10^{18}	135	50	[1,50]
112	165	5×10^{18}	135	50	[1,50]
113	125	5×10^{18}	180	50	[1,50]
114	165	5×10^{18}	180	50	[1,50]
115	125	5×10^{18}	225	50	[1,50]
116	165	5×10^{18}	225	50	[1,50]
117	125	5×10^{18}	270	50	[1,50]
118	165	5×10^{18}	270	50	[1,50]
119	125	5×10^{18}	315	50	[1,50]
120	165	5×10^{18}	315	50	[1,50]
121	125	5×10^{18}	90	75	[1,50]
122	165	5×10^{18}	90	75	[1,50]
123	125	5×10^{18}	135	75	[1,50]
124	165	5×10^{18}	135	75	[1,50]
125	125	5×10^{18}	180	75	[1,50]
126	165	5×10^{18}	180	75	[1,50]
127	125	5×10^{18}	225	75	[1,50]
128	165	5×10^{18}	225	75	[1,50]
129	125	5×10^{18}	270	75	[1,50]
130	165	5×10^{18}	270	75	[1,50]
131	125	5×10^{18}	315	75	[1,50]

Continued on next page

Table 2 – continued from previous page

Model	d [km]	η_{min} [$Pa\,s$]	θ [°]	r [km]	A
132	165	5×10^{18}	315	75	[1,50]
133	125	5×10^{18}	90	100	[1,50]
134	165	5×10^{18}	90	100	[1,50]
135	125	5×10^{18}	135	100	[1,50]
136	165	5×10^{18}	135	100	[1,50]
137	125	5×10^{18}	180	100	[1,50]
138	165	5×10^{18}	180	100	[1,50]
139	125	5×10^{18}	225	100	[1,50]
140	165	5×10^{18}	225	100	[1,50]
141	125	5×10^{18}	270	100	[1,50]
142	165	5×10^{18}	270	100	[1,50]
143	125	5×10^{18}	315	100	[1,50]
144	165	5×10^{18}	315	100	[1,50]
					End of the Table 2

7.3.5 MODEL RESULTS POST–PROCESSING

For all models, calculated temperature, velocity field and viscosity were extracted by evaluating solutions on a uniformly spaced grid with $\Delta x = \Delta y = 12.5\,km$ and $\Delta z = 5\,km$ for post processing. Plume waist width W was determined along each of R_1, R_2 and R_3 using a temperature isosurface and Matlab Listing A.3.

Plume volume flux was determined following *Albers and Christensen* [2001] by evaluating the two-dimensional integral on the bottom boundary:

$$Q = \Delta T^{-1} \int \int w(T - T_h)\mathrm{d}x\mathrm{d}y \tag{17}$$

In order to calculate the contribution of mantle plume to variations in topography, four more models were calculated without the presence of the thermal anomaly. The four models used both variations in the viscosity range (Table 2) as well as a dehydrating and a non dehydrating mantle. Dynamical (or thermal) topography depends on the mantle density variations due to temperature structure. Following earlier studies [*Albers and Christensen*, 2001; *Georgen and Lin*, 2002; *Georgen*, 2008;

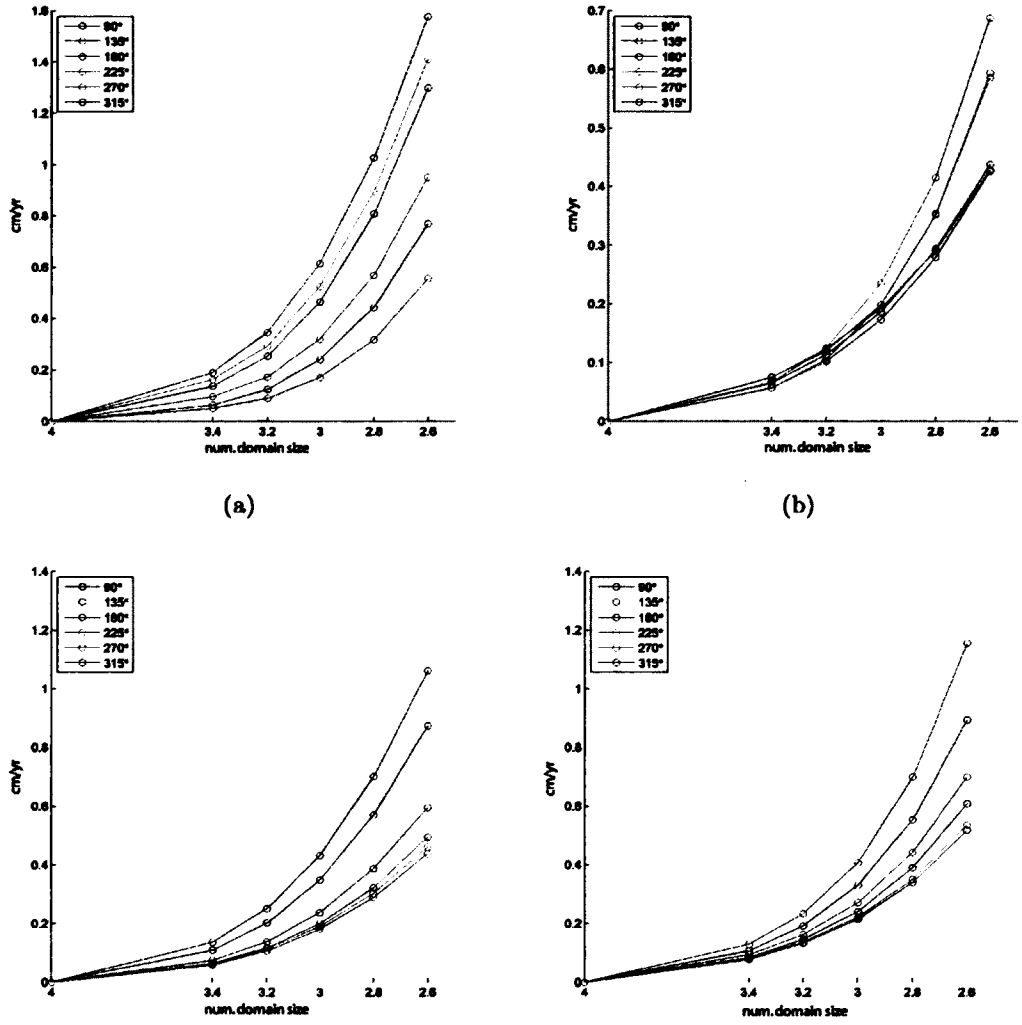

Figure 75. Absolute velocity difference in cm/yr as the function of the numerical domain size and plume conduit azimuthal location (θ). Comparisons made along the sides of the subdomain walls shown in (Figure 74) with velocity components perpendicular to the particular wall. Parameters corresponded to Models 1, 3, 5, 7, 9 and 11 (Table 2), $r = 50\,km$, $\eta_{min} = 1.5 \times 10^{19}\,Pa\,s$, $d = 125\,km$ and $A = 1$. a) South wall, b) West wall, c) East wall, and d) North wall.

Georgen and Sankar, 2010; *Georgen*, 2011], topographic variations were calculated using:

$$\Delta h = \alpha \frac{\rho_0}{\rho_c - \rho_w} \int_0^{z_0} (T - T_0) \mathrm{d}z \tag{18}$$

where T_0 is temperature of the model without the thermal anomaly (Code A.2). It is assumed that the vertical mantle columns are in isostatic equilibrium at the depth of 200 km.

Melting, melt fraction and crustal thickness are calculated in a post processing step using Matlab Listing A.1 with temperature and velocity solutions from the series of models. The melting model used is similar to that of *Reid and Jackson* [1981], *McKenzie and Bickle* [1988], and *Sparks and Parmentier* [1993] as followed by *Georgen and Sankar* [2010], with the solidus defined as:

$$T_{solidus} = 1160[^\circ C] + 3.25z \tag{19}$$

where z is depth in km. Melt fraction F is:

$$F = (T - T_{solidus})/350[^\circ C] \tag{20}$$

and melt production rate Γ:

$$\Gamma = \nabla F \cdot \vec{u} \tag{21}$$

To predict crustal thickens variations along the ridges it is assumed that mantle and plume are homogenous compositionally indistinguishable material with no heat exchange between melt and surrounding, and that melt migrates vertically. Following *Braun et al.* [2000] the melt fraction is limited to 18% as this value is assumed to be the amount of melt that is produced before exhaustion of the mineral clinopyroxene.

Integration of the melt production rate along the domain depth (z axis) gives the distribution of the vertical cumulative melt production rate (Figure 77). The depth at which integration starts is limited to 96 km to prevent unrealistic crustal thicknesses from plume conduit. Next, based upon the half spreading rates of the ridges, melt is allocated to each spreading axis. Finally, integration of the cumulative melt production rate along lines perpendicular to the ridges, divided by the ridge full spreading rate, yields crustal thickness [*Reid and Jackson*, 1981].

7.4 MODEL RESULTS AND DISCUSSION

7.4.1 AZORES LIKE TRIPLE JUNCTION, TEMPERATURE AND VELOCITY FIELD

Here, the dispersion of the plume material in the vicinity of the triple junction will be introduced using a few characteristic models. Figure 77 presents the base case results from Model 1 (Table 2). The plume conduit is located along R_3 (Figure 77(a)) and ascending plume material is channeled along its axis (Figure 77(b), 77(d)) resulting in elevated temperature to $\sim 250\,km$ east from the triple junction. A portion of the plume material reaches the $R_1 - R_2$ ridge axis, and it is asymmetrically diverted to the south (Figure 77(c)). The relatively small distance the plume material disperses along R_1 toward the north can be attributed to due to opposing top plate velocities parallel to R_1 (Figure 72). On the other hand, along R_2 plume dispersion is enhanced by the along axis components of surface plate divergence that are in the same direction. Only a small amount of plume material that crosses the $R_1 - R_2$ axis (Figure 77(b) for $X = [0, 500]\,km$).

Compared to Model 1, Model 2 increases the volume flux (Q) of the plume conduit by increasing the plume radius (from $r = 125\,km$ to $r = 165\,km$) (Table 1). Figure 78 shows that the general trend in the flow pattern is preserved. The overall shape of the plume dispersion in Figure 78(d) is roughly the same as the results from Model 1, although the plume extends over a larger area.

Moving the origin of the plume conduit by $50\,km$ eastward along the axis of R_3 (Model 25, Figure 79), compared to the base case, almost completely prevents plume material from crossing the $R_1 - R_2$ axis (Figure 79(b), 79(c)). Model 25 does not incorporate dehydration viscosity. If the dehydration parameter, as discussed earlier in the text, is allowed to assume values $A = [1, 50]$ depending on the difference between mantle temperature and solidus temperature, the effects can be seen in Figure 80. A comparison of figures 80(d) and 79(d) shows how, when dehydration viscosity is incorporated, the lateral flow of the plume material is suppressed by off–axis areas with high viscosity. Plume material does not trace out the lithosphere asthenosphere boundary in Figure 80(b) as compared to Figure 79(b), and plume material does not intersect the $R_1 - R_2$ axis in Figure 80(c).

Model 6 repositions the plume conduit along the axis of R_2 ($\theta = 180°$), at a

distance of $50\,km$ from the triple junction (Figure 81). As might be anticipated, plume material flows a longer distance south along R_2 than in Model 1 (Figure 77). In the shallower depths, when the topography of the lithosphere asthenosphere becomes pronounced, plume material starts to channelize along the ridge axes (Figure 81(d,e)). Along R_3, plume material reaches $\sim 240\,km$ away from triple junction, and it extends $\sim 160\,km$ to the west of the $R_1 - R_2$ axis (Figure 81(b)). The effects of dehydration are similar for plume located along R_2 (Figure 82) to those previously described.

Setting the plume origin $100\,km$ southward from triple junction along the R_2 axis (Figure 83) results in total absence of the plume material to the north of the triple junction and along R_3 (Figure 83(b-e)). Increasing the volume flux for a plume in the same position results in a portion of the plume material crossing R_3 axis at shallow depths (Figure 84).

All the results discussed so far were for the case of no viscosity contrast between plume material and the ambient mantle. Reducing the minimal cutoff viscosity to $\eta = 5 \times 10^{18}\,Pa\,s$ allows the plume material to have lower viscosity than the ambient mantle. As a result, there is an effective increase in the volume flux of the plume due to enhanced upwelling rates. These observation can be directly made by comparing Figure 77 to Figure 78 where there is an increase in the plume volume flux due to the change in the plume diameter from $125\,km$ to $165\,km$, and then comparing these solutions to Figure 85.

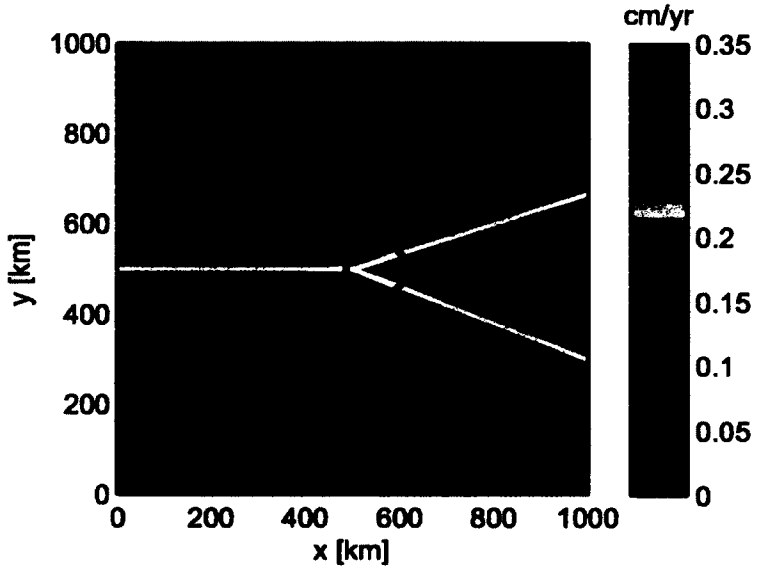

Figure 76. Cumulative melt production rate at the base of the lithosphere. White lines are limits of pooling regions for the ridges derived from ridge perpendicular half spreading rates. Red circle indicates the projection of the plume conduit. Result from Model 1 (Table 2).

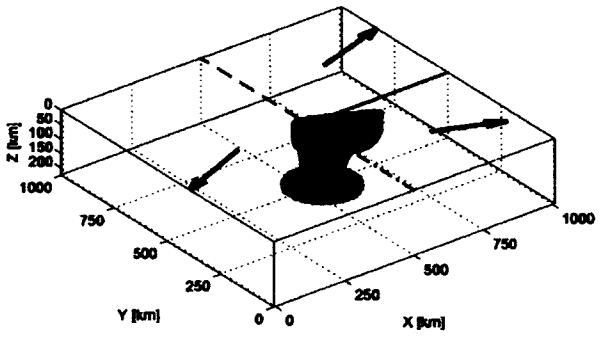
Z [km]
0
50
100
150
200
1000
750
500
250
0
Y [km]
0
250
500
750
1000
X [km]

(a)

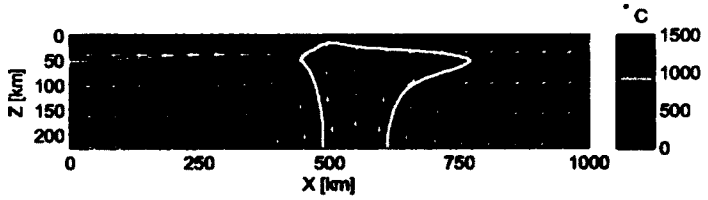
°C
1500
1000
500
0
Z [km]
0
50
100
150
200
0
250
500
750
1000
X [km]

(b)

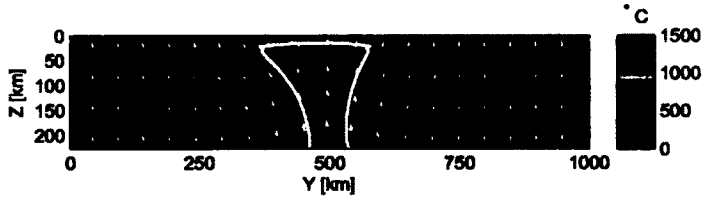
°C
1500
1000
500
0
Z [km]
0
50
100
150
200
0
250
500
750
1000
Y [km]

(c)

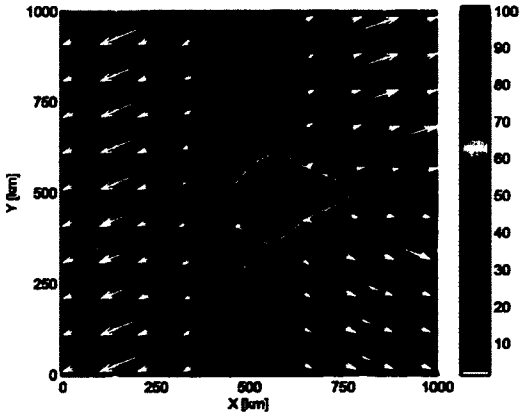
Y [km]
1000
750
500
250
0
0
250
500
750
1000
X [km]
100
90
80
70
60
50
40
30
20
10

(d)

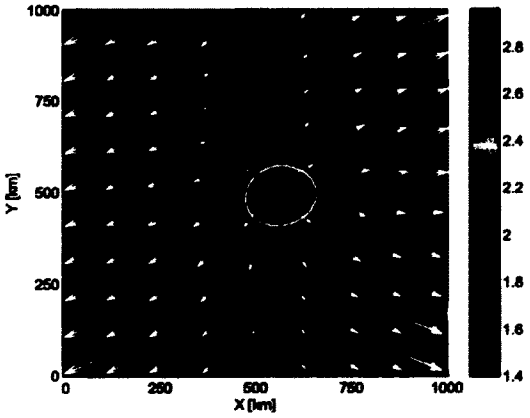
Y [km]
1000
750
500
250
0
0
250
500
750
1000
X [km]
2.8
2.6
2.4
2.2
2
1.8
1.6
1.4

(e)

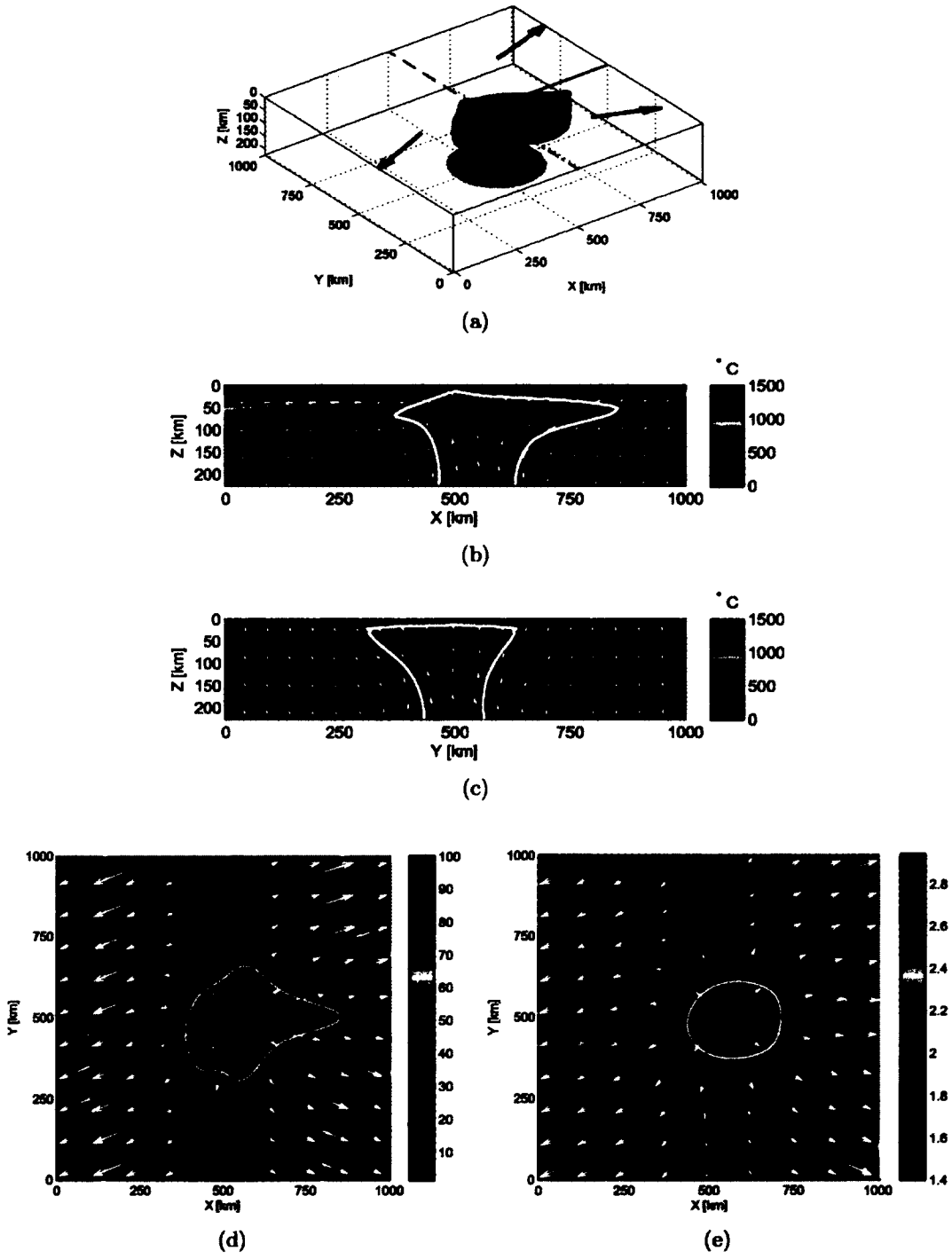

Figure 78. Results from Model 2, Table 2. See Figure 77 for details.

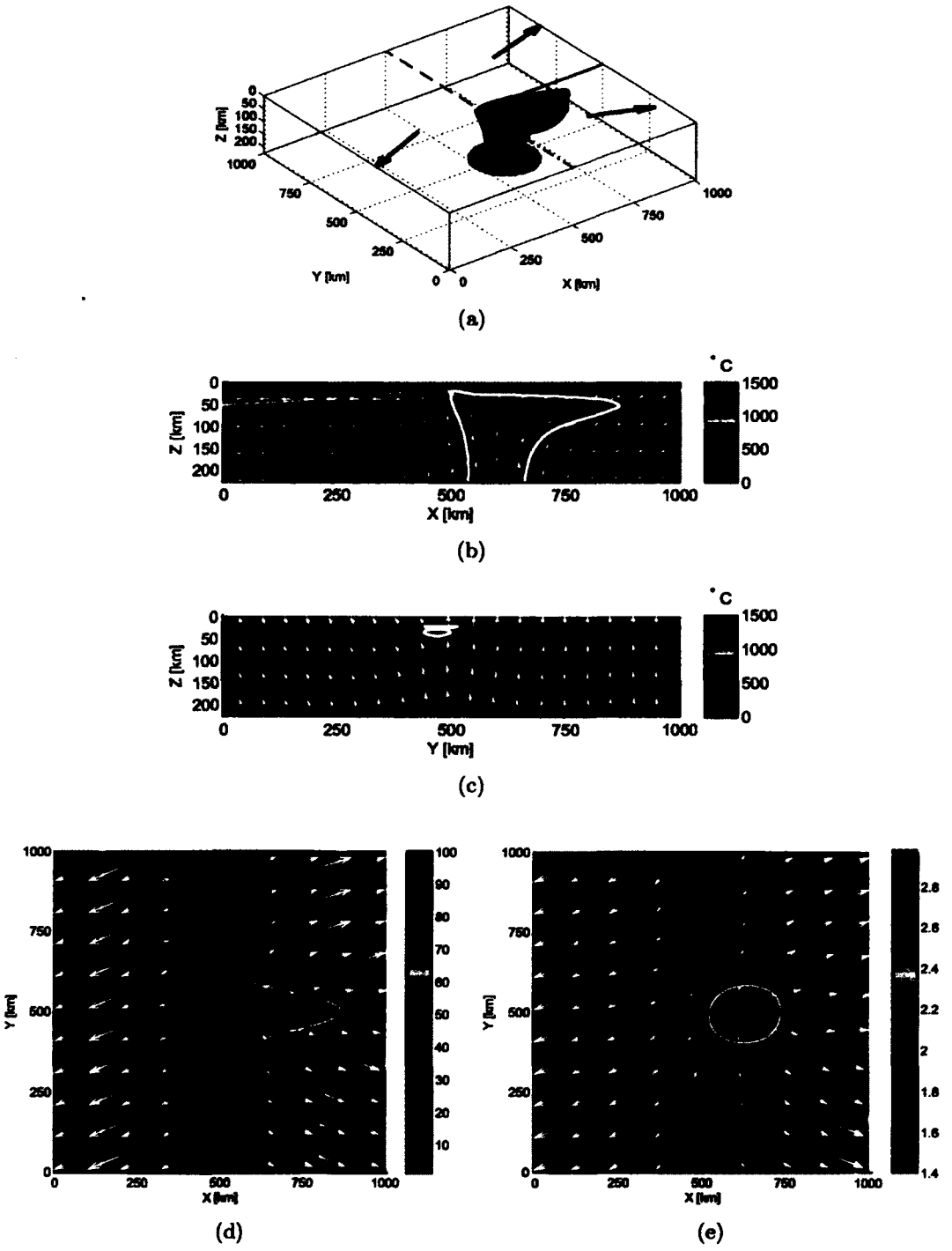

Figure 79. Results from Model 25, Table 2. See Figure 77 for details.

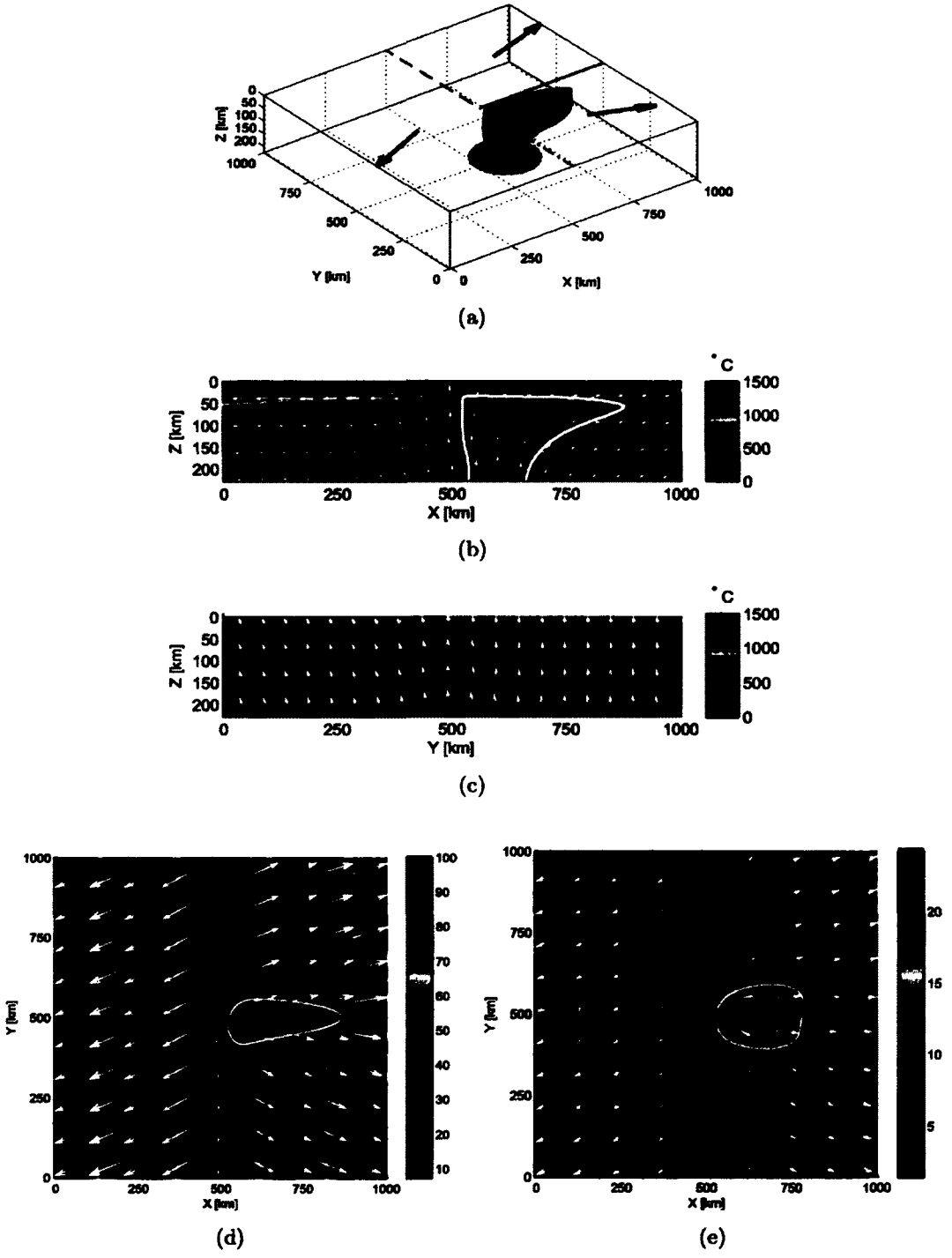

Figure 80. Results from Model 61, Table 2.See Figure 77 for details.

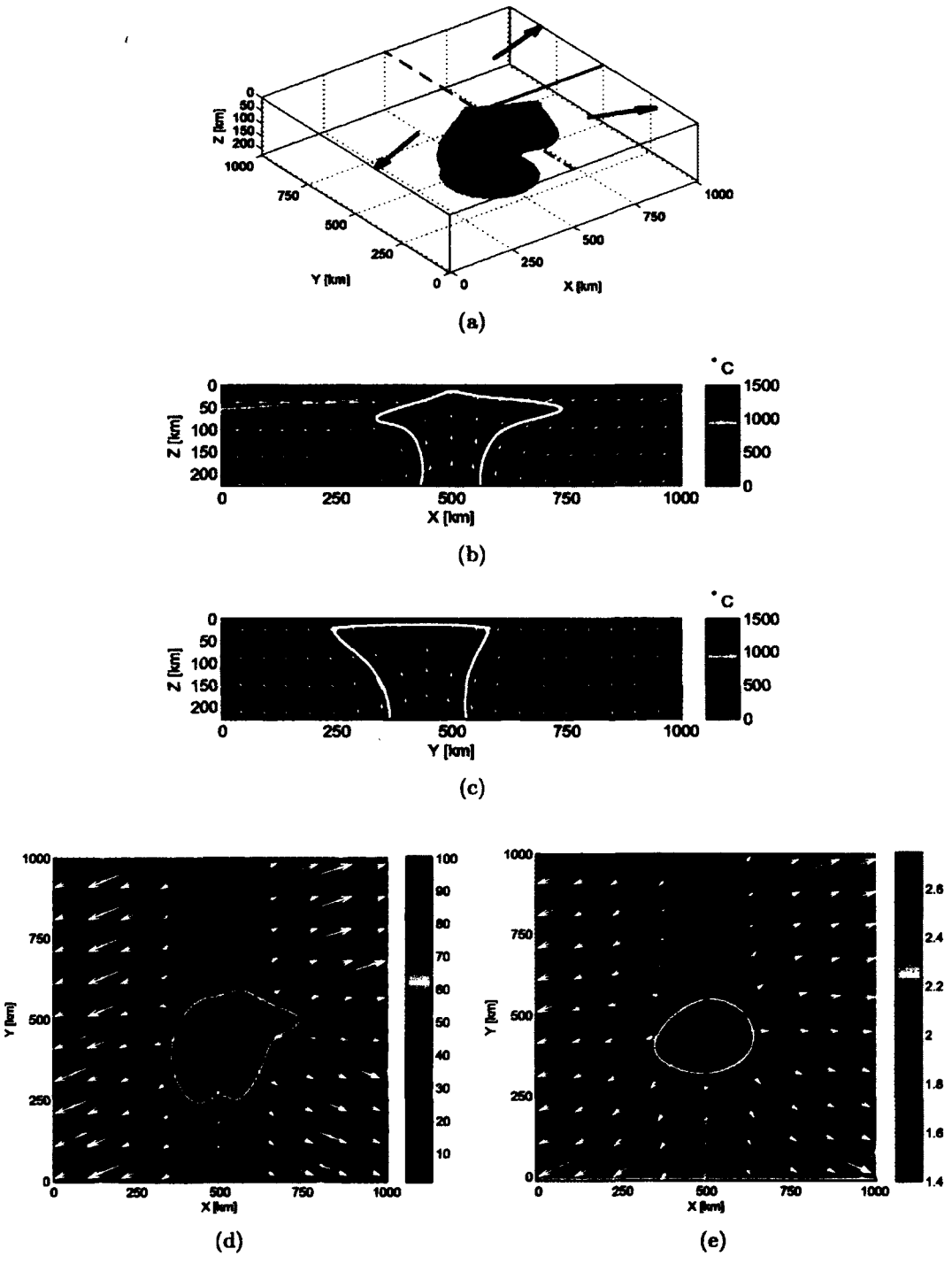

Figure 81. Results from Model 6, Table 2. See Figure 77 for details.

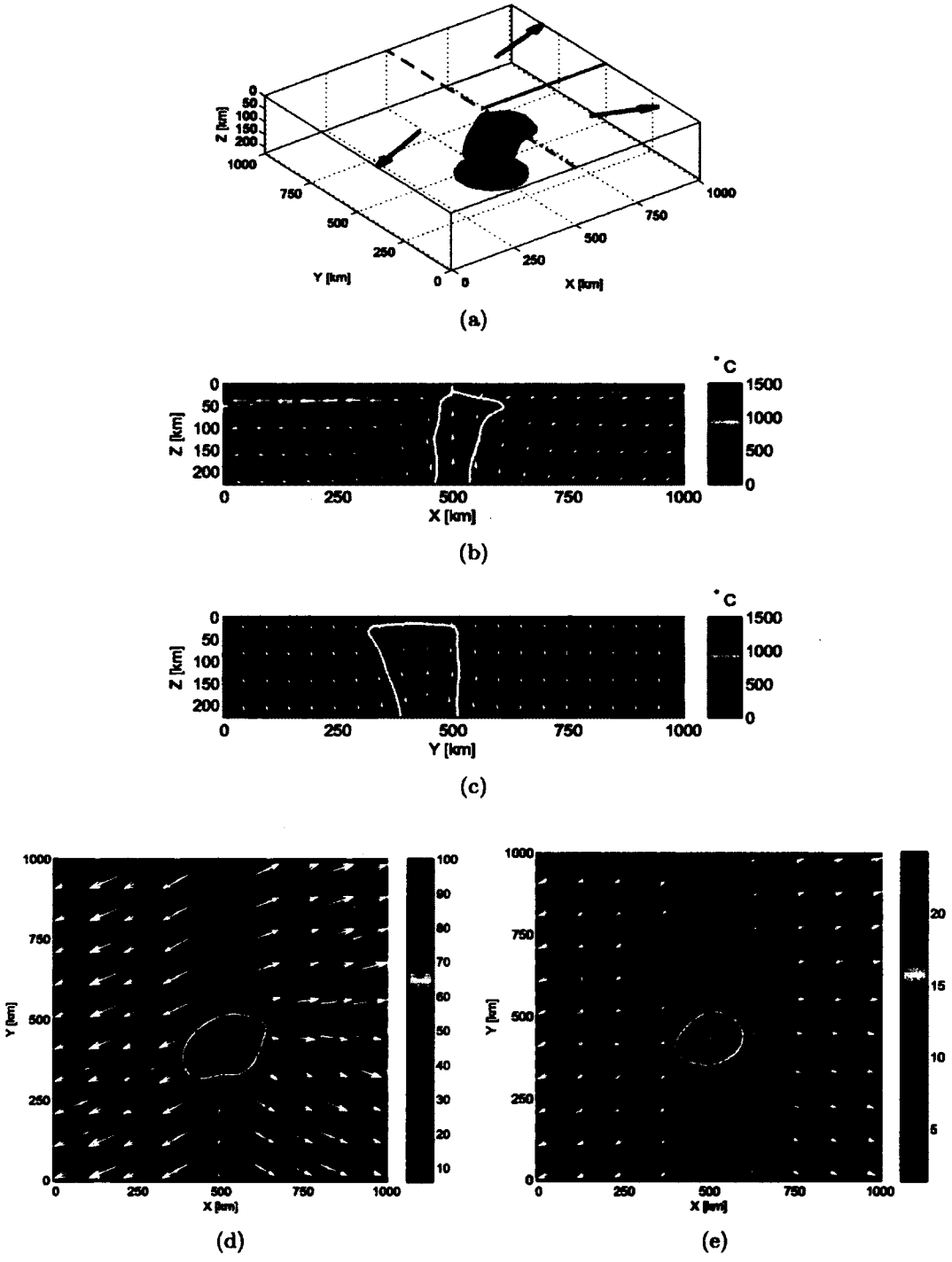

Figure 82. Results from Model 41, Table 2. See Figure 77 for details.

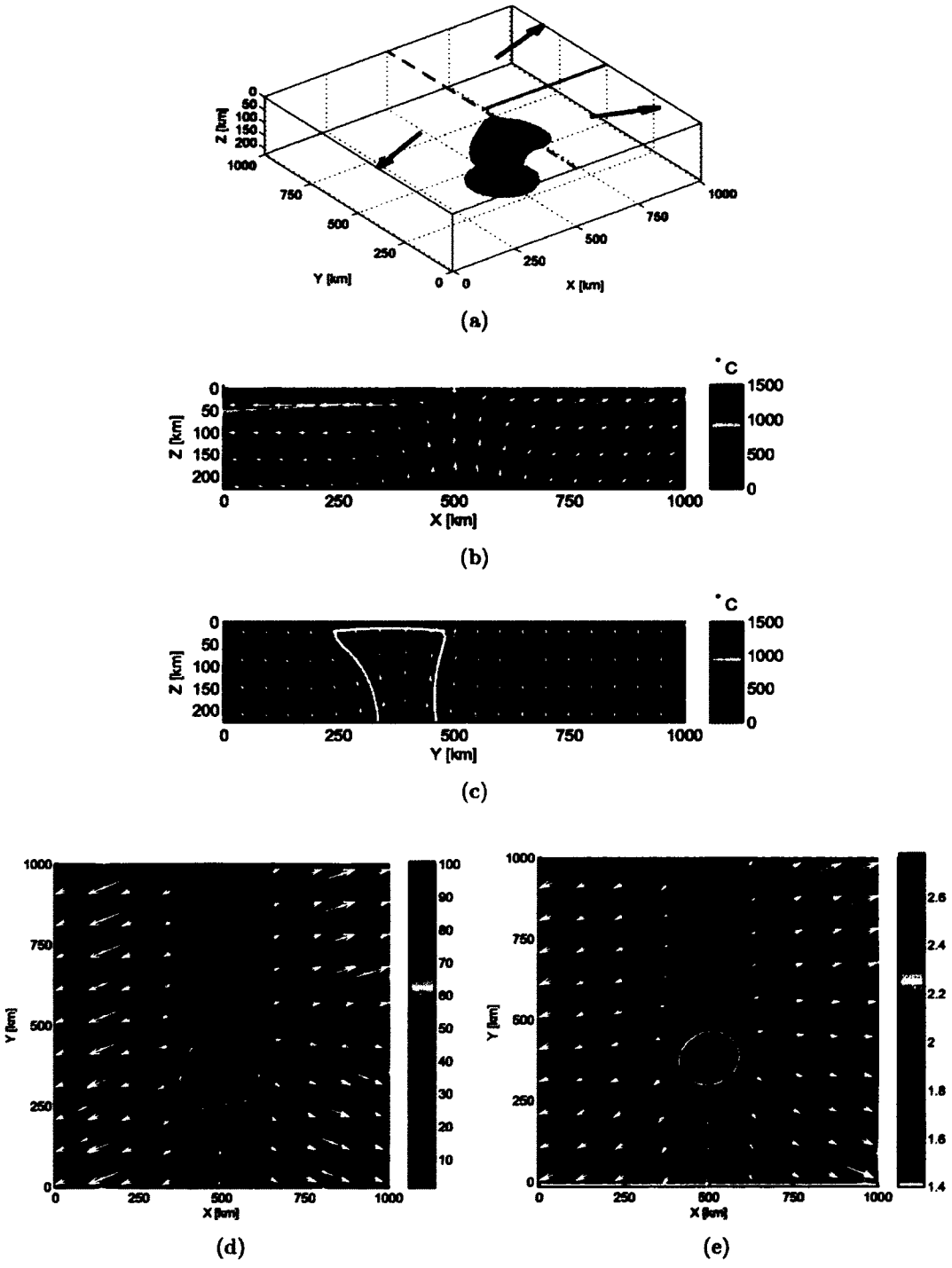

Figure 83. Results from Model 29, Table 2. See Figure 77 for details.

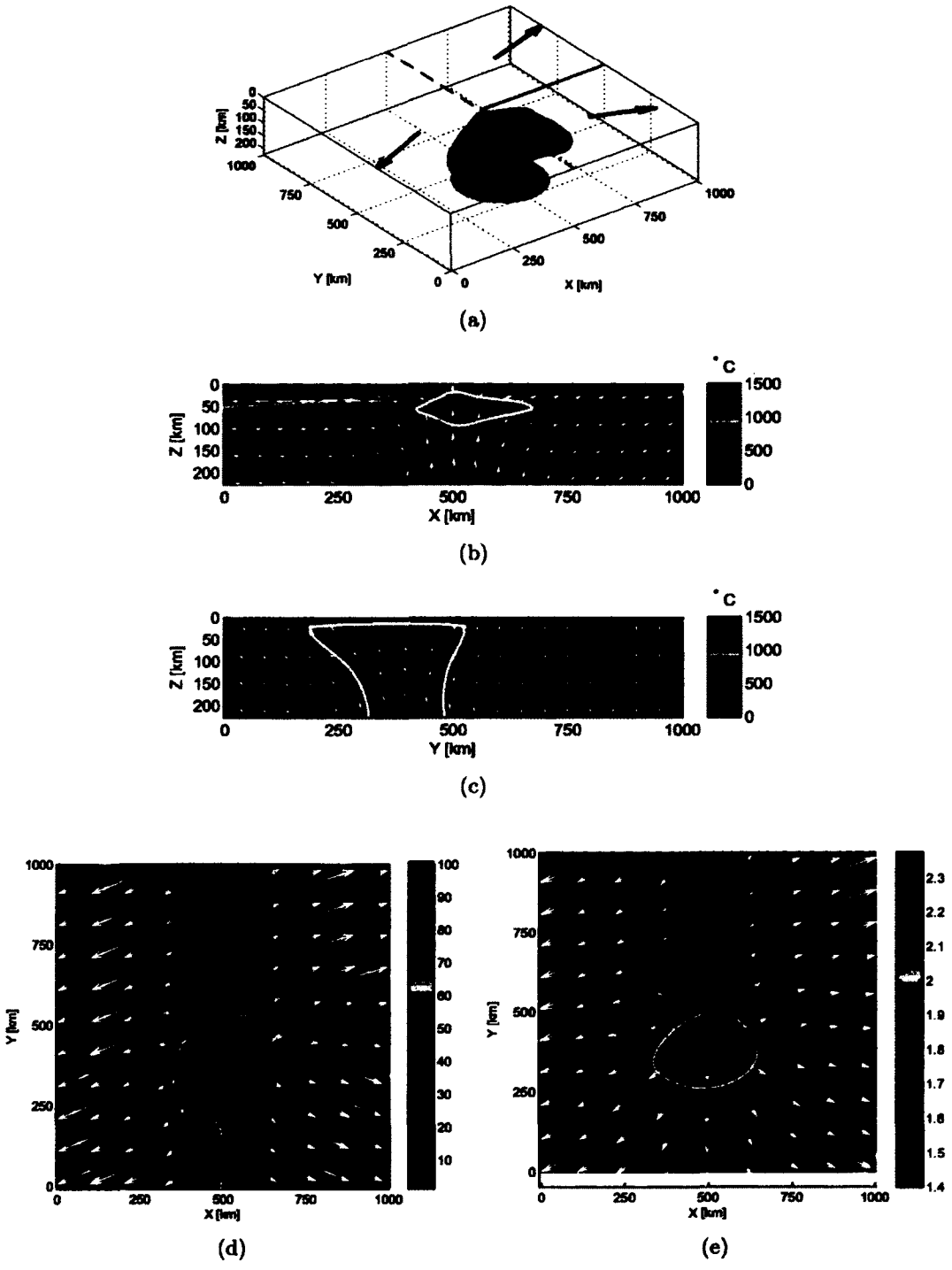

Figure 84. Results from Model 30, Table 2. See Figure 77 for details.

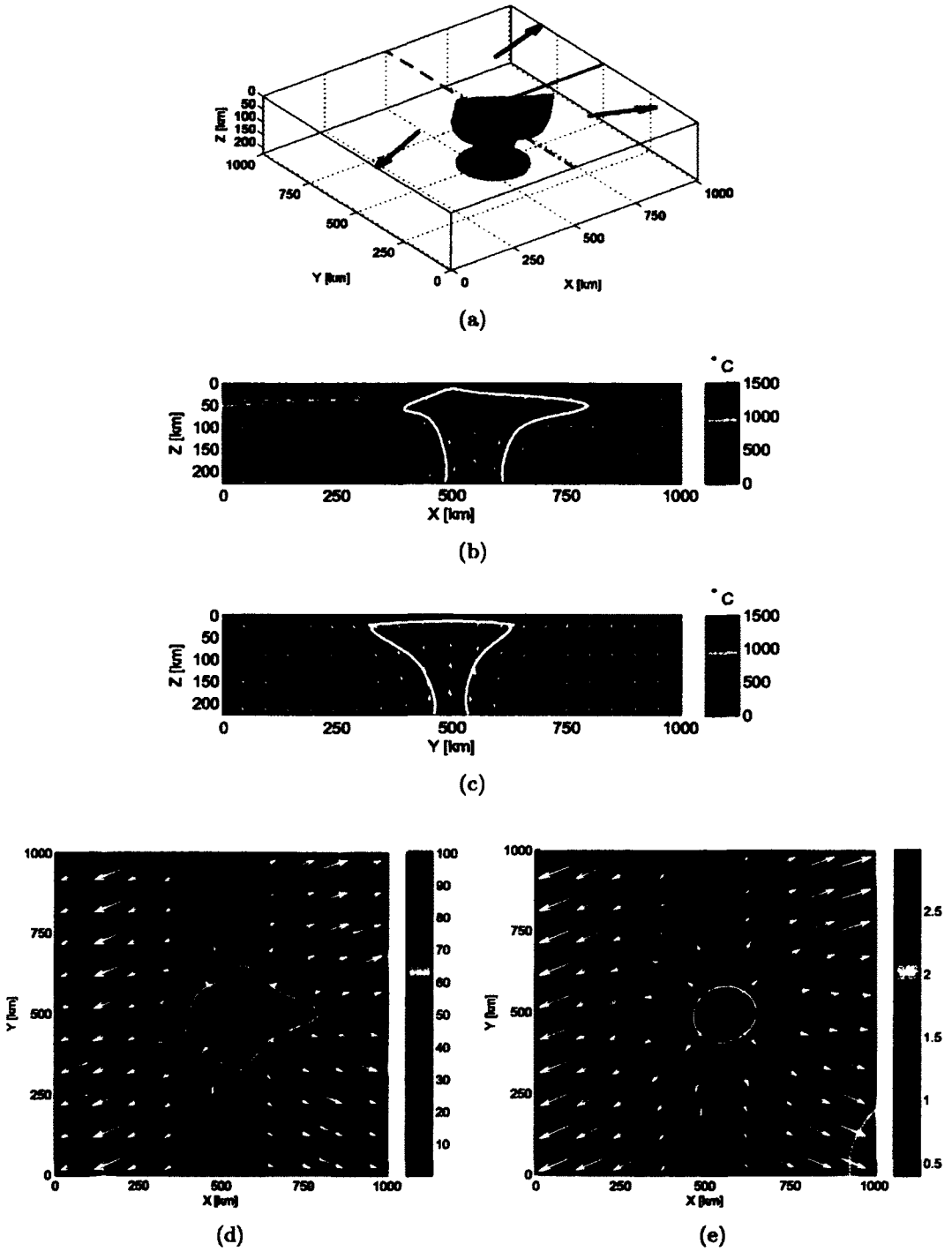

Figure 85. Results from Model 73, Table 2. See Figure 77 for details.

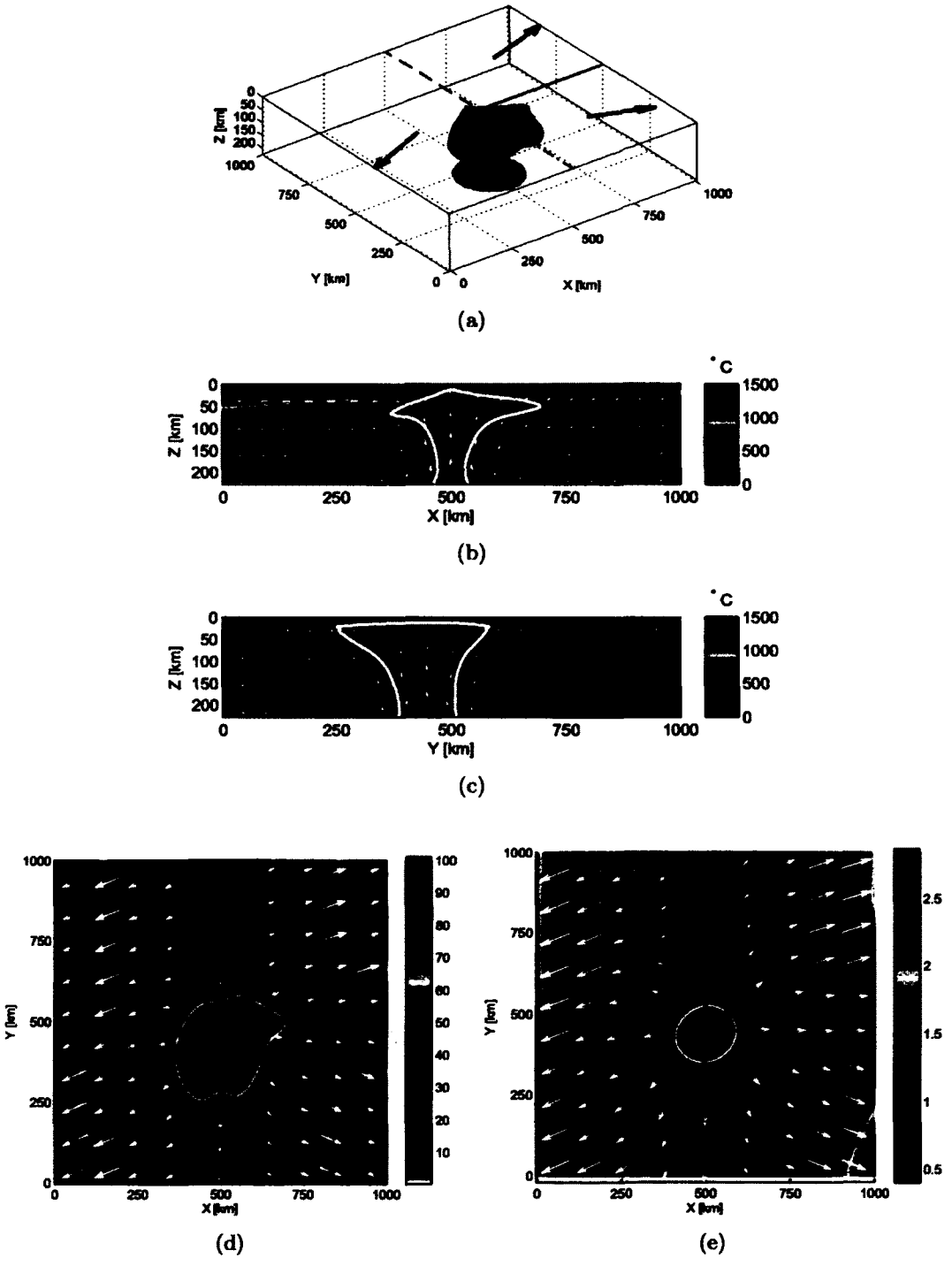

Figure 86. Results from Model 77, Table 2. See Figure 77 for details.

7.4.2 MANTLE PLUME CONTRIBUTION TO DYNAMICAL TOPOGRAPHY

The contribution of the mantle plume to the dynamical (thermal) topography along the ridges for each model from Table 2 is calculated as described above. As suggested by Equation 18, variations in dynamical topography profiles are directly proportional to the thickness of the mantle plume material underneath a given point along a ridge axis.

Figure 87 shows the thermal topography from a subset of models with the plume conduit located $100\,km$ from the triple junction and with the minimal viscosity cutoff limit $5 \times 10^{18}\,Pa\,s$, for all values of the azimuth (θ) and for runs both with and without dehydration. (The rest of the models are showing similar tends in isostatic topography and therefore will not be presented here.) The maximum value of the dynamical topography variation along the ridges is $\sim 2\,km$ (Figure 87(a), 87(c)) when the plume conduit is ridge centered (i.e., $\theta = 90°$ or $180°$). For a given ridge axis, the minimal along axis variations of dynamic topography is generally expected to result from a plume located farthest away from that ridge. For example Figure 87(b) shows that for the case with dehydration, the lowest dynamic topography along R_3 (for $x > 500\,km$) occurs with a weaker plume (smaller plume diameter) located along R_2 ($\theta = 180°$). In this case, the topographic variation is only $\sim 0.2\,km$.

The position of the peak values of dynamic topography along each of the ridge axes is related to the plume conduit location. For example, in Figure 87(a), the peaks are shifted towards greater x distances as azimuth decreases. An interesting detail can be noticed on Figure 87(a) for plumes located at $\theta = 225°$ and $\theta = 315°$. For $\theta = 315°$ plume material is flowing in the same direction as the v_3 component of passive mantle flow (Figure 72) and for $\theta = 225°$ it is flowing in the opposite direction. Dispersion of the plume material in this manner (same or opposite direction of the mantle flow) results in $\sim 0.4\,km$ difference in thermal topography (Figure 87(a)).

In general, the addition of dehydration rheology results in topographic peaks of lower amplitude and slightly greater along axis length. For example, for $\theta = 225$, Figure 87(a) without dehydration rheology shows a peak of about $\sim 100m$ higher than Figure 87(b) with dehydration. For the case of $\theta = 315°$ the influence of the plume on thermal topography along R_1 is $\sim 200\,km$ shorter when dehydration rheology is not used (Figure 87(c,d)).

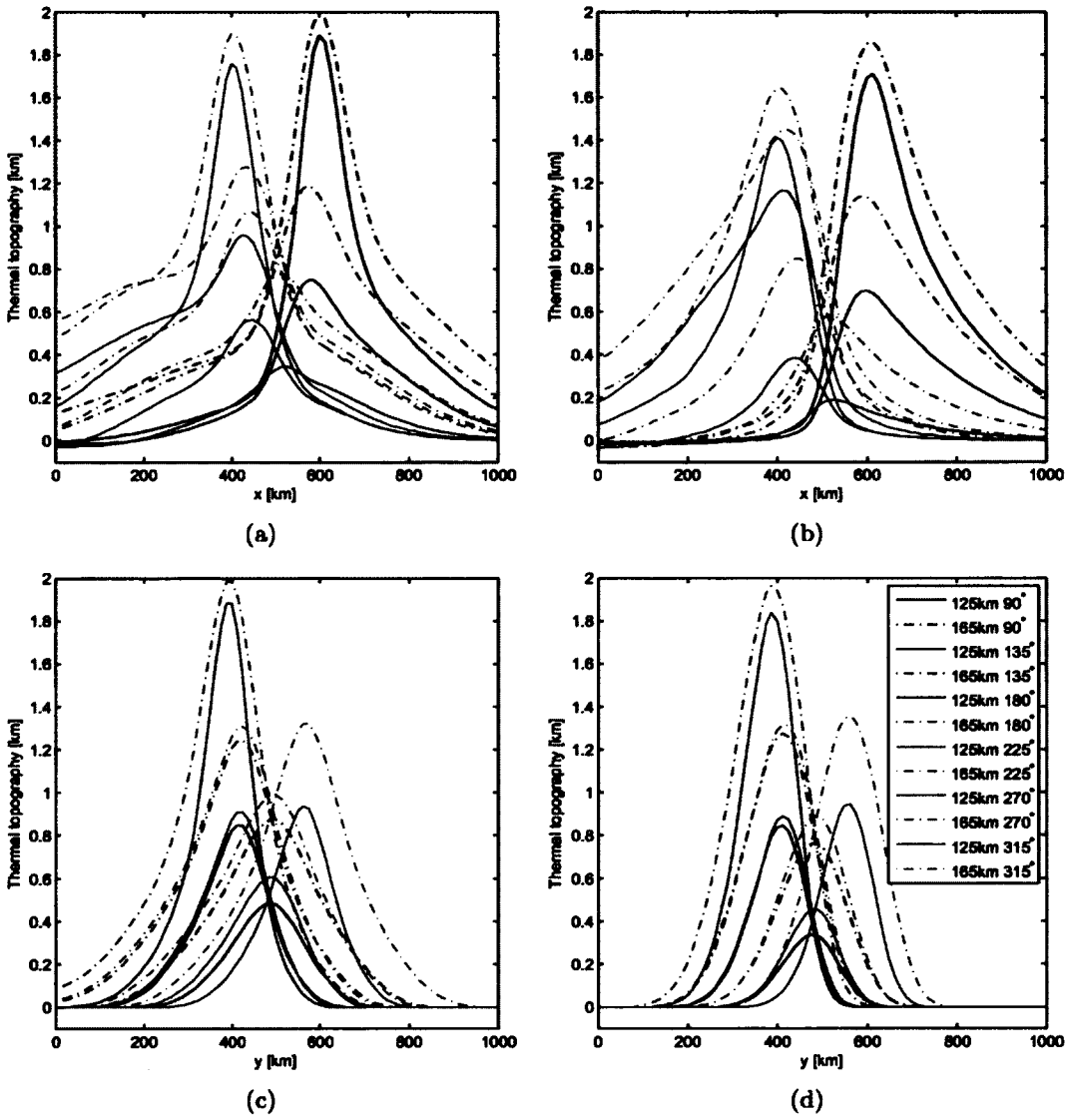

Figure 87. Dynamic topography for all models with $r = 100\,km$ and $\eta_{lmin} = 5 \times 10^{18}\,Pa\,s$. Azimuths are indicated by a common legend in (d). a) Calculated topographic variations along $y = 500\,km$. Distances greater than $x = 500\,km$ correspond to R_3. These models do not incorporate dehydration viscosity ($A = 1$) b) Same as (a) but with dehydration viscosity ($A = [1, 50]$). c) Calculated topographic variations along $x = 500\,km$ (i.e., the $R_1 - R_2$ axis). $A = 1$. d) Same as (c) with but with $A = [1, 50]$.

7.4.3 MODEL CRUSTAL THICKNESS ESTIMATION

Crustal thickness was calculated for all models in Table 2. In general, predicted crustal thickness decreases along the ridges as a function of the distance of the plume away from the triple junction and the specific location of the mantle plume (Figure 88). At distances of several hundred kilometers from the triple junction, the predicted crustal thickness for R_3 is approaches $0\,km$, which is consistent with observational data from ultra slow spreading ridges (e.g., *Dick et al.* [2003]). Along $R_1 - R_2$, crustal thicknesses are approximately $6 - 8\,km$ at large distances from the triple junction. For plume–affected lengths of the ridge axis, crustal thicknening is predicted to be significantly less when dehydration viscosisty is used compared to when viscosity is only dependent on pressure and temperature. This result is consistent with prior plume ridge interaction models that employ dehydration rheology (e.g., *Ito et al.* [1999]).

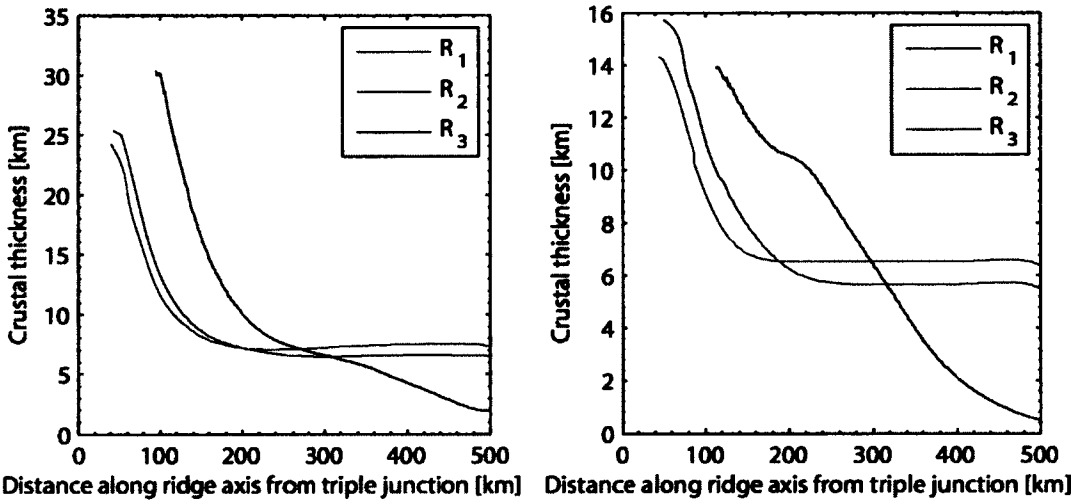

Figure 88. Crustal thickness predictions along each ridge axis as the function of distance from triple junction. Panel (a) shows results from Model 73, and panel (b) shows results from Model 109 (Table 2). These use the same plume conduit location and diameter, but in panel (a) $A = 1$ and in panel (b) $A = [1, 50]$. Figures do not plot crustal thicknesses close to the triple junction (less than $\sim 40\,km$ for R_1, R_2 and $\sim 100\,km$ for R_3) as these are undervalued because of the method chosen for the melt–ridge allocation (Figure 76). Note that the y-axes of the two panels differ.

For each model run, the maximal crustal variation along each of ridges was determined. For example, crustal thickness varies from $\sim 26\,km$ to $\sim 6\,km$ in Figure 88(a), resulting in $\sim 20\,km$ of crustal thickness variation. Figure 89 provides a summary plot.

Figures 89(a) and 89(b) show trends in the maximal crustal thickens variation along R_3. As the plume conduit changes azimuth from $\theta = 90°$ to $\theta = 270°$ maximal crustal thickness drops from $\sim 20\,km$ down to $\sim 6\,km$ (Figure 89(a)). The maximum crustal thickness variation of $\sim 21\,km$ along R_3 occurs when the plume conduit is located directly beneath it, $\theta = 90°$. In this case, the radial distance of the plume conduit from the triple junction should not significantly contribute to the maximal crustal variation. Because of the method chosen for the melt ridge allocation there is an irregularity in the magnitude of the crustal variation. Due to different treatments of rheology, without and with mantle dehydration respectively Figure 89(a) show the greater amplitudes of the variations than Figure 89(b).

Maximal crustal thickens variations along $R_1 - R_2$ and R_3 for the models with $\eta_{lmin} = 5 \times 10^{18}\,Pa\,s$ and $A = 1$ can be seen at Figure 89(c) and 89(d). The fact that difference in maximal crustal thickens variation from the plume azimuth is much more pronounced ($\sim 24\,km$) along R_3 than along $R_1 - R_2$ ($\sim 4\,km$) can be partially attributed to the way the melt is allocated to the ridge axis (Figure 76).

7.4.4 COMPARISON OF MODEL RESULTS TO THE AZORES TRIPLE JUNCTION

As discussed briefly in Section 7.2.2, excess volcanism has occurred for extended periods of geological time in the Azores region. The main portion of the Azores plateau construction started $\sim 10 - 15Ma$ [*Cannat*, 1999; *Escartin*, 2001], ending at ~ 3 to $\sim 7Ma$ depending on latitude [*Cannat*, 1999; *Escartin*, 2001]. Since this excess volcanic activity, a main process affecting the plateau has been rifting, in addition to localized volcanism in islands across the archipelago. The present day volcanoes in the Azores (Figure 70 bottom right insert) are mostly located along the Terceira Rift, with Flores and Corvo on the west side of the triple junction, about $120\,km$ from the Mid Atlantic Ridge.

As also discussed briefly in Section 7.2.2, observational data from the Azores region displays certain asymmetries with respect to the Mid Atlantic Ridge and the Terceira Rift. For example, elevated seafloor topography can be observed along most

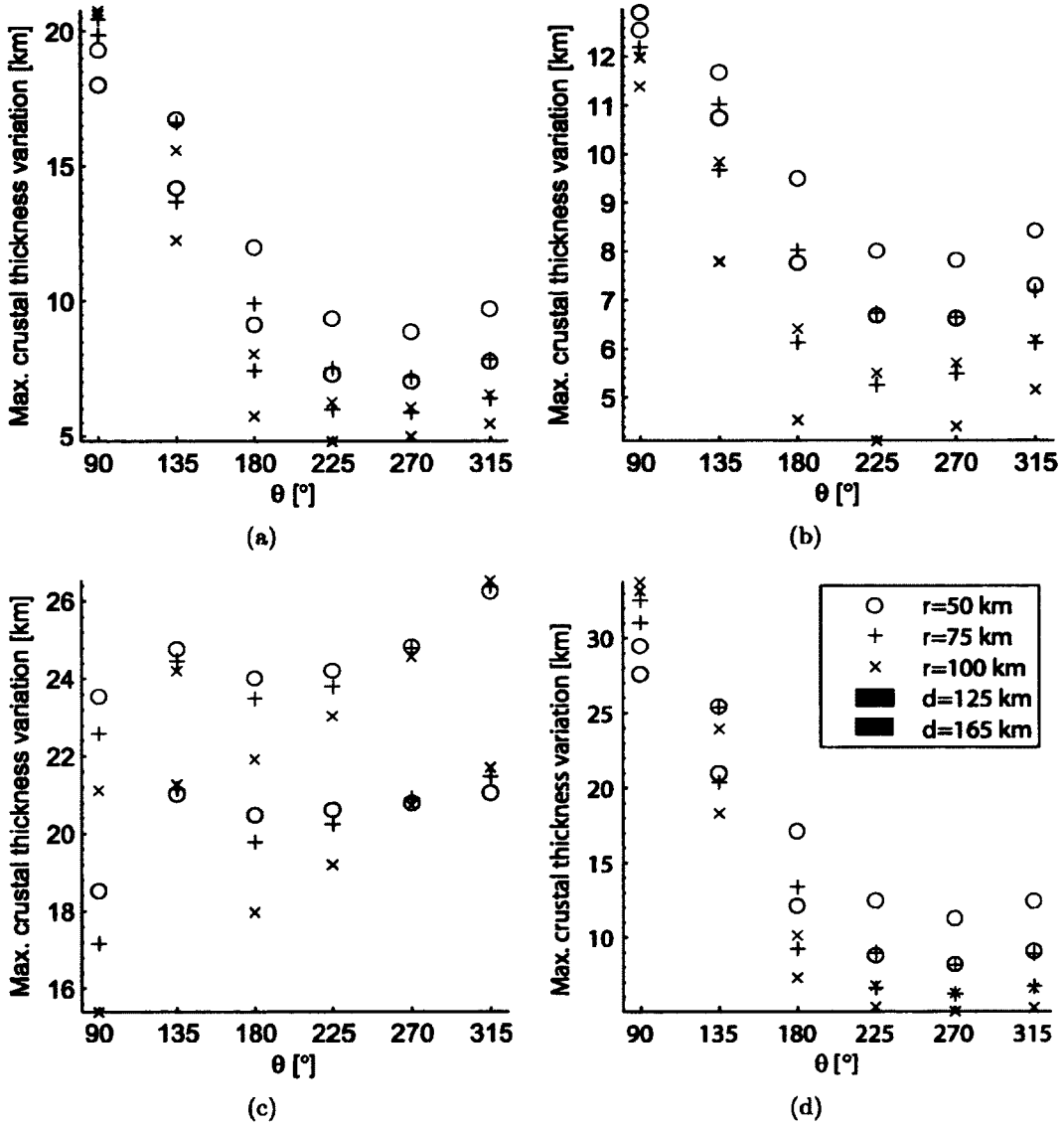

Figure 89. Maximal crustal thickens variation along various ridge axes as a function of plume conduit azimuth. Blue and red symbols indicate plume diameter (d) of 125 km and 165 km, respectively. Circle, "+" , and "x" symbols indicate the distance of the plume from the triple junction, according to the common legend in panel (d). a) Results from models along R_3 with $\eta_{min} = 1.5 \times 10^{19}\, Pa\, s$ and $A = 1$. b) Same as in panel (a) except with $A = [1, 50]$. c) Results from models along $R_1 - R_2$ with $\eta_{min} = 5 \times 10^{18}\, Pa\, s$ and $A = 1$. d) Same as in panel (c) except along R_3.

of the 550 km Terceira Rift [*Vogt and Jung*, 2004], which is not the case west of the Mid Atlantic Ridge (Figure 70 top left insert). Similar asymmetry also exists in a north-south direction about the inferred position of the mantle plume conduit, which is thought to be in the vicinity of Faial and Pico islands [*Cannat*, 1999; *Escartin*, 2001], with elevated topography extending farther toward the south than the north (Figure 70 top left insert). Gravity and geochemical data also reinforce these observations of asymmetry [*Dosso et al.*, 1993; *Detrick et al.*, 1995; *Thibaud et al.*, 1998; *Goslin*, 1999; *Maia et al.*, 2007; *Shorttle et al.*, 2010]. According to these data the maximal extent of the Azores plume effect towards the north is close to Kurchatov FZ (Figure 70), approximately 120 km from the triple junction. To the south anomalies can be observed to Atlantis FZ [*Detrick et al.*, 1995; *Thibaud et al.*, 1998] some $\sim 1500\,km$ away from the triple junction.

Crustal thicknesses for the Azores Plateau are higher than those for average oceanic crust. From surface wave dispersion measurement *Searle* [1976] calculated a crustal thickness of $\sim 8\,km$ for the central plateau. *Detrick et al.* [1995] used gravity and bathymetry data to determine crustal thicknesses of $> 8 - 9\,km$; this is likely to be the maximal estimate because all of the gravity anomaly is attributed to the crustal thickness variation (i.e., none is attributed to mantle temperature variation). Treating gravity anomaly data in similar manner, *Gente et al.* [2003] calculated crustal thickness along the Terceira Rift to be at most $5 - 10\,km$ thicker than along the Mid Atlantic Ridge, with the highest values around volcanic islands. On the other hand, from modeling of elastic plate rebound, *Luis et al.* [1998] calculated mean crustal thickness for the Azores region of about $10 - 12\,km$.

Comparison of the numerical models to general spatial patterns in seafloor anomalies, crustal thickness variations, and the distribution of present-day volcanism across the islands of the Azores archipelago indicates that some models are less likely than others to explain the geodynamics of plume-triple junction interaction in this setting. For example, models for which azimuth of the plume conduit was not between 90° and 180° do not seem to reproduce the long wavelength bathymetry of the plateau. Also, models with the plume located at 90° produce crustal thicknesses higher than observed. Additionally, models for which the plumes is located along R_3, 100 km away from the triple junction seem unlikely to be able to reproduce volcanism at Flores and Corvo islands.

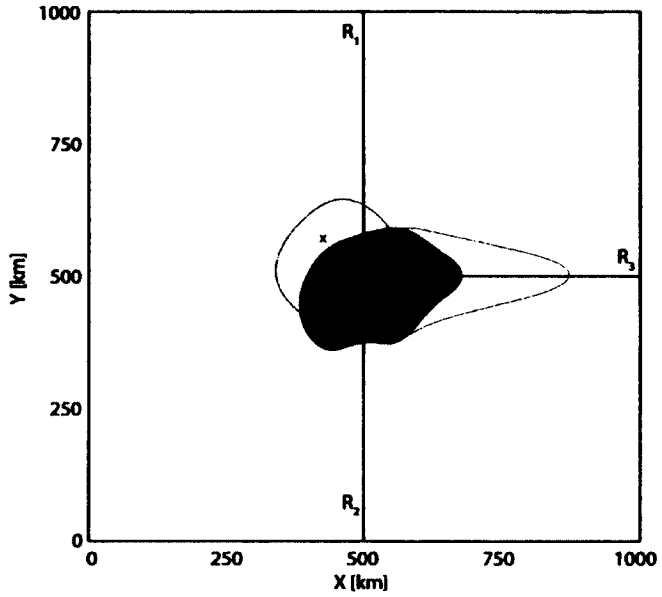

Figure 90. Horizontal slice of the model domain at 50 km depth, showing the areal dispersion of a plume with diameter 125 km for different positions of the plume stem. Green filled shape is the area occupied by plume material (defined as $T > 1395\,°C$) when the plume is located beneath the triple junction. Red and blue contours define the areal dispersion of plume material from Models 25 and 35 (Table 2), respectively, with "x" symbols indicating the location of the plume conduit center on the bottom of the model domain.

7.4.5 INFLUENCE OF THE TRIPLE JUNCTION ON PLUME MATERIAL DISPERSAL

One way of exploring the influence of the triple junction on the dispersion of the plume material is to compare the suite of models in Table 2 to corresponding cases where the plume is located beneath the triple junction (Figure 90). To accomplish this, the areal dispersion of each plume was calculated at a depth of 50 km (i.e., within the zone of partial melting), assuming that the plume is defined by temperatures greater than $1395\,°C$. This area was then normalized to the areal dispersion of a plume with corresponding properties (i.e., diameter, minimum viscosity, and value of the dehydration parameter A), but located beneath the triple junction.

The normalized area of the non triple junction centered plumes depends on the plume volume flux (Q), the azimuth of the plume, and the distance of the plume from

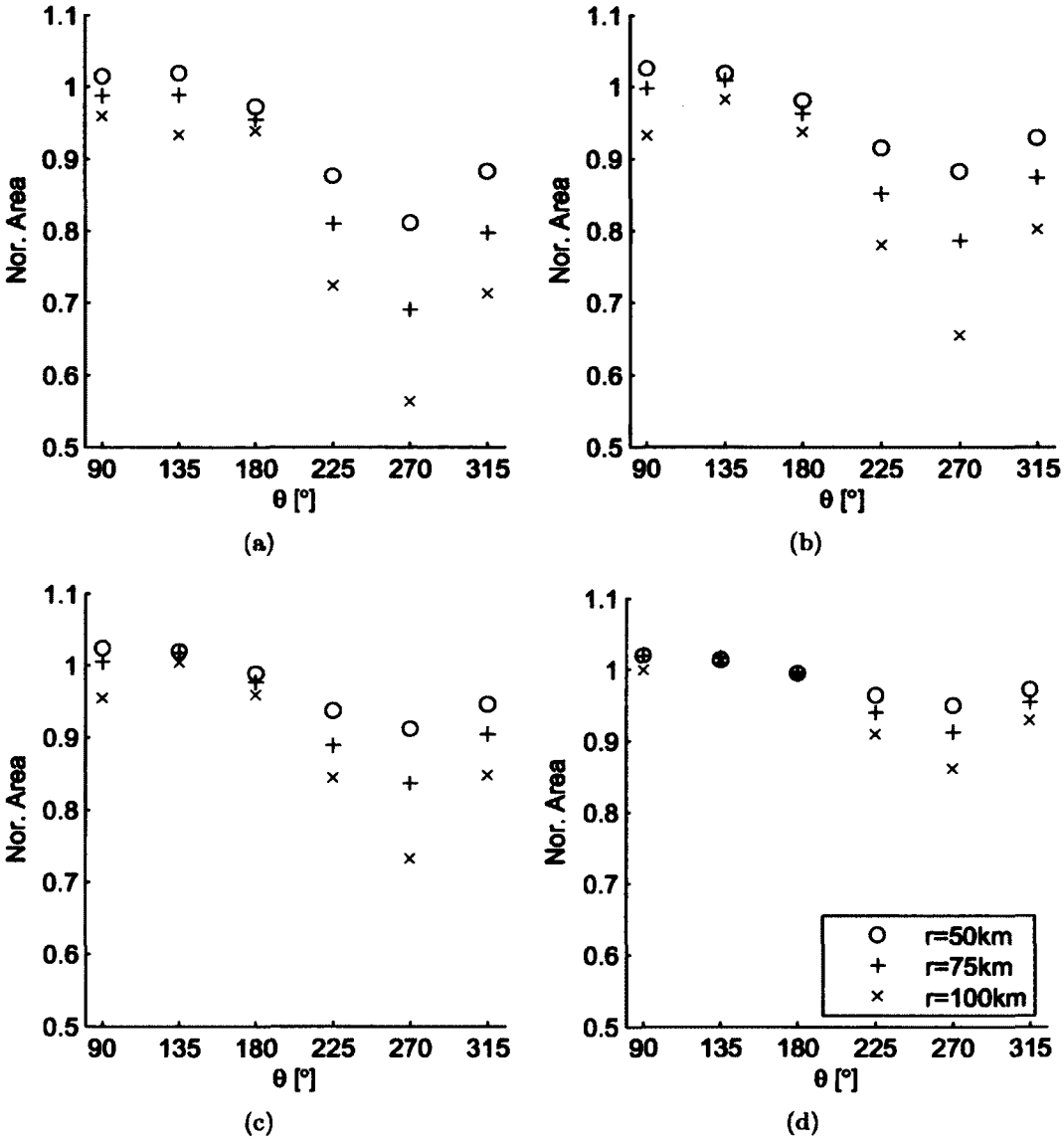

Figure 91. Normalized area of the plume at $50\,km$ depth to the case of the plume located beneath triple junction as the function of the azimuth of the plume's location relative to R_1. Different symbols for data points represent different radial distances of the plume conduit from the triple junction as indicated in legend (Figure 91(d)). Results obtained using runs from Table 2 with following parameters: a) $d = 125\,km$, $\eta_{min} = 1.5 \times 10^{19}\,Pa\,s$; b) $d = 165\,km$, $\eta_{min} = 1.5 \times 10^{19}\,Pa\,s$; c) $d = 125\,km$, $\eta_{min} = 5 \times 10^{18}\,Pa\,s$ and d) $d = 165\,km$, $\eta_{min} = 5 \times 10^{18}\,Pa\,s$

the triple junction (Figure 23). With plume strength increasing from Figure 91(a) to 91(b) and Figure 91(c) to 91(d), two trends can be observed: weaker dependence of the normalized area on the azimuth, and weaker dependence of the normalized area on the radial distance of the plume conduit. For example, Figure 91(a) and 91(b) for $\theta = 270°$ and $r = 50\,km$ have normalized area of ~ 0.8 and ~ 0.9 respectively. Figure 91(c) and 91(d) for $\theta = 270°$ show difference in normalized area between $r = 50\,km$ and $r = 100\,km$ of ~ 0.1.

If R_3 were not present, models with the plume located at $\theta = 270°$ and $\theta = 90°$ should be advected in a similar quantitative and qualitative manner because of comparable R_1 and R_2 spreading rates (components u_1 and u_3 in Figure 72). In this scenario, plume up–slope flow along the thickening lithosphere would occupy the same horizontal area. The presence of R_3 changes the shape of the lithosphere asthenosphere boundary around the triple junction, resulting in larger plume area. For cases where dehydration viscosity is not used (i.e., $A = 1$), plumes that are located under R_3 tend to be channeled along axis not only because of the large slope of the lithosphere, but also because of relatively low viscosity as a function of hydrostatic pressure and temperature (Equation 15). This also explains the smaller sensitivity of the normalized plume area to radial distance of the plume conduit from the triple junction for the $\theta = 90°$ cases, compared to the $\theta = 270°$ cases.

An example of the application of the methodology behind Figure 91 to a geologic setting, at least in a qualitative sense, could involve Shatsky Rise. Shatsky Rise is oceanic plateau located in the northwest Pacific, covering an area of $4.8 \times 10^5\,km^2$ [*Nakanishi et al.*, 1999] similar to the area of Spain. The convergence of three magnetic isochron lineation groups indicates that the rise as formed at a triple junction that was largely in ridge–ridge–ridge configuration [*Nakanishi et al.*, 1989]. The large size of the rise suggests that a mantle plume was involved in its formation [*Nakanishi et al.*, 1989]. Additionally, magnetic anomalies and isotopic data suggest a short duration of emplacement with large magma eruption rate [*Sager and Han*, 1993; *Mahoney et al.*, 2005]. Shatsky Rise contains three masssifs, with the age and size of the massifs decreasing from Tamu Massif in the southwest, to ORI Massif in the central portion of the plateau, to Shirshov Massif in the northeast [*Sager and Han*, 1993]. This sequence of massifs could be associated with the consecutive jumps of Pacific-Izanagi-Farallon triple junction [*Sager et al.*, 1988; *Nakanishi et al.*, 1999] following the location of the mantle plume. Although this modeling study focused on spreading

rates appropriate to the Azores plateau (i.e., ultraslow to slow values), a similar suite of models could be calculated for Shatsky Rise, which had rates in the intermediate to fast range [*Sager et al.*, 1988]. Properties of the relatively unconstrained plume and mantle viscosity structure during Shatsky Rise formation could be constrained by comparing calculated reductions in plume spatial extent to observed decreases in massif area, as determined from bathymetry, seismic, and magnetic data.

7.4.6 SCALING LAWS FOR PLUME–TRIPLE JUNCTION INTERACTION COMPARED TO PLUME–RIDGE INTERACTION

The primary goal of this section is to relate quantitatively the influence of the slower spreading ridge (R_3), as well as plume and triple junction geometry factors (Q, u, θ), to waist width (W) . Figure 92 shows total waist width (i.e., $W = W_1 + W_2 + W_3$, or the the sum of the waist widths along each of the three ridge axes) as a function of the fundamental length scale of plume ridge interaction (W_0), for $\theta = 90°$ and $\theta = 270°$. For both plume azimuths, there is a linear relationship between W and W_0. For $\theta = 90°$, there is low vertical scattering of data points belonging to the group with the same model parameters (η_{min}, A, d) and different radial distances (r) of the plume conduit from triple junction. However, for $\theta = 270°$, the scattering is significantly more pronounced. This can be partially accounted for by the asymmetric divergence vectors of the surface plates (Figure 72) and therefore different amounts of plume material reaching R_1, R_2 and R_3. The general drop of the total waist width for $\theta = 270°$ as opposed to $\theta = 90°$ is the result of the physical location of the plume conduit relative to R_3 and the definition of the waist width.

Figure 93 shows total waist widths defined in several different ways as a function of B_n, buoyancy number [*Feighner and Richards*, 1995] (Equation 2). Results from *Ito et al.* [1997] are plotted for comparison. For cases where $\theta = 180°$ (i.e., a ridge centered plume), waist widths as defined as $W = W_1 + W_2$ follow the trend from *Ito et al.* [1997]. In contrast, the contribution from triple junction geometry, (i.e., the presence of R_3) is seen as elevated values of W when $W = W_1 + W_2 + W_3$. Overall, Figures 92 and 93 suggest that the dynamical interactions between a plume and a triple junction may best be explored by treating triple junction as a single spreading ridge and by defining waist width as a sum of the waist width from R_1 and R_2, disregarding R_3. This also facilitates comparison of plume triple junction interaction models to earlier studies addressing the interaction of a plume with a

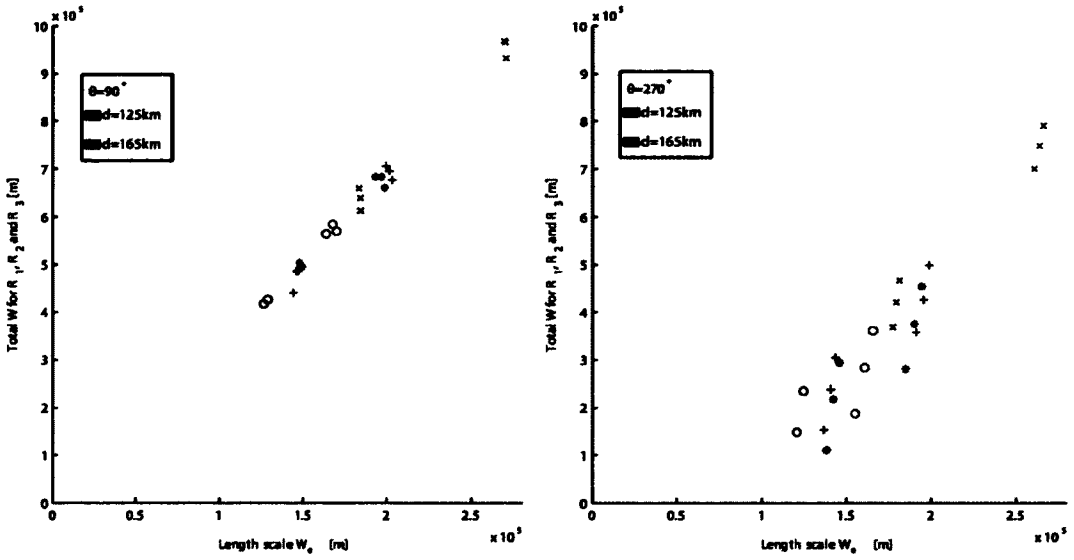

(a) (b)

Figure 92. Total waist width $W = W_1 + W_2 + W_3$ as the function of the W_0 length scale. In panel a) plume azimuth 90°, and in panel b) plume azimuth 270°. Red and blue symbols represent plumes with diameters of 165 km and 125 km respectively. Symbols are: + ($\eta_{min} = 1.5 \times 10^{19}\, Pa\, s$; $A = 1$), o ($\eta_{min} = 1.5 \times 10^{19}\, Pa\, s$; $A = [1, 50]$), x ($\eta_{min} = 5 \times 10^{18}\, Pa\, s$; $A = 1$), * ($\eta_{min} = 5 \times 10^{18}\, Pa\, s$; $A = [1, 50]$). All radial distances ($r = 50, 75, 100\, km$) of the plume conduit from triple junction are plotted with same color, same symbol.

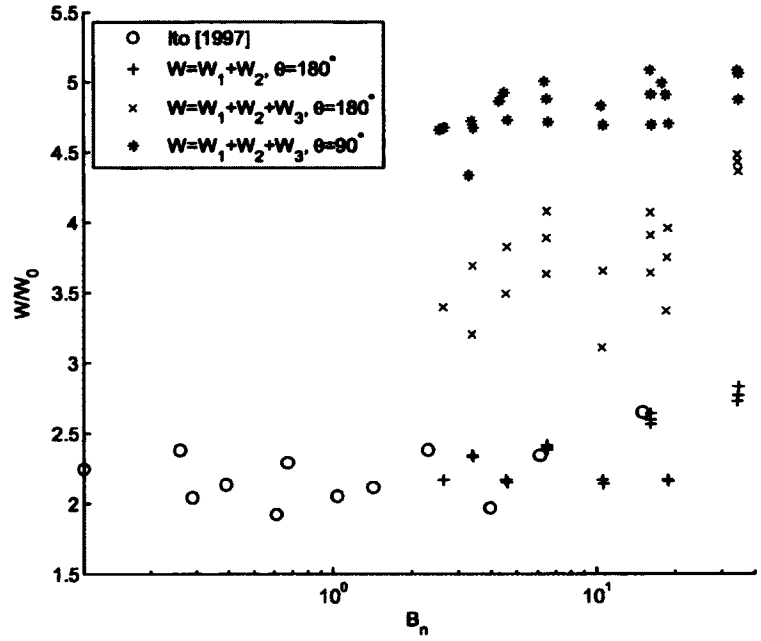

Figure 93. Normalized waist width as a function of buoyancy number for several different definitions of waist width, and for two azimuths of the plume conduit. Blue circles show data from *Ito et al.* [1997], a single ridge study, for comparison.

single ridge.

From earlier studies [*Ribe*, 1996; *Ito et al.*, 1997], the form of the functional dependence of waist width to resolve is:

$$W = W_0 F_1(B_n) F_3 \left(\frac{x_p}{W_0 F_2(B_n, \gamma)} \right) \tag{22}$$

with $W_0 = \sqrt{Q/U}$ is the length scale, x_p/W_0 is the scale of plume ridge separation distance, B_n buoyancy number [*Feighner and Richards*, 1995] (Equation 2), γ is the ratio of ambient to plume viscosity at a reference depth and F_1, F_2, F_3 are the functions to be determined. In case of $\eta_{min} = 1.5 \times 10^{19}\ Pa\,s$, the minimal ambient viscosity is equal to the minimum plume cutoff viscosity. Thus, $\gamma = 1$. For $\eta_{min} = 5 \times 10^{18}\ Pa\,s\ \gamma = 2$.

For the case of the R_1, R_2 centered plume (i.e., $x_p = 0$), from Equation 22 can be determined that $F_3 = 1$. By rearranging terms in Equation 22 and writing it as $F_1(B_n) = W/W_0$ we can plot this functional dependance and find its power–dependent relationship Figure 94. By doing a polynomial fit similar to *Ribe* [1996]

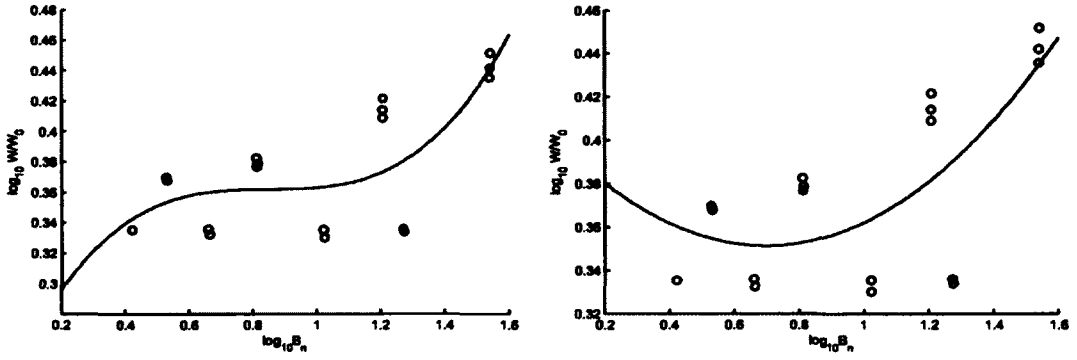

(a) (b)

Figure 94. Logarithmic plot of normalized waist width ($W = W_1 + W_2$) as a function of buoyancy number for the case $x_p = 0$ (or, more specifically, all the models from Table 2 with an azimuth of 180°). a) Solid black line is the best fit cubic polynomial fit representing F_1, with $R^2 = 0.5352$. b) Solid black line is the best fit square polynomial representing F_1, with $R^2 = 0.4944$.

and *Ito et al.* [1997], F_1 is calculated as:

$$log_{10}(F_1) = 0.2135 + 0.5213p - 0.6114p^2 + 0.2396p^3 \tag{23}$$

$$log_{10}(F_1) = 0.4084 - 0.1638p + 0.1176p^2 \tag{24}$$

where $p = log_{10}(B_n)$. For a third–order polynomial fit, $R^2 = 0.5352$ (Figure 94(a)), and for a second–order fit, $R^2 = 0.4944$ (94(b)).

For the case of when the plume is located off axis, (i.e., $x_p \neq 0$) waist width W depends on the separation distance as:

$$F_3 = \frac{W}{W(x_p = 0)} = \sqrt{1 - c_1 \left(\frac{x_p}{W_0 F_2}\right)^2} \tag{25}$$

where c_1 is fitting coefficient and F_2 is stretching function [*Ribe*, 1996; *Ito et al.*, 1997].

Case with $\gamma = 1$ have a shorter distance of plume ridge interaction as opposed to those with $\gamma = 2$ (Figure 95(a)). Increasing the value of γ as well B_n results in extended connectivity of the plume ridge system. The stretching function collapses the $\gamma = 2$ curve onto the $\gamma = 1$ curve. The stretching function is expressed in the same manner as *Ito et al.* [1997] with power dependence upon buoyancy number and

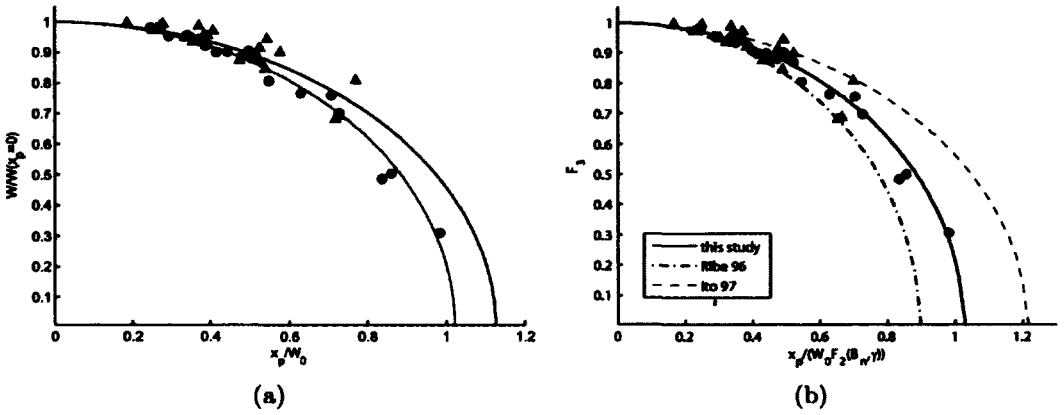

Figure 95. a) Waist width as a sum along R_1 and R_2 scaled by waist width when plume is ridge centered, as a function of the plume ridge distance x_p scaled by W_0. Red circles and blue triangles represent $\gamma = 1$ and $\gamma = 2$ respectively. Best fit lines are based on Equation 25: red line for $\gamma = 1$ ($R^2 = 0.97$) and blue line for $\gamma = 2$ ($R^2 = 0.79$). b) As for (a) but with applied stretching function. Solid blue line shows this study's F_3 function ($R^2 = 0.94$), dashed red line shows that of *Ito et al.* [1997] and dot dashed black line shows that of *Ribe* [1996].

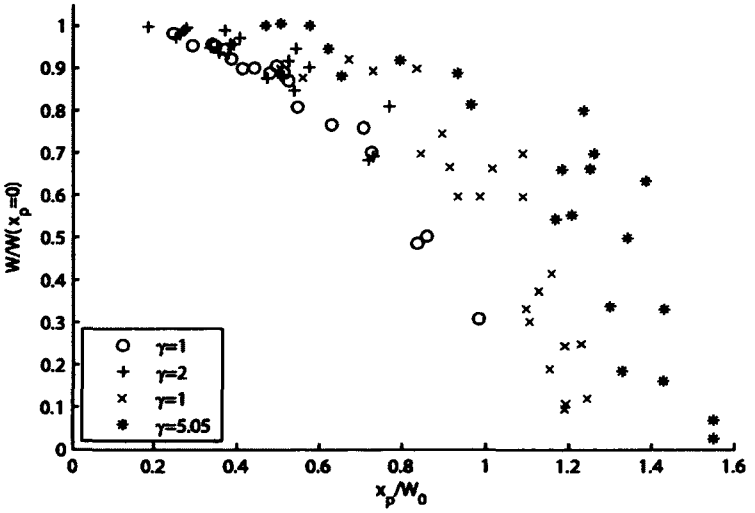

Figure 96. Waist width as a sum along R_1 and R_2 scaled by the width when the plume is centered beneath triple junction as a function of the plume ridge distance separation x_p scaled by W_0. Data points in light blue star and red x for $\gamma = 1$ and $\gamma = 5.05$ are taken from *Ito et al.* [1997] for comparison.

γ:

$$F_2 = B_n^{c_2}\gamma^{c_3} \tag{26}$$

Coefficient c_1 (Equation 25) is obtained as the best fit value for $\gamma = 1$ in Figure 95(a) and c_2 and c_3 are calculated as optimization parameters while applying stretching function (Equation 26) in Equation 25 and minimizing the best fit error. Values for the coefficient are $c_1 = 0.954$, $c_2 = 0.0027$ and $c_3 = 0.127$.

Finally, by setting $F_3 = 0$ in Equation 23 and solving for x it is possible to obtained the maximal distance of plume ridge interaction:

$$x_{max} = 1.024 W_0 F_2 \tag{27}$$

The portion of the plume material reaching $R_1 - R_2$ for plume x_p away from the ridge, assuming that the plume material is equally distributed to either side of the ridge when plume is located on the ridge axis and that linearly decreases with x_p to zero at x_{max} is:

$$Q_r = (0.50 - 0.48\frac{x_p}{W_0 F_2})Q \tag{28}$$

As with any other scaling law in the nature, the purpose of the above analysis is to provide a means of estimating a system's unknowns from observable data. For example, in the case of the plume located underneath a ridge axis, from measuring the waist width of the plume and knowing the spreading rate, one could deduce the plume volume flux. The analysis done in this section shows how the presence of the triple junction would change existing scaling laws from the single ridge case.

7.5 CONCLUSION

This study presents a parameter space investigation using a three-dimensional numerical model simulating the interaction of a mantle plume and a ridge-ridge-ridge triple junction. The main conclusions of this study are:

1. There is a strong dependence of plume dispersion on the parameters: azimuth of the plume conduit relative to R_1 (θ), radial distance of the plume conduit from the triple junction (r), dehydration parameter (A), and plume conduit diameter (d). The effects of using dehydration and non dehydration in mantle rheology were consistent with the previous studies [*Ito et al.*, 1999; *Hall and Kincaid*, 2003].

2. Within the suite of models, some solutions were less consistent with observational data from the Azores triple junction setting. For example, models with the plume located along R_3 at a distance of $100\,km$ away from the triple junction are unlikely to be able to reproduce volcanism at Flores and Corvo islands to the west of the Mid-Atlantic Ridge.

3. Scaling laws derived from the interaction of a mantle plume with a single ridge can be applied to triple junction-plume interaction.

CHAPTER 8

CONCLUSIONS

This study is focused on visualizing and numerical modeling of plate tectonics and plume dynamics. Creating visualizations for a subduction zone is particularly interesting in the case of Tonga because of the complex history of trench rollback there. Plate-plume interaction is visualized for the case of the Artemis structure on Venus. Visualization of static and kinematic interaction for the Hawaiian plume beneath the Pacific plate is also presented. Finally the framework for web–based multi–user field trips and activities is laid down that will enable all the visualization material mentioned above to be widely available for instruction. IRB-compliant data gathered from student interactions in multi–user field trips, are serving as learning outcomes assessments.

Using data mining from published studies and GeoMapApp (http://www.geomapapp.org) led to creation of COLLADA models. These models highlighted the questions about tectonic history of the Tonga region. The complex geological setting of the Tonga region inspired development of a number of animated COLLADA models that explain current formation hypotheses. The purpose of these models is to produce critical and creative thinking in the end user as well as to make a connection between kinematics and relevant observational data in the model. In the process of creating these instructional models new possibilities about the formation of the Tonga region emerged and thus, interconnected pedagogy and research.

Google Earth provides the capabilities for exploration of the Moon and Mars but not Venus or other bodies. As Venus hosts one of our solar system's super plumes, Artemis, we created a Venus virtual globe by draping Magellan SARS imagery over the Google Earth terrain. Google Venus provides a new and engaging means to explore Earth's sister planet, with lessons for the tectonics of both Venus and Earth. Digital exploration allows students and researchers to appreciate a wide range of spatial relationships on the surface and in the interior, and in three-dimensions at a truly global scale in a way not previously possible. Study of plume-plate interaction on Venus can help our understanding of plume-plate interaction on the Earth.

Similarly as for the Tonga region, I created animated COLADA models of the Pacific plate interacting with the Hawaiian deep mantle plume. The primary purpose of the model is to illustrate to students the origins of volcanism far away from the plate boundaries as well as to make a link between plate motion and the time progression in the volcanic tracks. Making the 3D model of the deep mantle plume from seismic data created the possibility to compare experiences of students learning from pictographic representation versus real data. Because of the peculiar shape of the deep mantle plume conduit it was concluded that it preserved a record of Pacific plate movement. The deflection measured from the model were in the general agreement with the prediction of studies.

Creating teaching materials highlighted a need for better organization and modular usage while enabling simultaneous multi user interactions. To satisfy this need, we created a client server client communication framework as well as improvements in the user interface for web based Google Earth. With the development of new Internet technologies we went over several iterations of the above framework constantly advancing its capabilities. This enabled us and other developers to create rich, more interactive and engaging learning experiences. Virtual field trips exercises and tools such as Lahar, Puerto Rico, and Colorado are already implemented using this framework. Large scale testing for functionality and classroom usability as well as for teaching productivity have already been conducted and preliminary results do look promising.

Another component of this research involved extensive numerical simulations (about 8000 hours of CPU time) of the interactions of a mantle plume and a plate boundary triple junction, to better understand the dynamics of upper mantle convection. A parameter space exploration yielded insight into how the presence of the triple junction influences mantle plume dispersion patterns. The development of scaling laws for plume-triple junction interaction allows the results of this study to be extended to other settings with similar ridge geometry.

BIBLIOGRAPHY

Albers, M., and U. R. Christensen (2001), Channeling of plume flow beneath mid-ocean ridges, *Earth Planet. Sci. Lett.*, *187*(1-2), 207 220.

Anderson, D. L. (1995), Lithosphere, asthenosphere, and perisphere, *Rev. Geophys.*, *33*(1), 125 149.

Arnaud, R., and M. C. Barnes (2006), *COLLADA: sailing the gulf of 3D digital content creation*, A.K. Peters.

Asimow, P. D., M. M. Hirschmann, and E. M. Stolper (2001), Calculation of peridotite partial melting from thermodynamic models of minerals and melts, IV. Adiabatic decompression and the composition and mean properties of mid-ocean ridge basalts, *J. Petrol.*, *42*(5), 963 998.

Banerdt, W. B., G. E. McGill, and M. T. Zuber (1997), Plains tectonics on Venus, in *Venus II: Geology, Geophysics, Atmosphere, and Solar Wind Environment*, edited by S. W. Bouger, D. M. Hunten, and R. J. Phillips, pp. 901 930, University of Arizona Press, Tucson, AZ.

Bannister, R. A., United States National Aeronautics, and Space Administration, and V. L. Hansen (2010), Geologic map of the Artemis Chasma quadrangle (V-48), Venus.

Basilevsky, A. T., and J. W. Head (2002), Venus: Timing and rates of geologic activity, *Geology*, *30*(11), 1015 1018.

Bjonnes, E. E., V. L. Hansen, B. James, and J. B. Swenson (2012), Equilibrium resurfacing of Venus: Results from new Monte Carlo, modeling and implications for Venus surface histories, *Icarus*, *217*(2), 451 461.

Bonnardota, M. A., M. Régniera, C. Christovab, C. E. Ruellana, and E. Tric (2009), Seismological evidence for a slab detachment in the Tonga subduction zone, *Tectonophysics*, *464*(1-4), 84 99.

Bown, J. W., and R. S. White (1994), Variation with spreading rate of oceanic crustal thickness and geochemistry, *Earth Planet. Sci. Lett.*, *121*(3), 435 449.

Braun, M. G., G. Hirth, and E. M. Parmentier (2000), The efects of deep damp melting on mantle fow and melt generation beneath mid-ocean ridges, *Earth Planet. Sci. Lett.*, *176*, 339 356.

Brickhouse, N. W. (1990), Teachers' beliefs about the nature of science and their relationship to classroom practice, *J. Teacher Edu.*, *41*(3), 53 62.

Bridges, N. T. (1995), Submarine analogs to Venusian pancake domes, *Geophys. Res. Lett.*, *22*(2), 2781 2784.

Bridges, N. T. (1997), Ambient effects on basalt and rhyolite lavas under Venusian, subaerial, and subaqueous conditions, *J. Geophys. Res.: Planets*, *102*(E4), 9243 9255.

Bridgman, P. W. (1931), Dimensional analisys, in *Dimensional analisys*, p. 113, Yale University Press, New Haven, Conn.

Brooks, W., and D. G. De Paor (2009), Construction and presentation of Google Earth models for undergraduate education, *Geological Society of America Abstracts with Programs*, *47*(7), 92.

Brooks, W. D., M. M. Dordevic, and D. G. De Paor (2010), Exploring planets and moons using Google Earth to convey a sense of place, scale, and time.

Brown, C., and R. E. Grimm (1995), Tectonics of Artemis Chasma: A Venusian "plate" boundary, *Icarus*, *117*(2), 219 249.

Brown, C. D., and R. E. Grimm (1996), Lithospheric rheology and flexure at Artemis Chasma, Venus, *J. Geophys. Res.: Planets*, *101*(E5), 12,697 12,708.

Buckley, B. C., J. Gobert, P. Horwitz, and L. O'Dwyer (2010), Looking inside the black box: Assessments and decision-making in biologica, *Int. J. Learning Technologies*, *5*(2).

Bullock, M. A., and D. H. Grinspoon (2001), The recent evolution of climate on Venus, *Icarus*, *150*(1), 19 37.

Bullock, M. A., D. H. Grinspoon, and J. W. Head (1993), Venus resurfacing rates: Constraints provided by 3-D Monte Carlo simulations, *Geophys. Res. Lett.*, *20*(19), 2147 2150.

Butler, D. (2006), Virtual globes: the web-wide world, *Nature*, *439*, 776 778.

Campbell, I. H., and R. W. Griffiths (1990), Implications of mantle plume structure for the evolution of flood basalts, *Earth Planet. Sci. Lett.*, *99*(1-2), 79 93.

Canales, J. P., G. Ito, R. S. Detrick, J. Sinton, T. Blacic, M. Behn, and J. Lin (2000), Origin of the Galapagos swell: bathymetry, gravity, and seismic constraints along the Galapagos spreading center, *Eos, Trans. Amer. Geophys. Union*, *81*.

Cannat, M. (1999), Mid-Atlantic ridge-Azores hotspot interactions along-axis migration of a hotspot-derived event of enhanced magmatism 10 to 4 ma, *Earth Planet. Sci. Lett.*, *173*, 257 269.

Chapple, W. M., and T. E. Tullis (1977), Evaluation of the forces that drive the plates, *J. Geophys. Res.*, *82*(14), 1967 1984.

Chase, C. (1978), Extension behind island arcs and motions relative to hot spots, *J. Geophys. Res.*, *83*(B11), 5385 5387.

Coffin, M. F., and O. Eldholm (1993), Scratching the surface: Estimating dimensions of large igneous provinces, *Geology*, *21*(6), 515 518.

Coffin, M. F., and O. Eldholm (1994), Large igneous provinces: crustal structure, dimensions, and external consequences, *Rev. Geophys.*, *32*(1), 1 36.

Coffin, M. F., and L. M. Gahagan (1995), Ontong Java and Kerguelen plateaux: Cretaceous icelands?, *J. Geol. Soc. (London, U. K.)*, *152*, 1047 1052.

Coffin, M. F., O. Eldholm, et al. (2005), Large igneous provinces, *Encyclopedia of Geology. Elsevier, Oxford*, pp. 315 323.

Coffin, M. F., et al. (2006), Large igneous provinces and scientific ocean drilling: Status quo and a look ahead, *Oceanography*, *19*(4), 150 160.

Courtillot, V., A. Davaille, J. Besse, and J. Stock (2003), Three distinct types of hotspots in the Earth's mantle, *Earth Planet. Sci. Lett.*, *205*, 295 308.

Crumpler, L. S., J. C. Aubele, D. A. Senske, S. T. Keddie, K. P. Magee, and J. W. Head (1997), Volcanoes and centers of volcanism on Venus, in *Venus II Geology, Geophysics, Atmosphere, and Solar Wind Environment*, edited by S. W. Bouger,

D. M. Hunten, and R. J. Phillips, pp. 697 756, The University of Arizona Press, Tucson, AZ.

Cruz, D., and S. D. Zellers (2006), Effectiveness of Google Earth in the study of geologic landforms, Geological Society of America, Abstracts with Programs.

De Paor, D. G. (2007a), The world is (almost) round: An introduction to Google Earth science, *Front Matter Technovations*, *1*(1), 10 11.

De Paor, D. G. (2007b), Embedding Collada models in geo-browser visualizations: A powerful tool for geological research and teaching, *Eos Trans. AGU*, *88*(52), IN32A 08.

De Paor, D. G. (2008a), Enhanced visualization of seismic focal mechanisms and centroid moment tensors using solid models, surface bump-outs, and Google Earth, *J. Virtual Explorer*, *29*.

De Paor, D. G. (2008b), Using Google SketchUp with Google Earth for scientific applications, Google Tech Talk.

De Paor, D. G. (2008c), How would you move mount Fuji — and why would you want to?, American Geophysical Union Annual Meeting.

De Paor, D. G. (2011a), Google Earth: Visualizing the possibilities for geoscience education and research, Geological Society of America Penrose Meeting.

De Paor, D. G. (2011b), Future implementation strategies for using Google Earth for geoscience education and presentation, Geological Society of America Penrose Meeting.

De Paor, D. G., and A. Pinan-Llamas (2006), Application of novel presentation techniques to a structural and metamorphic map of the Pampean orogenic belt, Northwest Argentina, *Geological Society of America Abstracts with Programs*, *38*(7), 326.

De Paor, D. G., and S. J. Whitmeyer (2008), Collaborative research: Enhancing the geoscience curriculum using geobrowsers-based learning objects, Proposal NSF-CLLI #0837040.

De Paor, D. G., and S. J. Whitmeyer (2010), Geological and geophysical modeling on virtual globes using KML, COLLADA, and Javascript, *Comput. Geosci.*, *37*, 100 110.

De Paor, D. G., and S. J. Whitmeyer (2011), Transforming undergraduate geoscience education with an innovative Google Earth-based curriculum, American Geophysical Union Fall Meeting.

De Paor, D. G., and N. Williams (2006), Solid modeling of moment tensor solutions and temporal aftershock sequences for the Kiholo Bay earthquake using Google Earth with a surface bump-out, *Eos Trans. AGU*, *87*(52), S53E 05.

De Paor, D. G., D. C. Bradley, G. E. Eisenstadt, and S. M. Phillips (1989), The Arctic Eurekan orogen a most unusual fold and thrust belt, *Geol. Soc. Am. Bull.*, *101*, 952 967.

De Paor, D. G., J. Daniels, and I. Tyagi (2007), Five geo-browser lesson plans, *Eos Trans. AGU*, *88*, IN43A 0904.

De Paor, D. G., S. J. Whitmeyer, and J. Gobert (2008a), Emergent models for teaching Geology and Geophysics using Google Earth, American Geophysical Union Annual Meeting.

De Paor, D. G., S. J. Whitmayer, and J. Gobert. (2008b), Emergent models for teaching geology and geophysics using Google Earth., in *Transaction, American Geophysical Union.*

De Paor, D. G., W. Brooks, M. M. Dordevic, N. Ranashinge, and S. C. Wild (2009), Visualizing the 2009 Samoan and Sumatran earthquakes using Google Earth-based COLLADA models, *Eos Trans. AGU*, *90*(52), U13E 2088.

De Paor, D. G., S. Whitemeyer, and G. Watson-Papelis (2010), Collaborative research: Virtual 4D field education in Google Earth, NSF-GEO #1034643.

De Paor, D. G., S. C. Wild, and M. M. Dordevic (2012a), Emergent and animated COLLADA models of the Tonga trench and Samoa archipelago: Implications for geosciences modeling, education, and research, *Geosphere*, *8*(2), 491 506.

De Paor, D. G., S. C. Wild, and M. M. Dordevic (2012b), Movie, http://www.lions.odu.edu/org/planetarium/steve/GS/Movies/movie1.wmv Last accessed 07/10/2013.

De Paor, D. G., S. C. Wild, and M. M. Dordevic (2012c), Movie, http://www.lions.odu.edu/org/planetarium/steve/GS/Movies/movie2.mov Last accessed 07/10/2013.

De Paor, D. G., S. C. Wild, and M. M. Dordevic (2012d), Movie, http://www.lions.odu.edu/org/planetarium/steve/GS/Movies/movie3.wmv Last accessed 07/10/2013.

De Paor, D. G., V. L. Hansen, and M. M. Dordevic (2012e), Google Venus, *Spec. Pap. - Geol. Soc. Am.*, *492*, 367 382.

DeMets, C., R. G. Gordon, D. F. Argus, and S. Stein (1990), Current plate motions, *Geophysical Journal International*, *101*(2), 425 478.

Detrick, R. S., H. D. Needham, and V. Renard (1995), Gravity anomalies and crustal thickness variations along the Mid-Atlantic Ridge between 33°N and 40°N, *J. Geophys. Res.: Solid Earth*, *100*(B3), 3767 3787.

Detrick, R. S., et al. (2002), Correlated geophysical, geochemical, and volcanological manifestations of plume-ridge interaction along the Galapagos spreading center, *Geochem., Geophys., Geosyst.*, *3*.

Dick, H. J. B., J. Lin, and H. Schouten (2003), An ultraslow-spreading class of ocean ridge, *Nature*, *426*(6965), 405 412.

Digital-Planet (2011), Earth's interior, Website, http://www.digitalplanet.org/DigitalPlanet/$New-June$.html, Last accessed 07/10/2013.

Donahue, T. M., and C. T. Russell (1997), The Venus atmosphere and ionosphere and their interaction with the solar wind: An overview, in *Venus II: Geology, Geophysics, Atmosphere, and Solar Wind Environment*, edited by S. W. Bouger, D. M. Hunten, and R. J. Phillips, pp. 3 31, University of Arizona Press, Tucson, AZ.

Donahue, T. M., D. H. Grinspoon, R. E. Hartle, and R. R. Hodges (1997), Ion/neutral escape of hydrogen and deuterium: Evolution of water, in *Venus II: Geology, Geophysics, Atmosphere, and Solar Wind Environment*, edited by S. W. Bouger, D. M. Hunten, and R. J. Phillips, pp. 385 414, University of Arizona Press, Tucson, AZ.

Dordevic, M. M. (2012), Designing interactive screen overlays to enhance effectiveness of Google Earth geoscience resources, in *Google Earth and Virtual Visualizations in Geoscience Education and Research: Geological Society of America Special Paper 492*, edited by S. Whitmeyer, J. Bailey, D. De Paor, and T. Ornduff, chap. 7, Geological Society of America.

Dordevic, M. M., and S. C. Wild (2012), Avatars and multi-student interactions in Google Earth - based field experiences, in *Google Earth and Virtual Visualizations in Geoscience Education and Research: Geological Society of America Special Paper 492*, edited by S. Whitmeyer, J. Bailey, D. De Paor, and T. Ornduff, chap. 35, Geological Society of America.

Dordevic, M. M., D. G. De Paor, and S. J. Whitmeyer (2009), Understanding volcanism on terrestrial planets and moons using virtual globes and COLLADA models, *Geological Society of America Abstracts with Programs*, *41*(7), 260.

Dordevic, M. M., D. G. De Paor, S. J. WHITMEYER, and M. R. Beebe (2010), Animated COLLADA models and virtual field trips featuring volcanism in various tectonic settings on planet Earth and other rocky planets and moons, in *2010 GSA Denver Annual Meeting*.

Dordevic, M. M., D. G. De Paor, S. J. Whitmeyer, and M. R. Beebe (2011), Animated COLLADA models and virtual field trips featuring volcanism in various tectonic settings on planet Earth and other rocky planets and moons, *Geological Society of America Abstracts with Programs*, *42*(5), 420.

Dosso, L., H. Bougault, and J.-L. Joron (1993), Geochemical morphology of the North Mid-Atlantic Ridge, 10°-24°N: Trace element-isotope complementarity, *Earth Planet. Sci. Lett.*, *120*(3-4), 443 462.

Durand-Manterola, H. J. (2010), Superrotation on Venus: Driven by waves generated by dissipation of the transterminator flow, *arXiv preprint arXiv:1005.3488*.

Escartin, J. (2001), Crustal thickness of V-shaped ridges south of the Azores interaction of the mid-Atlantic ridge (36-39N) and the Azores hot spot, *J. Geophys. Res.*, *106*, 21,719 21 735.

Feighner, M. A., and M. A. Richards (1995), The fluid dynamics of plume-ridge and plume-plate interactions: An experimental investigation, *Earth Planet. Sci. Lett.*, *129*(1-4), 171 182.

Ford, J. P., J. J. Plaut, C. M. Weitz, T. G. Farr, D. A. Senske, E. R. Stofan, G. Michaels, and . Parker, T. J. (1993), *Guide to Magellan Image Interpretation*, National Aeronautics and Space Administration Jet Propulsion Laboratory Publication.

Forsyth, D., and S. Uyeda (1975), On the relative importance of the driving forces of plate motion, *Geophys. J. Int.*, *43*(1), 163 200.

Foucher, J. P. (1982), The ocean-continent transition in the uniform lithospheric stretching model: Role of partial melting in the mantle [and discussion]., *Phil. Trans. R. Soc. A*, *305*, 27 43.

Frohlich, C. (1989), The nature of deep-focus earthquakes, *Ann. Rev. Earth Planet. Sci.*, *17*, 277 54.

Garrett, J. J. (2011), Ajax: A new approach to web applications, Website, http://www.adaptivepath.com/ideas/ajax-new-approach-web-applications, Last accessed 07/10/2013.

Gente, P., J. Dyment, M. Maia, and J. Goslin (2003), Interaction between the Mid-Atlantic Ridge and the Azores hot spot during the last 85 Myr: Emplacement and rifting of the hot spot-derived plateaus, *Geochem., Geophys., Geosyst.*, *4*(10).

GeoMapApp, M. S. D. S. (2012), Explore our planet with GeoMapApp, Website, http://www.geomapapp.org, Last accessed 07/10/2013.

Georgen, J. E. (2008), Mantle flow and melting beneath oceanic ridge-ridge-ridge triple junctions, *Earth Planet. Sci. Lett.*, *270*, 231 240.

Georgen, J. E. (2011), Lithospheric control on the spatial pattern of Azores hotspot seafloor anomalies: Constraints from a model of plume-triple junction interaction, *Geophys. Res. Lett.*, *38*(L19305).

Georgen, J. E., and J. Lin (2002), Three-dimensional passive flow and temperature structure beneath oceanic ridge-ridge-ridge triple junctions, *Earth Planet. Sci. Lett.*, *204*(1-2), 115 132.

Georgen, J. E., and R. Sankar (2010), Effects of ridge geometry on mantle dynamics in an oceanic triple junction region. Implications for the Azores Plateau, *Earth Planet. Sci. Lett.*, *298*(1-2), 23 34.

German, C. R., E. T. Baker, D. P. Connelly, J. E. Lupton, J. Resing, S. L. Prien, R. D. Walker, H. N. Edmonds, and C. H. Langmuir (2006), Hydrothermal exploration of the Fonualei rift and spreading center and the North East Lau spreading center, *Geochem. Geophys. Geosyst.*, *7*, Q11,022.

GIMP (2011), GIMP 2.6, Website, www.gimp.org, Last accessed 07/10/2013.

Gobert, J. (2000), A typology of models for plate tectonics: Inferential power and barriers to understanding, *Int. J. Sci. Edu.*, *22*(9), 937 977.

Gobert, J. (2005), Leveraging technology and cognitive theory on visualization to promote students' science learning and literacy, in *Visualization in Science Education*, edited by J. Gilbert, pp. 73 90, Springer-Verlag Publishers.

Gobert, J., S. C. Wild, and L. Rossi (2012), Testing the effects of prior coursework and gender on geoscience learning with Google Earth, in *Google Earth and Virtual Visualizations in Geoscience Education and Research: Geological Society of America Special Paper 492*, edited by S. J. Whitmeyer, J. E. Bailey, D. G. De Paor, and T. Ornduff, chap. 22, Geological Society of America.

Goodchild, M. F. (2006), The fourth R: rethinking GIS education, *ArcNews*, *28*(3), 1.

Goodchild, M. F. (2008), The use cases of digital Earth, *Int. J. Digital Earth*, *1*(1), 31 42.

Google (a), Google Earth plug-in, Website, http://earth.google.com/support/bin/answer.py?hl=en$\&$answer=176145, Last accessed 07/10/2013.

Google (b), What is Google Earth?, Website, http://www.google.com/earth/explore/products/plugin.html, Last accessed 07/10/2013.

Google (-a), Making Iframe-Shimmed content overlaid over the GE plug-in transparent?, Website, https://groups.google.com/forum/#!topic/google-earth-browser-plugin/86XqE5hP2OI, Last accessed 07/10/2013.

Google (-b), Point placemarks-draggable placemark, Website, http://code.google.com/apis/ajax/playground/?exp=earth#draggable_placemark, Last accessed 07/10/2013.

Google (-c), KmlScreenOverlay interface reference, Website, http://code.google.com/apis/earth/documentation/reference/interface_kml_screen_overlay.html, Last accessed 07/10/2013.

Gordon, R. G., A. Cox, and C. E. Harter (1978), Absolute motion of an individual plate estimated from its ridge and trench boundaries, *Nature*, *274*(5673), 752 755.

Goslin, J. (1999), Extent of Azores plume influence on the Mid-Atlantic Ridge north of the hotspot, *Geology*, *27*(11), 991 994.

Griffiths, R. W., and I. H. Campbell (1991), Interaction of mantle plume heads with the Earth's surface and onset of small-scale convection, *J. Geophys. Res.: Solid Earth*, *96*(B11), 18,295 18,310.

Griffiths, R. W., and M. A. Richards (1989), The adjustment of mantle plumes to changes in plate motion, *Geophys. Res. Lett.*, *16*(5), 437 440.

Grimm, R. E., and P. C. Hess (1997), The crust of Venus, in *Venus II: Geology, Geophysics, Atmosphere, and Solar Wind Environment*, vol. 1, edited by S. W. Bouger, D. M. Hunten, and R. J. Phillips, p. 1205.

GSI (2004), Estimation of Pacific plate motion by GPS, Website, http://cais.gsi.go.jp/Virtual_GSI/Tectonics/Pacific_GPS/index.html, Last accessed 07/10/2013.

Gudmundsson, O., and M. Sambridge (1998), A regionalized upper mantle (RUM) seismic model, *J. Geophys. Res.*, *130*(B4), 7121 7136.

Guest, J. E., and E. R. Stofan (1999), A new view of the stratigraphic history of Venus, *Icarus*, *139*(1), 55 66.

Hall, P. S., and C. Kincaid (2003), Melting, dehydration, and the dynamics of off-axis plume-ridge interaction, *Geochem. Geophys. Geosyst.*, *4*(9), 1 19.

Hall-Wallace, M. K., and C. M. McAuliffe (2002), Design, implementation, and evaluation of GIS-based learning materials in an introductory geoscience course, *J. Sci. Edu.*, *50*, 5 14.

Hamilton, W. B. (2005), Plumeless Venus preserves an ancient impact-accretionary surface, *Spec. Pap. - Geol. Soc. Am.*, *388*, 781 814.

Handelsman, J., et al. (2004), Scientific teaching, *Science*, *23*, 521 522.

Hansen, V. L. (2002), Artemis: Surface expression of a deep mantle plume on Venus, *Geol. Soc. Am. Bull.*, *114*(7), 839 848.

Hansen, V. L. (2006), Geologic constraints on crustal plateau surface histories, Venus: The lava pond and bolide impact hypotheses, *J. Geophys. Res.: Planets (1991-2012)*, *111*(E11).

Hansen, V. L., and I. López (2010), Venus records a rich early history, *Geology*, *38*(4), 311 314.

Hansen, V. L., and A. Olive (2010), Artemis, Venus: The largest tectonomagmatic feature in the solar system?, *Geology*, *38*(5), 467 470.

Hansen, V. L., and R. J. Phillips (1995), Formation of Ishtar Terra, Venus: Surface and gravity constraints, *Geology*, *23*(4), 292 296.

Hansen, V. L., and D. A. Young (2007), Venus's evolution: A synthesis, in *Convergent Margin Terranes and Associated Regions: A Tribute to W.G. Ernst*, edited by M. Cloos, W. D. Carlson, M. C. Gilbert, J. G. Liou, and S. S. Sorensen, pp. 255 273, Geological Society of America, Denver.

Hansen, V. L., J. J. Willis, and W. B. Banerdt (1997), Tectonic overview and synthesis, in *Venus II: Geology, Geophysics, Atmosphere, and Solar Wind Environment*, edited by S. W. Bouger, D. M. Hunten, and R. J. Phillips, pp. 797 844, University of Arizona Press, Tucson, AZ.

Hart, S. R., M. Coetzee, R. A. Workman, J. Blusztajn, K. T. M. Johnson, J. M. Sinton, B. Steinberger, and J. W. Hawkins (2004), Genesis of the Western Samoa seamount province: age, geochemical fingerprint and tectonics, *Earth Planet. Sci. Lett.*, *227*(3-4), 37 56.

Herrick, R. R., V. L. Sharpton, M. C. Malin, S. N. Lyons, and K. Feely (1997), Morphology and morphometry of impact craters, in *Venus II: Geology, Geophysics, Atmosphere, and Solar Wind Environment*, edited by S. W. Bouger, D. M. Hunten, and R. J. Phillips, pp. 1015 1046, University of Arizona Press, Tucson, AZ.

Hickson, I. (2012), Html5, Website, http://dev.w3.org/html5/spec/Overview.html, Last accessed 07/10/2013.

Hirth, G., and D. L. Kohlstedt (1995), Experimental constraints on the dynamics of the partially molten upper mantle: 2. Deformation in the dislocation creep regime, *J. Geophys. Res.: Solid Earth*, *100*(B8), 15,441 15,449.

Holt, W. E. (1995), Flow fields within the Tonga slab determined from the moment tensors of deep earthquakes, *Geophys. Res. Lett.*, *22*(8), 989 992.

Horwitz, P., J. Gobert, B. Buckley, and L. O'Dwyer (2010), Learning genetics with dragons: From computer-based manipulatives to hypermodels, in *Designs for learning environments of the future: International perspectives from the learning sciences.*, edited by M. J. Jacobson and P. Reimann, Springer Publishers.

Hunten, D. M. (2002), Exospheres and planetary escape, in *Atmospheres in the Solar System: Comparative Aeronomy AGU Geophysical Monograph*, edited by M. Mendillo, A. Nagy, and J. H. Waite, pp. 1015 1046, University of Arizona Press, Tucson, AZ.

Isacks, B., J. Oliver, and L. R. Sykes (1968), Seismology and the new global tectonics, *J. Geophys. Res.*, *73*(18), 229 246.

Ito, G., and J. Lin (1995a), Oceanic spreading center-hotspot interactions: Constraints from along-isochron bathymetric and gravity anomalies, *Geology*, *23*(18), 657 660.

Ito, G., J. Lin, and C. W. Gable (1996), Dynamics of mantle flow and melting at a ridge-centered hotspot: Iceland and the Mid-Atlantic Ridge, *Earth Planet. Sci. Lett.*, *144*(1-2), 53 74.

Ito, G., J. Lin, and C. Gable (1997), Interaction of mantle plumes and migrating mid-ocean ridges implications for the Galapagos plume-ridge system, *J. Geophys. Res.*, *102*(15), 403 17,417.

Ito, G., Y. Shen, G. Hirth, and C. J. Wolfe (1999), Mantle flow, melting, and dehydration of the Iceland mantle plume, *Earth Planet. Sci. Lett.*, *165*(1), 81 96.

Ito, G., J. Lin, and D. Graham (2003), Observational and theoretical studies of the dynamics of mantle plume-mid-ocean ridge interaction, *Rev. Geophys.*, *41*(41).

Ito, G. T., and J. Lin (1995b), Mantle temperature anomalies along the past and paleoaxes of the Galápagos spreading center as inferred from gravity analyses, *J. Geophys. Res.*, *100*(B3), 3733 3745.

Ivanov, M. A., and J. W. Head (1996), Tessera terrain on Venus: A survey of the global distribution, characteristics, and relation to surrounding units from Magellan data, *J. Geophys. Res.*, *101*(E6), 14,861 14.

Izenberg, N. R., R. E. Arvidson, and R. J. Phillips (1994), Impact crater degradation on Venusian plains, *Geophys. Res. Lett.*, *21*(4), 289 292.

Jacobson, M. J., and P. Reimann (Eds.) (2010), *Designs for learning environments of the future: International perspectives from the learning sciences*, Springer Publishers.

Jenkins, A., M. Healey, and R. Zetter (2007), Linking teaching and research in disciplines and departments, *York: Higher Education Academy.*

json (1999), Introducing JSON, Website, http://www.json.org/, Last accessed 07/10/2013.

Kali, Y., N. Orion, and E. Mazor (1997), Software for assisting high school students in the spatial perception of geological structures, *J. Sci. Edu.*, *45*, 10 21.

Karig, D. E. (1974), Evolution of arc systems in the Western Pacific, *Ann. Rev. Earth Planet. Sci.*, *2*, 51 78.

Kerrick, D. M., and J. A. D. Connolly (2001), Metamorphic devolatilization of subducted marine sediments and the transport of volatiles into the Earth's mantle, *Nature*, *411*(6835), 293 296.

Kincaid, C., and P. Olson (1987), An experimental study of subduction and slab migration, *J. Geophys. Res.*, *92*, 13,832 13,840.

King, J. (-), How to cover an IE windowed control (select box, ActiveX Object, etc.) with a DHTML layer, Website, http://www.macridesweb.com/oltest/IframeShim.html, Last accessed 07/10/2013.

Klein, E. M., and C. H. Langmuir (1987), Global correlations of ocean ridge basalt chemistry with axial depth and crustal thickness, *J. Geophys. Res.: Solid Earth (1978-2012)*, *92*(B8), 8089 8115.

Koppers, A. A. P., H. Staudigel, M. S. Pringle, and J. R. Wijbrans (2003), Short-lived and discontinuous intraplate volcanism in the south pacific: Hot spots or extensional volcanism?, *Geochem. Geophys. Geosyst.*, *4*(4), 1 49.

Kreemer, C. (2009), Absolute plate motions constrained by shear wave splitting orientations with implications for hot spot motions and mantle flow, *J. Geophys. Res.*, *114*.

Lawver, L. A., and J. W. Hawkins (1978), Diffuse magnetic anomalies in marginal basins: their possible tectonic and petrologic significance, *Tectonophysics*, *45*, 323 968.

Lay, T., C. J. Ammon, H. Kanamori, L. Rivera, K. D. Koper, and A. R. Hutko (2010), The 2009 Samoa-Tonga great earthquake triggered doublet, *Nature*, *466*, 964 968.

Lebonnois, S., et al. (2006), Venus atmospheric dynamics from VIRTIS on Venus express-preliminary results, in *European Planetary Science Congress 2006*, vol. 1, p. 424.

Libarkin, J. C. (2001), Development of an assessment of student conception of the nature of science, *J. Sci. Edu.*, *49*(5), 435 442.

Lopez, I. (2011), Embayed intermediate volcanoes on Venus: Implications for the evolution of the volcanic plains, *Icarus*, *213*(1), 73 85.

Luis, J. F., and J. M. Miranda (2008), Reevaluation of magnetic chrons in the North Atlantic between 35°N and 47°N: Implications for the formation of the Azores Triple Junction and associated plateau, *J. Geophys. Res.: Solid Earth*, *113*(B10).

Luis, J. F., J. M. Miranda, A. Galdeano, P. Patriat, J. C. Rossignol, and L. Mendes-Victor (1994), The Azores triple junction evolution since 10 ma from an aeromagnetic survey of the Mid-Atlantic Ridge, *Earth Planet. Sci. Lett.*, *125*(1-4), 439 459.

Luis, J. F., J. M. Miranda, A. Galdeano, and P. Patriat (1998), Constraints on the structure of the Azores spreading center from gravity data, *Mar. Geophys. Res.*, *20*(157-170), 157 170.

Lupton, J. E., D. G. Pyle, W. J. Jenkins, R. Greene, and L. Evans (2003), Evidence for an extensive hydrothermal plume in the Tonga-Fiji region of the south Pacific, *Geochem. Geophys. Geosyst.*, *5*.

Lvova, E. V. (2010), Mantle plume tectonics: The evolution of the main ideas, *Moscow Univ. Geol. Bull. (Engl. Transl.)*, *65*, 283 288.

Mackwell, S. J., M. E. Zimmerman, and D. L. Kohlstedt (1998), High-temperature deformation of dry diabase with application to tectonics on Venus, *J. Geophys. Res.: Solid Earth (1978-2012)*, *103*(B1), 975 984.

Mahoney, J., R. Duncan, M. Tejada, W. Sager, and T. Bralower (2005), Jurassic-Cretaceous boundary age and mid-ocean-ridge-type mantle source for Shatsky Rise, *Geology*, *33*(3), 185 188.

Mahoney, J. J., and K. J. Spencer (1991), Isotopic evidence for the origin of the Manihiki and Ontong Java oceanic plateaus, *Earth and Planet. Sci. Lett.*, *104*, 196 210.

Maia, M., J. Goslin, and P. Gente (2007), Evolution of the accretion processes along the Mid-Atlantic Ridge north of the Azores since 5.5 Ma: An insight into the interactions between the ridge and the plume, *Geochem., Geophys., Geosyst.*, *8*(3).

Martin, D. J., and R. Treves (2008), Visualizing geographic data in Google Earth for education and outreach, Abstract, American Geophysical Union.

Mc Donald, T. B., and D. G. De Paor (2008), Above Google Earth: Teaching and research applications of geobrowsers in atmospheric and ionospheric studies, *Geological Society of America Abstracts with Programs*, *40*(2), 9.

McDougall, I. (2010), Age of volcanism and its migration in the Samoa islands, *Geological Magazine, 147*, 705 717.

Mckenzie, D., and W. J. Morgan (1969), Evolution of triple junctions, *Nature, 224*, 122 133.

McKenzie, D., P. G. Ford, C. Johnson, B. Parsons, D. Sandwell, S. Saunders, and S. C. Solomon (1992), Features on Venus generated by plate boundary processes, *J. Geophys. Res., 97*(E8), 13,533 13,544.

McKenzie, D. P., and M. Bickle (1988), The volume and composition of melt generated by extension of the lithosphere, *J. Petrol, 25*, 625 679.

McKinnon, W. B., K. J. Zahnle, B. A. Ivanov, and H. J. Melosh (1997), Cratering on Venus: Models and observations, in *Venus II: Geology, Geophysics, Atmosphere, and Solar Wind Environment*, edited by S. W. Bouger, D. M. Hunten, and R. J. Phillips, pp. 969 1014, University of Arizona Press, Tucson, AZ.

Mitchell, N. C., and L. M. Parson (1993), The tectonic evolution of the Indian Ocean Triple Junction, anomaly 6 to present, *J. Geophys. Res., 98*, 1793 1812.

Montelli, R., G. Nolet, F. A. Dahlen, and G. Masters (2006), A catalogue of deep mantle plumes: New results from finite-frequency tomography, *Geochem., Geophys., Geosyst., 7*(11).

Moores, E. M., and R. J. Twiss (1995), *Tectonics*, W. H. Freeman and Company.

Morgan, J. P. (1971), Convection plumes in the lower mantle, *Nature, 230*, 42 43.

Morgan, W., and D. Rodriguez (1978), A second type of hotspot island, *J. Geophys. Res., 83*, 5355 5360.

Morgan, W. J. (1972), Deep mantle convection plumes and plate tectonics, *AAPG Bulletin, 56.*

Morgan, W. J. (1981), Hotspot tracks and the opening of the Atlantic and Indian Oceans, in *The Sea, ideas and observations on progress in the study of the seas*, vol. 7, edited by C. Emiliani, chap. 13, pp. 443 487, Interscience Publishers, New York.

Muller, R. D., M. Sdrolias, C. Gaina, and W. R. Roest (2008), Age, spreading rates and spreading symmetry of the world's ocean crust, *Geochem. Geophys. Geosyst.*, *9*.

Mussett, A. E., and M. A. Khan (2008), *Looking into the Earth: An introduction to Geological Geophysics*, Cambridge University Press.

Mutter, J. C., W. R. Buck, and C. M. Zehnder (1988), Convective partial melting: 1. A model for the formation of thick basaltic sequences during the initiation of spreading, *J. Geophys. Res., [Solid Earth and Planets]*, *93*(B2), 1031 1048.

Nakanishi, M., K. Tamaki, and K. Kobayashi (1989), Mesozoic magnetic anomaly lineations and seafloor spreading history of the northwestern Pacific, *J. Geophys. Res.: Solid Earth*, *94*(B11), 15,437 15,462.

Nakanishi, M., W. W. Sager, and A. Klaus (1999), Magnetic lineations within Shatsky Rise, northwest Pacific Ocean: Implications for hot spot-triple junction interaction and oceanic plateau formation, *J. Geophys. Res.: Solid Earth (1978-2012)*, *104*(B4), 7539 7556.

NASA (2005), untitled, Website, http://www.nasa.gov/images/content/136215main_BMarbleStill.jpg, Last accessed 07/10/2013.

Nimmo, F., and D. McKenzie (1998), Volcanism and tectonics on Venus, *Annu. Rev. Earth Planet. Sci.*, *26*(1), 23 51.

Niu, Y. L. (1997), Mantle melting and melt extraction processes beneath ocean ridges: Evidence from abyssal peridotites, *J. Petrol.*, *38*(8), 1047 1074.

Norton, I. O. (1995), Plate motions in the North Pacific - the 43 Ma nonevent, *Tectonics*, *14*(5), 1080 1094.

Okal, E. A., et al. (2009), Field survey of the Samoa tsunami of 29 September 2009, *Seismological Res. Lett.*, *81*(4), 577 591.

Olson, P. (1990), Hot spots, swells and mantle plumes, in *Magma transport and storage*, edited by M. P. Rayan, pp. 33 51, John Wiley & Sons.

Orion, N., D. Ben-Chiam, and Y. Kali (1997), Relationship between Earth-science education and spatial visualization, *J. Sci. Edu.*, *47*, 129 132.

Parker, R. L., and D. W. Oldenburg (1973), Thermal model of ocean ridges, *Nature*, *242*, 137 139.

Parkhurst, D., K. Law, , and E. Niebur (2002), Modeling the role of salience in the allocation of overt visual attention, *Vision Research*, *42*(1), 107 123.

Patriat, P., and J. Achache (1984), India-Euroasia collision chronology has implications for crustal shortening and driving mechanism of plates, *Nature*, *311*.

Patterson, T. C. (2007), Google Earth as a (not just) geography educational tool, *J. Geography*, *106*(4), 145 152.

Peacock, S. A. (1990), Fluid processes in subduction zones, *Science*, *248*(4953), 329 37.

Pelletier, B., and J. M. Auzende (1996), Geometry and structure of the Vitiaz trench lineament (SW Pacific), *Mar. Geophys. Res.*, *18*, 305 335.

Pence, N., E. Weisbrot, S. J. Whitmeyer, D. G. De Paor, and J. Gobert (2010), Using Google Earth for advanced learning in the geosciences, *Geological Society of America Abstracts with Programs*, *42*(1), 115.

Phillips, R. J., and V. L. Hansen (1994), Tectonic and magmatic evolution of Venus, *Annu. Rev. Earth Planet. Sci.*, *22*, 597 654.

Phillips, R. J., and N. R. Izenberg (1995), Ejecta correlations with spatial crater density and Venus resurfacing history, *Geophys. Res. Lett.*, *22*(12), 1517 1520.

Phillips, R. J., and K. Lambeck (1980), Gravity fields of the terrestrial planets: Long-wavelength anomalies and tectonics, *Rev. Geophys.*, *18*(1), 27 76.

Phillips, R. J., R. F. Raubertas, R. E. Arvidson, I. C. Sarkar, R. R. Herrick, N. Izenberg, and R. E. Grimm (1992), Impact craters and Venus resurfacing history, *J. Geophys. Res.: Planets (1991-2012)*, *97*(E10), 15,923 15,948.

Phillips, R. J., M. A. Bullock, and S. A. Hauck (2001), Climate and interior coupled evolution on Venus, *Geophys. Res. Lett.*, *28*(9), 1779 1782.

Prototype (-), Prototype, Website, http://www.prototypejs.org/, Last accessed 07/10/2013.

Rakshit, R., and Y. Ogneva-Himmelberger (2008), Application of virtual globes in education, *Geography Compass*, *2*(2), 1995 2010.

Rakshit, R., and Y. Ogneva-Himmelberger (2009), Teaching and learning guide for: Application of virtual globes in education, *Geography Compass*, *3*(4), 1579 1595.

Rashid, O., I. Mullins, P. Coulton, and R. Edwards (2006), Extending cyberspace: Location based games using cellular phones, *ACM Computers in Entertainment*, *4*(1).

Raymond, C. A., J. M. Stock, and S. C. Cande (2000), *Fast Paleogene motion of the Pacific hotspots from revised global plate circuit constraints*, American Geophysical Union.

Reid, I., and H. R. Jackson (1981), Oceanic spreading rate and crustal thickness, *Mar. Geophys. Res.*, *5*, 165 172.

Rensink, R., J. O'Regan, and J. Clark (1997), To see or not to see: The need for attention to perceive changes in scenes, *Psychological Science*, *8*(5), 368 373.

Reynolds, S. J., J. K. Johnson, M. D. Piburn, D. E. Leedy, J. A. Coyan, and M. M. Busch (2005), Visualization in undergraduate geology course, in *Visualization in science education*, edited by J. K. Gilbert, Springer Inc.

Ribe, N., U. R. Christensen, and J. Theissing (1995), The dynamics of plume-ridge interaction, 1 Ridge-centered plumes, *Earth Planet. Sci. Lett.*, *134*(1-2), 155 168.

Ribe, N. M. (1996), The dynamics of plume-ridge interaction: 2. Off-ridge plumes, *J. Geophys. Res.: Solid Earth*, *101*(B7), 16,195 16,204.

Richards, M. A., and R. W. Griffiths (1988), Deflection of plumes by mantle shear-flow - experimental results and a simple theory, *Geophysical Journal-Oxford*, *94*(3), 367 376.

Rosenbaum, G., and G. S. Lister (2004), Neogene and quaternary rollback evolution of the Tyrrhenian sea, the Apennines and the Sicilian maghrebides, *Tectonics*, *23*.

Ross, R. M., D. Duggan-Haas, R. Kissel, and C. Bessemer (2008), Why does the Earth look the way it does?, Website, http://www.virtualfieldwork.org/Welcome.html, Last accessed 07/10/2013.

Roush, W. (2007), Second earth, *Technology Review.*

Rudge, J. F., T. Kleine, and B. Bourdon (2010), Broad bounds on Earth's accretion and core formation constrained by geochemical models, *Nat. Geosci.*, *3*(6), 439 443.

Ryan, W. B. F., et al. (2009), Global multi-resolution topography synthesis, *Geochem. Geophys. Geosyst.*, *10.*

Sager, W. W., and H. C. Han (1993), Rapid formation of Shatsky Rise oceanic plateau inferred from its magnetic anomaly, *Nature*, *364*, 610 613.

Sager, W. W., D. W. Handschumacher, T. W. C. Hilde, and D. R. Bracey (1988), Tectonic evolution of the northern Pacific plate and Pacific-Farallon-Izanagi triple junction in the Late Jurassic and Early Cretaceous (M21-M10), *Tectonophysics*, *155*, 345 364.

Sao Pedro, M. A., R. S. J. d. Baker, O. Montalvo, A. Nakama, and J. D. Gobert (2010), Using text replay tagging to produce detectors of systematic experimentation behavior pattern, Proceedings of the 3rd International Conference on Educational Data Mining.

Schaber, G. G., et al. (1992), Geology and distribution of impact craters on Venus: What are they telling us?, *J. Geophys. Res.: Planets (1991-2012)*, *97*(E8), 13,257 13,301.

Schellart, W. (2004), Quantifying the net slab pull force as a driving mechanism for plate tectonics, *Geophys. Res. Lett.*, *31*(7).

Schilling, J. G. (1991), Fluxes and excess temperatures of mantle plumes inferred from their interaction with migrating mid-ocean ridges, *Nature*, *352*, 397 403.

Schubert, G., and D. T. Sandwell (1995), A global survey of possible subduction sites on Venus, *Icarus*, *117*(1), 173 196.

Schubert, G. S., V. S. Solomatov, P. J. Tackely, and D. L. Turcotte (1997), Mantle convection and thermal evolution of Venus, in *Venus II: Geology, Geophysics, Atmosphere, and Solar Wind Environment*, edited by S. W. Bouger, D. M. Hunten, and R. J. Phillips, pp. 1245 1288, University of Arizona Press, Tucson, AZ.

Sclater, J. G., C. Bowin, R. Hey, H. Hoskins, J. Peirce, J. Phillips, and C. Tapscott (1976), The Bouvet Triple Junction, *J. Geophys. Res.*, *81*, 1857 1869.

Searle, R. C. (1976), Lithospheric structure of the Azores Plateau from Rayleigh-Wave Dispersion, *Geophys. J. R. Astron. Soc.*, *44*(3), 537 546.

Searle, R. C. (1980), Tectonic pattern of the Azores spreading center and triple junction, *Earth Planet. Sci. Lett.*, *51*, 415 434.

Searle, R. C., and J. Francheteau (1986), Morphology and tectonics of the Galapagos Triple Junction, *Mar. Geophys. Res.*, *8*(2), 95 129.

Selkin, P. A., D. G. De Paor, J. Gobert, K. B. Kirk, S. Kluge, G. A. Richard, and S. J. Whitmeyer (2009), Emerging digital technologies for geoscience education and outreach, *Geological Society of America Abstracts with Programs*, *47*(7), 165.

Shen, Y., and D. W. Forsyth (1995), Geochemical constraints on initial and final depths of melting beneath mid-ocean ridges, *J. Geophys. Res.*, *100*(B2), 2211 2237.

Shorttle, O., J. Maclennan, and S. M. Jones (2010), Control of the symmetry of plume-ridge interaction by spreading ridge geometry, *Geochem., Geophys., Geosyst.*, *11*(7).

Sights (-), The HTML5 test, Website, http://html5test.com/results.html, Last accessed 07/10/2013.

Silveira, G., E. Stutzmann, A. Davaille, J.-P. Montagner, L. Mendes-Victor, and A. Sebai (2006), Azores hotspot signature in the upper mantle, *Journal of Volcanology and Geothermal Research*, *156*(23-34), 23 34.

Simons, M., S. C. Solomon, and B. H. Hager (1997), Localization of gravity and topography: Constraints on the tectonics and mantle dynamics of Venus, *Geophys. J. Int.*, *131*(1), 24 44.

Simpson, C., and D. G. De Paor (2010), Restoring maps and memoirs to four-dimensional space using virtual globe technology: A case study from the Scottish Highlands, in *Continental Tectonics and Mountain Building*, edited by R. D. Law, R. W. H. Butler, R. E. Holdsworth, M. Krabbendam, and R. A. Strachan, p. 335, Geological Society of London, Special Publication.

Simpson, C., D. G. De Paor, M. R. Beebe, and J. Strand (2012), Transferring maps and data from pre-digital-era theses to Google Earth: A case study from the Vredefort dome, South Africa, in *Google Earth and Virtual Visualizations in Geoscience Education and Research: Geological Society of America Special Paper 492*, edited by S. Whitmeyer, J. Bailey, D. De Paor, and T. Ornduff, chap. 13, Geological Society of America.

Sleep, N. H. (1990), Hotspots and mantle plumes - some phenomenology, *J. Geophys. Res., [Solid Earth and Planets]*, *95*(B5), 6715 6736.

Smith, G. P., D. A. Wiens, K. M. Fischer, L. M. Dorman, S. C. Webb, and J. A. Hildebrand (2001), A complex pattern of mantle flow in the Lau backarc, *Science*, *292*(5517), 713 716.

Smrekar, S. E., and E. R. Stofan (1997), Corona formation and heat loss on Venus by coupled upwelling and delamination, *Science*, *277*(5330), 1289 1294.

Smrekar, S. E., W. S. Kiefer, and E. R. Stofan (1997), Large volcanic rises on Venus, in *Venus II: Geology, Geophysics, Atmosphere, and Solar Wind Environment*, edited by S. W. Bouger, D. M. Hunten, and R. J. Phillips, pp. 845 879, University of Arizona Press, Tucson, AZ.

SoftComplex (2010), Tigra slider control, Website, http://www.softcomplex.com/products/tigra_slider_control/, Last accessed 07/10/2013.

Solomon, S. C., J. W. Head, W. M. Kaula, D. McKenzie, B. Parison, R. J. Phillips, G. Schubert, and M. Talwani (1991), Venus tectonics: Initial analysis from Magellan, *Science*, *252*(5003), 297 312.

Sparks, D. W., and E. M. Parmentier (1993), The structure of three-dimensional convection beneath oceanic spreading centers, *Geophys. J. Int.*, *112*, 19,727 19,728.

Stadler, G., M. Gurnis, C. Burstedde, L. C. Wilcos, L. Alisic, and O. Ghattas (2010), The dynamics of plate tectonics and mantle flow: From local to global scales, *Science*, *329*(5995), 1033 1038.

Stahley, T. (2006), Earth from above, *The Science Teacher*, *73*(7), 44 48.

Steinberger, B., and R. J. O'Connell (1998), Advection of plumes in mantle flow: implications for hotspot motion, mantle viscosity and plume distribution, *Geophysical Journal International*, *132*, 412 434.

Stenback, J., P. L. Hégaret, and A. L. Hors (-), Interface HTML menu element, Website, http://www.w3.org/TR/DOM-Level-2-HTML/html.html#ID-72509186, Last accessed 07/10/2013.

Stofan, E. R., V. E. Hamilton, D. M. Janes, and S. E. Smrekar (1997), Coronae on Venus: Morphology and origin, in *Venus II: Geology, Geophysics, Atmosphere, and Solar Wind Environment*, edited by S. W. Bouger, D. M. Hunten, and R. J. Phillips, pp. 931 968, University of Arizona Press, Tucson, AZ.

Stofan, E. R., S. W. Anderson, D. A. Crown, and J. J. Plaut (2000), Emplacement and composition of steep-sided domes on Venus, *J. Geophys. Res.: Planets (1991-2012)*, *105*(E11), 26,757 26,771.

Strom, R. G., G. G. Schaber, and D. D. Dawson (1994), The global resurfacing of Venus, *J. Geophys. Res.*, *99*(E5), 10,899 10.

Sykes, L. R. (1966), The seismicity and deep structure of island arcs, *J. Geophys. Res.*, *71*(12), 2981 3006.

Syracuse, E. M., and G. A. Abers (2006), Global compilation of variations in slab depth beneath arc volcanoes and implications, *Geochem. Geophys. Geosyst.*, *7*(5), 1 18.

Tarduno, J. A. (2007), On the motion of Hawaii and other mantle plumes, *Chemical Geology*, *241*(3-4), 234 247.

Taylor, F., and D. Grinspoon (2009), Climate evolution of Venus, *J. Geophys. Res.: Planets (1991-2012)*, *114*(E9).

Thibaud, R., P. Gente, and M. Maia (1998), A systematic analysis of the Mid-Atlantic Ridge morphology and gravity between 15°N and 40°N: Constraints of the thermal structure, *J. Geophys. Res.: Solid Earth*, *103*(B10), 24,223 24,243.

Turcotte, D., and G. Schubert (2002), *Geodynamics*, Cambridge University Press.

USGS (2009), Magnitude 8.1 Samoa Islands region., Website, http://earthquake.usgs.gov/earthquakes/recenteqsww/Quakes/us2009mdbi.php, Last accessed 07/10/2013.

Uyeda, S., and H. Kanamori (1979), Back-arc opening and the mode of subduction, *J. Geophys. Res.*, *84*(B3), 1049 1061.

Van der Hilst, R. (1995), Complex morphology of subducted lithosphere in the mantle beneath the Tonga trench, *Nature*, *374*, 154 157.

van Kesteren, A. (2012), XMLHttpRequest, Website, http://www.w3.org/TR/XMLHttpRequest/, Last accessed 07/10/2013.

Vita-Finzi, C., R. J. Howarth, S. W. Tapper, and C. A. Robinson (2005), Venusian craters, size distribution, and the origin of coronae, *Spec. Pap. - Geol. Soc. Am.*, *388*, 815 823.

Vogt, P. R., and W. Y. Jung (2004), The Terceira Rift as a hyper-slow, hotspot-dominated oblique spreading axis. A comparison with other slow-spreading plate boundaries, *Earth Planet. Sci. Lett.*, *218*(1-2), 77 90.

Wang, X. (2004), Infinite Prandtl number limit of Rayleigh-Benard convection, *Communications on Pure and Applied Mathematics*, *57*, 1265 1285.

Wernicke, J. (2009), *The KML handbook: geographic visualization for the Web*, Addison-Wesley.

Wetherill, G. W. (1990), Formation of the Earth, *Annu. Rev. Earth Planet. Sci.*, *18*, 205 256.

White, R., J. Bown, and J. Smallwood (1995), The temperature of the Iceland plume and origin of outward-propagating V-shaped ridges, *Journal of the Geological Society*, *152*(6), 1039 1045.

White, R. S., D. McKenzie, and R. K. O'Nions (1992), Oceanic crustal thickness from seismic measurements and rare earth element inversions, *J. Geophys. Res.: Solid Earth*, *97*(B13), 19,683 19,715.

Whitehead, J. A., H. J. B. Dick, and H. Schouten (1984), A mechanism for magmatic accretion under spreading centers, *Nature*, *312*(5990), 146 148.

Whitmayer, S. J. (-), Google Earth lads and exercises, Website, http://csmres.jmu.edu/Geollab/Whitmeyer/web/visuals/exercises.html, Last accessed 07/10/2013.

Whitmeyer, S. J., and D. G. De Paor (2008), Large-scale emergent cross sections of crustal structures in Google Earth, *Geological Society of America Abstracts with Programs*, *40*(6), 189.

Whitmeyer, S. J., D. G. De Paor, J. Gobert, N. Pence, and E. Liz Weisbrot (2011), Enhancing the geoscience curriculum using geo-browser based learning objects, Presentation: CCLI/TUES Principal Investigators Conference.

Wikipedia (2011), Monster milktruck, Website, http://en.wikipedia.org/wiki/Monster_Milktruck, Last accessed 07/10/2013.

Wild, S. C., M. M. Dordevic, and D. G. De Paor (2011), Tonga, Website, http://www.lions.odu.edu/org/planetarium/steve/GS/API/, Last accessed 07/10/2013.

Williams, M. (-), Replay routes, Website, http://maps.myosotissp.com/, Last accessed 07/10/2013.

Wilson, L., and J. W. Head III (2002), Tharsis-radial graben systems as the surface manifestation of plume-related dike intrusion complexes: Models and implications, *J. Geophys. Res.*, *107*(E8), 5057.

Wolfe, C. J., I. T. Bjarnason, J. C. VanDecar, and S. C. Solomon (1997), Seismic structure of the Iceland mantle plume, *Nature*, *385*(6613), 245 247.

Wolfe, C. J., S. C. Solomon, G. Laske, J. A. Collins, R. S. Detrick, J. A. Orcutt, D. Bercovici, and E. H. Hauri (2009), Mantle shear-wave velocity structure beneath the Hawaiian hot spot, *Science*, *326*(5958), 1388 90.

Yoshii, T. (1975), Regionality of group velocities of Rayleigh waves in the Pacific and thickening of the plate, *Earth Planet. Sci. Lett.*, *25*(3), 305 312.

APPENDIX A

MATLAB CODES FOR NUMERICAL MODELING DATA PROCESSIONING

Listing A.1. Matlab code for calculating the crustal thicknes

```
%limit the melt fraction in %
MeltLimit = 18;
filenames={'run610_deh_T_u_v_w_mu','run612_deh_T_u_v_w_mu','
    run613_deh_T_u_v_w_mu'};

%ridge half spreading rates in cm/yr
u = 1.205;
u1 = 1.00;
v = 0.4;

dxHi = 0.005;
dxLow = 0.05;
dz = 0.02;
[X,Y,Z]=meshgrid(0:dxLow:4,0:dxLow:4,0:dz:0.9);
[Xi,Yi]=meshgrid(0:dxHi:4,0:dxHi:4);

angel = atan(v/u);
angel2 = atan(v/u1);

%integration along Y for R3
xx = 0:dxHi:2;
yy = tan(angel)*xx;
yy2 = tan(angel2)*xx;
xx = xx+2;
ymax = 2 + yy;
ymin = 2 - yy2;
yInt=[xx;ymin;ymax];

%integration limits along X for R1 and R2
xx = 0:dxHi:2;
yy = tan(pi/2-angel)*xx;
yy = [fliplr(yy)+2,yy+2];
yy(22)=[];
xInt = [0:dxHi:4;yy];

%labeling of plots%
azimuts=[90,90,135,135,180,180,225,225,270,270,315,315];
diameters=[125,165,125,165,125,165,125,165,125,165,125,165];
symbols={'o','+','x'};

```

```
40  for f=1:length(filenames)
41      file{f} = load(['d:\' filenames{f}]);
42      b = file{f};
43      %calculate solidus from ride
44      solidus =(0.9- b(:,3)) * 250 * 3.25 + 1160;
45
46      %iterate throu all the angles and diameters
47      iterator = 4:5:size(file{f},2);
48
49      for i= 1:length(iterator)
50          %construct melt fraction for each column iterator(i)
51          b(:,end+1) = (b(:,iterator(i)) - solidus(:)) / 350;
52
53          %disregard melting fractions smaler than 0 by converting
                them to 0
54          b(b(:,end)<0, end) = 0;
55          b(b(:,end)> MeltLimit/100, end) = MeltLimit/100;
56          tic
57          F = griddata(b(:,1),b(:,2),b(:,3),b(:,end),X,Y,Z);
58          W= griddata(b(:,1),b(:,2),b(:,3),b(:,iterator(i)+3),X,Y
                ,Z);
59          toc
60          %gradient in 1/m
61          [Fx,Fy,Fz] = gradient(F,dxLow, dxLow, dz);
62
63          %melting rate in 1/yr, from nondimezional rate to cm/yr
64          meltRate = (Fz.*W);
65          meltRate(meltRate<0)=0;
66          result = zeros(size(meltRate,1), size(meltRate,2));
67          %melt depth start mds 0.5 = 100km, dz increments
68          mds = 0.52;
69
70          for ii=1:size(meltRate,1)
71              for j=1:size(meltRate,2)
72                  result(ii,j) =  trapz(mds:dz:0.9, meltRate(ii,j,
                        mds/dz+1:end));
73              end
74          end
75
76          [Xa,Ya] = meshgrid(0:dxLow:4,0:dxLow:4);
77          result =  interp2(Xa,Ya,result,Xi,Yi);
```

```
78
79          yy=0:dxHi:4;
80          %integration in xy plane along y axis for pooling to R3
81          for ii = (size(result,1)-1)/2+1: size(result,1)
82             miny = yInt(2,ii-(size(result,1)-1)/2);
83             Maximum = yInt(3,ii-(size(result,1)-1)/2);
84             range = yy(yy<=Maximum & yy>=miny);
85             val = result(yy<=Maximum & yy>=miny, ii);
86             if length(range)>1
87                   r3(ii-(size(result,1)-1)/2) = trapz(range, val);
88             else
89                   r3(ii-(size(result,1)-1)/2) = val*(Maximum-miny)
                        ;
90             end
91          end
92
93          %integration in xy plane along x axis for pooling to R1
               and R2
94          for ii=1:(size(result,2));
95             miny = 0;
96             Maximum = xInt(2,ii);
97             range = yy(yy<=Maximum & yy>=miny);
98             val = result(ii, yy<=Maximum & yy>=miny);
99             r12(ii) = trapz(range, val);
100         end
101
102         r12=r12*250/(2*u);
103         r3 = r3*250/(2*v);
104
105         r1=fliplr(r12(1:end/2+1));
106         r2=r12(end/2:end);
107
108         figure(1)
109             plot([0:dxHi:2]*250, r1,'r'); hold on
110             plot([0:dxHi:2]*250, r2,'c'); hold on
111             plot([0:dxHi:2]*250, r3,'b');
112
113
114         r12=r12-r12(100);
115         r3=r3-r3(end);
116
```

```
117             figure(2)
118                 hold on
119                 if(diameters(i)==125)
120                     scatter(azimuts(i), max(r3),'b',symbols{f})
121                 else
122                     scatter(azimuts(i), max(r3),'r',symbols{f})
123                 end
124
125             figure(3)
126                 hold on
127                 if(diameters(i)==125)
128                     scatter(azimuts(i), max(r12),'b',symbols{f})
129                 else
130                     scatter(azimuts(i), max(r12),'r',symbols{f})
131                 end
132             fprintf('column %d out of 12',i)
133         end
134     end
```

Listing A.2. Matlab code for calculating dynamical topography

```
1  % Input filenames located in c:\;
2  filenames={'run610_deh_T', 'run612_deh_T', 'run613_deh_T'};
3  % Cut along which axes x or y?
4  cutAlongAxes='y';
5  % Cut is made at what coordinate normal to the cut axes?
6  cutAt = 2;
7  % Base model, temperature with no plume present
8  base = load('d:\run610_base_deh_T');
9
10 %% Integration constants
11 scaleLength = 250;
12 integralLowLimit = 200;
13 deptOfTheBoxNonDim = 0.9;
14 alpha = 3e-5;
15 rhom = 3300;
16 rhow = 1030;
17 rhoc = 2700;
18 tolerance = 0.00001;
19 colors = rand(20,3);
20 cutAlongAxes = lower(cutAlongAxes);
21 matlabpool(4)
```

```
parfor f=1:length(filenames)
  tic
  b{f} = load(['d:\' filenames{f}]);
  toc
end
matlabpool close;
for f=1:length(filenames)
  fig = figure(f);
  a=b{f};
  clf;
  axes1 = axes('Parent',fig);
  box(axes1,'on');
  hold(axes1,'all');
  leg = {};
  angle = 45;
  set(fig,'name',filenames{f});
  % Set the value of the T-T_0 inside of the integral
  for i=4:size(a,2)
    a(:,i) = a(:,i)-base(:,4);
  end
  % If the number that you are cutting along is not the define at
      the grid, program is going to select the closest one to it.
  if cutAlongAxes == 'x'
    span = unique(a(:,1));
    cutAtAxis = 'y';
    cutAt = mladen.getCloseNumb(cutAt, a(:,2));
  else
    span = unique(a(:,2));
    cutAtAxis = 'x';
    cutAt = mladen.getCloseNumb(cutAt, a(:,1));
  end

  res = zeros(1,length(span));

  for j=1:size(a,2)-3
    switch cutAlongAxes
      case 'x'
        for i=1:length(span)
          c = a(...
              a(:,1)>=span(i)-tolerance &...
              a(:,1)<=span(i)+tolerance &...
```

```
62                  a(:,2)>=cutAt-tolerance &...
63                  a(:,2)<=cutAt+tolerance & ...
64                  a(:,3)>=deptOfTheBoxNonDim-integralLowLimit/
                        scaleLength ,...
65                  [1,2,3,3+j]);
66              res(i) =  trapz(c(:,3),c(:,4));
67            end
68          case 'y'
69            for i=1:length(span)
70              c = a(...
71                  a(:,1)>=cutAt-tolerance &...
72                  a(:,1)<=cutAt+tolerance &...
73                  a(:,2)>=span(i)-tolerance &...
74                  a(:,2)<=span(i)+tolerance & ...
75                  a(:,3)>=deptOfTheBoxNonDim-integralLowLimit/
                        scaleLength ,...
76                  [1,2,3,3+j]);
77              res(i) =  trapz(c(:,3),c(:,4));
78            end
79        end
80        x_dim = span*250;
81        res_dim = res*250*alpha*rhom/(rhoc-rhow);
82        plot1 = plot(x_dim, res_dim,'Parent',axes1);
83        set(plot1,'Color',colors(j,:));
84        ylim([-0.1,2]);
85
86        if mod(j,2)== 0
87          set(plot1,'LineStyle','-.');
88          leg{end+1}= ['165km ' num2str(angle)];
89        else
90         angle = angle + 45;
91         leg{end+1}= ['125km ' num2str(angle)];
92        end
93
94        xlabel([cutAlongAxes,' [km]']);
95        ylabel('Thermal topography [km]');
96        hold on
97      end
98      legend(leg);
99    end
```

Listing A.3. Matlab code for calculating the isosufrace of the plume and finding waist widths along R_1 R_2 and R_3.

```
%%ploting the isosurface and data extraction along r1 r2 r3
filenames= {'510_cp_T', '510_cp_deh_T','610_cp_T','610_cp_deh_T'};
excess_plime_temperature = 180;
tolerance = 0.00001;

%Domain parameters
param.box.xmax = 4;
param.box.ymax = 4;
param.box.zmax = 0.9;
param.tj.x = 2;
param.tj.y = 2;

matlabpool(4)
for f=1:numel(filenames)
  fprintf('Loading file %s\n ',filenames{f})
  a = load(['d:\' filenames{f}]);
  howManuParameters = size(a,2)-3;
  fprintf('File loaded!\n')
  [X,Y,Z] = meshgrid(...
    0:0.01:param.box.xmax,...
    0:0.01:param.box.ymax,...
    0:0.01:param.box.zmax);
  A = [];
  parfor i=1:howManuParameters
    R={};
    tic
    V = griddata(a(:,1),a(:,2),a(:,3),a(:,i+3),X,Y,Z);
    plume = isosurface(V,excess_plime_temperature/4+1350);
    t=toc;
    fprintf('Finished %d/%d\tTime used: %d s\t File: %s\n',i,...
      howManuParameters,int8(t),filenames{f})
    R1R2 = plume.vertices(find(plume.vertices(:,1) >= param.tj.x *
        100 + 1 - tolerance &...
      plume.vertices(:,1)<= param.tj.x * 100 + 1 + tolerance)
          ,[1,2,3]);
    R3 = plume.vertices(find(plume.vertices(:,2) >= param.tj.y * 100
        + 1 - tolerance &...
      plume.vertices(:,2)<= param.tj.y * 100 + 1+tolerance),[1,2,3])
          ;
```

```
36
37      [R1x,R1xI]= max(R1R2(:,2));
38      [R2x,R2xI]= min(R1R2(:,2));
39
40      [R3x,R3xI]= max(R3(:,1));
41      [R4x,R4xI]= min(R3(:,1))
42      R.R1x = (R1R2(R1xI,2)-1)/100;
43      R.R1y = (R1R2(R1xI,3)-1)/100;
44
45      R.R2x = (R1R2(R2xI,2)-1)/100;
46      R.R2y = (R1R2(R2xI,3)-1)/100;
47
48      R.R3x = (R3(R3xI,1)-1)/100;
49      R.R3y = (R3(R3xI,3)-1)/100;
50
51      R.R4x = (R3(R4xI,1)-1)/100;
52      R.R4y = (R3(R4xI,3)-1)/100;
53
54      keys = fieldnames(R);
55      for j=1:numel(keys)
56          if isempty(R.(keys{j}))
57            R.(keys{j}) = -1;
58          end
59      end
60      A(i,:)=[i,R.R1x,R.R1y,R.R2x,R.R2y,R.R3x,R.R3y,R.R4x,R.R4y];
61    end
62    dlmwrite(['d:\' filenames{f} '_OUT'], A, 'delimiter', '\t','
          precision', 5)
63  end
64  matlabpool close
```

Listing A.4. Matlab code extracting maximal velocity parallel to ridges along R_1 R_2 and R_3.

```
1  tolerance = 0.0000001;
2  tj.x = 2;
3  tj.y = 2;
4  %List of filenames to run. Located in c:\
5  filenames= {'run610_T_u_v_w_mu','run612_T_u_v_w_mu','
       run613_T_u_v_w_mu'};
6  matlabpool(4)
7  ridges = cell(numel(filenames),1);
```

```
files = cell(numel(filenames),1);
%Paralelized file loading since it is most slow op.
parfor f = 1:numel(filenames)
  tic
  fprintf('Loading file %s, %s \n ', filenames{f}, num2str(f))
  files{f} = load(['d:\' filenames{f}]);
  toc
  fprintf('File loaded! %s \n', num2str(f))
end
matlabpool close

for f = 1:numel(filenames)
  a = files{f};
  % Selecting sides of the box as East E, Weast etc.
  xmax = max(a(:,1));
  ymax = max(a(:,2));

  R1 = a(a(:,1) >= tj.x - tolerance & a(:,1) <= tj.x + tolerance
      &...
    a(:,2) >= tj.y - tolerance  & a(:,2) <= ymax + tolerance , 1:end)
        ;

  R2 = a(a(:,1) >= tj.x - tolerance & a(:,1) <= tj.x + tolerance
      &...
    a(:,2) >= 0 - tolerance  & a(:,2) <= tj.y + tolerance , 1:end);

  R3 = a(a(:,1) >= tj.x - tolerance & a(:,1) <= xmax + tolerance
      &...
    a(:,2) >= tj.y - tolerance  & a(:,2) <= tj.y + tolerance , 1:end)
        ;


  R1_uni = unique(R1(:,2));
  R2_uni = unique(R2(:,2));
  R3_uni = unique(R3(:,1));

  R1_data = zeros(numel(R1_uni), (size(a,2) - 3)/5 + 1);
  R2_data = zeros(numel(R2_uni), (size(a,2) - 3)/5 + 1);
  R3_data = zeros(numel(R3_uni), (size(a,2) - 3)/5 + 1);

%loop over the angles
```

```
44  %loop over every item in unique R1, R2, R3
45  for j = 1:numel(R1_uni)
46     % find the biggest absolute value for each unique val
47    tmp = R1(R1(:,2) == R1_uni(j), 1:end);
48    for i = 1:(size(a,2) - 3)/5
49      R1_data(j, i + 1) = max(abs(tmp(:, 6 + 5 * (i - 1))));
50      R1_data(j, 1) = R1_uni(j);
51    end
52  end
53  for j = 1:numel(R2_uni)
54     % find the biggest absolute value for each unique val
55    tmp = R2(R2(:,2) == R2_uni(j), 1:end);
56    for i = 1:(size(a,2) - 3)/5
57        R2_data(j, i + 1) = max(abs(tmp(:, 6 + 5 * (i - 1))));
58        R2_data(j, 1) = R2_uni(j);
59    end
60  end
61  for j = 1:numel(R3_uni)
62     % find the biggest absolute value for each unique val
63    tmp = R3(R3(:,1) == R3_uni(j), 1:end);
64    for i = 1:(size(a,2) - 3)/5
65      R3_data(j, i + 1) = max(abs(tmp(:, 5 + 5 * (i - 1))));
66      R3_data(j, 1) = R3_uni(j);
67    end
68  end
69
70  leg = {'90\circ' '135\circ' '180\circ' '225\circ' '270\circ' '315\
       circ'};
71  figure(1)
72  axes('XTickLabel',{'0','50','100','150','200','250','300','350','
       400','450','500'});
73  hold on
74  plot(R1_data(:,1),R1_data(:,2:2:end))
75  legend on
76  legend(leg)
77  xlabel('Distance away from TJ along R1 [km]');
78  ylabel('Maximal velocity [cm/yr]');
79
80  figure(2)
81  axes('XTickLabel',{'0','50','100','150','200','250','300','350','
       400','450','500'});
```

```
82  hold on
83  plot(R1_data(:,1),R1_data(:,3:2:end))
84  legend on
85  legend(leg)
86  xlabel('Distance away from TJ along R1[km]');
87  ylabel('Maximal velocity [cm/yr]');
88  set(gcf,'PaperUnits','inches','PaperSize',[8.27,11.69],'
        PaperPosition',[0 0 6 6]);
89  print('-dpng ','-r300', [filenames{f} '_R1_max_v_165'])
90  print('-depsc','-r300', [filenames{f} '_R1_max_v_165'])
91
92  figure(3)
93  axes('XDir','reverse','XTickLabel',fliplr({'0','50','100','150','
        200','250','300','350','400','450','500'}));
94  hold on
95  plot(R2_data(:,1),R2_data(:,2:2:end))
96  legend on
97  legend(leg)
98  xlabel('Distance away from TJ along R2 [km]');
99  ylabel('Maximal velocity [cm/yr]');
100
101 figure(4)
102 axes('XDir','reverse','XTickLabel',fliplr({'0','50','100','150','
        200','250','300','350','400','450','500'}));
103 hold on
104 plot(R2_data(:,1),R2_data(:,3:2:end))
105 legend on
106 legend(leg)
107 xlabel('Distance away from TJ along R2 [km]');
108 ylabel('Maximal velocity [cm/yr]');
109
110 figure(5)
111 axes('XTickLabel',{'0','50','100','150','200','250','300','350','
        400','450','500'});
112 hold on
113 plot(R3_data(:,1),R3_data(:,2:2:end))
114 legend on
115 legend(leg)
116 xlabel('Distance away from TJ along R3 [km]');
117 ylabel('Maximal velocity [cm/yr]');
118
```

```
119    figure(6)
120    axes('XTickLabel',{'0','50','100','150','200','250','300','350','
           400','450','500'});
121    hold on
122    plot(R3_data(:,1),R3_data(:,3:2:end))
123    legend on
124    legend(leg)
125    xlabel('Distance away from TJ along R3 [km]');
126    ylabel('Maximal velocity [cm/yr]');
127  end
```

Listing A.5. Matlab code for velocity comparison for different numerical domains size.

```
1  %% Velocity comparison
2  %
3  % * In order to determine the validity of the results i want to
       compare
4  % velocity profiles for 4 diffeente sizes of the box with TJ beeing
5  % centered in the middle of the box and plume beeing 50km radial
       distance
6  % from the triple junction.
7  % * I will compare normal velocity components to the vertical sides
       of the
8  % numerical box of the size 2.4 x 2.4 centered around the TJ.
9  %
10 %% Numerical domains sizes :
11 % # 2.6 x 2.6 TJ(1.3, 1.3)
12 % # 2.8 x 2.8 TJ(1.4, 1.4)
13 % # 3.0 x 3.0 TJ(1.5, 1.5)
14 % # 3.2 x 3.2 TJ(1.6, 1.6)
15 %
16 %% Loading COMOSL results
17 cBox = 2.4;
18 tolerance = 0.0000001;
19 filenames= {'run310_4.0x4.0x0.9_T_u_v_w_mu','run310_3.4x3.4x0.9
       _T_u_v_w_mu','run310_T_u_v_w_mu','run310_3.0x3.0x0.9_T_u_v_w_mu',
       'run310_2.8x2.8x0.9_T_u_v_w_mu','run310_2.6x2.6x0.9_T_u_v_w_mu'};
        %List of filenames to run. Located in c:\
20 matlabpool(4)
21 boxes = cell(length(filenames),1);
22 files = cell(length(filenames),1);
```

```
%Paralelized file loading since it is most slow op.
parfor f = 1:numel(filenames)      tic
  fprintf('Loading file %s, %s \n ', filenames{f}, num2str(f))
  files{f} = load(['d:\' filenames{f}]);
  toc
  fprintf('File loaded! %s \n', num2str(f))
end
matlabpool close

colors = rand(6,3);
colors(:,4) = 90:45:315;

for f = 1:numel(filenames)
  a = files{f};
  % Selecting sides of the box as East E, Weast etc.
  xmin = max(a(:,1))/2 - cBox/2;
  xmax = max(a(:,1))/2 + cBox/2;
  y = max(a(:,2))/2 + cBox/2;

  box.N = a(a(:,1) >= xmin - tolerance &...
    a(:,1) <= xmax + tolerance &...
    a(:,2) >= y - tolerance  &...
    a(:,2) <= y + tolerance , 1:end);
  box.N(:,1) =  box.N(:,1) - xmin; %Translate box to the origin

  y = max(a(:,2))/2 - cBox/2;

  box.S = a(a(:,1) >= xmin - tolerance &...
    a(:,1) <= xmax + tolerance &...
    a(:,2) >= y - tolerance  &...
    a(:,2) <= y + tolerance , 1:end);
  box.S(:,1) =  box.S(:,1) - xmin;

  ymin = max(a(:,2))/2 - cBox/2;
  ymax = max(a(:,2))/2 + cBox/2;
  x = max(a(:,1))/2 + cBox/2;

  box.E = a(a(:,2) >= ymin - tolerance &...
    a(:,2) <= ymax + tolerance &...
    a(:,1) >= x - tolerance  &...
    a(:,1) <= x + tolerance , 1:end);
```

```
64    box.E(:,2) =  box.E(:,2) - ymin;
65    x = max(a(:,1))/2 - cBox/2;
66
67    box.W = a(a(:,2) >= ymin - tolerance &...
68      a(:,2) <= ymax + tolerance &...
69      a(:,1) >= x - tolerance  &...
70      a(:,1) <= x + tolerance , 1:end);
71    box.W(:,2) =  box.W(:,2) - ymin;
72    boxes{f} = box;
73  end
74
75  angles = (size(a,2)-3)/5-1;
76  [X,Y] = meshgrid(0:0.01:cBox, 0:0.01:0.9);
77
78  side = {'N','E','W','S'};
79  for s = 1:length(side)
80    angle = 45;
81    diameter = '125';
82    if side{s} == 'W' || side{s} =='E'
83      sideN = 5;
84      sideCoor = 2;
85      velStr = 'U';
86    else
87      sideN = 6;
88      sideCoor = 1;
89      velStr = 'V';
90    end
91    for i = 0:angles
92      %Small loop for writing correct diameters and angles
93      if mod(i+1,2) == 0
94        diameter = '165';
95      else
96        diameter = '125';
97        angle = angle + 45;
98      end
99      c1 = boxes{1}.(side{s});
100     c2 = boxes{2}.(side{s});
101     c3 = boxes{3}.(side{s});
102     c4 = boxes{4}.(side{s});
103     c5 = boxes{5}.(side{s});
104     c6 = boxes{6}.(side{s});
```

```
105
106     val1 = abs(c1(:, sideN + 5*i) - c2(:, sideN + 5*i));
107     val1_min = min(val1);
108     val1_max = max(val1);
109
110     val2 = abs(c1(:, sideN + 5*i) - c3(:, sideN + 5*i));
111     val2_min = min(val2);
112     val2_max = max(val2);
113
114     val3 = abs(c1(:, sideN + 5*i) - c4(:, sideN + 5*i));
115     val3_min = min(val3);
116     val3_max = max(val3);
117
118     val4 = abs(c1(:, sideN + 5*i) - c5(:, sideN + 5*i));
119     val4_min = min(val4);
120     val4_max = max(val4);
121
122     val5 = abs(c1(:, sideN + 5*i) - c6(:, sideN + 5*i));
123     val5_min = min(val5);
124     val5_max = max(val5);
125
126     Ncomp1 = griddata(c1(:,sideCoor), c1(:,3), val1, X, Y);
127     Ncomp2 = griddata(c1(:,sideCoor), c1(:,3), val2, X, Y);
128     Ncomp3 = griddata(c1(:,sideCoor), c1(:,3), val3, X, Y);
129     Ncomp4 = griddata(c1(:,sideCoor), c1(:,3), val4, X, Y);
130     Ncomp5 = griddata(c1(:,sideCoor), c1(:,3), val5, X, Y);
131
132     figure(1);
133     clf
134     imagesc(0:0.1:cBox,0:0.1:0.9,Ncomp1)
135     hold on
136     plot([cBox/2 cBox/2],[0  0.9],'LineWidth',2,'Color',[0 0 0])
137     axis equal;
138     set(gca, 'YDir', 'normal');
139     colorbar;
140     axis tight;
141     caxis([0  1]);
142
143     figure(2);
144     clf
145     imagesc(0:0.1:cBox,0:0.1:0.9,Ncomp2)
```

```
146     hold on
147     plot([cBox/2 cBox/2],[0  0.9],'LineWidth',2,'Color',[0 0 0])
148     axis equal;
149     set(gca,'YDir','normal');
150     colorbar;
151     axis tight;
152     caxis([0  1]);
153
154     figure(3);
155     clf
156     imagesc(0:0.1:cBox,0:0.1:0.9,Ncomp3)
157     hold on
158     plot([cBox/2 cBox/2],[0  0.9],'LineWidth',2,'Color',[0 0 0])
159     axis equal;
160     set(gca,'YDir','normal');
161     colorbar;
162     axis tight;
163     caxis([0  1]);
164
165     figure(4);
166     clf
167     imagesc(0:0.1:cBox,0:0.1:0.9,Ncomp4)
168     hold on
169     plot([cBox/2 cBox/2],[0  0.9],'LineWidth',2,'Color',[0 0 0])
170     axis equal;
171     set(gca,'YDir','normal');
172     colorbar;
173     axis tight;
174     caxis([0  1]);
175
176     figure(5);
177     clf
178     imagesc(0:0.1:cBox,0:0.1:0.9,Ncomp4)
179     hold on
180     plot([cBox/2 cBox/2],[0  0.9],'LineWidth',2,'Color',[0 0 0])
181     axis equal;
182     set(gca,'YDir','normal');
183     colorbar;
184     axis tight;
185     caxis([0  1]);
186
```

```
187     figure(6)
188     clf
189     axes('Parent',figure(6),...
190       'YTick',[0:0.1:1.5],...
191       'YMinorTick','on',...
192       'YGrid','on');
193     plot([-4 -3.4 -3.2 -3 -2.8 -2.6],[0 val1_max val2_max val3_max
          val4_max val5_max],'r—','Marker','square')
194     ylim([0,1.5])
195     set(gca,'XTick',[-4 -3.4 -3.2 -3 -2.8 -2.6]);
196     set(gca,'XTickLabel',{'4','3.4','3.2','3','2.8','2.6'});
197
198     if side{s} == 'N' && strcmp(diameter, '125')
199         figure(7)
200         hold on
201         plot([-4 -3.4 -3.2 -3 -2.8 -2.6],[0 val1_max val2_max
              val3_max val4_max val5_max],'Marker','o', 'Color', colors
              (colors(:,4)==angle, 1:3))
202     end
203     if side{s} == 'N' && strcmp(diameter, '165')
204         figure(8)
205         hold on
206         plot([-4 -3.4 -3.2 -3 -2.8 -2.6],[0 val1_max val2_max
              val3_max val4_max val5_max],'Marker','o', 'Color', colors
              (colors(:,4)==angle, 1:3))
207     end
208     if side{s} == 'E' && strcmp(diameter, '125')
209         figure(9)
210         hold on
211         plot([-4 -3.4 -3.2 -3 -2.8 -2.6],[0 val1_max val2_max
              val3_max val4_max val5_max],'Marker','o', 'Color', colors
              (colors(:,4)==angle, 1:3))
212     end
213     if side{s} == 'E' && strcmp(diameter, '165')
214         figure(10)
215         hold on
216         plot([-4 -3.4 -3.2 -3 -2.8 -2.6],[0 val1_max val2_max
              val3_max val4_max val5_max],'Marker','o', 'Color', colors
              (colors(:,4)==angle, 1:3))
217     end
218     if side{s} == 'S' && strcmp(diameter, '125')
```

```
219         figure(11)
220         hold on
221         plot([-4 -3.4 -3.2 -3 -2.8 -2.6],[0 val1_max val2_max
                val3_max val4_max val5_max],'Marker','o', 'Color', colors
                (colors(:,4)==angle, 1:3))
222     end
223     if side{s} == 'S' && strcmp(diameter, '165')
224         figure(12)
225         hold on
226         plot([-4 -3.4 -3.2 -3 -2.8 -2.6],[0 val1_max val2_max
                val3_max val4_max val5_max],'Marker','o', 'Color', colors
                (colors(:,4)==angle, 1:3))
227     end
228     if side{s} == 'W' && strcmp(diameter, '125')
229         figure(13)
230         hold on
231         plot([-4 -3.4 -3.2 -3 -2.8 -2.6],[0 val1_max val2_max
                val3_max val4_max val5_max],'Marker','o', 'Color', colors
                (colors(:,4)==angle, 1:3))
232     end
233     if side{s} == 'W' && strcmp(diameter, '165')
234         figure(14)
235         hold on
236         plot([-4 -3.4 -3.2 -3 -2.8 -2.6],[0 val1_max val2_max
                val3_max val4_max val5_max],'Marker','o', 'Color', colors
                (colors(:,4)==angle, 1:3))
237     end
238     legend({'90\circ','135\circ','180\circ','225\circ','270\circ','
            315\circ'},'Location', 'NorthWest')
239     set(gca,'XTick',[-4 -3.4 -3.2 -3 -2.8 -2.6]);
240     set(gca,'XTickLabel',{'4','3.4','3.2','3','2.8','2.6'});
241   end
242 end
```

APPENDIX B

JAVASCRIPT CODES FOR EDUCATIONAL MODELS

Listing B.1. Main JavaScript code for Hawaii.

```
1  var ge = null;
2  var a = 10; //total number of models to load
3  var mn = 1; // number of components to each time step
4  var f = "ee"; // file name
5  var aa = 1;
6  var bb = 1;
7  var cc = 1;
8  var dd = 1;
9  var dinLat = new Array
       (20.5,21,20.45,20.55,20.75,20.7,20.64,19.9,20.6,20.9);
10 var dinLon =new Array
       (-78.4,-78.4,-78.35,-78.35,-78.55,-78.45,-78.5,-77.1,-78.3,-78.8)
       ;
11 var fixedLat=20.5-1.01;
12 var fixedLon=-78.4-77.3;
13 var blockAltitude = 0;
14 var c=0;
15 var t;
16 var timeValue;
17 var tt=1;
18 var rem=1;
19
20 google.load("earth", "1");
21 google.setOnLoadCallback(init);
22
23 function init() {
24   google.earth.createInstance('map3d', initCallback, failureCallback
         );
25 }
26 function initCallback(instance) {
27   ge = instance;
28   ge.getWindow().setVisibility(true);
29   ge.getNavigationControl().setVisibility(ge.VISIBILITY_AUTO);
30   makeModel();
31   resetView();
32   resetModelAltitude(-30);
33 }
34 function failureCallback(errorCode){
35 }
36 getURL = function(url) {
```

```
37    var escapeHTML = function(s) {
38      return s.split('&').join('&amp;').split('<').join('&lt;').split(
          '"').join('&quot;');
39    }
40    url? url : url = '';
41    var el= document.createElement('div');
42    el.innerHTML= '<a href="'+ escapeHTML(url)+'">x</a>';
43    return el.firstChild.href;
44  }
45  function makeModel() {
46    var hrefs=["eel.dae","plume.dae","plume1.dae","plume1.dae"];
47
48    for(var i=1;i<5;i++){
49      var loc = ge.createLocation('');
50      var link = ge.createLink('');
51      var href= getURL('./dae/')+hrefs[i-1];
52      var placemark = ge.createPlacemark('');
53      window['model'+i] = ge.createModel('');
54      var model = window['model'+i];
55      ge.getFeatures().appendChild(placemark);
56      link.setHref(href);
57      model.setLink(link);
58      loc.setLatitude(19.67);
59      loc.setLongitude(-155.53);
60      loc.setAltitude(blockAltitude);
61      model.setLocation(loc);
62      model.setAltitudeMode(ge.ALTITUDE_RELATIVE_TO_SEA_FLOOR);
63      placemark.setGeometry(model);
64    }
65  }
66  function resetModelAltitude(sliderValue) {
67    document.getElementById('altitude').innerHTML= sliderValue+"km";
68    var loc = ge.createLocation('');
69    loc.setLatitude(fixedLat);
70    loc.setLongitude(fixedLon);
71    blockAltitude = sliderValue*1000;
72    loc.setAltitude(blockAltitude);
73    model1.setLocation(loc);
74
75    var loc = ge.createLocation('');
76    loc.setLatitude( 19.67);
```

```
77    loc.setLongitude(-155.53);
78    loc.setAltitude(blockAltitude-100000);
79    model2.setLocation(loc);
80
81    var loc = ge.createLocation('');
82    loc.setLatitude( 19.67);
83    loc.setLongitude(-155.53);
84    loc.setAltitude(blockAltitude-100000);
85    model3.setLocation(loc);
86
87    var loc = ge.createLocation('');
88    loc.setLatitude(19.84780);
89    loc.setLongitude(-155.924827);
90    loc.setAltitude(blockAltitude-100000);
91    model4.setLocation(loc);
92  }
93  function resetView() {
94    var la = ge.getView().copyAsLookAt(ge.
          ALTITUDE_RELATIVE_TO_SEA_FLOOR);
95    la.setLatitude(fixedLat);
96    la.setLongitude(fixedLon);
97    la.setHeading(17);
98    la.setRange(5000000);
99    la.setTilt(30);
100   ge.getView().setAbstractView(la);
101 }
102 function restorePlates(timeValue,aa,bb,cc,dd) {
103   var link1 = ge.createLink('');
104   var link2 = ge.createLink('');
105   var link3 = ge.createLink('');
106   var link4 = ge.createLink('');
107   var ss=[];
108   var href1= getURL('./dae/')+"ee1.dae";
109   var href2= getURL('./dae/')+"plume.dae";
110   var href3= getURL('./dae/')+"plume1.dae";
111   var href4 = getURL('./dae/')+"blank.dae";
112   for (var i=1; i<=a;i++){
113     ss[i]= getURL('./dae/')+f+ i +".dae"
114     switch(timeValue){
115     case i:
116       href1= ss[i];
```

```
117         var loc = ge.createLocation('');
118         loc.setLatitude(dinLat[i-1]-1.01);
119         loc.setLongitude(dinLon[i-1]-77.3);
120         loc.setAltitude(blockAltitude);
121         model1.setLocation(loc);
122         fixedLat = dinLat[i-1]-1.01;
123         fixedLon = dinLon[i-1]-77.3;
124
125         href2= getURL('./dae/')+"plume.dae";
126         loc = ge.createLocation('');
127         loc.setLatitude( 19.67);
128         loc.setLongitude(-155.53);
129         loc.setAltitude(blockAltitude-100000);
130         model2.setLocation(loc);
131
132         href3= getURL('./dae/')+"plume1.dae";
133         loc = ge.createLocation('');
134         loc.setLatitude( 19.67);
135         loc.setLongitude(-155.53);
136         loc.setAltitude(blockAltitude-100000);
137         model3.setLocation(loc);
138         rem=i;
139
140         href4 = getURL('./dae/')+"blank.dae";
141         loc = ge.createLocation('');
142         loc.setLatitude(19.84780);
143         loc.setLongitude(-155.924827);
144         loc.setAltitude(blockAltitude-100000);
145         model4.setLocation(loc);
146         break;
147       }
148       if(bb==0){
149         href3=getURL('./dae/')+"blank.bae";
150         href4=getURL('./dae/')+"blank.dae";
151       }
152       if(aa==0){
153         href4=getURL('./dae/')+"dplume.dae";
154         href3=getURL('./dae/')+"blank.bae";
155         href2=getURL('./dae/')+"blank.bae"
156       }
157       if(cc==0){
```

```
158         href1=getURL('./dae/')+"balnk.dae";
159       }
160     }
161     link2.setHref(href2);
162     model2.setLink(link2);
163
164     link3.setHref(href3);
165     model3.setLink(link3);
166
167     link4.setHref(href4);
168     model4.setLink(link4);
169
170     link1.setHref(href1);
171     model1.setLink(link1);
172   }
173   function updateOptions(value){
174     switch(value){
175     case 5:
176       if(bb==1)
177       bb=0;
178       else
179       bb=1;
180       restorePlates(rem,aa,bb,cc,dd);
181       break;
182     case 6:
183       if(cc==1)
184       cc=0;
185       else
186       cc=1;
187       restorePlates(rem,aa,bb,cc,dd);
188       break;
189     case 7:
190       if(aa==1)
191       aa=0;
192       else
193       aa=1;
194       restorePlates(rem,aa,bb,cc,dd);
195       break;
196     case 8:
197       if(dd==1)
198       dd=0;
```

```
199       else
200       dd=1;
201       restorePlates(c,aa,bb,cc,dd);
202       break;
203     }
204 }
205 function timedCount(value){
206     if(value==0){
207       tt=1;
208       clearTimeout(t);
209     }
210     else{
211       tt=0;
212       t=setTimeout("timedCount()",1000);
213       if (c==(a/mn))
214       c=0;
215       else
216       c=c+1
217       restorePlates(c,aa,bb,cc,dd);
218     }
219 }
220 function resetCount(){
221     t=0;
222     c=0;
223     restorePlates(c,aa,bb,cc);
224 }
```

Listing B.2. Main HTML code for Hawaii.

```
1  <!DOCTYPE html PUBLIC "-//W3C//DTD XHTML 1.0 Transitional//EN" "http
       ://www.w3.org/TR/xhtml1/DTD/xhtml1-transitional.dtd">
2  <html xmlns="http://www.w3.org/1999/xhtml" xml:lang="en">
3    <head>
4      <title>Hawaii</title>
5      <script src="http://www.google.com/jsapi?key="></script>
6      <script type="text/javascript" src="js/main.js"></script>
7    </head>
8    <h2>Hawaii deep mantle plume</h2>
9    <div><h4>Controles</h4>
10     <div>
11       Elevate lithospheric block diagram:
```

```
12        <input type="range"  id="sliderValue" value="0" min="-30" max=
              "3500" onchange="resetModelAltitude(this.value)"/> <span id
              ='altitude'>0 km</span>
13      </div>
14      <p>
15      <div>
16        <input type="button" value="Start/Stop" onClick="timedCount(tt
              )"/>
17        <input type="button" value="Reset" onClick="resetCount()"/>
18        <input type="button" value="Carton Mantle plume crossection"
              onclick='updateOptions(5)'  />
19        <input type="button" value="Data/Carton Mantle plume" onclick
              ='updateOptions(7)'  />
20        <input type="button" value="S/H Slice" onclick='updateOptions
              (6)'  />
21      </div>
22    </div>
23    <div ALIGN=CENTER id="map3d" style="width: 1000px; height: 800px;"
        > </div>
24    </body>
25  </html>
```

VITA

Mladen M. Dordevic
Department of Physics
Old Dominion University
Norfolk, VA 23529

Education:
Old Dominion University, Norfolk, VA, **M.S.** Physics, May 2010
University of Belgrade, Belgrade, Serbia, **B.S.** Physical chemistry, June 2008

Recent Experience:
Old Dominion University, Norfolk, VA
Teaching Assistant - physics and astronomy 2008-2012
Research Assistant - geophysics 2009-2013
Hamilton College, Clinton, NY
Google Earth module developer August 2011

Recent Publications:
Dordevic, M. M., and S.C. Wild (2012), Avatars and multi-student interactions in Google Earth-based virtual field experiences, in *Google Earth and Virtual Visualizations in Geoscience Education and Research: Geological Society of America Special Paper 492*, edited by Whitmeyer, S. J., J.E. Bailey, D. G. De Paor, and T. Ornduff, T., chap.35, Geological Society of America, doi:10.1130/2012.2492(22).
Dordevic, M. M. (2012), Designing Interactive Screen Overlays to Enhance Effectiveness of Google Earth Geoscience Resources, in *Google Earth and Virtual Visualizations in Geoscience Education and Research: Geological Society of America Special Paper 492*, edited by Whitmeyer, S. J., J.E. Bailey, D. G. De Paor, and T. Ornduff, T., chap.7, Geological Society of America, doi:10.1130/2012.2492(22).
Boggs, K. J. E., and M. M. Dordevic, and S. T. Shipley (2012), Google Earth© Models with COLLADA and WxAzygy© Transparent Interface: An example from Grotto Creek, Front Ranges, Canadian Cordillera *Geoscience Canada*(39)

Typeset using LaTeX.